UNIVERSITY OF OKLAHOMA

GRADUATE COLLEGE

A COLLOID AND INTERFACE STUDY OF PER- AND POLYFLUOROALKYL SUBSTANCES (PFAS) REMOVAL FROM WATER THROUGH FOAMING

A DISSERTATION

SUBMITTED TO THE GRADUATE FACULTY

in partial fulfillment of the requirements for the

Degree of

DOCTOR OF PHILOSOPHY

By

MUCHU ZHOU
Norman, Oklahoma
2024

A COLLOID AND INTERFACE STUDY OF PER- AND POLYFLUOROALKYL SUBSTANCES (PFAS) REMOVAL FROM WATER THROUGH FOAMING

A DISSERTATION APPROVED FOR THE
SCHOOL OF SUSTAINABLE CHEMICAL, BIOLOGICAL AND MATERIALS ENGINEERING

BY THE COMMITTEE CONSISTING OF

Dr. Reza Foudazi, Chair

Dr. Brian P. Grady

Dr. Edgar A. O'Rear III

Dr. Bor-Jier (Ben) Shiau

© Copyright by MUCHU ZHOU 2024
All Rights Reserved.

This dissertation is dedicated to my beloved parents, whose unwavering love and support have been integral to my lifelong pursuit of knowledge and eventual academic accomplishments.

ACKNOWLEDGEMENTS

I am profoundly grateful to my advisor, Dr. Reza Foudazi, for his unwavering support and understanding throughout my Ph.D. journey. Since joining Dr. Foudazi's laboratory in January 2016 as a senior undergraduate at New Mexico State University, he has been a pivotal figure in my academic and professional development. Dr. Foudazi not only introduced me to the realm of scientific research but also guided me with patience and insight through its complexities. It was under Dr. Foudazi's mentorship that I first ventured into the scientific world, an experience marked by his patient guidance, mentorship, and encouragement. Dr. Foudazi's role in my development as a scientist cannot be overstated; his guidance was both a beacon and a foundation throughout my Ph.D. studies.

I extend my sincere appreciation to my dissertation committee members, Drs. Brian P. Grady, Edgar A. O'Rear, and Bor-Jier (Ben) Shiau, for their invaluable contributions, constructive feedback, and support throughout my Ph.D. project.

My research would not have been possible without the generous financial support from the Bureau of Reclamation (Grant No R21AC10418-00). I am also thankful for the access and resources provided by the Institute for Applied Surfactant Research (IASR) at the University of Oklahoma, including the use of tensiometers and foam analyzers, as well as Dr. Novruz G. Akhmedov and the NMR Facility at the same university for NMR training and analyses.

Special thanks to Dr. Javen Weston for his assistance with the SAXS, and to Dr. Zhehui Jin and Kaijie Zhang for their collaborative efforts in conducting the MD simulations. Their expertise and support have been crucial to the success of our research.

I am deeply grateful to my labmates and friends, whose camaraderie and assistance have made my Ph.D. experience both enjoyable and enriching.

Finally, I must express my heartfelt gratitude to my parents for their unconditional support and understanding. Despite initial reservations, their belief in my path to a Ph.D. has been unwavering. My journey to this point would have been impossible without them, especially considering my mother's own challenges during this time (my mother was undergoing spinal fusion surgery in China when I was writing my dissertation).

Table of Contents

List of Tables

List of Figures

Abstract

Despite their widespread use in products like nonstick pans and firefighting foams, per- and polyfluoroalkyl substances (PFAS)—a group of synthetic fluorinated organic compounds—have permeated the environment globally, particularly affecting water sources and being linked to numerous health issues. Foam fractionation offers a promising solution for separating PFAS from water by harnessing their unique surface-active properties for effective separation. Thus, a deep comprehension of PFAS's air-water interfacial properties becomes crucial for enhancing the feasibility of using foam fractionation for PFAS removal from PFAS-contaminated water in the future. However, the correlation between the interfacial properties of PFAS and their foam properties remains underexplored and not well systematically investigated. Moreover, the efficient removal of short-chain PFAS (i.e., four carbons, C4) through foam fractionation poses a significant challenge, highlighting a critical area for future research.

Hence, this dissertation initially delves into the air-water interfacial properties of PFAS, focusing on dynamic surface tension and interfacial dilatational rheology. It reveals that the PFAS with shorter chain length (C4) display lower adsorption capabilities, as indicated by the Gibbs and Langmuir isotherms, and a notable absence of interfacial dilatational modulus, likely contributing to their limited foaming capacity. In contrast, for the PFAS with longer chain length (C8), the dilatational elastic (storage) modulus is greater than the dilatational loss modulus, with both significantly influenced by the concentration and oscillation rate. A notable maximum in dilatational modulus relative to PFAS concentration aligns with predictions made using the Lucassen and van den Tempel model, highlighting the competition between molecular adsorption and molecular exchange between the air-water interface (subsurface) and the bulk for the PFAS with longer chain length (C8). In addition, according to the classic Ward-Tordai model, the

diffusion coefficients of the PFAS with longer chain length (C8) are dependent on their bulk concentrations, showcasing that, at equal concentrations, the PFAS with shorter chain length (C4) demonstrate lower diffusion coefficients.

In this dissertation, foaming and defoaming properties of PFAS are studied, demonstrating that the PFAS with longer chain length (C8), particularly those with sulfonic acid head, exhibit superior foamability, foam stability, and higher liquid retention within the foam structure. Through dimensional analysis, connections between foaming behavior and various dimensionless numbers are established. For instance, our results show that the foaming kinetics for long-chain (C8) PFAS are strongly associated with parameters such as the Reynolds and Boussinesq numbers. However, accurately predicting the foaming kinetics of short-chain (C4) PFAS proves challenging without incorporating dimensionless numbers that account for the effects of interfacial dilatational rheology. Notably, the analysis reveals a peak in the rate of foam expansion correlating with the capillary number, coinciding with the highest observed dilatational modulus. Moreover, we find a significant correlation between the defoaming properties of long-chain (C8) PFAS and dimensionless numbers, emphasizing the role of the Boussinesq number in understanding PFAS defoaming behavior.

This research also investigates the impact of electrolyte addition. It finds that introducing electrolytes lowers PFAS surface tension, increases their maximum surface excess concentration, and shifts the critical micelle concentration (CMC) to lower PFAS concentrations. The type and valence of the salts play a significant role in altering the diffusion coefficients and dilatational modulus of PFAS. For example, the addition of NaCl results in a decrease and then an increase in both the dilatational elastic and loss moduli for long-chain (C8) PFAS with sulfonic acid head, indicating changes in interfacial viscoelasticity with increasing NaCl concentration. A similar

trend but with different significance is observed, especially for dilatational elastic modulus, when $CaCl_2$ is added. This study also shows that salt addition modifies PFAS foam characteristics; notably, $CaCl_2$ enhances foam stability for long-chain (C8) sulfonic acid PFAS by affecting factors such as the Boussinesq number, the ratio of surface tension to interfacial elasticity, and the ratio of surface tension to interfacial loss modulus. Moreover, the presence of NaCl, in concentrations ranging from 5-50 mM, improves both foamability and stability for long-chain (C8) carboxylic acid PFAS, influenced by changes in the capillary number and the balance between surface tension and interfacial elasticity.

As ongoing research, to advance our understanding of how PFAS molecules interact with salt ions, preliminary investigations within the bulk phase have been conducted by using nuclear magnetic resonance (NMR) spectroscopy and small-angle X-ray scattering (SAXS). Findings from these methods suggest a preferential interaction of the sulfonic acid groups in C8 PFAS with Ca^{2+} ions, whereas the carboxylic acid groups show a tendency to interact with Na^{+} ions. Molecular dynamics (MD) simulations performed by collaborators reveal that introducing Ca^{2+} ions to long-chain (C8) sulfonic acid PFAS systems leads to the development of complex structures at the air-water interface.

Chapter 1. Introduction

1.1. Introduction to per- and polyfluoroalkyl substances (PFAS)

Per- and polyfluoroalkyl substances (PFAS) encompass a broad category of synthetic chemicals, where perfluoroalkyl compounds are fully fluorinated and polyfluoroalkyl compounds are only partially fluorinated. For perfluoroalkyl compounds, the carbon chains are entirely saturated with fluorine (F) atoms, replacing all hydrogen (H) atoms. This results in a perfluoroalkyl group ($-C_nF_{2n+1}$) that is connected to a water-loving (hydrophilic) headgroup, such as carboxylic acid (-COOH) or sulfonic acid ($-SO_3H$), with **Figure 1.1** showing the structure of perfluorooctanoic acid (PFOA) as the typical PFAS structure.[1,2] Polyfluoroalkyl substances, in contrast, feature only partial fluorine substitution. This gives PFAS molecules a hydrophilic head and a fluorinated, hydrophobic and oleophobic (lipophobic) tail,[3,4] enabling their use as surfactants.

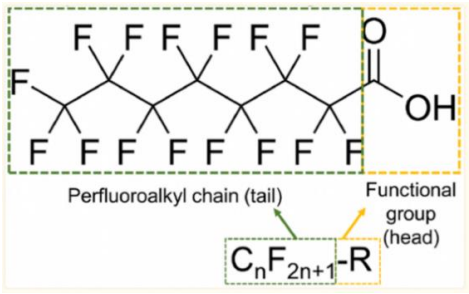

Figure 1.1 Typical structure of PFAS.

Surfactants, or surface-active agents, have the remarkable ability to migrate to and adsorb at the different interfaces (air-liquid, liquid-liquid, air-solid, liquid-solid), serving to lower the surface or interfacial energy of these systems. These compounds are ubiquitous in industrial products like soaps, detergents, and makeup removers. Due to the characteristics of their fluorinated tails and the carbon-fluorine (C-F) bonds' low polarizability, fluorinated surfactants

exhibit superior surface activity compared to hydrocarbon-based surfactants.[5] The C-F bond, being one of the strongest single bonds, displays lower polarity and higher bond energy (>481.16 kJ/mol, varying with fluorocarbon types), contributing to the persistence of PFAS in the environment and their nickname as "forever chemicals".[6–8] The bond strength of C-F increases in the order of CF_3H> CF_2H_2 > CFH_3. The polarization of the C-F bond intensifies with the addition of fluorine atoms, due to an increased partial positive charge around the carbon atom, enhancing the bond's ionic character and the energy required for its dissociation.[8]

Over 4,000 PFAS compounds (5000-10000 PFAS according to Wang et al.[6]) have been identified, exhibiting a wide range of physicochemical, thermal, and biological properties.[9] The diversity and complexity of PFAS pose significant challenges in their classification and management, crucial for the development of regulations and treatment methods for specific PFAS types. Despite extensive discussion in literature and government reports, inconsistencies in PFAS terminology persist among different authors.[3] Additionally, Buck et al.[3] have noted the growing multitude of names used to describe PFAS, with some names ambiguously referring to different compounds, highlighting the need for a standardized system for PFAS nomenclature to deliver clear and accurate names, terminology, and acronyms of PFAS. For example, both $CF_3(CF_2)_6COOH$ and $CF_3CF_2CH_2(CF_2)_4COOH$ are PFAS and carboxylic acid, but it is undesirable to call the latter fluorocarbon.[3]

1.1.1. Non-polymeric PFAS

PFAS, can be primarily categorized into two classes: non-polymers and polymers, as depicted in **Figure 1.2**, which provides a hierarchical overview of the PFAS family.[3,7,9–11] Within the non-polymer category, further subdivision identifies perfluoroalkyl and polyfluoroalkyl

substances. Notably, non-polymer PFAS are more prone to transport in wildlife and humans due to their higher reactivity and mobility.[10]

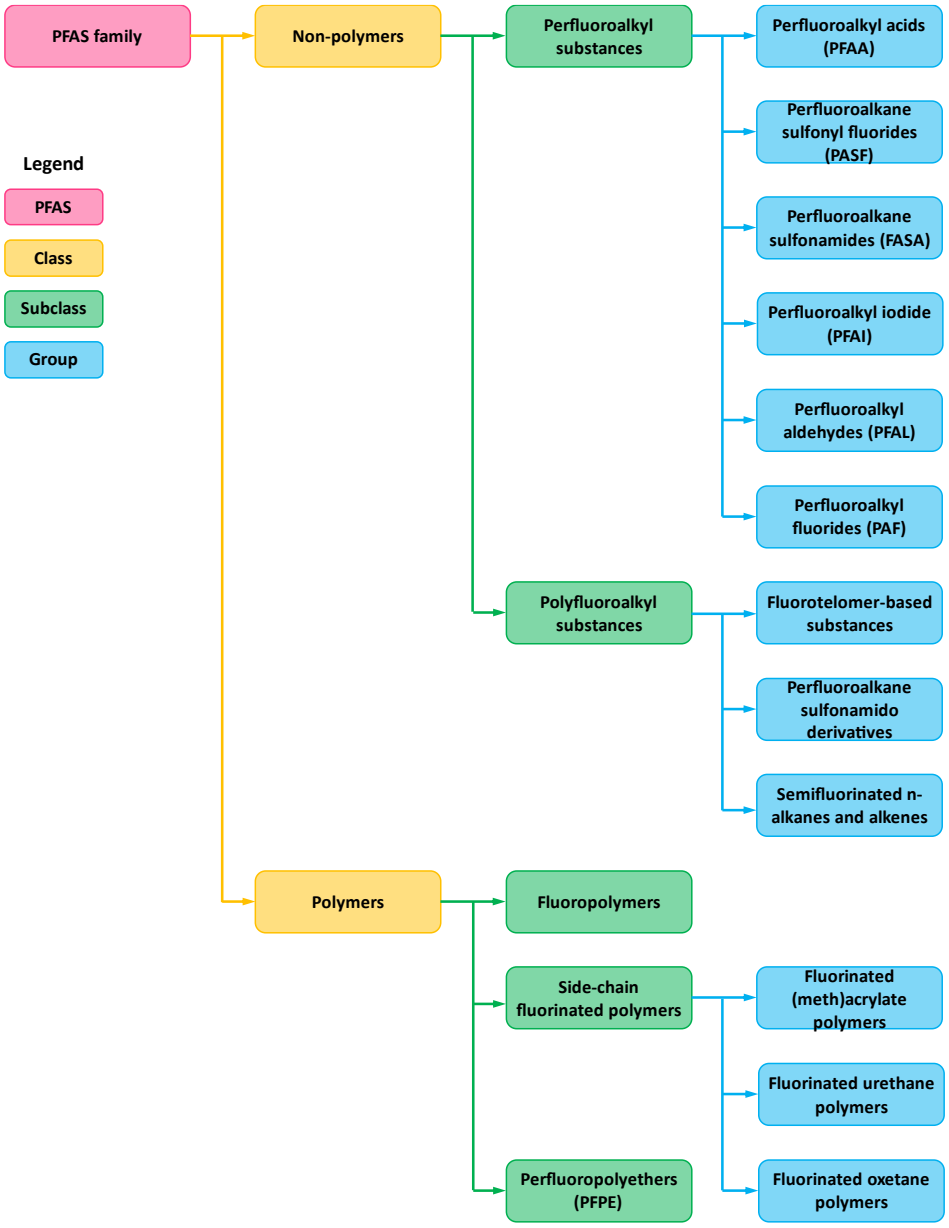

Figure 1.2 Classifications of PFAS.

1.1.1.1. Non-polymeric PFAS: carbon-chain length classification

The non-polymeric PFAS can be categorized based on the carbon-chain length.[3] Typically, PFAS are identified by the number of carbon atoms in their chain, for instance, perfluorobutanoic

acid (PFBA, n=4) and perfluorooctadecanoic acid (PFODA, n=18).[7] The Organization for Economic Co-operation and Development (OECD) and the United States Environmental Protection Agency (U.S. EPA) define long-chain PFAS as those with eight or more carbons ($n \geq 8$) if the headgroup is carboxylic acid group (-COOH), while long-chain PFAS are characterized by having six or more carbons ($n \geq 6$) if the headgroup is sulfonic acid group (-SO_3H).[2,3,7] Illustrations of typical long-chain and short-chain PFAS are provided in **Figures 1.3A** and **1.3B**, respectively. The chain length of PFAS significantly influences their physicochemical properties: long-chain PFAS typically exhibit a molecular weight exceeding 400 g/mol, reduced water solubility (e.g., 3.2×10^{-3} mg/L for polyfluorooctanesulfonic acids, PFOS, at 25 ℃), enhanced lipophilicity (e.g., $\log K_{ow} = 4.49$ for PFOS), decreased surface tension (approximately 45 mN/m for 200 ppm PFOS potassium salt in water, as determined by our research), and increased hydrophobicity.

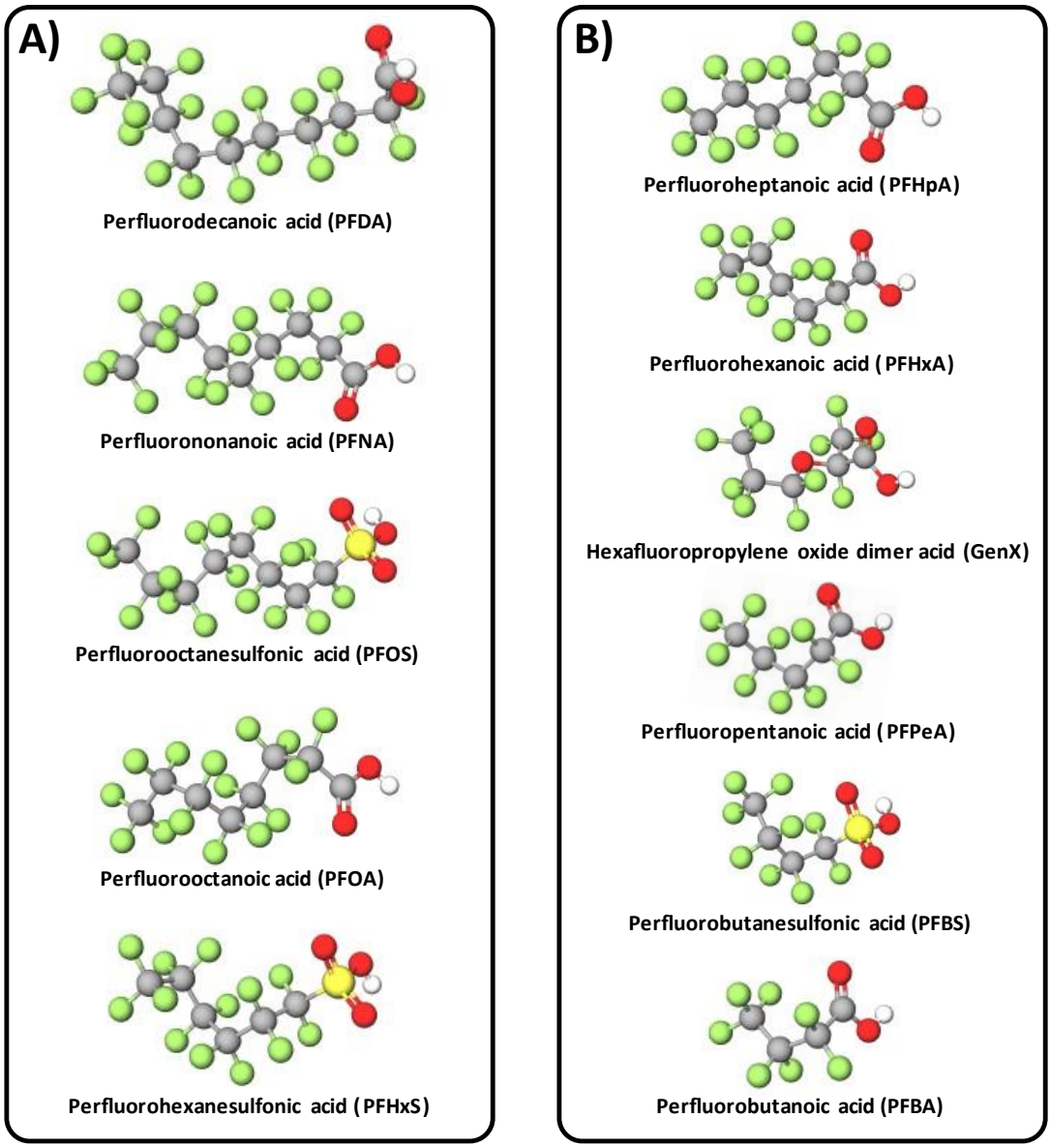

Figure 1.3 Structure of typical A) long-chain and B) short-chain non-polymeric PFAS.

Unlike long-chain PFAS, short-chain PFAS such as perfluorobutanesulfonic acid (PFBS) possess higher solubility in water (344 mg/L at at 25 ℃), reduced lipophilicity ($\log K_{ow} = 1.82$ for PFBS), and increased surface tension (around 59 mN/m for 200 ppm aqueous solutions of PFBS potassium salt, as determined by our research), enhancing their hydrophilicity.[2] The short-chain PFAS have been used as an alternative to replace the long-chain PFAS due to their reduced bioaccumulation in living organisms to avoid the toxicity problems.[7] However, efforts to replace

PFOS with short-chain alternatives like F-53B (2-[(6-chloro-1,1,2,2,3,3,4,4,5,5,6,6-dodecafluorohexyl)oxy]-1,1,2,2-tetrafluoroethanesulfonic acid potassium salt) have not fully addressed toxicity and bioaccumulation concerns. Additionally, F-53B's degradation challenges and similarity in bioaccumulation rates to PFOS indicate that simply substituting PFOS with short-chain PFAS does not eliminate the risks associated with these substances.[12]

1.1.1.2. Non-polymeric PFAS: perfluoroalkyl substances

Perfluoroalkyl substances can often be derived from polyfluoroalkyl substances under suitable conditions, exemplified by the transformation of $C_nF_{2n+1}SO_2NHCH_2CH_2OH$ into $C_nF_{2n+1}SO_3H$ in the environment.[3] Among these, perfluoroalkyl acids (PFAA) are the most commonly encountered and are considered the most toxic. PFAA are frequently highlighted in research and regulatory efforts not only because they are widely utilized in various applications, also because they are the terminal products from the degradation of fluoropolymers.[3,7]

PFAA can be further divided, based on their functional headgroups (i.e., -COOH or $-SO_3H$), into perfluoroalkyl carboxylic acids (PFCA) and perfluoroalkyl sulfonic acids (PFSA), as detailed in **Table 1.1**.[6] PFOS and perfluorooctanoic acids (PFOA), shown in **Figure 1.3**, are among the most detected and discussed PFAA in environmental studies.[3] Ammonium perfluorooctanoate (APFO), once used to prevent the production of lower molecular weight polymers, saw its phase-out in 2002. Sulflon® S-111, the ammonium salt of perfluorononanoic acid (PFNA), serves as another industrial example of PFCA. Additionally, PFSA tend to be more bioaccumulative than PFCA of equivalent chain length.[2,3] Giesy et al.[13] reported the detection of PFOS in the human body in 2001, leading to the discontinuation of production for long-chain PFSA including perfluorodecanesulfonic acid (PFDS), PFOS, perfluorohexanesulfonic acid (PFHxS) and their precursors in 2002. Beyond PFCA and PFSA, the PFAA group also encompasses perfluoroalkyl

sulfinic acids (PFSiA), perfluoroalkyl phosphonic acids (PFPA), and perfluoroalkyl phosphinic acids (PFPiA), as shown in **Table 1.1**. Other notable perfluoroalkyl substances include perfluoroalkyl sulfonyl fluoride (PASF), perfluoroalkyl sulfonamides (FASA), perfluoroalkyl iodides (PFAI), perfluoroalkyl aldehydes (PFAL), and perfluoroalkyl fluorides (PAF), with PASF and FASA noted for their potential to degrade into PFAA.[3,11]

Table 1.1 Classifications, chemical structure, and examples of perfluoroalkyl substances.

Group	Subgroup	Chemical formula	Examples	Uses
Perfluoroalkyl acid (PFAA)	Perfluoroalkyl carboxylic acids (PFCA)	C_nF_{2n+1}-COOH	Perfluorobutanoic acid (PFBA, n=4)	Surfactants
			Perfluoropentanoic acid (PFPeA, n=5)	
			Perfluorohexanoic acid (PFHxA, n=6)	
			Perfluoroheptanoic acid (PFHpA, n=7)	
			Perfluorooctanoic acid (PFOA, n=8)	
			Perfluorononanoic acid (PFNA, n=9)	
			Perfluorodecanoic acid (PFDA, n=10)	
			Perfluoroundecanoic acid (PFUnA, n=11)	
			Perfluorododecanoic acid (PFDoA, n=12)	
			Perfluorotridecanoic acid (PFTrA, n=13)	
			Perfluorotetradecanoic acid (PFTeA, n=14)	
	Perfluoroalkyl carboxylates (PFCA)	C_nF_{2n+1}-COO^-M^+	Sodium perfluorooctanoate (NaPFO, n=8)	
			Ammonium perfluorooctanoate (APFO, n=8)	
	Perfluoroalkyl sulfonic acids (PFSA)	C_nF_{2n+1}-SO_3H	Perfluorobutanesulfonic acid (PFBS, n=4)	
			Perfluoropentanesulfonic acid (PFPeS, n=5)	
			Perfluorohexanesulfonic acid (PFHxS, n=6)	
			Perfluoroheptanesulfonic acid (PFHpS, n=7)	
			Perfluorooctanesulfonic acid (PFOS, n=8)	
			Perfluorononanesulfonic acid (PFNS, n=9)	

			Perfluorodecanesulfonic acid (PFDS, n=10)	
	Perfluoroalkyl sulfonnates (PFSA)	C_nF_{2n+1}-SO_3^- M^+	Potassium perfluorooctanesulfonate (KPFOS, n=8)	
	Perfluoroalkyl sulfinic acids (PFSiA)	C_nF_{2n+1}-SO_2H	Perfluorooctanesulfinic acid (PFOSi)	Intermediate environmental transformation products
	Perfluoroalkyl phosphonic acid (PFPA)	C_nF_{2n+1}-PO_3H_2	Pentafluorobenzylphosphonic acid (PFBPA, n=4)	Surfactants
			Perfluorohexylphosphonic acid (PFHxPA, n=6)	
			Perfluorooctylphosphonic acid (PFOPA, n=8)	
			Perfluorodecylphosphonic acid (PFDPA, n=10)	
	Perfluoroalkyl phosphinic acid (PFPiA)	C_nF_{2n+1}-PO_2H-C_mF_{2m+1}	Bis(perfluorooctyl)phosphinic acid (PFOPiA, n=8)	
Perfluoroalkyl sulfonyl fluoride (PASF)		C_nF_{2n+1}-SO_2F	Perfluorooctane sulfonyl fluoride (POSF, n=8)	Raw materials for surface coating products, and surfactants
			Perfluorobutane sulfonyl fluoride (PBSF, n=4)	
Perfluoroalkyl sulfonamides (FASA)		C_nF_{2n+1}-SO_2NH_2	Perfluorooctane sulfonamide (FOSA, n=8)	
Perfluoroalkyl iodide (PFAI)		C_nF_{2n+1}-I	Perfluorohexyl iodide (PFHxI, n=6)	
Perfluoroalkyl aldehydes (PFAL)		C_nF_{2n+1}-CHO	Perfluorononanal (PFNAL, n=8)	Intermediate environmental transformation products
Perfluoroalkyl fluorides (PAF)		C_nF_{2n+1}-COF	Perfluorooctanoyl fluoride (POF, n=7)	Raw materials for PFOA production, surface coating products, and surfactants

Note: **Table 1.1** is generated according to Buck et al., Wang et al., Phong Vo et al., Ambaye et al., and States Environmental Protection Agency.[3,6,7,10,11]

1.1.1.3. Non-polymeric PFAS: polyfluoroalkyl substances

PFAA typically originate from precursors such as fluorotelomer-based substances and perfluoroalkane sulfonamido-based substances, which fall under the broader category of polyfluoroalkyl substances, as depicted in **Figure 1.2**.[3,6,11] **Table 1.2** outlines the polyfluoroalkyl substance family. The inception of industrial applications for fluorotelomer-based products can be

traced back to the utilization of two primary raw materials: PFAI and n:2 fluorotelomer iodides (n:2 FTI), as highlighted in **Tables 1.1** and **1.2**, respectively. These substances were first detected in environmental samples approximately a decade or more ago.[3] It is notable that compounds such as n:2 FTI, n:2 fluorotelomer alcohols (n:2 FTOH), and n:2 fluorotelomer olefins (n:2 FTO) have been identified in the atmosphere, underscoring their pervasive presence.[14] The alternative names for n:2 polyfluoroalkyl phosphoric acid esters (PAP) are polyfluoroalkyl phosphates and fluorotelomer phosphates. These compounds are differentiated by the number of -CH_2CH_2O- groups they contain, with monoesters (monoPAP) and diesters (diPAP) denoting the specific variants. Both monoPAP and diPAP have found use as defoaming agents in pesticide formulations, leading to their detection in both environmental and human serum samples.[3,15] This widespread distribution and the transformation of PFAA precursors into PFAA highlight the complex lifecycle of these chemicals and their persistent nature in both the environment and biological systems.

Table 1.2 Classifications, chemical structure, and examples of polyfluoroalkyl substances.

Group	Subgroup	Chemical formula	Examples	Uses
Fluorotelomer-based substances	n:2 Fluorotelomer alcohols (n:2 FTOH)	C_nF_{2n+1}-CH_2CH_2OH	10:2 Fluorotelomer alcohol (10:2 FTOH)	Raw materials for surface coating products, and surfactants
	n:2 Fluorotelomer iodides (n:2 FTI)	C_nF_{2n+1}-CH_2CH_2I	8:2 Fluorotelomer iodide (8:2 FTI)	
	n:2 Fluorotelomer olefins (n:2 FTO)	C_nF_{2n+1}-$CH=CH_2$	6:2 Fluorotelomer olefin (6:2 FTO)	
	n:2 Fluorotelomer acrylates (n:2 FTAC) and methacrylates (n:2 FTMAC)	C_nF_{2n+1}-$CH_2CH_2OC(O)CH=CH_2$ and C_nF_{2n+1}-$CH_2CH_2OC(O)C(CH_3)=CH_2$	8:2 Fluorotelomer acrylate (8:2 FTAC)	Raw materials for fluorotelomer-based polymers used in surface coating products
			6:2 Fluorotelomer methacrylate (6:2 FTMAC)	
	n:2 Polyfluoroalkyl phosphoric acid esters (PAP)	C_nF_{2n+1}-$CH_2CH_2OP=O(OH)_2$ and C_nF_{2n+1}-$(CH_2CH_2O)_2P=OOH$	8:2 Fluorotelomer phosphate diester (8:2 diPAP)	Surfactants and surface

			8:2 Fluorotelomer phosphate monoester (8:2 monoPAP)	coating products
	n:2 Fluorotelomer sulfonic acids (FTSA)	C_nF_{2n+1}-$CH_2CH_2SO_3H$	8:2 Fluorotelomer sulfonic acid (8:2 FTSA)	Surfactants and intermediate environmental transformation products
	n:2 Fluorotelomer carboxylic acids (FTCA)	C_nF_{2n+1}-CH_2COOH	8:2 Fluorotelomer carboxylic acid (8:2 FTCA)	Intermediate environmental transformation products
Perfluoroalkane sulfonamido derivatives	N-alkyl perfluoroalkane sulfonamides (FASA)	C_nF_{2n+1}-SO_2NH- C_mH_{2m+1}	N-Ethyl perfluorobutane sulfonamide (EtFBSA)	Surfactants and surface coating products
			N-Methyl perfluorooctane sulfonamide (MeFOSA)	
			N-Butyl perfluorooctane sulfonamide (BuFOSA)	
	(N-alkyl) Perfluoroalkane sulfonamidoethanols (FASE)	C_nF_{2n+1}-$SO_2NCH_2CH_2OH$-C_mH_{2m+1}	Perfluorooctane sulfonamidoethanol (FOSE)	
			N-Ethyl perfluorobutane sulfonamidoethanol (EtFBSE)	
	N-alkyl perfluoroalkane sulfonamidoethyl acrylates and methacrylates [FAS(M)AC]	C_nF_{2n+1}-$SO_2NCH_2CH_2OC$=OCH=CH_2-C_mH_{2m+1} and C_nF_{2n+1}-$SO_2NCH_2CH_2OC$=$OC(CH_3)$=CH_2-C_mH_{2m+1}	N-Ethyl perfluorooctane sulfonamidoethyl acrylate (EtFOSAC)	
	(N-alkyl) Perfluoroalkane sulfonamido acetic acids (FASAA)	C_nF_{2n+1}-SO_2NCH_2COOH-C_mH_{2m+1}	N-Ethyl perfluorooctane sulfonamidoacetic acid (EtFOSAA)	Intermediate environmental transformation products
Semifluorinated n-alkanes and alkenes	Per- and polyfluoroalkanes and per- and polyfluoroalkenes	C_nF_{2n+1}-$(CH_2)_mH$ and C_nF_{2n+1}-CH=$CH(CH_2)_{m-2}H$	Perfluorohexylhexadecane	Ski wax and medical applications
	Per- and polyfluoroether carboxylic acid (PFECA)	C_nF_{2n+1}-O-C_mF_{2m+1}-O-$CHF(C_PF_{2P})$-$COOH$	4,8-Dioxa-3H-perfluorononanoate (DONA)	Alternatives for long-chain PFAA
			Hexafluoropropylene oxide dimer acid (HFPO-DA)	

	Per- and polyfluoroether sulfonic acid (PFESA)	C_nF_{2n+1}-O-C_mF_{2m+1}-O-CHF(C_PF_{2P})-SO_3H	Chlorinated PFESA	

Note: **Table 1.2** is generated according to Buck et al., and States Environmental Protection Agency.[3,11]

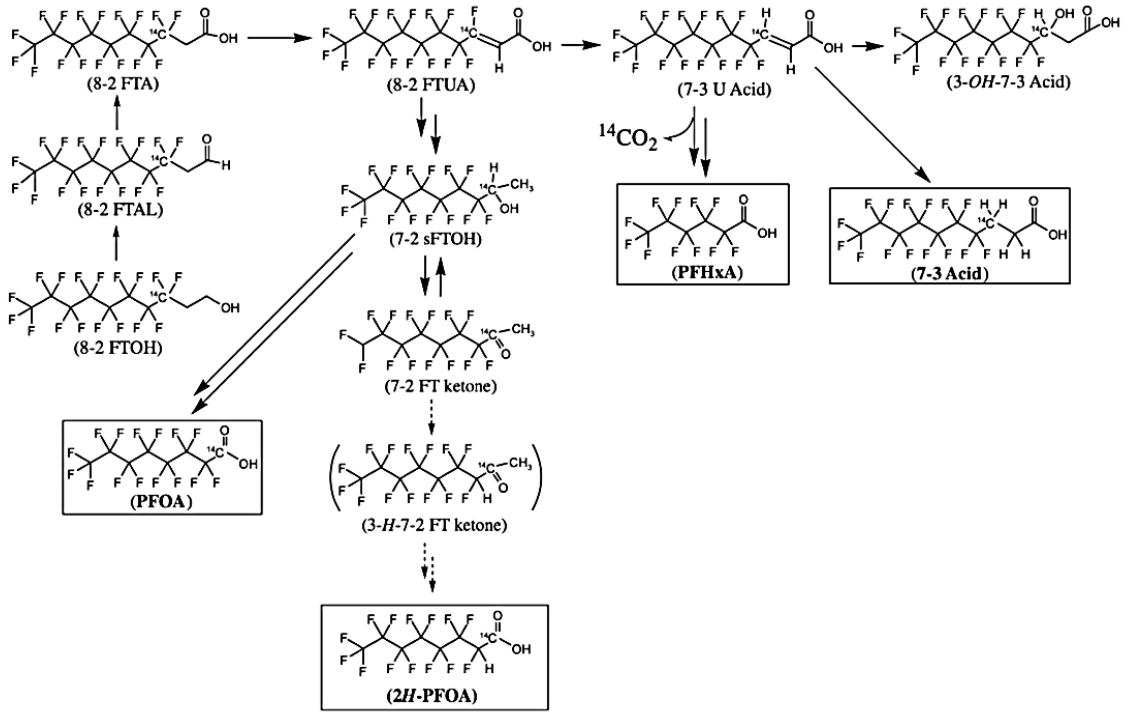

Figure 1.4 Biodegradation pathways of 8:2 fluorotelomer alcohol proposed by Wang et al.[16]

Figure 1.4, based on the work of Wang et al.,[16] outlines the biotransformation pathways of 8:2 FTOH, highlighting its environmental and biological transformation. Perfluoroalkane sulfonamido substances are characterized by their fully fluorinated tails and sulfonamido head groups, with an additional -C_mH_{2m+1} group attached to the sulfonamido group. These substances, including perfluoroalkane sulfonamides (FASA) and perfluoroalkane sulfonamidoethanols (FASE), serve as foundational components (building blocks) for manufacturing various fluorinated products, such as those used in surface coating treatments. Similar to fluorotelomer-based compounds, perfluoroalkane sulfonamido substances have been detected in both the

environment and the human body. The degradation of perfluoroalkane sulfonamido substances, as shown in **Figure 1.5**,[3] typically leads to the formation of long-chain PFAA, with PFOA and PFOS being among the most significant outcomes.

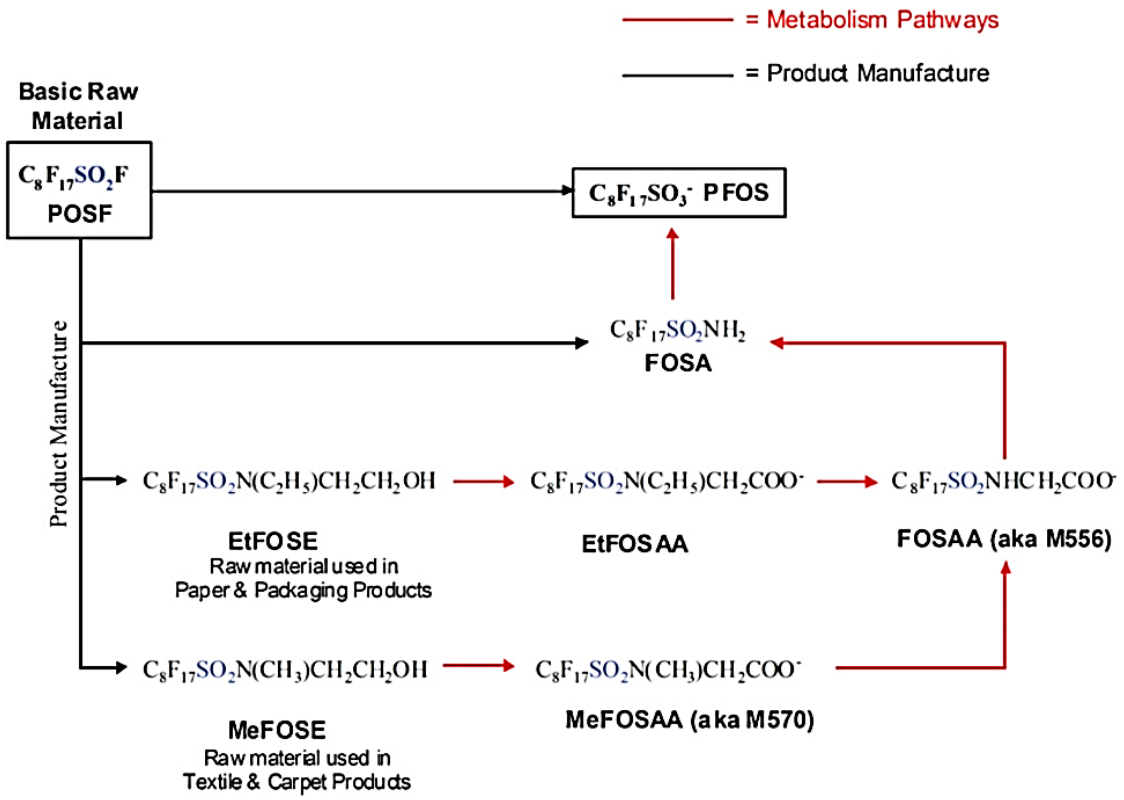

Figure 1.5 Transformation pathways of perfluoroalkane sulfonamido substances.[3]

1.1.1.4. Non-polymeric PFAS: other classifications

As identified by Buck et al.,[3] non-polymeric PFAS can also be sorted by their structural configurations into linear or branched categories. Environmental samples typically feature PFOS as a blend of linear carbon chains and a multitude of branched isomers. This insight underlines the importance of future research on PFAS isomers, focusing on their development and properties. Such studies are crucial for tracing PFAS contamination back to its source, given that distinct

manufacturing and degradation pathways produce various PFAS isomers. Understanding these differences is essential for accurately determining the origins and impacts of PFAS.[3]

1.1.2. Polymeric PFAS

Polymeric PFAS are categorized into three main subgroups: fluoropolymers, side-chain fluorinated polymers, and perfluoropolyethers (PFPE), each distinguished by their structural characteristics and applications, as summarized in **Table 1.3**. Fluoropolymers (also known as fluoroplastics) are recognized for their carbon-only polymer backbones with fluorine atoms directly bonded to them. In certain contexts, these materials are specifically referred to as perfluoropolymers, distinguishing them from partially fluorinated polymers or fluoroelastomers.[3,17] An example of a perfluoropolymer is polytetrafluoroethylene (PTFE), widely known for its use in non-stick cookware. Ethylene tetrafluoroethylene copolymer (ETFE) serves as an example of a partially fluorinated polymer. Compared to perfluoropolymers, partially fluorinated polymers exhibit distinct properties; for instance, perfluoropolymers tend to be more stable and softer. Ammonium salts of PFOA or perfluorononanoic acid (PFNA) are often employed as fluorosurfactant additives (processing aids) in the manufacture of fluoropolymers with a certain grade.[3]

Table 1.3 Classifications, chemical structure, and examples of polymeric PFAS.

Subclass	Examples	Chemical formula	Uses
Fluoropolymers	Polytetrafluoroethylene (PTFE)	$-(CF_2CF_2)_n-$	Plastics
	Fluorinated ethylene propylene (FEP)	$-(CF_2CF_2)_n-(CF(CF_3)CF_2)_m-$	
	Perfluoroalkoxyl (PFA)	$-(CF_2CFORCF_2)_n-$	
	Polyvinyl fluoride (PVF)	$-(CH_2CHF)_n-$	
	Polychlorotrifluoroethylene (PCTFE)	$-(CH_2CFCl)_n-$	
	Polyvinylidene fluoride (PVDF)	$-(CH_2CF_2)_n-$	
	Ethylene tetrafluoroethylene copolymer (ETFE)	$-(CH_2CH_2CF_2CF_2)_n-$	

	Ethylene chlorotrifluoroethylene copolymer (ECTFE)	-$(CH_2CH_2CF_2CFCl)_n$-	
Side-chain fluorinated polymers	Fluorinated acrylate polymers	Backbone-CH-C=OO-$CH_2CH_2N(C_nH_{2n+1})SO_2$- -$C_nF_{2n+1}$ or Backbone-CH-C=OO-$CH_2CH_2N(CH_2CH_2)SO_2$-C_nF_{2n+1}	Surfactants and surface coating products
	Fluorinated methacrylate polymers	Backbone-$C(CH_3)$-C=OO-$CH_2CH_2N(C_nH_{2n+1})SO_2$- -$C_nF_{2n+1}$ or Backbone-$C(CH_3)$-C=OO-$CH_2CH_2N(CH_2CH_2)SO_2$-C_nF_{2n+1}	
	Fluorinated urethane polymers	Backbone-NHC=OO-$CH_2CH_2N(C_nH_{2n+1})SO_2$-$C_nF_{2n+1}$ or Backbone-NHC=OO-$CH_2CH_2N(CH_2CH_2)SO_2$-C_nF_{2n+1}	
	Fluorinated oxetane polymers	Backbone-CH_2OCH_2-CF_3 or Backbone-CH_2OCH_2-C_2F_5 or Backbone-CH_2OCH_2-$CH_2C_4F_9$	
Perfluoropolyethers (PFPE)		F-$(C_mF_{2m}O)_n$-CF_3	Surfactants, surface coating products, and functional fluids
		$HOCH_2O$-$(C_mF_{2m}O)_n$-CH_2OH	

Note: **Table 1.3** is generated according to Buck et al., and Ebnesajjad.[3,17]

On the contrary, side-chain fluorinated polymers do not possess per- or polyfluorinated backbones. Instead, they contain a backbone with variable composition with per- or polyfluoroalkyl side chains attached. This structure allows for the potential breakdown of these side chains into PFAA, raising concerns regarding their environmental persistence and potential health impacts. The side-chain fluorinated acrylate polymers are extensively utilized in the textile industry as surface coating materials. The key attribute that makes these polymers particularly valuable is their ability to repel water, stains, and oils, making them ideal for producing waterproof

or stain-resistant fabrics. The side-chain fluorinated oxetane polymers are employed mainly as fluorosurfactants and coating additives.[3]

PFPE are distinguished by the presence of -CF_2-, -CF_2CF_2-, and -$CF(CF_3)CF_2$- groups along their backbone, interspersed with oxygen atoms. They are also considered to be the most stable and inert polymers, attributed to the highly electronegative C-F bond.[3,17] The polymeric PFAS are notable for their insolubility in most organic solvents, with the exception of Teflon® amorphous polymers (AF), and lack surface activity. These polymers can contaminate the environment in form of microplastics.[18] The substitution of hydrogen with fluorine atoms in carbon chains bestows numerous beneficial and unique properties; for example, minor fluorination of a polyolefin film can transform its surface to become polar and neutral, enhancing its adhesiveness.[17] Over recent decades, a diverse array of polymeric PFAS has been synthesized to leverage these unique characteristics, including but not limited to fluorinated elastomers, fluorinated polyolefins, fluorinated polymethyl siloxane, fluorinated poly(meth)acrylates, and PFPE. The forthcoming Subchapter will delve into the historical context and applications of fluorinated compounds, which have significantly contributed to the global dissemination of PFAS.

1.2. The history of PFAS and their dissemination in the environment

PFAS have found widespread use across a variety of sectors, including aqueous film forming foams (AFFFs), non-stick cookware, pharmaceuticals, cosmetics, textiles, food packaging, surfactants, and semiconductors, thanks to their exceptional physicochemical characteristics such as water and oil repellency, alongside remarkable thermal and chemical stability.[1,7,12,17,19–21] The genesis of PFAS can be traced back to chemical explorations by DuPont in the 1930s, with the invention of PTFE often celebrated as a fortuitous blend of genius and chance within Dr. Roy Plunkett's quest for safer, more reliable fluorinated refrigerants.[17,22] Concurrently, in the 1930s,

foundational theories on polymer structures began to take shape. Between 1945 and 1947, Teflon®, DuPont's brand name for PTFE, gained international fame. Remarkably, Teflon® continues to be produced today, standing out among various fluorinated compounds for its longevity.[17,22] A timeline highlighting key milestones in PFAS development is depicted in **Figure 1.6**.

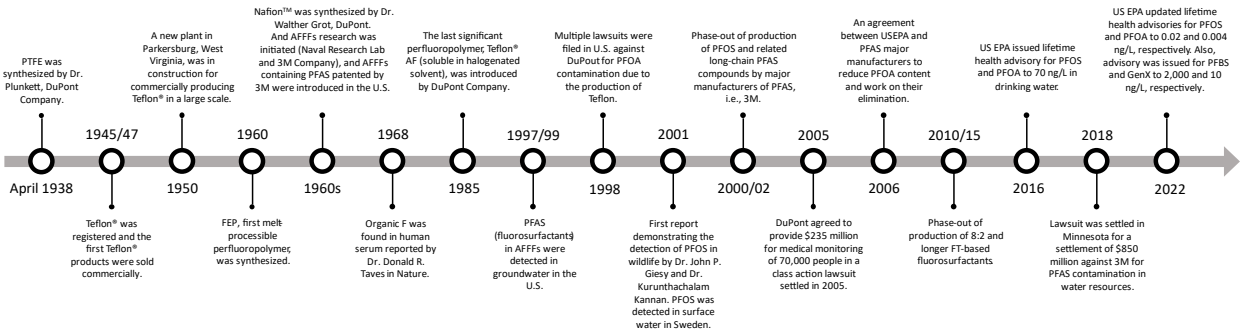

Figure 1.6 Timeline showing the events associated with PFAS development.

Figure 1.7 captures a momentous page from Dr. Plunkett's notebook, detailing his groundbreaking discovery of PTFE. While Dr. Plunkett's identification of this novel white powder marked a significant breakthrough, its practical applications remained uncertain until its potential was recognized by Lieutenant General Leslie Richard Groves, the director of the Manhattan Project. General Groves was in search of a material resistant to corrosion that could be utilized in the uranium enrichment process for atomic weapons development, leading to PTFE being designated as "K-416" and placed under a "Secrecy Order" by the U.S. Patent Office, due to its strategic importance.[17] In the years following, the Teflon® family saw significant expansions. In 1960, a copolymer of hexafluoropropylene and tetrafluoroethylene known as fluorinated ethylene propylene (FEP) was introduced, marking the first melt-processible perfluoropolymer. A decade later, in 1970, DuPont introduced ethylene tetrafluoroethylene copolymer (ETFE) resins under the brand name Tefzel™. This innovation was followed in 1972 by the introduction of another significant category of fluoropolymers within the Teflon® brand, perfluoroalkoxy alkane (PFA,

copolymers of tetrafluoroethylene and perfluoroethers). These developments underscored the versatile and expanding applications of fluoropolymers, cementing DuPont's role in pioneering fluoropolymer technology.

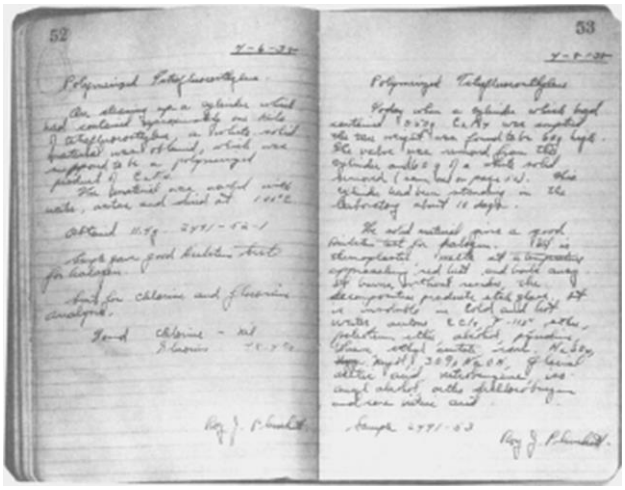

Figure 1.7 Photograph of the notebook page of Dr. Roy Plunkett, showing the discovery of PTFE (Teflon®) by DuPont Company in 1938.[17]

Following DuPont's successful development and mass production of Teflon®, a diverse range of other fluoropolymers have been brought to market. Among these, Dyneon™ fluorothermoplastics, introduced by 3M™, encompasses a broad-spectrum including PTFE, PFA, FEP, tetrafluoroethylene-hexafluoropropylene-vinylidene fluoride (THV), and polyvinylidene fluoride (PVDF). Additionally, polychlorotrifluoroethylene (PCTFE), initially produced by 3M Company and branded as Kel-F®, saw its production ceased by 3M in 1995, after which the brand was acquired by Daikin and rebranded as Neoflon™. A notable innovation in the field of fluoropolymers was the discovery of Nafion® (structure shown in **Figure 1.8**) by Dr. Walther Grot of DuPont in the 1960s. Nafion® is a unique sulfonated tetrafluoroethylene-based side-chain fluorinated polymer, synthesized through the copolymerization of perfluorinated vinyl ether monomers with tetrafluoroethylene.[23]

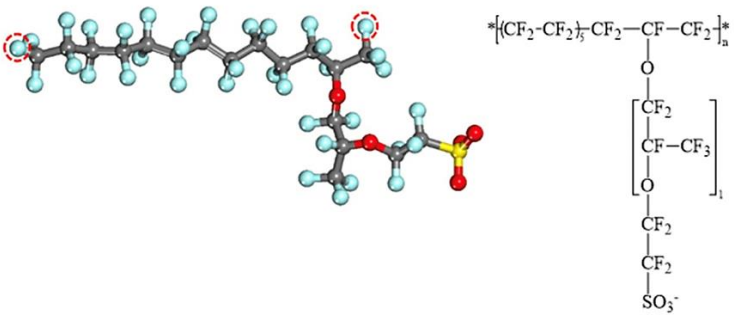

Figure 1.8 Typical chemical structure of Nafion®.[24]

In addition to DuPont's pioneering work with Nafion®, several other companies have developed similar materials, highlighting the global interest and diverse applications of Nafion-like materials. For instance, Aciplex® was developed by Asahi Chemical Company, Flemion® by Asahi Glass Company, and fumapem®F by Fumatech GmbH.[23,25] Dow Chemical Company introduced a variant of Nafion® with a modified side chain featuring a single ether oxygen (-O-CF_2-CF_2-SO_3H), showcasing the versatility and adaptability in the design of these materials.[23] Originally, the development of Nafion® was driven by its potential as a permselective membrane for ion separation in electrochemical cells, aimed at large-scale production of NaOH and Cl_2. However, research interest soon expanded to its application as proton-conducting membranes for fuel cells, illustrating the material's versatility.[23] In recent years, Nafion® and similar materials have found wide-ranging applications, including ion exchange membranes for the chlor-alkali electrolysis process,[26] water electrolysis,[27] polymer electrolyte membranes for fuel cells,[23–25,28] and as humidity sensors.[29]

Despite their ongoing production and widespread use, research into Nafion® materials continues, driven by the need to address certain limitations such as performance degradation at high temperatures (≥ 80 °C) and cost concerns. These challenges also highlight the environmental consideration of potential PFAA release, as the per- or polyfluoroalkyl side chains may break

down.[28,30] Nevertheless, the global production of fluorinated polymers remains substantial, with an estimated 273,000 metric tons of fluoropolymers and 30,000 metric tons of fluoroelastomers produced in 2012–2013.[10]

It should be mentioned that the Nafion materials are still in production, and many research groups have been working on improving the performance of Nafion due to its limitations, i.e., performance lost at high temperature (≥ 80 ℃) and expensiveness, hence, giving rise to the potential of PFAA release as the per- or polyfluoroalkyl side chains break down.[28,30] To date, the global production of fluorinated polymers is still quite large, for example, the estimated production of fluoropolymers and fluoroelastomers in 2012–2013 was 273,000 and 30,000 metric tons, respectively.[10]

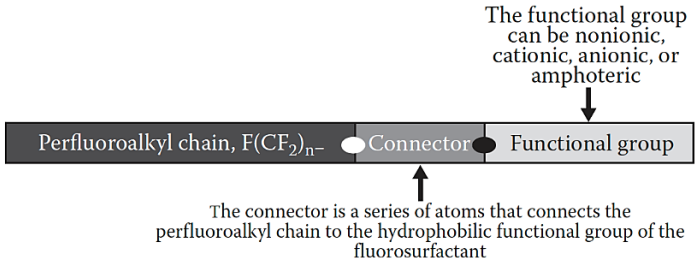

Figure 1.9 Typical commercial fluorinated surfactant schematic.[4]

AFFFs, formulated with perfluorinated compounds, are a primary source for the dissemination of PFAS, as these substances infiltrate soil and subsequently enter aquatic ecosystems, including both groundwater and surface waters.[7,10] Furthermore, PFAS contamination has been identified across numerous military training sites and civilian airports, attributed to the extensive application of AFFFs in firefighting drills and exercises.[21] Previously noted, PFAS function as surface-active agents, with the history of PFAS-based surfactants (fluorinated surfactants) spanning over 70 years to date. **Figure 1.9** depicts a common commercial fluorinated surfactant, featuring either an ionic, nonionic, or amphoteric functional group linked to a

perfluoroalkyl chain ($CF_3(CF_2)_n$-). This perfluoroalkyl chain is more rigid compared to hydrocarbon chains, a characteristic attributed to the strength of the C-F bonds. As discussed in Subchapter *1.1*, the perfluoroalkyl chain's hydrophobic and oleophobic properties, combined with its low surface energy, enable fluorocarbon surfactant molecules to move toward the air-liquid interface. Furthermore, the distinctive adsorption and aggregation behavior of fluorocarbon surfactants is linked to their ionic characteristics, the substantial molecular volume, and the rigidity of the perfluoroalkyl moiety.[4]

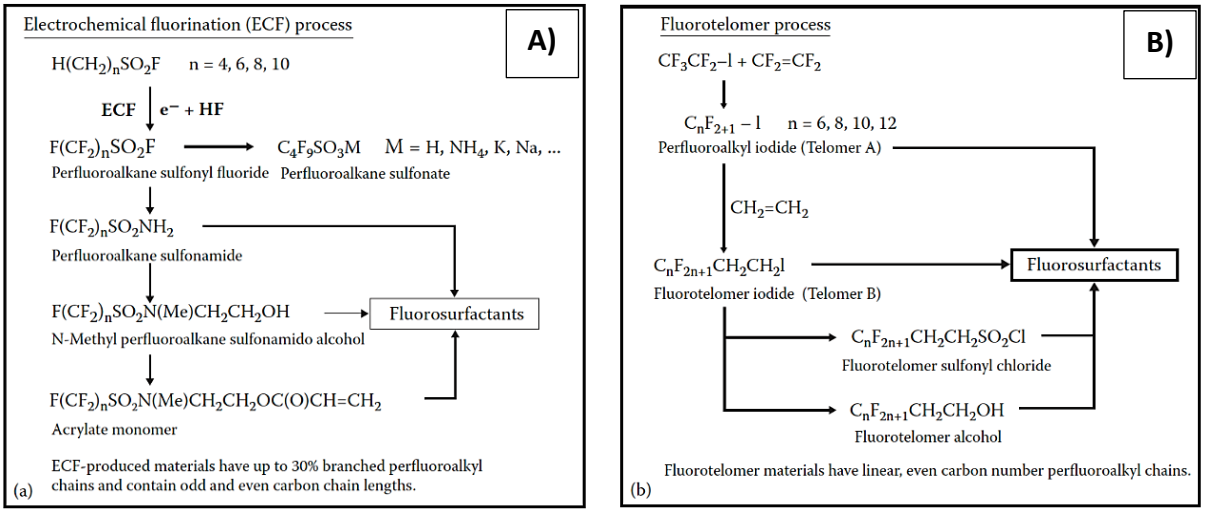

Figure 1.10 Two principal commercial processes of production of perfluoroalkyl moiety including A) electrochemical fluorination (ECF) process, and B) telomerization process.[4]

The initial generation of commercially available fluorosurfactants includes PFSA (such as PFOS) and PFCA (such as PFOA), manufactured through the electrochemical fluorination (ECF) process. This method, a free radical reaction, produces a mix of both linear and branched perfluoroalkyl substances.[4] **Figure 1.10A** illustrates the primary commercial method for producing fluorosurfactants via the electrochemical fluorination (ECF) process. Subsequent to the ECF technique, a different production method known as the fluorotelomer process emerged approximately 10-15 years later, depicted in **Figure 1.10B**. Since the 1960s, fluorosurfactants have

been integral to aqueous film-forming foams (AFFFs), developed to combat large-scale fires fueled by hydrocarbon liquids and polar solvents. The use of AFFFs, enriched with fluorosurfactants known for their superior film-forming capabilities, has been pivotal in effectively managing such fires globally.[31]

Prior to the development of AFFFs, water was the initial substance utilized as a firefighting foam. Nevertheless, the use of water alone to tackle fires caused by hydrocarbon liquids or polar solvents proved highly ineffective due to a greater density of water. The introduction of foam-based firefighting agents solved this problem because the foams are always on the top of water. The first firefighting foams, developed in the 1910s to combat organic liquid fires, consisted of aqueous solutions of acidic aluminum sulfate, sodium bicarbonate, and saponin, which served as the foaming agent. Nonetheless, this early formula struggled to produce efficient foams.[4] A breakthrough came in the 1930s with a new foam formulation that employed water-soluble protein as the foaming agent. The exploration into film-forming fluoroprotein (FFFP) and AFFFs began in earnest in 1963, with significant research conducted by the Naval Research Laboratory and 3M Company. The USS Forrestal disaster in 1967 significantly hastened the widescale adoption of fluorosurfactant-enriched firefighting foams, demonstrating their critical importance in modern firefighting efforts.

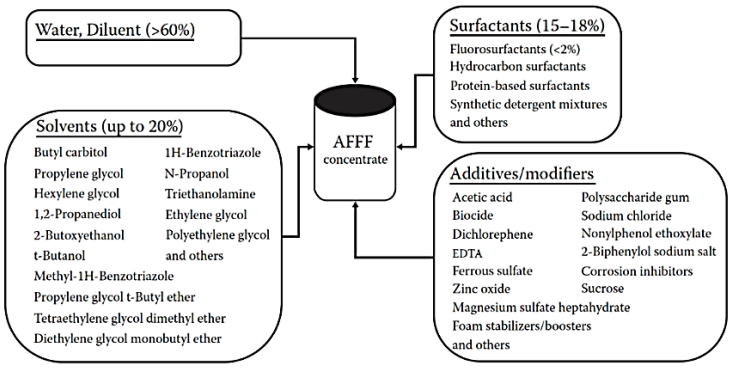

Figure 1.11 Typical composition of AFFF concentrate.[4]

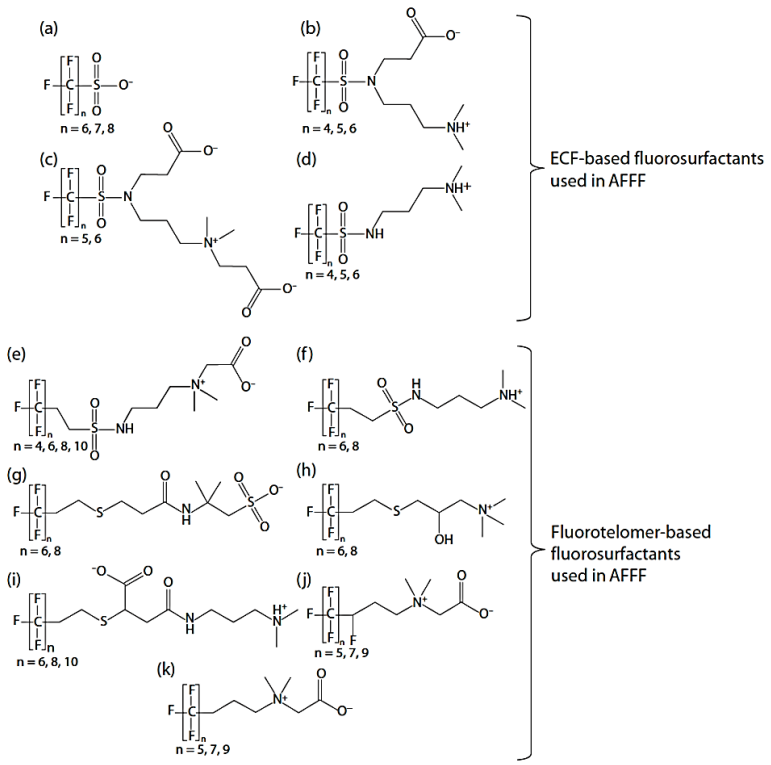

Figure 1.12 Common fluorosurfactants used in the formulation of AFFFs.[4]

AFFFs are specifically deployed to tackle Class B fires, which are ignited by organic oils. While the exact formula of AFFFs is often held as proprietary and confidential by manufacturers, the fundamental components of AFFF concentrates—which are later diluted with water for application—include surfactants, with fluorosurfactants being a key component, alongside water, organic solvents, and various additives such as polymers and salts, as illustrated in **Figure 1.11**.[32] **Figure 1.12** outlines the main types of fluorosurfactants utilized in AFFFs. As previously described, the production of these fluorosurfactants relies on two principal methods: the electrochemical fluorination (ECF) process, which is typically employed to synthesize long-chain fluorosurfactants, and the fluorotelomer process. The fluorosurfactants generated via the ECF process, including PFSA, perfluoroalkyl sulfonamido amino carboxylic acid (PFASAC),

perfluoroalkyl sulfonamido amino dicarboxylic acid (PFASAdiC), and perfluoroalkyl sulfonamido amine (PFASA), are depicted in parts A-D of **Figure 1.12**.[33] It is important to note that the ECF process also results in the production of fluorinated intermediates and by-products.

With the cessation of PFOS and related long-chain PFAS production in the 2000s, there was a shift towards developing short-chain fluorosurfactants. However, these were unable to meet the performance standards required for AFFFs.[4] The fluorosurfactants derived from the telomerization process, such as fluorotelomer sulfonamide alkylbetaine (FTAB), fluorotelomer sulfonamide amine, fluorotelomer thioamido sulfonic acid (FTSAS), and fluorotelomer thioether hydroxy ammonium (FTSHA), are illustrated in **Figure 1.12E-H**. Atochem Forafac™ and Ciba-Geigy Lodyne™ are two notable brands of telomerization-based AFFF fluorosurfactants, with the former being acquired by DuPont in 2002. Currently, six-carbon fluorotelomer surfactants are favored in AFFF formulations due to their reduced toxicity and bioaccumulation potential. Efforts are ongoing to develop fluorine-free AFFFs to minimize the health impacts of PFAS, particularly on firefighters. The variety in AFFF formulations plays a significant role in the extent of PFAS penetration into the soil.[7] This highlights the complex challenge of balancing effective fire suppression with environmental and health safety.

Another significant source of PFAS is found in PFAS-based coating materials. The inherent property of PFAS to repel water and oil has led to their application as coatings on various items, including cookware and food takeout boxes, presenting a lucrative opportunity for businesses. The US EPA has identified food packaging materials as the predominant source of PFAS exposure.[7] Such PFAS-infused packaging materials, encompassing fast food takeout boxes, paper tableware, baking papers, instant noodle cups, and beverage containers, can leach into water resources from landfills.[7,10,34]

Additionally, commercial household products like non-stick cookware, cleansing products, lubricants, paints, ski waxes, and water-proof clothing significantly contribute to the dissemination of PFAS, alongside food packaging materials. Unlike PFAS concentrations found in water resources, the levels present in household products and equipment tend to be considerably higher. For example, PFOS concentrations in chromium industry's emission suppressors can exceed 20 g/kg, and the concentration of 10:2 FTOH in impregnating agents is about 919 mg/L.[33] The variability in the composition and concentration of PFAS in coating materials across different countries adds layers of complexity to the issue of PFAS contamination. The following Subchapter will delve into the current state of PFAS contamination, a subject that has garnered widespread scholarly interest.

1.3. Contemporary overview of PFAS contamination

Due to the extensive application of PFAS, these chemicals have proliferated globally, contaminating diverse environments worldwide. **Figure 1.13** presents a map illustrating the scope of PFAS pollution across the U.S. as of February 2024. In response to the growing concern, the US EPA set a lifetime health advisory level for PFOS and PFOA in drinking water at 70 ng/L in 2016.[35] This threshold was significantly lowered on June 15, 2022, with the EPA establishing new concentration limits for PFOS and PFOA at 0.02 ng/L and 0.004 ng/L, respectively.[36,37] Furthermore, the EPA has issued lifetime health advisories for PFBS and hexafluoropropylene oxide (HFPO) dimer acid (known as GenX) and its ammonium salt in drinking water, setting the limits at 2000 ng/L for PFBS and 10 ng/L for GenX.[37] State-level responses vary, with some states implementing their own PFAS concentration standards. For instance, New Jersey established health-based Maximum Contaminant Levels (MCLs) of 13 ng/L for PFOA, 14 ng/L for PFOS, and 13 ng/L for PFNA in 2018.[38] The discovery of PFAS in additional locations underscores the

need for lifetime health advisories for other PFAS compounds, highlighting the ongoing challenge of managing and mitigating PFAS contamination.

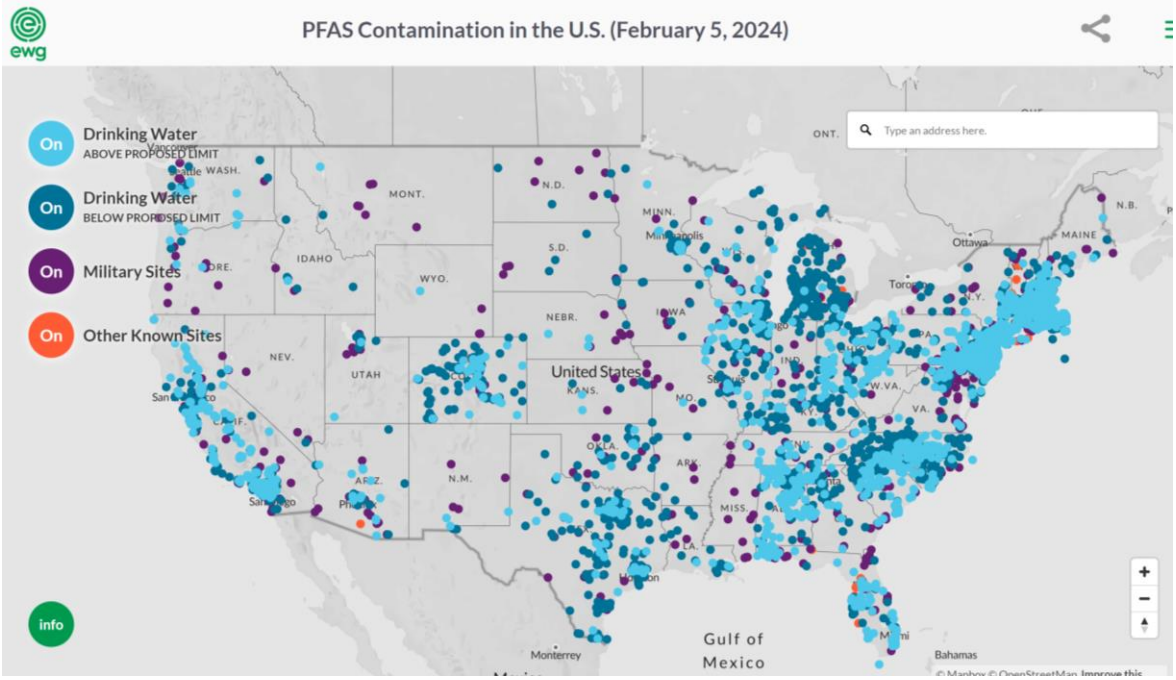

Figure 1.13 PFAS contamination in the U.S. by February 2024. Image retrieved from https://www.ewg.org/interactive-maps/pfas_contamination/.

Figure 1.14 illustrates the escalating trend of PFAS pollution across the U.S. over recent decades, indicating an increase in the identification of PFAS-contaminated sites nationwide. PFAS compounds are consistently found in various environmental matrices, including water resources, soil, and even within human bodies. **Figure 1.15** succinctly depicts the pathways through which humans are exposed to PFAS, highlighting that significant exposure is due to the prevalent use of PFAS-infused products, such as Teflon, AFFFs, and fluorosurfactants, as outlined in Subchapter *1.2*. This extensive utilization of PFAS-related items leads to their release and accumulation in the environment, exacerbating human exposure to these persistent compounds.

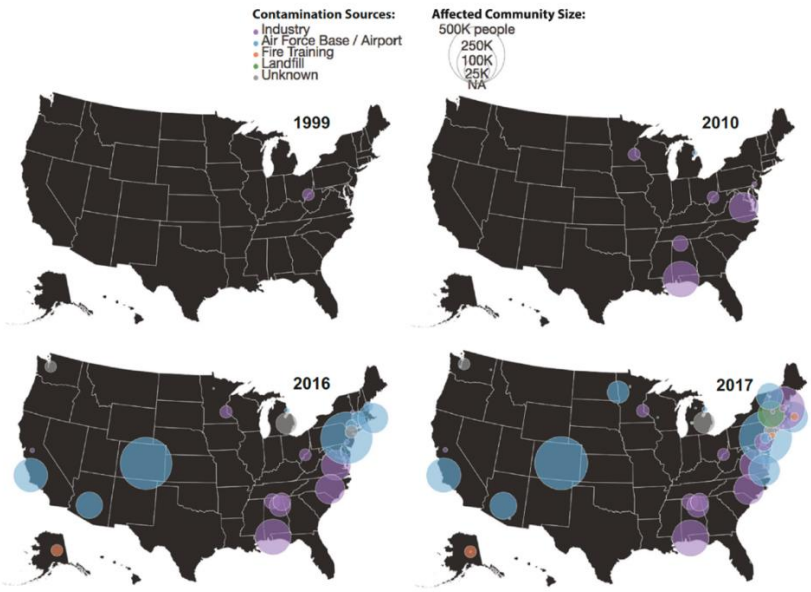

Figure 1.14 Discovery of PFAS-contaminated sites between 1999 to 2017, leading to occurrence of PFAS in the drinking water in the U.S.[39]

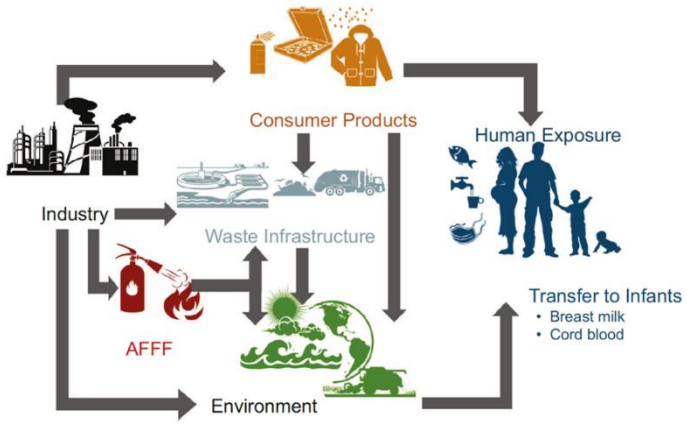

Figure 1.15 Pathways of human exposure to PFAS.[39]

As highlighted in **Figure 1.6**, the presence of organic fluorine in human serum was first reported by Taves in 1968, a discovery that would later be linked to PFAS contamination.[3,13,40] In 2001, PFOS contamination was globally demonstrated in wildlife for the first time.[3,13] Cousins et al.[41] reported that PFAS concentrations in surface water and groundwater vary widely, with levels ranging from the limit of detection up to approximately 2.0 ppm. It is important to recognize that

drinking water may serve as a significant source of PFAS contamination, leading to heightened exposure levels in humans.[42] According to Hu et al.,[21] PFAS were detected in 97% of human serum samples in the U.S. National Health and Nutrition Examination Survey. Similarly, Blake et al.[42] reported that PFOS and PFOA can be found in 90% of the U.S. population. The estimated annual PFAS load in biosolids is approximately 2749–3450 kg, with half of this quantity directly or indirectly entering the soil, reaching depths of up to 120 cm.[43] **Table 1.4** provides a concise overview of PFAS concentrations from various sources.

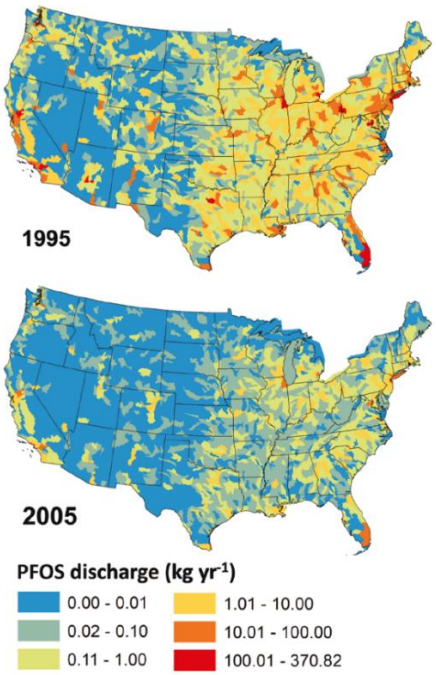

Figure 1.16 PFOS emission from wastewater treatment plants (WWTPs) into water resources in the U.S. in 1995 and 2005.[39]

Following the phase-out of long-chain PFAS from 2000 to 2002 (depicted in **Figure 1.6**), there was a noticeable decrease in PFAS discharge into soil and water resources (shown in **Figure 1.16**) and in PFAS levels in human serum. However, Sunderland et al.[39] highlighted that the accumulation of newer PFAS types, such as GenX, has not been adequately considered for most populations, suggesting the presence of unaccounted PFAS in human serum. The upcoming

Subchapter will delve into the toxicity of PFAS, underlining the urgent need for strategies to mitigate PFAS pollution in the environment.

Table 1.4 Concentrations of selected PFAS across various sources.

Source	PFAS	Content	References
AFFFs	PFBA	0.081-27.65 ppm	7
	PFBS	0.039-253.7 ppm	
	PFHxS	293 ppm	33
	PFOS	1338 ppm	
	PFOS	568.0 ppm	7
	PFOA	0.026-0.208 ppm	
	6:2 FTS	63.6-129 ppm	33
	6:2 FTOH	0.535-13.25 ppm	7
	8:2 FTOH	26.5-54.78 ppm	
	10:2 FTOH	5.8-120.721 ppm	
PTFE packaging materials	PFOA	17.5–45.9 ng/g	44
	PFOS	33.7–81.3 ng/g	
Popcorn bags	PFOA	290 µg/kg	45
		9 µg/kg	46
Fried chicken box	PFOA	17.74 ng/dm^2	47
	PFOS	92.48 ng/dm^2	
Impregnation products	8:2 FTOH	662 ppm	33
	PFNA	0.8 ppm	
	PFOA	0.2 ppm	
		15.2 ppm	7
	PFOS	634.9 ppm	
	PFBS	26.8 ppm	
Cleaner	PFOA	1.1 µg/kg	48
	PFOS	1.6 µg/kg	
Carpet	PFBA	14.7 µg/kg	
	PFBS	26.8 µg/kg	
Ski wax	PFBA	362.1 µg/kg	
	PFOA	2033.1 µg/kg	
	PFOS	159.8 µg/kg	
Surface water (France)	PFOA	0.00018-23.6 ppb	7
	PFOS	16.5 ppb	
	PFBA	19.6 ppb	
	PFBS	0.57 ppb	
Surface water (Melbourne)	PFBS	140 ng/L	49

Freshwater (China)		9.7-77 ng/L	
Groundwater (China)	PFBA	0.25-76 ppt	7
	PFOA	1.2-2510 ppt	
	PFBS	21.2 ppt	
	PFOS	0.40-20.2 ppt	
Groundwater (Will Rogers World Airport, OKC, U.S.)	PFBS	1.3 ppb	https://www.ewg.org/interactive-maps/pfas_contamination/#about
	PFOS	10 ppb	
	PFOA	3.3 ppb	
	PFNA	170 ppt	
Drinking water (U.S.)	PFOA	0.02-0.35 ppt	21
	PFOS	0.04-1.80 ppt	
Drinking water (Sweden)	PFBA	1.55-1.97 ppt	7
	PFOA	1.22-1.41 ppt	
	PFBS	1.40 ppt	
	PFOS	3.40 ppt	
Drinking water (China)	PFBA	0.09-3.20 ppt	50
	PFBS	0.38-1.10 ppt	
	PFOS	0.60-10.0 ppt	
	PFOA	0.16-2.1 ppt	
Landfill and landfill leachate	PFHxA	2.32 ppm	51
	PFOA	766.67 ppt	
	PFHxS	1.79 ppm	
	PFOS	526.67 ppt	
Soil	PFOS	6.29–13.5 ng/g	52
	PFAS	8-50 µg/kg	53
Photolithography wastewater	PFAS	1000 ppm	54
AFFFs wastewater	PFAS	3-6 g/L	
Wastewater effluent	PFAS	15.5-234 ppt	50

1.4. Imperatives for addressing PFAS contamination

The pervasive application of PFAS has raised significant concerns due to their potential for bioaccumulation and toxicity.[20,55] As previously outlined, human exposure to PFAS predominantly occurs through contaminated soil, water, and animals, products containing PFAS, emissions from PFAS production sites and factories, household dust, air, and even breastfeeding, encompassing ingestion, dermal contact, and inhalation as pathways.[10,19,56,57] Among these,

exposure via drinking water is particularly alarming owing to the high aqueous solubility of many PFAS compounds.[21] Studies have linked PFAS exposure to a range of health effects, including thyroid disruption, immunotoxicity, hepatotoxicity, and carcinogenicity, associating them with liver and kidney diseases, obesity, altered thyroid and immune function, reproductive issues, high cholesterol, and disturbances in lipid and insulin regulation, with potential links to cancer.[10,21,39,58]

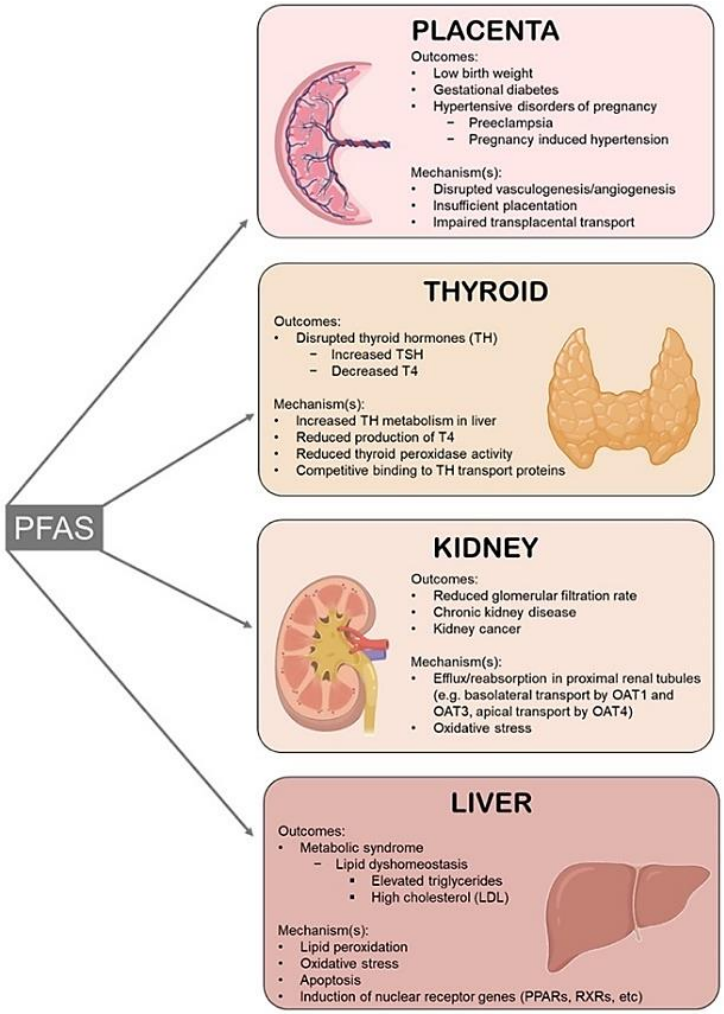

Figure 1.17 Summary of health effects linked to the PFAS exposure, showing the health outcomes and hypothesized mechanisms.[42]

The initial development and industrial use of PFAS date back to the 1940s, yet the first health concerns related to PFAS exposure were not reported until 1961 by DuPont. In the 1980s, the discovery of birth defects in children born to women exposed to PFAS intensified the scrutiny

on the health impacts of these chemicals.[42] Additionally, during this period, it was found that the concentration of organic fluorine in the serum of 3M employees was tenfold higher compared to individuals not working with PFAS.[39] **Figure 1.17** illustrates the potential health effects linked to PFAS exposure. While PFOA has been classified as a possible carcinogen by the International Agency for Research on Cancer (IARC), there remains a lack of data for PFOS.[39]

From an ecological perspective, the robust carbon-fluorine bonds in PFAS make them resistant to environmental degradation, posing a particular challenge in aquatic settings and leading to significant environmental contamination concerns. This durability in the environment underscores the urgent need for measures to address PFAS pollution effectively.[10]

Recent research has shed light on the toxicity of PFAS and their health impacts on humans and the environment, offering new insights into the complexities of PFAS exposure. Zhang et al.[59] reported a significant association between exposure to PFOS, PFOA, and PFDA and levels of thyroid stimulating hormone (TSH) in pregnant women, who appear particularly vulnerable during the first six months of pregnancy. Blomberg et al.[60] and Liu et al.[61] found that newborns' primary exposure to PFAS stems from maternal serum concentrations and breast milk. Rickard et al.[62] highlighted the direct and indirect impacts of PFAS on women's reproductive systems. However, the body of research on PFAS's health effects on humans predominantly consists of review articles, with a noted lack of experimental data, underscoring the need for further empirical studies to solidify these findings due to inconsistencies among current studies.

Liu et al.[49] focused on the effects of PFAS on Chlorella Pyrenoidosa, a type of algae, focusing on the impact of emerging PFAS mixtures, which are often used as substitutes for long-chain PFAS following their phase-out. Their findings suggest a synergistic toxicity effect of the PFBS and perfluorobutane sulfonamide (FBSA) mixture, more potent than individual exposures.

This synergy was observed to 1) impair photosynthetic efficiency by inhibiting genes related to electron transport in photosystems, 2) accumulate toxicity through the buildup of reactive oxygen species due to disrupted peroxisomal metabolism, and 3) inhibit algae growth by interfering with DNA replication. Pierozan et al.[63] also reported a synergistic effect of a PFOS and PFOA mixture on cellular death mechanisms, such as DNA/RNA damage and lipid peroxidation. **Figure 1.18** illustrates the mechanisms and gene expression heatmaps related to the toxicity of PFAS mixtures on algae.

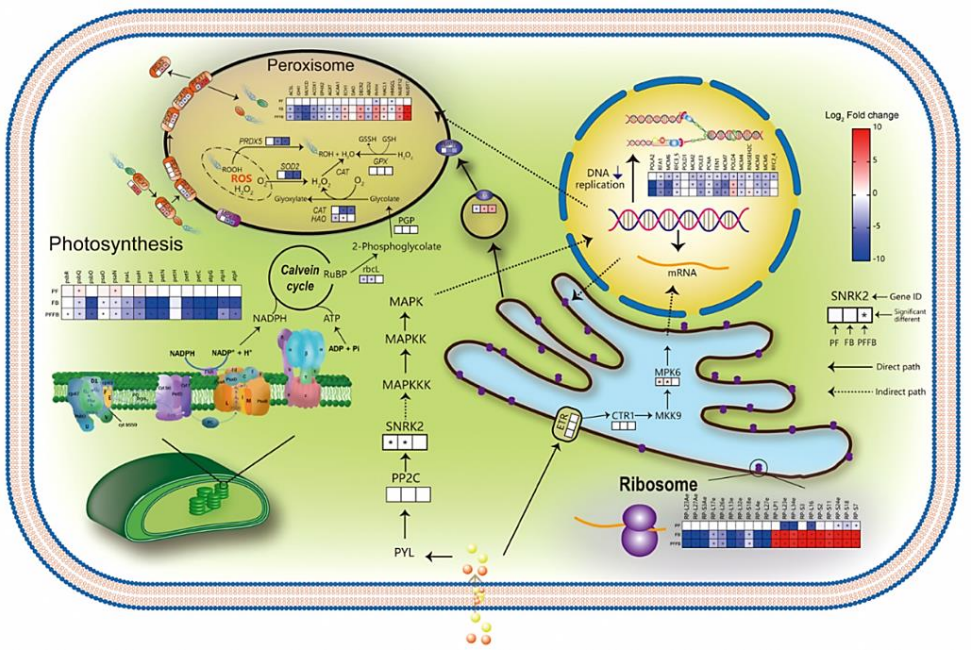

Figure 1.18 The schematic of pathways and gene expression heatmaps associated with photosynthesis, peroxisome, mitogen-activated protein kinase signal pathway, DNA replication, and ribosome of Chlorella pyrenoidosa.[49]

The prevailing issue with PFAS research is its focus on the most commonly identified compounds within this vast chemical family, which are present in the environment and human bodies as mixtures. The critical challenge remains that PFAS are continually produced, as suitable alternatives have yet to be identified. The subsequent Subchapter will provide a concise overview of this dissertation.

1.5. Problem statement

The global issue of PFAS contamination has been highlighted and discussed previously, with an emerging awareness of its environmental repercussions prompting the adoption of established remediation techniques, such as ion exchange, reverse osmosis (RO), nanofiltration (NF), and absorbents like granular activated carbon (GAC)[64] for mitigation efforts. Nonetheless, these conventional methods encounter multiple obstacles, including significant energy demands, the generation of extensive secondary waste, and limited efficacy in removing short-chain PFAS.[65] In addition, PFAS presence leads to increased membrane fouling and exacerbates pore plugging, consequently increasing the time and energy needed for the desalination process.[66,67]

Foam fractionation, traditionally used for the separation of dissolved or colloidal particles from aquatic environments, has been modified for PFAS removal, demonstrating potential in water treatment via ozone-augmented processes.[68] While in situ groundwater remediation through air sparging has achieved some success in converting polyfluorinated precursors into PFAA,[69–71] it falls short of effectively eliminating or breaking down these compounds. Additionally, challenges such as the creation of excessively large bubbles or insufficient bubble quantities impede effective PFAS extraction, attributed to poor interaction between bubbles and contaminated water. Despite reports of successful PFAS removal through foam fractionation, research exploring the relationship between PFAS's interfacial properties, and their foaming behavior remains scant. It is crucial to acknowledge that the interfacial characteristics of surfactants, including surface tension and interfacial rheology, significantly influence their foaming abilities.[72–80] Hence, this dissertation aims to investigate and measure the interfacial properties of particular PFAS, covering both long-chain and short-chain varieties. Furthermore, it delves into an analysis of the foaming capabilities and the stability of the foam produced by these chosen PFAS.

1.6. Research questions and hypotheses

Numerous research teams, including those led by Lee et al.,[81] Meng et al.,[82] and Zhang et al.,[83] have developed foam aeration columns to assess the effectiveness of PFAS removal processes. Despite these advancements, such methods demonstrate notable deficiencies in eliminating short-chain PFAS effectively, for example, a 30% removal efficiency for PFBS as noted by Meng et al.[82] Although short-chain PFAS are known to exhibit higher surface tensions than that of long-chain PFAS,[84] factors beyond surface tension, such as the interfacial modulus, surface concentration at the air-water interface, and the diffusion coefficient from the bulk phase to the subsurface/interface, play critical roles in foaming dynamics. However, comprehensive studies on these factors for both long-chain and short-chain PFAS are scarce. Given the suboptimal removal rates of short-chain PFAS, it is hypothesized that their inefficacy is due to lower saturated surface concentrations, reduced diffusion coefficients, and lower interfacial modulus, all of which negatively impact their foaming characteristics.

While several studies mention PFAS removal via foam fractionation, there exists a significant gap in systematic research into the foaming behavior of PFAS, such as differences in foam height and bubble diameter. Investigations into hydrocarbon surfactants have highlighted the role of certain dimensionless numbers, which symbolize processing and interfacial attributes, in influencing foaming behavior including foaming expansion rate and bubble size.[85,86] This leads to critical questions for PFAS aqueous solutions: how is the foaming behavior of PFAS solutions correlated with these dimensionless numbers, such as the Reynolds number? Which dimensionless numbers are most significant in determining the foaming properties of PFAS? Furthermore, how do the primary factors affecting foamability vary across different PFAS compounds? Considering both foam collection and foam breakup, the study of defoaming properties, including foam stability,

becomes equally critical. Based on earlier hypotheses, it is hypothesized here that the lower maximum surface excess concentration, slower diffusion rate from bulk to subsurface/interface, and reduced interfacial modulus of short-chain PFAS, i.e., four carbons (C4) ones, would result in a notably shorter foam half-life compared to that of long-chain (C8) PFAS foams.

Efforts to enhance PFAS removal efficiency through foam fractionation have led to the utilization of additives, such as salts and co-surfactants.[54,81,82,87–90] Among tested salts, NaCl has been the focus, with findings indicating an enhancement in PFAS removal efficiency correlating with increased NaCl concentrations. Additionally, the ion valence of the salts is recognized as a significant factor in PFAS removal, although studies on the use of divalent and trivalent salts are relatively scarce.[81] In our study, we hypothesize that the observed enhancements in removal efficiency upon adding electrolytes are likely attributable to elevated maximum surface excess and interfacial modulus, leading to an improved foaming capacity and foam stability for PFAS.

1.7. Objectives

This dissertation is dedicated to providing a detailed examination of the interfacial and foam characteristics of PFAS, aiming to uncover the relationship between the interfacial properties of PFAS and their impact on foaming behavior and stability. The research is directed towards achieving the following objectives:

- Fundamentally study the PFAS adsorption at the air-water interface through the measurements of dynamic surface tension and interfacial dilatational rheology, and the employment of adsorption isotherms;
- Investigate the impact of PFAS chain length on their interfacial properties by measuring the surface tension, applying the adsorption isotherms, and performing the dilatational rheology;

- An investigation of PFAS adsorption capabilities at the air-water interface in environments enriched with electrolytes of various valences, informed by dynamic surface tension and interfacial dilatational rheology studies;
- Study the diffusion for long-chain (C8) and short-chain (C4) PFAS by estimating the diffusion coefficients, in both the absence and presence of electrolytes of differing valences by measuring the dynamic surface tension using the bubble pressure tensiometer;
- An investigation on the interactions between PFAS polar headgroups and salt ions within the bulk phase by performing nuclear magnetic resonance (NMR) spectroscopy and small-angle X-ray scattering (SAXS);
- An examination of the foaming process, including foaming speed, expansion ratio of foaming, and liquid content by using a foam analyzer and undertaking dimensionless analysis for different PFAS;
- Study the defoaming behavior of various PFAS through analysis of foam half-life, bubble size, and liquid content by using the foam analyzer.

1.8. Dissertation outline

This dissertation is structured to cover various aspects of PFAS, starting with an introductory Chapter on PFAS categorization, historical development, widespread use, contamination issues, and associated toxicities. Chapter 2 demonstrates the methodology including experimental and models adopted for the related research work. Chapter 3 delves into the adsorption of PFAS at the air-water interface and their dilatational interfacial rheology, focusing on compounds with primarily eight- and four-carbon chain lengths. Chapter 4 investigates the air-water interfacial properties of PFAS in the presence of electrolytes (NaCl and $CaCl_2$) at differing concentrations. Chapter 5 presents ongoing collaborative research into how electrolytes (NaCl and

$CaCl_2$) affect PFAS structural and intermolecular interactions at the air-water interface. Chapter 6 explores PFAS foaming behavior, establishing correlations between foaming capacity and interfacial properties through dimensional analysis. In Chapter 7, the defoaming and foam stability of PFAS are examined to discern the relationship between PFAS foam stability, characterized by foam half-life, and their interfacial properties. The concluding Chapter summarizes the dissertation, proposing further work and future research directions.

Chapter 2. Methodology

2.1. Materials

PFSA potassium salts including perfluorobutanesulfonic acid potassium salt (KPFBS), perfluorohexanesulfonic acid potassium salt (KPFHxS), and perfluorooctanesulfonic acid potassium salt (KPFOS) were used instead of the acids due to higher purity and better solubility. KPFBS (potassium nonafluoro-1-butanesulfonate, 98%, CAS: 29420-49-3), KPFHxS (tridecafluorohexane-1-sulfonic acid potassium salt, ≥ 98.0%, CAS: 3871-99-6), and KPFOS (heptadecafluorooctanesulfonic acid potassium salt, ≥ 98.0%, CAS: 2795-39-3) were purchased from Sigma-Aldrich. PFOA (purity 95%, CAS: 335-67-1), representing a typical type of PFCA, was also obtained from Sigma-Aldrich. **Figure 2.1** shows the chemical structure of KPFOS, PFOA, KPFHxS, and KPFBS.

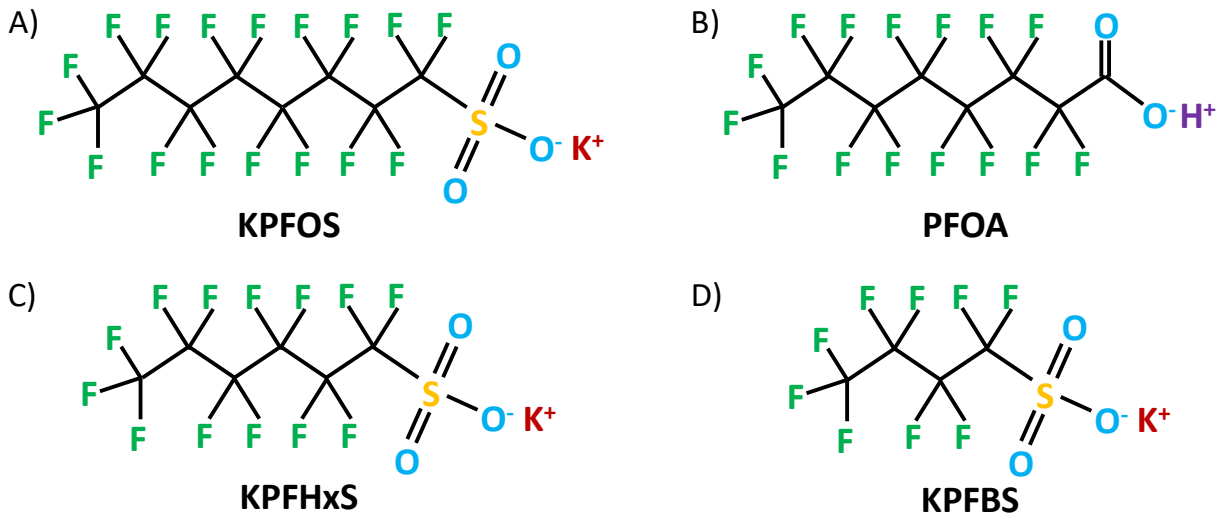

Figure 2.1 Molecular structure of A) KPFOS, B) PFOA, C) KPFHxS, and D) KPFBS.

Sodium chloride (NaCl) was purchased from Fisher BioReagents (purity ≥ 99.0%, CAS: 7647-14-5), and calcium chloride ($CaCl_2$) was purchased from Thermo Scientific (purity 97%, CAS: 10043-52-4). Deuterium oxide (D_2O, 99.8%, isotopic, CAS:7789-20-0) was purchased from Thermo Scientific. Haxafluorobenzene (99%, CAS: 392-56-3) was also purchased from Thermo Scientific. All chemicals were used as received without further purification. **Tables 2.1** to **2.3** show the sample formulation of PFAS aqueous solutions investigated in Chapter 3-7.

Table 2.1 Composition of PFAS aqueous solutions used in measurement of air-water interfacial properties.

	Concentration range (mM)	Focused concentration (mM)
KPFOS	0.0002-1.11	0.40
KPFHxS	-	0.40
KPFBS	0.0003-88.71	0.40
KPFOS+KPFBS	-	0.40 (1:1)

Table 2.2 PFAS sample formulation used for studying the salt effect on PFAS air-water interfacial properties.

	PFAS concentration range (mM)	Focused PFAS concentration (mM)	Salt	Salt concentration (mM)
KPFOS	0.0002-1.11	0.40	NaCl	0.5, 1, 5, 10, 50, 100, 200
			$CaCl_2$	0.1, 0.5, 1, 5, 10, 50, 100
PFOA	0.0002-10	0.40	NaCl	0.5, 1, 5, 10, 50, 100, 200
			$CaCl_2$	0.1, 0.5, 1, 5, 10, 50, 100
KPFBS	0.0003-88.71	0.40	$CaCl_2$	0.1, 100

Table 2.3 PFAS sample composition used in measurement of NMR spectroscopy and SAXS.

PFAS	Molecular weight (g/mol)	Concentration (mM)	w/w %	Salt	Concentration (mM)	CMC (mM)	N (*CMC)	Temperature
KPFOS	538.22	1.1	0.06	-	-	7-8.5	below CMC	room
				$CaCl_2$	200	n.a.	n.a.	room
				$CaCl_2$	100	0.2	5.6	room
				$CaCl_2$	10	0.9-1	1.1	room
				NaCl	200	n.a.	n.a.	room
				NaCl	100	0.4	2.8	room

				NaCl	10	n.a.	n.a.	room
PFOA	414.07	9.7	0.4	-	-	9.7	1.0	room
				$CaCl_2$	100	4.8	2.0	room
				$CaCl_2$	10	7.3	1.3	room
				NaCl	100	7.3	1.3	room
		12.1	0.5	NaCl	100	7.3	1.3	room

2.2. Sample preparation

The ultrapure deionized water, generated through Millipore Synergy® Water Purification System, was used for all PFAS sample preparations, the exception is the samples used for performing ^{19}fluorine nuclear magnetic resonance (NMR) spectroscopy. Higher concentration of PFAS aqueous solutions were prepared in polypropene bottles as PFAS stock solutions for further dilution. The stock solutions were continuously mixed for two days to completely dissolve the solid PFAS. For the PFAS solutions containing salts, a certain amount of salts was weighed and dissolved in the PFAS solutions.

To prepare the samples for performing NMR spectroscopy, a certain amount of solid PFAS was dissolved in the D_2O. Then the sample was placed in a capillary NMR tube and equilibrated at room temperature for at least 24 hrs prior to the measurements. A drop of hexafluorobenzene was added to the NMR tubes and used as the chemical shift reference. To prepare samples for conducting small-angle X-ray scattering (SAXS) measurements, a PFAS aqueous solution was placed in a thin-walled quartz capillary tube with a wall thickness of 0.01 mm (*Charlessupper company*) and sealed with epoxy glue (**Figure 2.5C**). The solutions were also equilibrated at room temperature for at least 24 hrs prior to the scattering measurements.

2.3. Surface tension measurement

2.3.1. Wilhelmy plate tensiometer

A Wilhelmy plate tensiometer (*Dataphysics, DCAT 25*) equipped with a Wilhelmy plate (PT 11, Dataphysics, length 10 mm, width 19.9 mm, and thickness 0.2 mm) was employed to obtain the surface tension of PFAS aqueous solutions at 25 ± 0.5 ℃. The wetted length for all measurements was 3 mm. The data points of surface tension as a function of time were collected for 1 hr. For each sample composition, 2-5 replicates were measured. The tensiometer was calibrated with ultrapure deionized water prior to use. To ensure the dryness and cleanness of the Wilhelmy plate, the plate was washed thoroughly and cleaned using a Bunsen burner prior to each measurement. 50 mL of aqueous sample was transferred into a clean glass vessel for the measurement.

2.3.2. Pendant drop tensiometer

To further investigate the interfacial properties of PFAS in air-water environments, specifically focusing on PFOA, an optical tensiometer (*Attension KSV Instruments, Biolin Scientific, Finland*) was employed. This involved observing either a pendant drop of the aqueous solution suspended in air, or an air bubble generated within the PFAS solution. These phenomena were meticulously documented, with the Young-Laplace equation subsequently applied to derive the surface tension values. For generating air bubbles, a J-shaped needle (*dataphysics, 6000105, SNC 107/069 Dosing needle Outer-Ø 1.07mm; Inner-Ø - 10.00% Discount13.400.69mm; Length 57 mm; Width 10 mm; Upwards 7 mm*) was utilized, a procedure detailed in **Figure 2.2A**. Each sample composition was subjected to a minimum of two replicate tests to ensure the accuracy and reliability of the results.

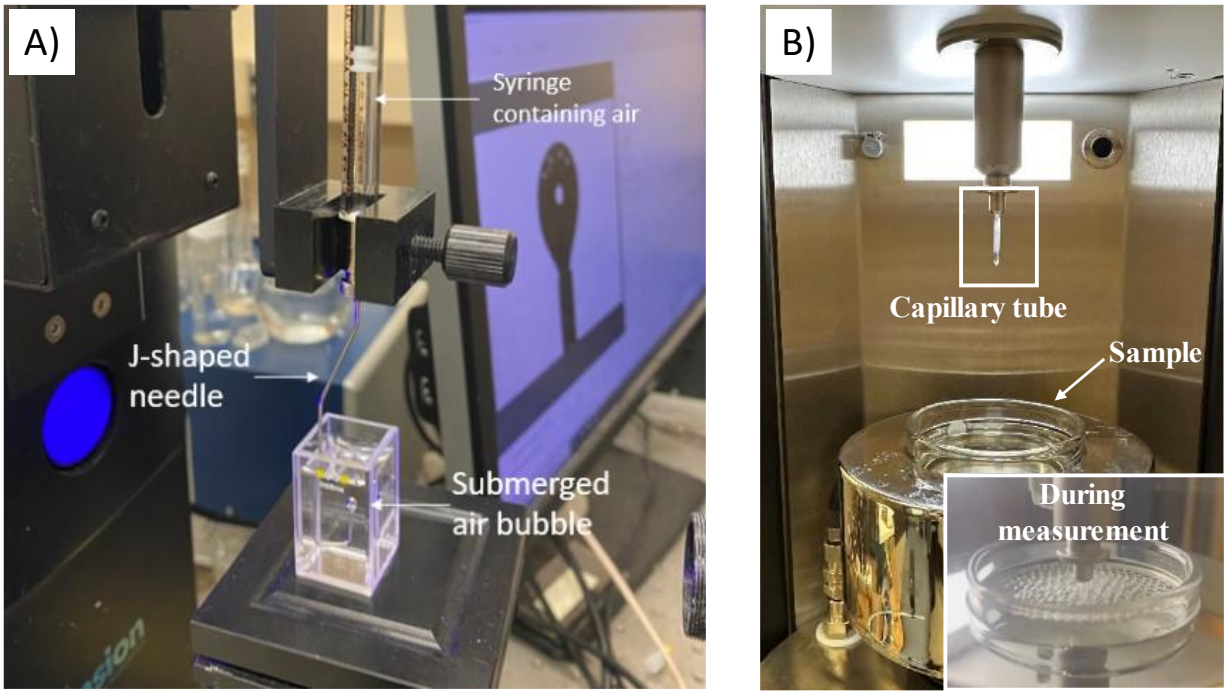

Figure 2.2 A) The rising bubble method by using the J-shaped needle. B) Bubble pressure tensiometer used in this study, the capillary tube and sample holder are highlighted. The bubbles are generated during the surface tension measurement.

2.3.3. Bubble pressure tensiometer

To assess the rapid adsorption dynamics of PFAS at the air-water interface, we utilized the bubble pressure tensiometer (*KRÜSS, BP100*) as seen in **Figure 2.2B**. The experiment setup included a capillary tube with a diameter of 0.228 mm. We placed a minimum of 70 mL of the PFAS solution in a glass vessel (*VWR 216-0067, 70 mm, Boro 3.3*). For each sample composition, we ensured that at least two replicates were performed to confirm the consistency of our observations. A crucial step in the preparation involved the cleaning of the capillary tube with milli-Q water before each measurement session.

2.4. Interfacial dilatational rheology

Dilatational interfacial rheology of PFAS-adsorbed air-water interface was characterized by using a pendent drop oscillation method with an optical tensiometer (*Attension KSV Instruments*,

Biolin Scientific, Finland) at room temperature (~22 ℃). The surface tension and pendant drop volume change were recorded, and Young-Laplace equation was used to obtain the surface tension. The setup of pendant drop tensiometer for measuring the dilatational interfacial rheology is depicted in **Figure 2.3**. A micro-syringe containing the PFAS aqueous solution was fixed onto a syringe pump attachment for sinusoidal control of pendant drop volume oscillation. The micro-syringe was connected to a stainless-steel needle by using a thin tube. The needle was placed upside down to create the pendant drop in a covered glass cuvette, which contained ~10-15 ml of PFAS solution to minimize evaporation from the drop. Once the target volume of pendant drop was reached (~20 µL, which was the relatively large pendant drop volume before the pendant drop drops), the pendant drop was subjected to oscillation without aging the surface for at least 10 cycles within the amplitude range of the instrument (total volume change was ~0.8 µL) at the same frequency, ensuring the oscillation occurs in the linear viscoelastic region. The applied frequencies were 0.05, 0.1, 0.2, 0.3, 0.4 and 0.5 Hz, respectively. Experiments were done in 3-5 replicates for each sample formulation at each frequency.

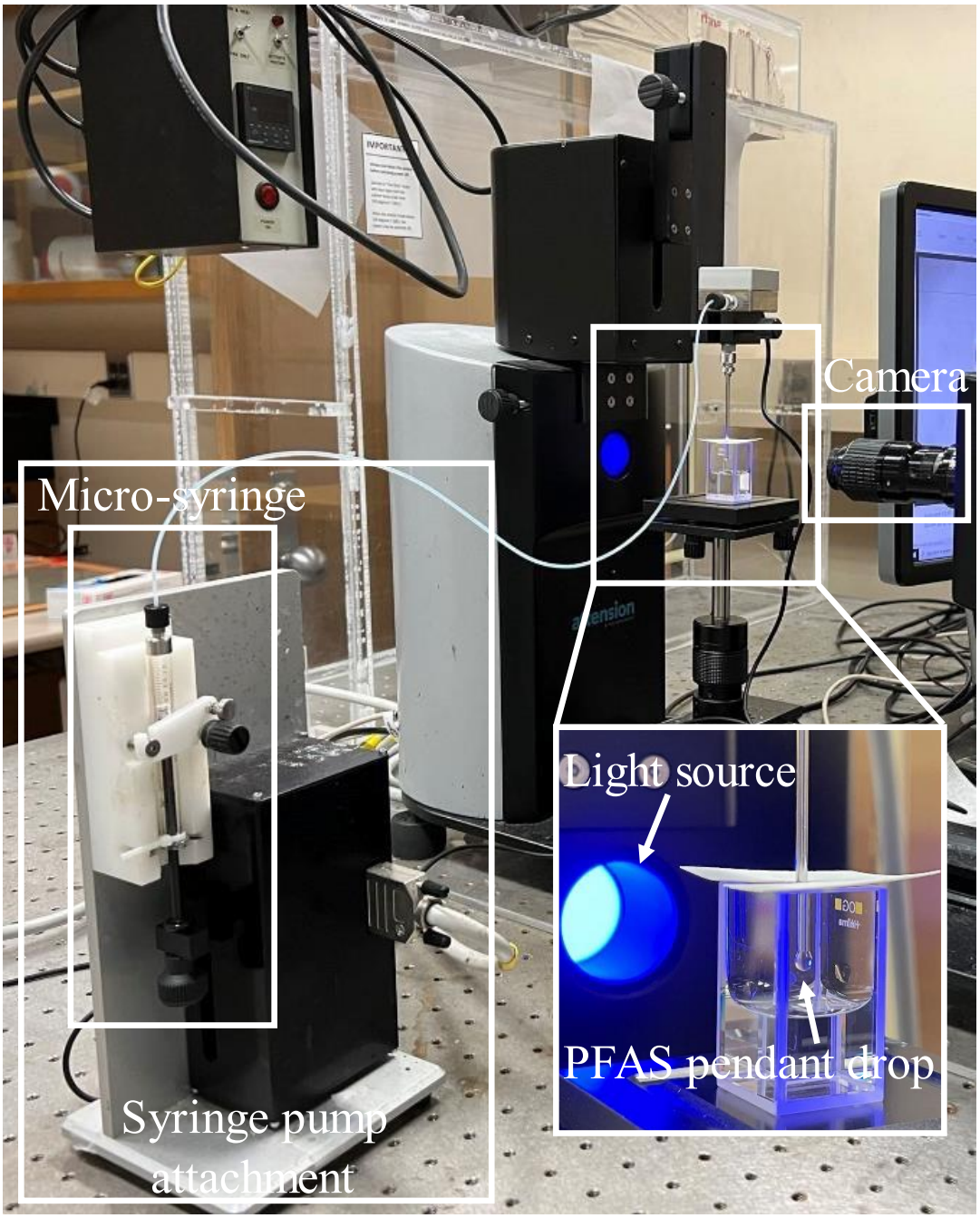

Figure 2.3 The experimental setup for conducting interfacial dilatational rheology.

2.5. Foaming/defoaming behavior analysis

The dynamic foaming behavior of PFAS aqueous solutions was recorded and analyzed by using the foam analyzer (*Krüss Scientific, DFA 100*) with a software of ADVANCE and the setup

is shown in **Figure 2.4A**. About 30 mL of PFAS aqueous solution was added into a prism column (CY4572) of 40 mm inner diameter with a max volume of 230 mL, which was fixed onto the sample holder. An O-ring was placed onto the sample holder, followed by a glass filter and another O-ring for sealing as seen in **Figure 2.4B**. Two glass filters with a pore size ranging of 16-40 µm (FL4503, ⌀ 50 mm) and 40-100 µm (FL4502, ⌀ 50 mm), respectively, were used to aerate the PFAS aqueous solution.

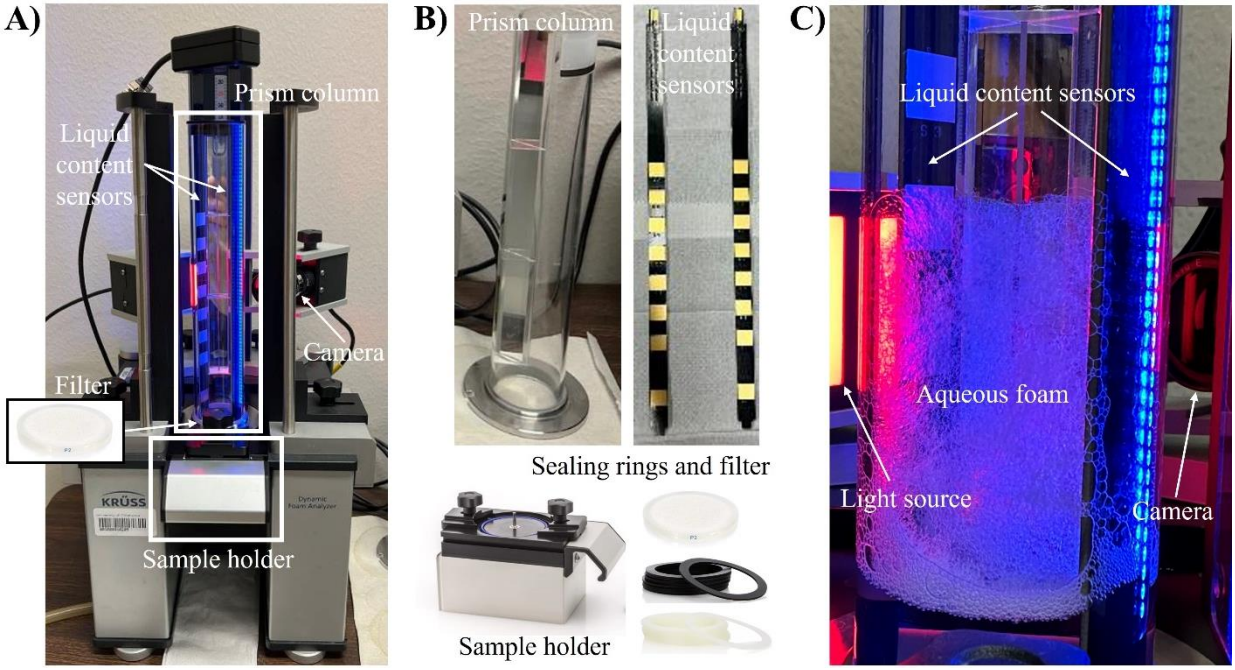

Figure 2.4 The foam analyzer (*Krüss Scientific, DFA 100*) used in this study: A) *DFA 100* setup overview; B) details showing the elements of prism column, liquid content sensors, O-rings, glass filter, and sample holder; and C) foam sample in the prism column used for morphology observation by using the camera on the back.

The PFAS aqueous solution in the prism column was sparged with air at various air flow rates ranging from 0.2 to 1.0 L/min for different aeration times of 30 s, 60 s, 120 s, and 300 s to create the PFAS aqueous foams. Two liquid content sensors were placed inside the vessel, and each of the sensors had seven chips to measure the resistance (the inverse of the electrical conductivity) across the foam at different heights and one chip on the bottom as the reference sensor (**Figure 2.4B**). A camera (2 fps at 1280 × 1024 px), of which the vertical position can be

changed, was used to record the morphology of foam during the foaming process and the bubble collapse through the prism attachment of the prism column as seen in **Figure 2.4C**. The camera was placed at the bottom, 60 mm above the liquid surface (H_{l0}). The foam analyzer was operated at 60 frames per minute for the relevant data sets. Trials for this experiment are conducted at room temperature and neutral pH. For each formulation, at least two replicates were tested. **Table 2.4** shows the setup of *DFA 100* to aerate the PFAS aqueous solutions.

Table 2.4 Setup of *DFA 100*.

Pore size range of filter (μm)	16-40 and 40-100
Sample volume (mL)	30
Air flow rate (L/min)	0.2-1.0
Aeration time (s)	30-300
Observation time (s)	1000
Camera position	60 mm from H_{l0}

The investigation into the dynamic defoaming characteristics of PFAS aqueous solutions was also conducted using a *DFA 100*, as mentioned above. The aeration process was mentioned in detail earlier. After stopping the aeration, the foam's morphology and the dynamics of bubble collapse were documented using a camera as mentioned for the air injection process. 1000 s was set as the observation time for observing the bubbles. The setting parameters of *DFA 100* to aerate the PFAS solutions for the purpose of studying the defoaming properties can be also found in **Table 2.4**.

2.6. Nuclear magnetic resonance (NMR) spectroscopy

The ^{19}F NMR spectroscopy was performed and recorded on the *Varian Inova 600 MHz NMR Spectrometer* at the NMR Facility located at the University of Oklahoma. The ^{19}F NMR

spectroscopy was operated at 376.72 MHz. The ^{19}F NMR chemical shift for haxafluorobenzene is -164.9 ppm. All NMR spectra were processed by using MestreNova™ software.

2.7. Small-angle X-ray scattering (SAXS)

SAXS experiments were conducted using the *Xeuss 3.0* equipment (*Xenocs*), depicted in **Figure 2.5A**, at the University of Tulsa. To prevent any disruption, the capillaries were subjected to a vacuum environment for approximately 15 mins, shown in **Figure 2.5B**. **Figure 2.5C** also displays the positioning of the capillaries in a multicapillary sample holder within the experiment chamber. The duration of scanning for each sample was set at 80 minutes.

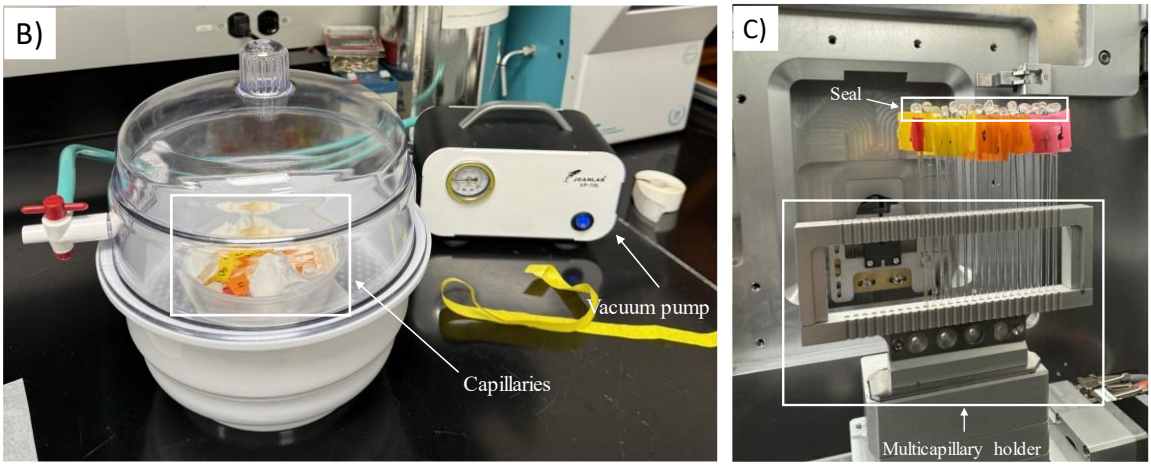

Figure 2.5 A) Description of *Xeuss 3.0* equipment. B) Capillaries under the vacuum. And C) capillaries in the multicapillary sample holder.

2.8. Adsorption isotherms

An interface tends to maintain the smallest area since a given molecule is pulled back into the bulk due to the attractive interaction resulting from other bulk liquid molecules. A certain amount of energy is required to keep this smallest area to ensure the total energy is the minimum, thus, the definition of surface tension is shown below:[91]

$$\gamma = (\frac{\partial F}{\partial A})_{T,V} \qquad \textit{Equation (2.1)}$$

where F is the force needed to minimize the surface area, and A is the surface area. The curve fitting in the pendant drop tensiometer to obtain the surface tension is based on the Young-Laplace equation shown below:[75,92]

$$\Delta P = \gamma(\frac{1}{R_1} + \frac{1}{R_2}) \qquad \textit{Equation (2.2)}$$

where ΔP is the pressure difference between two phases and R_1 and R_2 are the inner and outer radii of curvature. The surface tension decreases with increasing surfactant concentration until the critical micelle concentration (CMC) is reached, at which point excess surfactant molecules form micelles. Above the CMC, the surface tension remains the same since, to a first approximation,

surface coverage and the concentration of the monomeric form of surfactant are both constant.[93] The surface excess concentration is defined as the difference between the surfactant concentration at the interface and its concentration in the bulk.

The Gibbs equation is used to measure the surface excess concentration:[91]

$$\Gamma_i = -\frac{\partial \gamma}{\partial \mu_i} \qquad \textit{Equation (2.3)}$$

where μ_i is the chemical potential of i-th component. When $\mu_i = RTlnC_i$ (dilute systems), the Gibbs adsorption isotherm simplifies as:[91,93]

$$\Gamma_i = -\frac{1}{nRT}\left[\frac{d\gamma}{d(lnC_i)}\right]_T \qquad \textit{Equation (2.4)}$$

where $R = 8.3145\ J/K \cdot mol$ is the gas constant, T is the temperature in Kelvin, C_i is the bulk concentration of i-th component (C_i is in mol/L), $n = 1$ for non-ionic surfactants or ionic surfactants in the presence of electrolytes and $n = 2$ for ionic surfactants without adding electrolytes, and Γ_i is the surface excess concentration of i-th component.[94] Only single-component system is studied in the present work, and thus, $i = 1$ here. With the assumption of ideal dilute systems, the slope of γ as a function of lnC can be used for the estimation of surface excess concentration.[93] Determination of the surface excess concentration requires calculation of the derivative (see **Figures 3.3** and **3.4**). Calculation of derivatives from a discrete data set has significant problems, hence, Martínez-Balbuena et al.[91] proposed fitting the experimental data of surface tension before CMC via a polynomial and calculating the derivative analytically.

The most frequently used non-linear equation for surfactant adsorption at the air-liquid interface is Langmuir adsorption isotherm, which is:[93]

$$\Gamma = \Gamma_m \frac{K_L C}{1 + K_L C} \qquad \textit{Equation (2.5)}$$

where Γ_m is the maximum surface excess concentration (determined in the region where the plot of γ vs. lnC is constant), and K_L is the equilibrium Langmuir adsorption constant. The Langmuir adsorption isotherm only applies below the CMC since the equation does not consider aggregation of micelles. Gu et al.[95] proposed a S-type adsorption isotherm, which is known as the Extended Langmuir isotherm:[96]

$$\Gamma = \Gamma_m \frac{K_L C^n}{1+K_L C^n} \qquad \textit{Equation (2.6)}$$

where K_L is the equilibrium constant of surface aggregation process, and n is the average aggregation number of the surface aggregate. The adsorption coefficient K_i, defined in *Equation (2.7)*, is a function of surfactant concentration.[71]

$$K_i = \frac{\Gamma(C)}{C} \qquad \textit{Equation (2.7)}$$

2.9. Interfacial dilatational rheology model

Oscillating the pendant drop or bubble is used to characterize the dilatational interfacial viscoelasticity, which is related to surfactant diffusion to and from the interface as the interfacial area is varied. Interfacial viscoelasticity plays a key role in the foam properties since it influences the formation of bubbles/films and their instability due to the Ostwald ripening, coalescence, and drainage.[74] The dilatational interfacial modulus is obtained as follows:[75,97,98]

$$E = A_0 \frac{\Delta\gamma}{\Delta A} = \frac{d\gamma}{dlnA} \qquad \textit{Equation (2.8)}$$

where A_0 is the average surface area around which an amplitude area variation (ΔA) is observed due to the volume oscillation, and $\Delta\gamma$ is the amplitude of the surface tension difference from the average γ_0. E is a complex number with the dilatational storage modulus, E' (dilatational surface elasticity), the real part and the dilatational loss modulus, E'' , the imaginary part. The two can be calculated from the ϕ phase angle between γ and A:[75,97,99,100]

$$E = |E|\cos(\phi) + i|E|\sin(\phi) = E' + i2\pi f\eta_s \qquad \textit{Equation (2.9)}$$

where $|E| = \sqrt{(E')^2 + (E'')^2}$, $E' = |E|\cos(\phi)$, $E'' = |E|\sin(\phi) = 2\pi f\eta_s$, f is frequency, and η_s is the dilatational surface viscosity.

Considering the diffusion-controlled adsorption mechanism, Lucassen and van den Tempel proposed the following equations (L-T model)[101,102] for the description of interfacial dilatational rheology.

$$|E| = E_0 \frac{1+\xi+i\xi}{1+2\xi+2\xi^2} \qquad \textit{Equation (2.10)}$$

$$\phi = \arctan\left[\frac{\xi}{1+\xi}\right] \qquad \textit{Equation (2.11)}$$

where $E_0 = -\left(\frac{d\gamma}{dln\Gamma}\right)_{eq} = -\Gamma\frac{d\gamma}{d\Gamma}$ is Gibbs Elasticity (elasticity limit at high frequency),[103] ξ is a dimensionless characteristic parameter based on the diffusion-controlled mechanism, defined by:

$$\xi = \left(\frac{\omega_D}{\omega}\right)^{0.5} \qquad \textit{Equation (2.12)}$$

$$\omega_D = \frac{D_{L-T}}{2}\left(\frac{dC}{d\Gamma}\right)^2 \qquad \textit{Equation (2.13)}$$

where ω_D is called characteristic frequency, around which a maximum in the imaginary part of modulus will appear, and $\omega = 2\pi f$. The E_0 can be estimated based on the adsorption models. It should be noted that the diffusion coefficient obtained from the L-T model, D_{L-T}, describes the dynamic exchange of surfactant molecules from/to the air-water interface.

2.10. Dimensional analysis

The dimensional analysis is applied to investigate the foaming behavior of PFAS aqueous solutions. This Subchapter talks about the Buckingham π theorem that used for dimensional analysis, taking the example of $\frac{H_f}{H_l}$, which is known as foam rate of expansion. H_f is the foam height, and H_l is the liquid height. The similar concept is foam ratio, which is defined as the ratio

of foam volume to the initial liquid volume, $\frac{V_f}{V_l}$. V_f is the foam volume, and V_l is the volume of liquid. In foam fractionation cases, the cross-section of foaming column remains the same.

$\frac{H_f}{H_l}$ is related to several dimensionless numbers, such as Reynolds number and Capillary numebr.[85,86,104,105] The equilibrium status of foams is considered in the dimensional analysis of expansion rate of foaming as well as liquid content. For foaming kinetics, the status of foams before reaching equilibrium is considered. Listing all independent variables as shown in *Equation (2.14)*,

$$H_f = f_1(\rho, \gamma, \eta, \eta_s, E, t_e, Q_{air}, R, D_c, D_f, H_l, g) \qquad \textit{Equation (2.14)}$$

where ρ is the density of PFAS aqueous solutions, η is the bulk viscosity of PFAS aqueous solutions, t_e is the foaming time that used to reach to the equilibrium status, Q_{air} is the air flow rate, R is the Sauter mean radius of bubbles, D_c is the diameter of the prism column, D_f is the average pore size of glass filter, and g is the gravitational acceleration. Basic variables (repeating variables), called base, are selected. Considering the case of bubble rising, variables of ρ, Q_{air}, and H_{l0} are selected as the basic variables, which include the basic units of length (m), time (s) and mass (kg). H_{l0} is the initial liquid level. The π groups are determined according to $k = n - m$, where n is the total number of variables and m is the number of basic variables selected in the problem. Then *Equation (2.14)* becomes:

$$\frac{H_f}{H_{l0}} = f_2(\pi_1 = \frac{\gamma}{\rho^1 \cdot {Q_{air}}^2 \cdot H_{l0}^{-3}}, \pi_2 = \frac{\eta}{\rho^1 \cdot {Q_{air}}^1 \cdot H_{l0}^{-1}}, \pi_3 = \frac{\eta_s}{\rho^1 \cdot {Q_{air}}^1}, \ \pi_4 = \frac{E}{\rho^1 \cdot {Q_{air}}^2 \cdot H_{l0}^{-3}}, \pi_5 =$$

$$\frac{t_f}{{Q_{air}}^{-1} \cdot H_{l0}^3}, \pi_6 = \frac{R}{H_{l0}^1}, \pi_7 = \frac{D_c}{H_{l0}^1}, \pi_8 = \frac{D_f}{H_{l0}^1}, \pi_9 = \frac{g}{{Q_{air}}^2 \cdot H_{l0}^{-5}}) \qquad \textit{Equation (2.15)}$$

Equation (2.15) can be rearranged as follows by combining variables to form the dimensionless groups:

$$\frac{H_f}{H_{l0}} = f_3\left(Re_b = \pi_2^{-1}\cdot\pi_7^{-2}\cdot\pi_6, Ca = \pi_1^{-1}\cdot\pi_2\cdot\pi_7^{-2}, We_b = \pi_1^{-1}\cdot\pi_7^{-4}\cdot\pi_6, Fr_b = \pi_7^{-4}\cdot\pi_9^{-1}\cdot\right.$$

$$\left.\pi_6, Bq = \pi_2^{-1}\cdot\pi_3\cdot\pi_6^{-1}, \Theta = \pi_1\cdot\pi_4^{-1}, \zeta_p = \frac{t_e}{{Q_{air}}^{-1}\cdot H_{l0}^3}, \frac{R}{H_{l0,}}, \frac{D_c}{H_{l0}}, \frac{D_f}{H_{l0}}\right) \qquad \textit{Equation (2.16)}$$

where the Reynolds number for bubble rising is $Re_b = (\rho\cdot Q_{air}\cdot R)/(\eta\cdot {D_c}^2)$, the Capillary number $Ca = (Q_{air}\cdot\eta)/(\gamma\cdot {D_c}^2)$, the Weber number for bubble rising is $We_b = (\rho\cdot Q_{air}^2\cdot R)/(\gamma\cdot {D_c}^4)$, the Froude number for bubble rising is $Fr_b = {Q_{air}}^2/({D_c}^4\cdot R\cdot g)$, the Boussinesq number $Bq = \eta_s/(\eta\cdot R)$, the interface number $\Theta = \gamma/E$ is the ratio of surface tension to interfacial dilatational modulus, and the processing number $\zeta_p = (t_e\cdot Q_{air})/H_{l0}^3$. The combination of Reynolds number and Froude number gives the Galilei number, which is $Ga_b = Re_b^2/Fr_b = (\rho^2\cdot R^3\cdot g)/\eta^2$ for bubble rising case. Due to the limited data of using smaller D_f, only 40-100 μm as the D_f is considered in the dimensional analysis. The *Equation (2.16)* can be rewritten as follows:

$$\frac{H_f}{H_{l0}} = f_4(Re_b, Ca, We_b, Fr_b, Bq, \Theta, \zeta_p, \frac{R}{H_{l0,}}, \frac{D_c}{H_{l0}}, \frac{D_f}{H_{l0}}) \qquad \textit{Equation (2.17)}$$

$$\frac{H_f}{H_{l0}} = f_5(Ca, We_b, Ga_b, Bq, \Theta, \zeta_p, \frac{R}{H_{l0,}}, \frac{D_c}{H_l0}, \frac{D_f}{H_{l0}}) \qquad \textit{Equation (2.18)}$$

Generally, the *Equations (2.17-18)* can be rewritten to a monomial form as shown below to predict the foaming behavior, herein foaming expansion rate:

$$\frac{H_f}{H_{l0}} = Const * Re_b^a * Ca^b * We_b^c * Fr_b^d * Bq^e * \Theta^f * \zeta_p^g * (\frac{R}{H_{l0}})^h * (\frac{D_c}{H_{l0}})^i * (\frac{D_f}{H_{l0}})^j$$

Equation (2.19)

$$\frac{H_f}{H_{l0}} = Const * Ca^a * We_b^b * Ga_b^c * Bq^d * \Theta^e * \zeta_p^f * (\frac{R}{H_{l0}})^g * (\frac{D_c}{H_{l0}})^h * (\frac{D_f}{H_{l0}})^i$$

Equation (2.20)

where $const, a, b, c, d, e, f, g, h,$ and i are constants need to be fitted. If replacing Reynolds number and Froude number by Galilei number ($Ga_b = Re_b^2/Fr_b$), *Equation (2.19)* becomes *Equation (2.20)*. In this dissertation, the Solver function in Excel spreadsheet is used to obtain the as-mentioned coefficients. Either the *Equation (2.19)* or *Equation (2.20)* is taken the natural logarithm to linearize the equation prior to applying the Solver function. 0.5 is used as the initial guess for all coefficients. The *Equation (2.21)* shown below is set as the objective which needs to be the smallest in the Solver function to obtain the coefficients.

$$O = \frac{\sum_{i=1}^{n} \sqrt{|y_i - \hat{y}_i|}}{n} \qquad \textit{Equation (2.21)}$$

where y_i is the observed value, $\hat{y}_i$ is the predicted value, n is the sample size. In some cases, the coefficients need to be manually adjusted to obtain the relatively small O for the prediction after the first run of Solver function by using 0.5 as the initial values. Once the coefficients are obtained, the predicted values vs the experimental values are plotted to verify the goodness of fitting. To further determine how well the model fits the data, the R^2 of the model fitting is calculated according to the equations below:

$$\sum_{i=1}^{n} e_i = \sum_{i=1}^{n} (y_i - a_0 - a_1 m_i - a_2 n_i - \cdots - a_j p_i) \qquad \textit{Equation (2.22a)}$$

$$S_r = \sum_{i=1}^{n} (e_i)^2 = \sum_{i=1}^{n} (y_i - a_0 - a_1 m_i - a_2 n_i - \cdots - a_j p_i)^2 \qquad \textit{Equation (2.22b)}$$

$$S_t = \sum_{i=1}^{n} (y_i - \bar{y})^2 \qquad \textit{Equation (2.22c)}$$

$$R^2 = \frac{S_t - S_r}{S_t} \qquad \textit{Equation (2.22d)}$$

where e_i is the error or called residual, a_i is the coefficients, $m_i, n_i, \ldots, p_i$ are the independent variables, S_r is the residual sum of squares, S_t is the total sum of squares, $\bar{y}$ is the mean of the experimental values, R^2 is the coefficient of determination.

*Chapter 3. Air-water Interfacial Properties of Per- and Polyfluoroalkyl Substances (PFAS) with Different Chain Lengths**

3.1. Introduction

Foam aeration (fractionation or flotation) has been reported as a promising remediation approach for PFAS removal since the amphiphilic PFAS accumulates at the air-water interface during foaming.[69–71] In 2021, Burns et al.[106] implemented surface-active foam fractionation (SAFF) system in a water treatment plant for the removal of PFAS from the groundwater with a capacity of treating 90-110 m^3/day. Lee et al.[81] established a foam flotation reactor to foam PFOS and PFOA aqueous solutions and investigated the effect of metallic activators such as Fe^{3+} and Ca^{2+}. The highest PFOS removal efficiency, reaching 99.5%, occurred when Fe^{3+} was introduced. Electrophilic cations, such as Fe^{3+}, are reported to enhance adsorption of PFAS at the air-water interface as well as promote the formation of aggregates or hemimicelles.[81] Meng et al.[82] prepared aqueous formulations similar to AFFFs consisting of PFOA, PFOS, perfluorohexanesulphonic acid (PFHxS), and PFBS, and tested the PFAS removal efficiency by using a home-made aeration foam collection device. PFAS removal efficiency increased with an increase of aeration flow rate and aeration time. Additionally, the initial concentration of PFAS had an impact on their removal efficiency, with lower initial concentrations leading to greater fractional PFAS recovery. This observation is seemingly inconsistent with the Gibbs isotherm; however, the authors did not provide a clear explanation. Most foam aerations have limitations in efficiently removing short-

* **Zhou, M.**, Abbasian, Z., Shiau, B., Grady, BP., Foudazi, R. Colloids and Surfaces A: Physicochemical and Engineering Aspects (2024): 134129.)

chain PFAS, for example, a removal efficiency of only 46.7% for perfluorohexanoic acid (PFHxA),[106] while the efficiency for removing PFBS is only around 30%.[82]

One key variable that influences the foaming process is the interfacial properties of the surface-active agents, i.e. surface tension and interfacial rheology.[72–80] Tumura et al.[107] demonstrated that the maximum rate of surface tension reduction, $(\frac{d\gamma_t}{dt})_{max}$, strongly affects initial foam height, foam stability, and the length of lamellae (drainage film, or called Plateau Boader). A rate of ~20 mN/m·s according to Tumura et al.[107] leads to the most stable polyoxyethylene dodecylethers foams, where the most elongated lamellae are present. On the other hand, the foam film ruptures in the case of too high or too low surface tension reduction rate $(\frac{d\gamma_t}{dt})$. A too large surface tension reduction rate gives rise to excess lamellae thinning, whereas if the surface tension reduction rate decrease is too small the surface tension gradient is not sufficient to elongate the lamellae. Similar investigations were conducted by Kanokkarn et al.[108], emphasizing the significance of $(\frac{d\gamma_t}{dt})_{max}$ on foamability and foam stability. Beneventi et al.[109] proposed that foam stability is influenced by the factors such as equilibrium surface tension, adsorption kinetics, and interfacial rheology. Notably, their study suggests that high surface activity, e.g. low surface tension, and high surface modulus govern foam stability rather than molecular diffusion. Liquid drainage and bubble coarsening are also affected by the viscoelasticity of the interface.[72,73] For instance, Wang et al.[99] examined the relationship between dilatational interfacial rheology and foam properties (foaming capacity and foam stability). Their study suggests there is an optimal viscoelastic modulus, at which the highest foaming capacity is obtained, but this optimal modulus varies from surfactant to surfactant.

The aim of this Chapter is to study the dilatational interfacial rheology of PFAS with various chain lengths (mostly eight- and four-carbon) through periodically pulsating the pendant

drop by using the drop profile tensiometer as well as their adsorption at the air-water interface via the measurement of surface tension by using the Wilhelmy plate tensiometer and to provide a better understanding for PFAS removal efficiencies through foam fractionation. We simply apply the polynomial fit followed by the employment of Gibbs and Langmuir isotherms to the entire PFSA concentration range before CMC without segmenting the concentration range.[110] Consequently, the surface excess and maximum surface excess concentrations of PFSA that have chain lengths of eight and four carbons are determined. Furthermore, dilatational interfacial moduli (E' and E'') of eight-carbon PFSA are calculated and fitted with the Lucassen and van den Tempel model. Additionally, the concentration-dependency and frequency-dependency of E' and E'' are discussed. While previous research has highlighted that the bubble instability is governed by the interfacial modulus,[109,111–113] the interfacial dilatational rheology of PFAS molecules has yet to be studied. Our study marks the first investigation into the interfacial dilatational modulus of PFAS, focusing on PFSA potassium salts with chain lengths of eight and four carbons. Moreover, this work suggests an additional explanation for the difficulty in removing short-chain PFAS at lower concentrations using either adsorbents or foam fractionation, attributing to the lack of interfacial dilatational modulus. The difficulty in removing short-chain PFAS is widely acknowledged as a significant challenge within the field of environmental science.[82,87,106]

3.2. Surface tensions of PFAS

Figure 3.1A shows the surface tension as a function of time of 0.4 mM aqueous solutions of PFAS potassium salts with four-carbon (C4), six-carbon (C6), and eight-carbon (C8). The PFAS with eight carbons (KPFOS) have the lowest surface tension (black square points), whereas KPFBS which have four carbons have the highest surface tension (blue triangle points). The surface tension of KPFHxS (C6, red round points) lies in between KPFOS and KPFBS. A typical

mixture of KPFOS and KPFBS with a mole ratio of 1:1 and same total concentration as single PFAS has the surface tension (green triangle points) in between KPFOS and KPFBS, indicating competitive adsorption of long-chain (C4) and short-chain (C4) PFAS. Silva et al.[114], Schaefer et al.,[115] and Brusseau[116] reported that the surface tension increases at a given concentration by decreasing the chain length for both PFSA and PFCA. In addition, as the chain length decreases, the adsorption coefficient K_i decreases. As seen in **Figure 3.1B**, the surface tension is plotted as a function of $t^{-0.5}$ to obtain the equilibrium surface tension by an extrapolation to $t^{-0.5} \to 0$ according to *Equation (3.1)*.[93,117]

$$\gamma - \gamma_e = \frac{2RT\Gamma_m^2}{C}\left(\frac{1}{\pi D_{eff} t}\right)^{0.5} \qquad \textit{Equation (3.1)}$$

where γ_e is the equilibrium surface tension, ($\gamma = \gamma_e$ when $t^{-0.5}$ is approaching zero), D_{eff} is the effective diffusion coefficient, and t is the time. Equilibrium surface tensions at 0.4 mM are summarized in **Table 3.1**.

The surface tension of KPFOS and KPFBS aqueous solutions with different concentrations was measured as shown in **Figure 3.2**. KPFOS is approaching the solubility limit in the water at the concentration of 1.1-1.2 mM (~ 600 ppm). The short-chain PFAS have a higher solubility limit in the water. **Table 3.1** summarizes the values of solubility limit reported in the literature. **Figure 3.3A** shows the equilibrium surface tension of KPFOS at varied concentrations. The standard deviation due to the repetitive measurements is shown for surface tension as well as dilatational modulus. The uncertainty calculation can be found in Appendix A. The application of Gibbs isotherm, *Equation (2.4)*, to the surface tension below CMC allows the estimation of Γ_m. However, the CMC of KPFOS in the water is not observed within the solubility (blue square points). The previous work done by Silva et al.,[114] Costanza et al.,[110] and Shinoda et al.[118] are also shown in **Figure 3.3A**. It should be noted that different tensiometries were used in the literature to obtain

the surface tension of PFSA. A du Noüy ring tensiometer was used in Silva et al.'s work,[114] Wilhelmy plate tensiometry was employed in Costanza et al.'s work,[110] while Shinoda et al.'s used the drop profile method to obtain the surface tension of KPFOS.[118] The comparison of employing different tensiometers for PFAS surface tension are not discussed here, it will discussed separately. For the data from the previous work,[110,114,118,119] the CMC is absent as well.

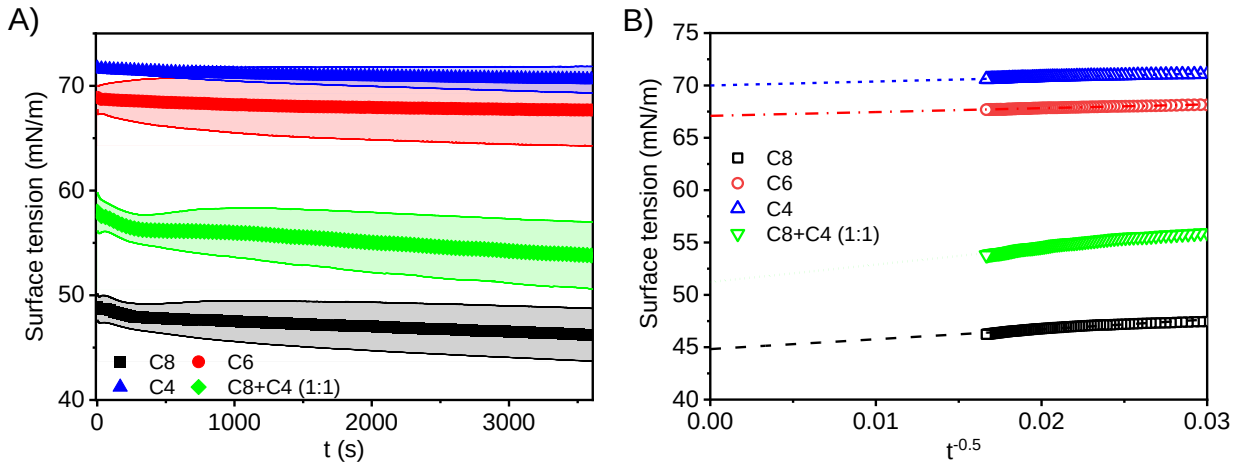

Figure 3.1 A) Dynamic surface tension of 0.4 mM KPFOS, KPFHxS, KPFBS (C8, C6, and C4) and KPFOS+KPFBS aqueous solutions at 25 °C. B) Extrapolation examples show the surface tension as a function of $t^{-0.5}$ in the range of 0 to 0.03 to obtain the equilibrium surface tension according to *Equation (3.1)*.

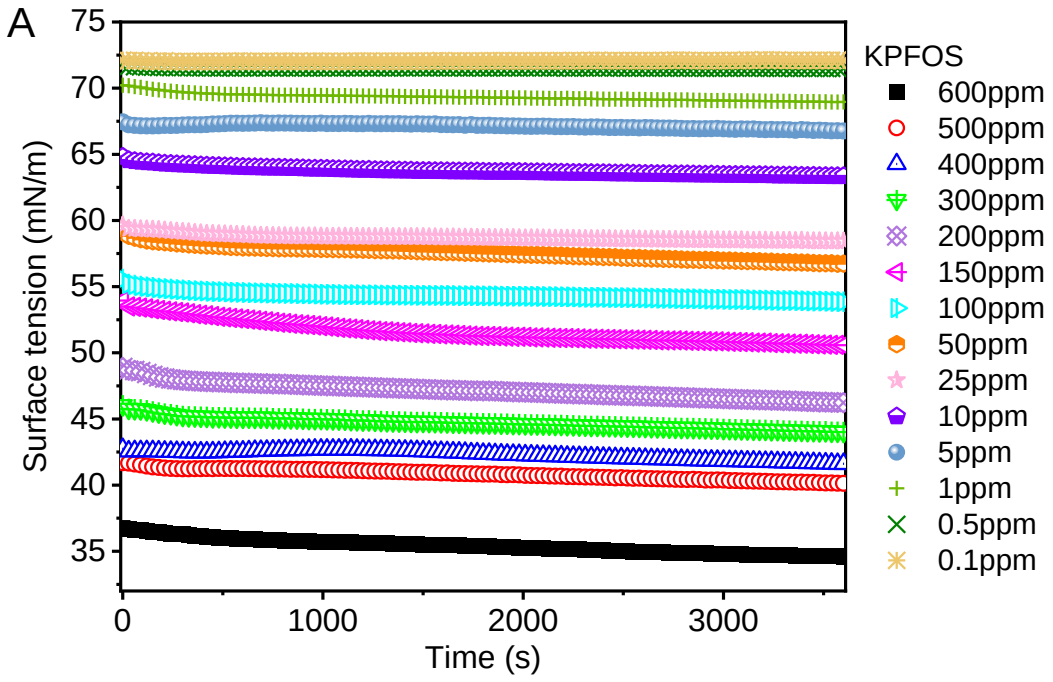

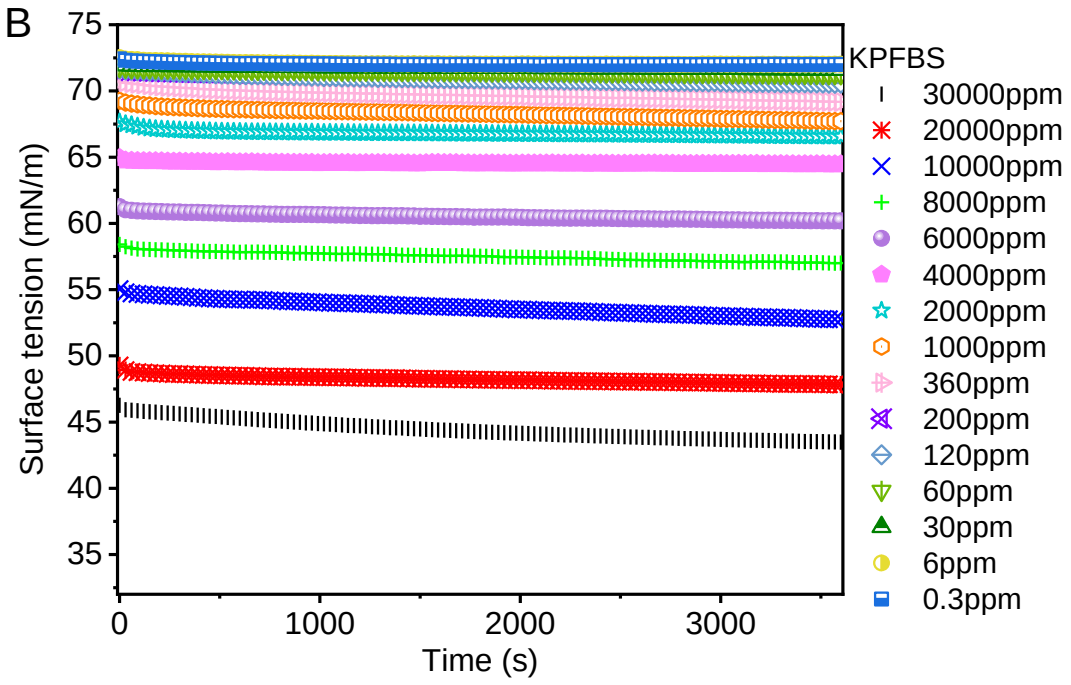

Figure 3.2 A) Dynamic surface tension of KPFOS aqueous solutions with varied concentrations as a function of time at 25 °C. And B) dynamic surface tension of KPFBS aqueous solutions with varied concentrations as a function of time at 25 °C.

The CMC is important for fluorinated surfactants since most surfactant properties depend on the CMC. As is generally true for all surfactants, for PFAS the CMC is related to aqueous solubility, i.e., higher aqueous solubility, higher CMC.[31,120] In addition, the CMC generally scales with the Krafft temperature (T_K); above T_K surfactant solubility dramatically increases due to the melting of solid hydrated surfactants.[31] KPFOS has the T_K of 80 ℃.[31] **Figure 3.3B** shows KPFBS equilibrium surface tension versus natural logarithm of concentrations conducted in the present work. In addition, the data sets from Campbell et al.[121] and Silva et al.[114] are shown. Similar to KPFOS, the CMC of KPFBS is not observed within the studied the concentration range for both our work and previous work,[114,121] although a CMC of 22 mM was reported for KPFBS.[122] The CMC shifts to the higher concentration regime with decreasing the chain length of PFSA, it is also true for PFCA, for example, the CMC is 700 mM for C4 PFCA and 9.1 mM for C8 PFCA.[31,123] The shift of CMC with changing the chain length can be correlated to the change of enthalpy

intercept in the equation $\Delta H_m^\circ = \Delta H_m^* + T_c \Delta S_m^\circ$, where ΔH_m° is the enthalpy change, ΔS_m° is the entropy change, and T_c is the enthalpy-entropy compensation temperature.[124] An increase in ΔH_m^* with decreasing the chain length of hydrocarbon surfactants was reported by Chen et al.,[124] indicating the decreased surfactant hydrophobicity as well as micelle stability.

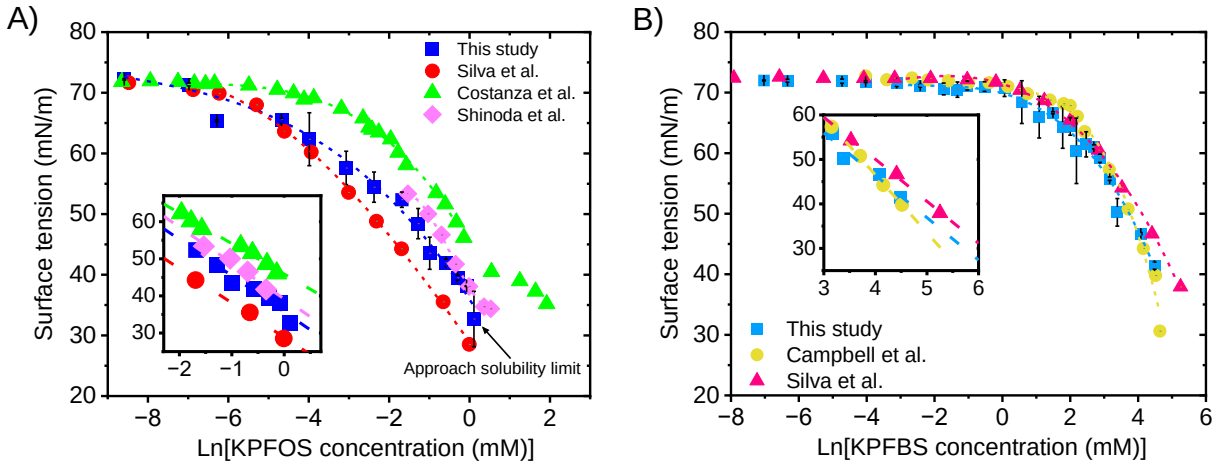

Figure 3.3 A) Equilibrium surface tension of KPFOS measured in this study (at 25 °C) as a function of KPFOS concentration, and comparison to the previous studies.[110,114,118] Dashed lines: polynomial fitting (n=3) to the surface tension of KPFOS. Some of the very low concentration data points are removed in the polynomial fitting to obtain a more accurate fitting (green and red data sets). Inset: the data points in the concentration range of 0.14 to 1.1 mM are fitted by using Gibbs adsorption isotherm. B) Equilibrium surface tension of KPFBS measured in this study (at 25 °C) as a function of KPFBS concentration, and comparison to the previous studies.[114,121] Dashed lines: polynomial fitting (n=3) to the surface tension of KPFBS. Some of the very low concentration data points are removed in the polynomial fitting to obtain a more accurate fitting. Inset: the data points in the concentration range of 18 to 191 mM are fitted by using Gibbs adsorption isotherm.

3.3. Surface excess of PFAS

For KPFOS, the surface tension in the concentration range of around 0.14 to 1.1 mM, where the surface tension shows a linear relationship as a function of natural log of concentration, are used to fit with Gibbs isotherm for estimating Γ_m (see **Figure 3.3A** inset). The fitted parameters are shown in **Table A1**, and the R^2 for all cases is greater than 0.95. This approximation gives Γ_m of KPFOS for our experimental data as 1.18 ± 0.11 molecule/nm^2 (listed in **Table 3.1**). Additionally, the same approach yields 1.13 ± 0.08 molecule/nm^2, 1.00 ± 0.05 molecule/nm^2, and 1.17 ±0.14 molecule/nm^2 for the work done by Silva et al., Constanza et al., and Shinoda et al.

Steffen et al.[119] have done the surface tension measurement for PFOS, and the Γ_m of PFOS calculated using Steffen et al.'s data is 1.54 ± 0.07 molecule/nm^2.The Gibbs model is used to fit the KPFBS surface tension in the range of 18 to 191 mM as seen in **Figure 3.3B** inset, and the fitted parameters are listed in **Table A2**. Γ_ms of KPFBS are 1.16 ± 0.22, 1.58 ± 0.05, and 1.15 ± 0.06 molecule/nm^2 for the current work, Campbell et al., and Silva et al., respectively. Γ_ms, except for the Campbell value, are very similar for KPFBS and KPFOS, which is expected if the head group controls the area per molecule.

As mentioned previously, polynomial fitting can be employed to fit the surface tension at concentrations lower than the CMC, then Γ can be obtained by applying *Equation (2.4)*. To check the accuracy of our procedures, **Figure 3.4** shows the polynomial fitting of KPFOS with various orders (n=2,3,4), indicating the third order is sufficient for obtaining the accurate derivatives. **Figure 3.3A** dashed lines show the third-order polynomial fitting to the surface tension of KPFOS as a function of natural logarithm of concentration with a R^2 greater than 0.99 (**Table A3**). Some data points at very low concentrations are removed for the fitting to avoid a peak within the fitting range. Γ of KPFOS obtained based on the third-order polynomial fitting for the current work and previous work is plotted as **Figure 3.5A**. The Langmuir isotherm shown in *Equation (2.5)* is used to fit the Γ as a function of concentration (solid lines in **Figure 3.5A**), and the fitted parameters are shown in **Table A4** with a R^2 greater than 0.94. Even though Γ_m is available from the Gibbs equation, Γ_m was treated as a fitting parameter in our approach. The Langmuir-type adsorption behavior is associated with the assumption of monolayer adsorption[94]; however, the fit with R^2>0.94 does not fully prove the presence of KPFOS monolayer at the air-water interface since the surfactant adsorption is a complex process and several factors can affect the shape of the adsorption curve to make the final curve well-fitted with Langmuir isotherm.

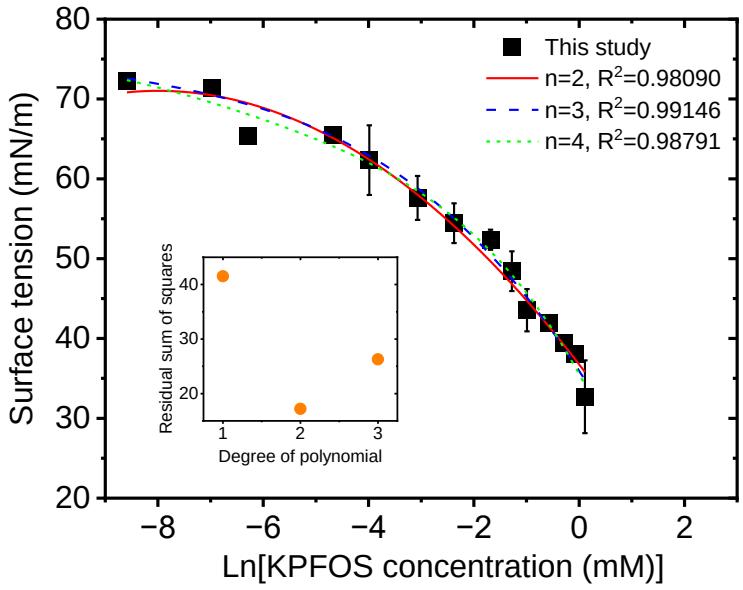

Figure 3.4 A) Second-order, B) third-order, and C) fourth-order of polynomial fitting to the surface tension of KPFOS conducted in this study. Inset: residual sum of squares (RSS) of the polynomial fitting.

Dashed lines in **Figure 3.5A** are the fitting lines obtained by employing Extended Langmuir isotherm, expressed in *Equation (2.6)*, with a R^2 of 0.99 for all cases (**Table A5**). The Γ_m obtained from Langmuir and Extended Langmuir models is summarized in **Table 3.1**. For KPFOS data in this study, the Extended Langmuir Γ_m is 1.98 ± 0.12 molecule/nm^2 compared to ~1.20-3.50 molecule/nm^2 obtained for the data reported in previous works. Costanza et al.[110] obtained Γ_m of 1.43 ± 0.17 molecule/nm^2 (1.28 ± 0.15 mg/m^2) for KPFOS by applying Langmuir/Szyszkowksi equation in the KPFOS concentration range of 0.0002-0.17 mM, compared to KPFOS Γ_m of 1.98 ± 0.12 molecule/nm^2 obtained by fitting within the entire concentration range of 0.0002-1.10 mM. For PFOS in acid form, Γ_m is 1.88 ± 0.04 molecule/nm^2, similar to that of KPFOS as seen in **Table 3.1**. The polynomial fitting and Extend Langmuir model fitting to PFOS data from Steffen et al.[119] are shown in **Figure 3.6**. According to **Table A5**, the n values for all data excluding Shinoda et al.'s are > 0 but < 1, suggesting multi-site adsorption,[95] rather than the formation of hemimicelles or aggregates at the surface which is the case if $n > 1$.

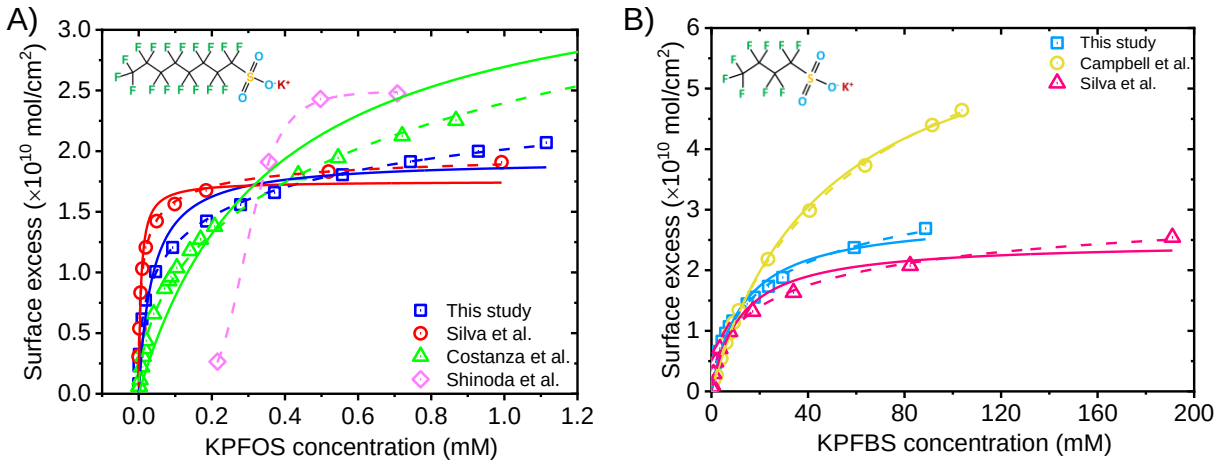

Figure 3.5 A) Surface excess concentration of KPFOS as a function of KPFOS bulk concentration for the data generated in the current work, Silva et al.[114], Costanza et al.[110], and Shinoda et al.[118] The solid lines are the Langmuir isotherm fitting, and the dashed lines are the fitting using Extended Langmuir isotherm. The most pronounced deviation from Langmuir model is observed for Shinoda et al.'s data. The last four points of Costanza et al.'s data are not showing since they are above the solubility limit. B) Surface excess concentration of KPFBS as a function of KPFBS bulk concentration for data generated in the current work, Campbell et al.[121], and Silva et al.[114] The solid lines are the Langmuir isotherm fitting, and the dashed lines are the fitting using Extended Langmuir isotherm. Noting that the surface excess concentration plotted here is obtained by applying a third-order polynomial fitting.

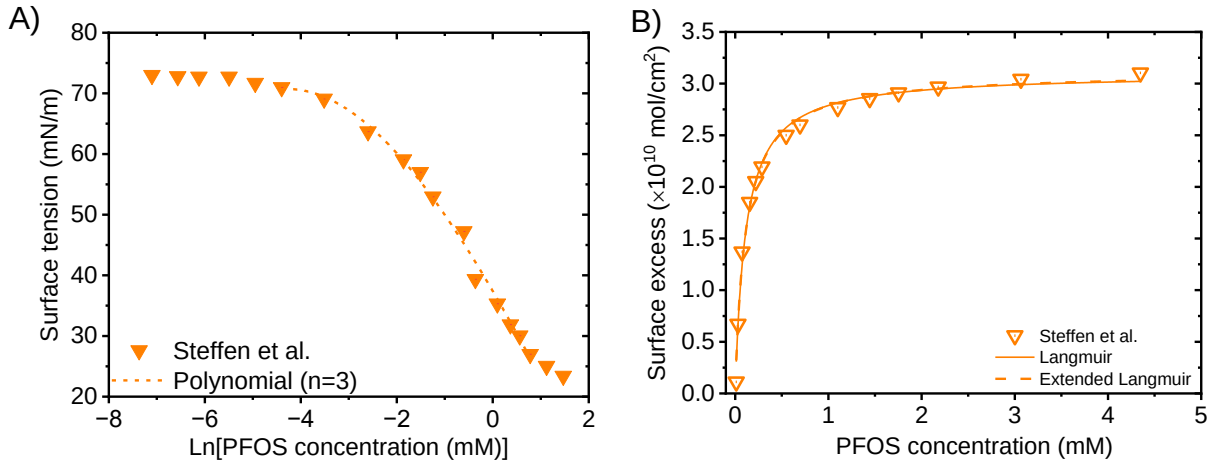

Figure 3.6 A) Polynomial fitting (n=3) to the surface tension of PFOS, data retrieved from Steffen et al.[119] B) Surface excess concentration of PFOS as a function of PFOS bulk concentration for the data retrieved from Steffen et al.[119] The dashed line is the fitting curve using Extended Langmuir isotherm.

A third-order polynomial fitting is also applied to KPFBS surface tension versus natural logarithm of concentration as seen in **Figure 3.3B**. Some of the very low concentration data points of KPFBS are again excluded for polynomial fitting. Fitted parameters are shown in **Table A6**. The R^2 of third-order polynomial fitting of KPFBS is generally lower than that of KPFOS (~ 0.99).

Γ of KPFBS as a function of concentration is plotted in **Figure 3.5B** and fitted by Langmuir and Extended Langmuir models (fitted parameters can be found in **Tables A7** and **A9**). The data of current work and Silva et al. is quite similar, while the Γ of Campbell et al. is greater. Extended Langmuir isotherm fittings suggest that no KPFBS hemimicelles are formed and multi-site adsorption also takes place for KPFBS since $0 < n < 1$. Γ_m of KPFBS obtained by fitting the Langmuir and Extend Langmuir models are summarized in **Table 3.1**. K_L of KPFOS based on the Langmuir isotherm is much greater than that of KPFBS (**Tables A4** and **Table A7**), suggesting that the long-chain (C8) PFAS interact more strongly with the air-water interface compared to the short-chain (C4) PFAS (higher desorption rate for KPFBS).

Table 3.1 Summary table of PFAS properties (KPFOS, KPFHxS, and KPFBS).

PFAS	Molecular weight (g/mol)	Solubility in water (mM)	CMC (mM)	γ (mN/m) for 0.4 mM aqueous solution at 25˚C	$\Gamma_{m,G}$ (molecule/nm^2)	$\Gamma_{m,L}$ (molecule/nm^2)	$\Gamma_{m,EL}$ (molecule/nm^2)
KPFOS	538.22	0.93[121]	8.0[31]	43.540 ± 2.648	1.18 ± 0.11	1.16 ± 0.05	1.98± 0.12
			1.86[125]		1.13 ± 0.08 (Silva et al.[114])	1.05 ± 0.04 (Silva et al.[114])	1.23 ± 0.05 (Silva et al.[114])
		1.06[31]	8.50[126]		1.00 ± 0.05 (Constanza et al.[110])	2.20 ± 0.09 (Constanza et al.[110])	3.42 ± 0.15 (Constanza et al.[110])
			7[122]		1.17 ± 0.14 (Shinoda et al.[118])	-	1.50 ± 0.01 (Shinoda et al.[118])
PFOS	500.13	1.36[127]	5.50-8.50[119]	-	1.54 ± 0.07 (Steffen et al.[119])	1.87 ± 0.02 (Steffen et al.[119])	1.88 ± 0.04 (Steffen et al.[119])
		1.00[127]	2.40[120]				
KPFHxS	438.20	3.19[121]	18.20[120]	67.536 ± 3.896	-		
			12[122]				
KPFBS	338.19	136.61[121]	22[122]	71.160 ± 0.737	1.16 ± 0.22	1.74 ± 0.06	2.34± 0.13
					1.58 ± 0.05 (Campbell et al.[121])	3.99 ± 0.08 (Campbell et al.[121])	4.71 ± 0.23 (Campbell et al.[121])

					1.15 ± 0.06 (Silva et al.[114])	1.49 ± 0.09 (Silva et al.[114])	2.09 ± 0.17 (Silva et al.[114])
KPFOS+ KPFBS (1:1)	-	-	-	51.233 ± 4.072	-		

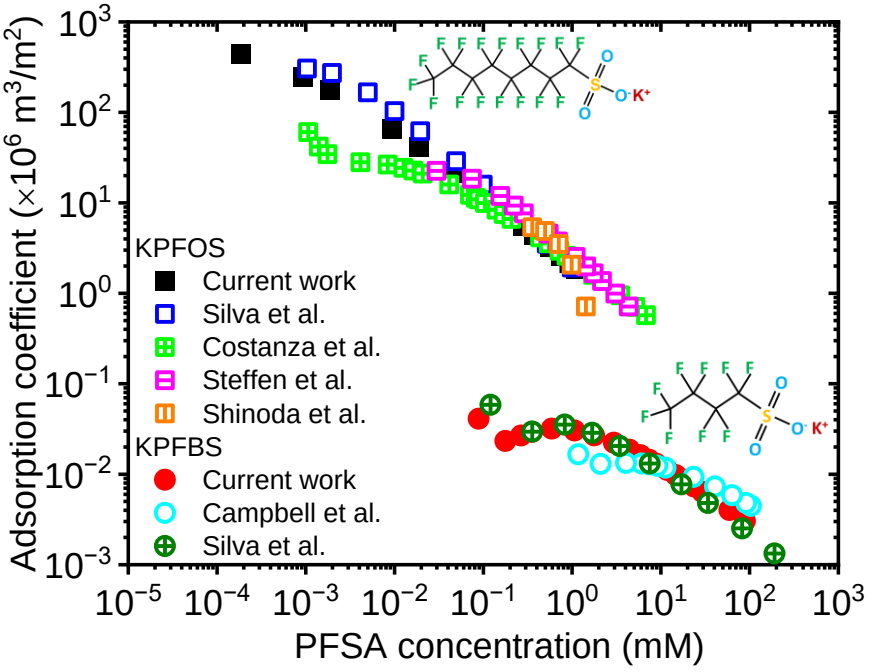

Figure 3.7 Adsorption coefficient K_i of KPFOS and KPFBS as a function of concentration for the current work and previous studies.

The Extended Langmuir model Γ_ms are 1.98 ± 0.12 and 2.34 ± 0.13 molecule/nm^2 while Silva et al.[114] had values of 1.23 ± 0.05 and 2.09 ± 0.17 molecule/nm^2 for KPFOS and KPFBS respectively. This result is in direct contradiction from the results from the Gibbs equation where no difference between KPFOS and KPFBS was found. Although Campbell et al.[121] found chain length did not change Γ_m, the KPFBS tend to have a higher surface excess concentration than that of the KPFOS at the same concentration, which is in an agreement with results obtained from Langmuir/Extended Langmuir models.[128] A higher Γ_m for KPFBS implies a more closely-packed interface, and thus, the KPFBS molecules tend to be oriented more perpendicularly to the air-water

interface.[129] Moreover, Γ_m is a result of a balance between the hydrophobic interaction among the fluorinated chains and the Coulombic repulsion between the neighboring sulfonate head groups.[121] The smaller Γ_m for KPFOS indicates tighter packing of the tails, which means water is able to be better excluded from the tails. *Equation (2.7)* is used to calculate the adsorption coefficient K_i of KPFOS and KFPBS for the current and previous studies as shown in **Figure 3.7**. The data from the different studies for a given surfactant are superimposed on one another. However, the absorption coefficient of long-chain KPFOS is much higher than that of short-chain KPFBS indicating stronger adsorption behavior of the former. Moreover, when the concentration of KPFBS is below than 1 mM, the K_i becomes less dependent on the concentration. Lyu et al.[71] also reported that PFAS adsorption at the air-water interface decreases with a decrease in the chain length. However, only PFOA were discussed in Lyu et al.'s work.

3.4. Interfacial dilatational rheology of PFAS

The dilatational interfacial rheology was measured, and **Figure 3.8** shows the typical normalized surface tension and surface area oscillation of 0.4 mM KPFOS and 0.4 mM KPFBS aqueous solutions at 0.5 Hz. At the same bulk concentration, C8 PFAS had surface tension oscillations upon oscillating the volume of a pendant drop, whereas no surface tension oscillation was observed for C4 PFAS possibly due to the fact that not enough molecules are at the interface. For the former, surface area oscillates with a phase lag with respect to surface tension, demonstrating that the interface is viscoelastic.[130] To ensure the weak signal for KPFBS is not due to insufficient migration of PFAS to the interface, 100-min waiting time was applied prior to the oscillation, and the normalized surface tension and surface area oscillation curves of 0.4 mM KPFOS and 0.4 mM KPFBS aqueous solutions at 0.5 Hz are shown in **Figure 3.9**. Nevertheless, for C4 PFAS, the surface tension oscillation is still absent. For C8 PFAS, the range of surface

tension oscillation slightly increases after the 100-min wait. The failure of surface tension oscillation of KPFBS can be attributed to the high surface tension and low K_L, hindering the appearance of surface moduli.[131] Therefore, only the results of KPFOS are discussed below. Note that the pendant drop volume was manually maintained constant by a slight liquid volume compensation during the 100-min waiting duration to ensure the bulk concentration was kept the same.

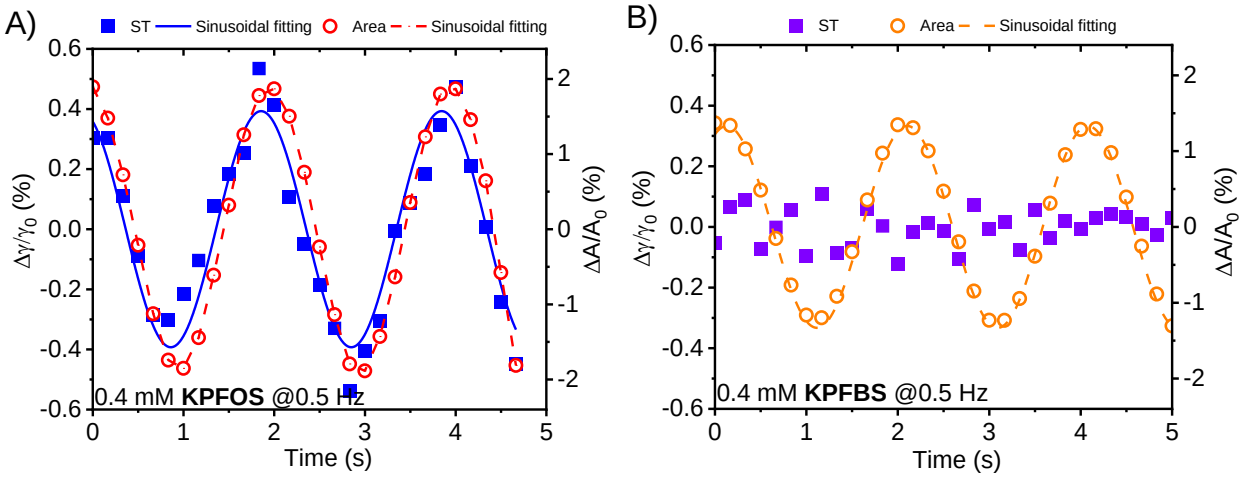

Figure 3.8 Normalized surface tension (ST) and surface area oscillations of A) long-chain and B) short-chain PFAS-adsorbed air-water interface obtained from performing the dilatational interfacial rheology at 0.5 Hz.

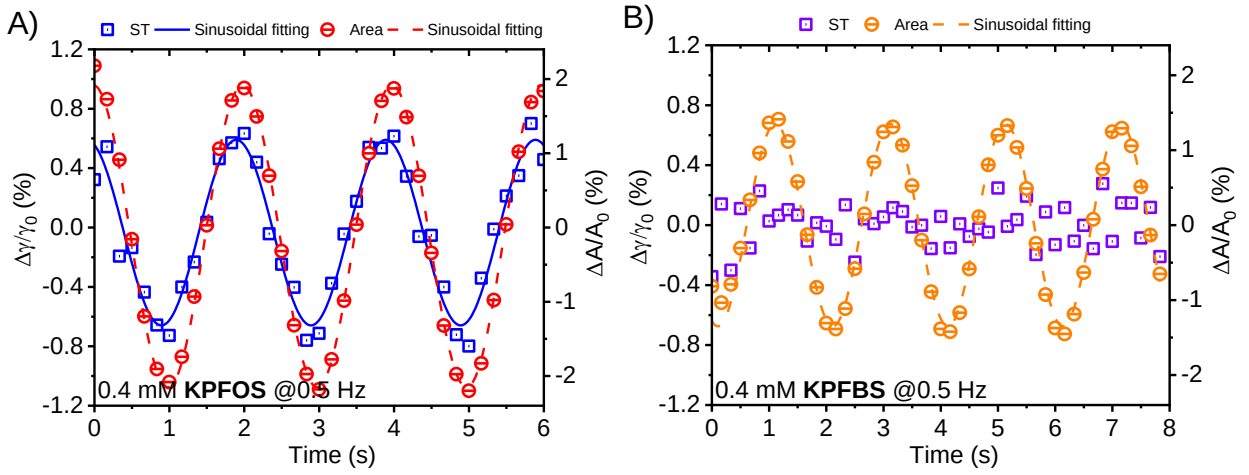

Figure 3.9 Normalized surface tension (ST) and surface area oscillations of A) long-chain and B) short-chain PFAS-adsorbed air-water interface obtained from performing the dilatational rheology after applying a waiting time of 100 mins at 0.5 Hz.

Figure 3.10 depicts the effect of waiting time on the dilatational storage modulus, E', and loss modulus, E'', of KPFOS-adsorbed air-water interface, suggesting the waiting time effect is negligible. The failure of surface tension oscillation of KPFBS can be attributed to its lower K_L (**Tables A7** and **A8**) and fast diffusion, hindering the appearance of surface moduli at the studied frequencies.[131] A lower K_L suggests stronger interaction between the surfactant and the interface as well as a less favorable adsorption due to a less negative free energy change.[132] Therefore, only the results of KPFOS are discussed below.

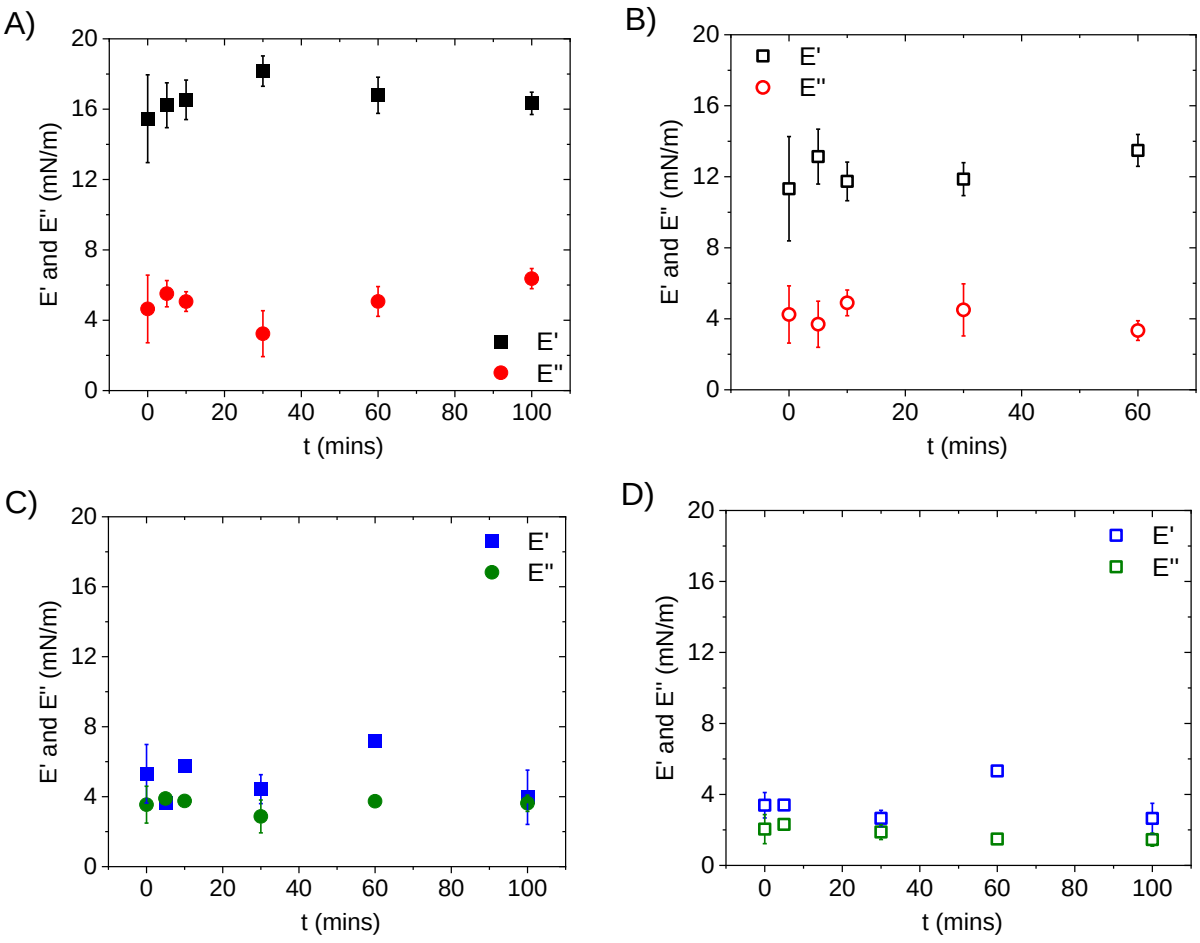

Figure 3.10 E' and E'' of 0.4 mM KPFOS-adsorbed air-water interfaces as a function of waiting time prior to pulsating the pendant drop at A) 0.5 Hz and B) 0.1 Hz; and 1.1 mM KPFOS-adsorbed air-water interfaces as a function of waiting time prior to pulsating the pendant drop at C) 0.5 Hz and D) 0.1 Hz.

3.4.1. Concentration dependency

The dilatational storage modulus, E', and loss modulus, E'', of KPFOS-adsorbed air-water interface for different KPFOS concentrations at a fixed frequency are plotted in **Figure 3.11**. No significant effect of waiting time on dilatational moduli of KPFOS was found (graphs are not shown). E' is higher than E'' at both 0.5 Hz and 0.1 Hz, revealing that elasticity of the viscoelastic interface is dominant for KPFOS. Fainerman et al.[133] pointed out that the compressibility of surfactant molecules at the interface needs to be considered. In other words, E' will have a monotonic increase at a high surfactant concentration region if the surfactant molecules are incompressible. Hence, KPFOS molecules are compressible within the studied concentration range. A maximum in E' and E'' is observed when the KPFOS bulk concentration is around 0.4 mM at both 0.5 Hz and 0.1 Hz. The appearance of a maximum in E' with concentration was also observed for other surfactants, such as nonionic surfactants C_{12} dodecyl dimethyl phosphine oxide (C_{12}DMPO) and Tritons, and ionic surfactant sodium dodecyl sulfate (SDS).[130,133]

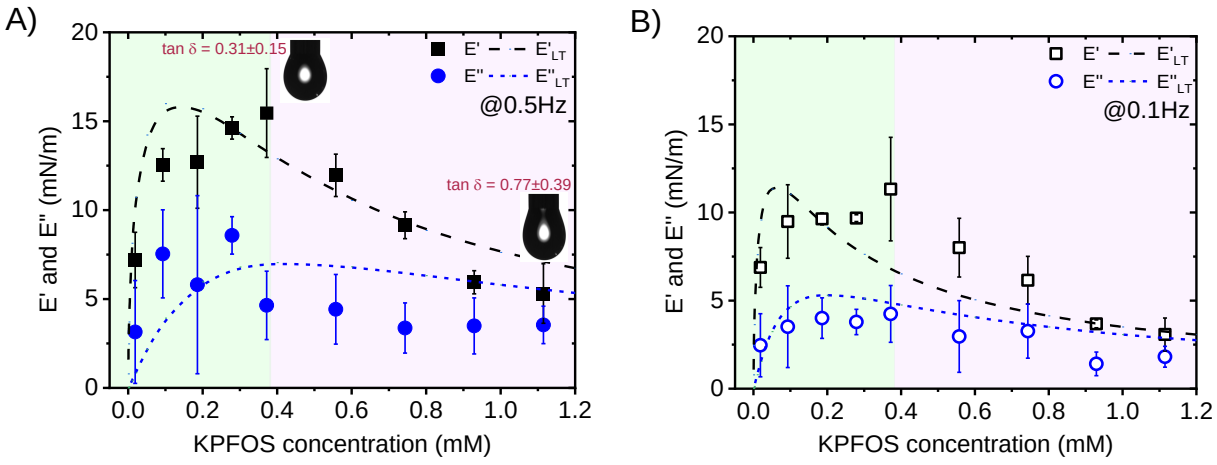

Figure 3.11 E' and E'' of KPFOS-adsorbed air-water interface as a function of KPFOS bulk concentration at a fixed frequency of A) 0.5 Hz and B) 0.1 Hz. The pendant drops of 0.4 mM and 1.2 mM of KPFOS aqueous solution are shown in the A) along with the $\tan\delta$ value. The dashed lines in both A) and B) are obtained by fitting a constant diffusion coefficient by using Lucassen and van den Tempel model (*Equations 2.10-2.13*).

As seen in **Figure 3.11**, two distinct regions are associated with the appearance of the maximum in E' and E''. In the green region, the dilatational interfacial moduli increase with

KPFOS concentration because the Gibbs adsorption or molecular adsorption onto the air-water interface is the dominant factor.[102] Additionally, a transition from an expanded state of the adsorbed KPFOS molecules to a more compact state occurs until reaching the modulus maximum, although desorption of some KPFOS molecules can take place due to the increased surface pressure.[133] At 0.4 mM, the rate of molecular adsorption and molecular exchange is approaching balance. Beyond the maximum point, molecular exchange between the bulk/subsurface and the interface becomes the dominant mechanism (purple region in **Figure 3.11**).[102] In this region, the Marangoni Effect is more significant since molecular adsorption cannot compensate the molecular exchange anymore due to a faster mass transfer, and this, in turn, hinders a high modulus.[134] Additionally, $\tan\delta = E''/E'$ of KPFOS at 0.4 mM and 1.2 mM (above the solubility limit) are 0.31 ± 0.15 and 0.77 ± 0.39 (**Figure 3.11A**) respectively, indicating that the interface is more viscous (almost gel-like since $E' \approx E''$) for the latter vs. the former.

The dashed lines shown in **Figure 3.11** represent the fitting curves of E' and E'' by using *Equations (2.10-2.13)*, giving a $D_{L-T} = 8.00 \times 10^{-12}\ \mathrm{m^2/s}$ for both 0.5 Hz and 0.1 Hz. According to L-T model, the concentration at which the E' maximum appears is smaller than the concentration of E'' peak, indicating that the molecular exchange has a more pronounced effect on $E'$of KPFOS. However, the experimental data show that the desorption of KPFOS molecules has a more significant impact on E''.[102] Moreover, the decrease of predicted E' and E'' in the purple area also suggests the compressibility of KPFOS in this concentration region. The deviation of model prediction from the experimental results can be attributed to (1) the development of the original L-T model, where the diffusion coefficient refers to the dynamic exchange of surfactant molecules from/to the air-water interface rather than the surfactant molecule transport from the

bulk to surface, and (2) the difficulty of KPFOS desorption from the interface, giving rise to the shift of E' maximum to higher concentration region for experimental.

3.4.2. Frequency dependency

Figure 3.12 demonstrates the frequency-dependency of E' and E'' of KPFOS at the concentration of 0.4 mM (around maximum in E') and 1.2 mM (approaching solubility limit). As mentioned earlier, the dominance of elasticity for KPFOS interface becomes weaker for 1.2 mM compared to 0.4 mM concentration. Additionally, both E' and E'' increase with frequency for both concentrations. The dilatational modulus E has been reported to be dependent on frequency, for example, both E' and E'' of C_{12}DMPO are higher at 0.1 Hz compared to that of 0.01 Hz.[100] The increase of E for $C_{14}EO_8$ in the range of 0.005 Hz to 0.2 Hz was reported by Miller et al.[130], and Fainerman et al.[133] reported the dependencies of E on frequency for surfactant polyethylene glycol octylphenyl ethers (Triton X 45 and Triton X 165). The dashed lines in **Figure 3.12** are the L-T model curves, where $D_{L-T} = 8.00 \times 10^{-12}$ m^2/s was obtained earlier. Both E' and E'' predicted by L-T model are dependent on the frequency, which is in an agreement with the experimental data.

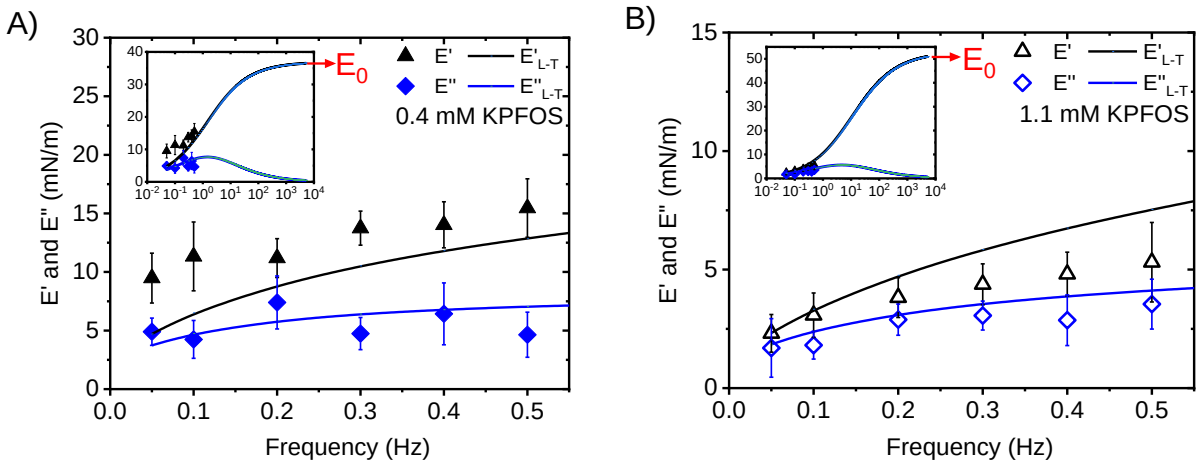

Figure 3.12 E' and E'' of KPFOS-adsorbed air-water interfaces as a function of frequency at a fixed bulk concentration of A) 0.4 mM and B) 1.2 mM. The dashed lines in both A) and B) are obtained by using Lucassen and

van den Tempel model (*Equations 2.10-2.13*) with a $D_{L-T} = 8.00 \times 10^{-12}\ m^2/s$. Insets: Lucassen and van den Tempel model curves in a wider frequency range, showing the prediction of E_0 and the maximum of E''.

Kotsmar et al.[100] observed an E'' maximum at 0.01 Hz for 0.001 mM β-casein protein. While it is often mentioned that the frequency at E'' maximum is close to ω_D,[102,103] L-T model predicts that $E'' = \frac{E_0}{5}$ when the frequency is equal to ω_D. According to *Equation (2.13)* by using the experimental data, we have $\omega_{D,Exp}(0.4\ mM) = 0.73\ Hz$ and $\omega_{D,Exp}(1.1\ mM) = 7.32\ Hz$. As shown in **Figure 3.12** insets, the maximum of E'' is found from the L-T model curve extended to the higher frequency region. In addition, E' approaches E_0 at high frequencies as seen in **Figure 3.12** insets. Expectedly, E_0 is a function of concentration and $E_{0,exp}(0.4\ mM) = 36.94\ mN/m$ and $E_{0,exp}(1.1\ mM) = 52.93\ mN/m$ are obtained by using $E_0 = -\Gamma\frac{d\gamma}{d\Gamma}$. On the other hand, the mixture of KPFOS and KPFBS with equimolar shows a reduced E' as seen in **Figure 3.13**, revealing competitive adsorption between the PFAS with different chain lengths.

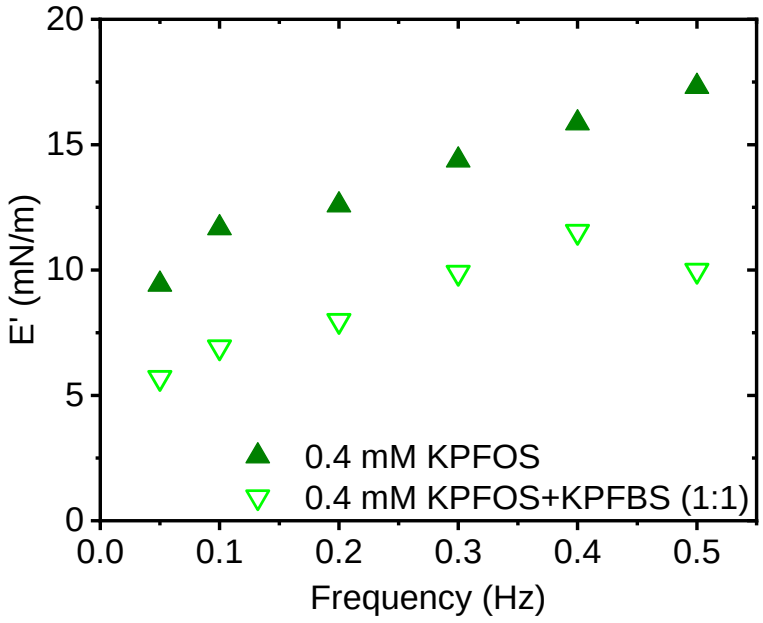

Figure 3.13 Dilatational elastic modulus (E') of 0.4 mM KPFOS and 0.4 mM KPFOS+KPFBS (1:1) air-water interface as a function of frequency.

3.5. Conclusions

In this study, dynamic surface tensions of PFAS with different chain lengths were studied by using the Wilhelmy plate tensiometry. Specifically, two chain lengths were the main focus: eight-carbon KPFOS and four-carbon KPFBS. Both KPFOS and KPFBS did not exhibit a CMC within the studied concentrations. At a given concentration, the equilibrium surface tension of PFAS follows the order of: KPFOS < KPFOS+KPFBS < KPFHxS < KPFBS. We compared our surface tensions of PFAS with data in the literature, and fitted them with Gibbs, Langmuir, and Extended Langmuir models. The Langmuir fitting results show that the maximum surface excess concentration of short-chain PFSA is slightly higher than that of the long-chain PFSA. This work presented a simple approach to determine the maximum surface excess concentration of PFAS within a broader concentration range up to the PFAS solubility limit. Additionally, estimated adsorption coefficient showed that at the same bulk concentration, short-chain PFSA have a lower adsorption coefficient.

At the low bulk concentration, short-chain PFAS do not have sufficient molecules at the air-water interface to initiate the surface tension oscillation when the pendant drop was subjected to oscillate. Therefore, the same surface tension is necessary for comparison rather than the same bulk concentration. For KPFOS, the dilatational surface elasticity (E') was larger than the dilatational loss modulus (E'') and both were concentration-dependent. A maximum of dilatational modulus vs. concentration was observed at both 0.5 Hz and 0.1 Hz. The maximum indicates the competition of molecular adsorption and molecular exchange for long-chain (C8) PFAS adsorption at the interface. The reduction of dilatational modulus at higher concentrations suggests the compressibility of KPFOS molecules within the studied concentration range. Both E' and E'' of KPFOS are dependent on the deformation frequency. E' and E'' were fitted with Lucassen and van

den Tempel model to obtain the D_{L-T}. A maximum of E' and E'' was observed for the fitting, whereas E'' maximum is less apparent compared to E' maximum for the experimental results. However, the models did not describe the data accurately, which is possibly due to the different definitions of diffusion coefficient and the model development in the originally proposed Lucassen and van den Tempel model.

This is the first study to examine the interfacial dilatational rheology of PFAS with various chain lengths, providing crucial information into the air-water interfacial modulus of PFAS. The significance of the interfacial modulus in the foaming process is often mentioned but has not been extensively explored. Further research into the interfacial shear and dilatational rheology of PFAS is essential to expand our fundamental understanding of interfacial rheology, focusing on, but not limited to, PFAS mixture systems and PFAS in the absence or presence of salts.

*Chapter 4. Effect of Electrolytes on the Per- and Polyfluoroalkyl Substances (PFAS) Air-water Interfacial Properties**

4.1. Introduction

As introduced in the previous Chapters, foam fractionation or called aeration is one promising remediation method to remove PFAS from contaminated water due to the amphiphilicity of PFAS, allowing them to be adsorbed at the air-water interface.[69,70,135–137,71,81–83,87–89,106] The Chapter 3 already studies the interfacial properties including surface adsorption and interfacial dilatational rheology of PFAS, but the effect of additives such as salts on the interfacial properties of PFAS is not addressed in Chapter 3.

It should be noted that salts could always be present in PFAS-contaminated water, such as NaCl. In addition, the removal efficiency of PFAS using the foam fractionation has been measured and reported when the system contains the electrolytes. For example, Meng et al.[82] tested the PFOS removal efficiency in the presence of 0-5 mM NaCl, and their results revealed that the PFOS removal efficiency increases with an increase in NaCl concentration, however, the advantage of adding NaCl on improving PFOS removal efficiency disappears if aerating for more than 2 hrs. Morrison et al.[87] investigated the effects of temperature and high salinity on the removal efficiency of PFAS, and their results showed that NaCl in the AFFFs and the lower temperature help in improving the PFAS removal efficiency. The concentration of NaCl affects the PFAS removal efficiency, for instance, the removal percentage of PFBS is improved from 25 % to 60 % during

* This Chapter is in preparation for submission to peer-reviewed journals. **Zhou, M.**, McCray, HB., Shiau, B., Grady, BP., Foudazi, R.

the aeration of 60 min when increasing the concentration of NaCl from 0.113 M to 0.599 M. It also has been reported in the literature that the high salinity is beneficial for PFAS removal.[88] However, the effect of divalent salts was not studied in Morrison et al.'s work. Lee et al.[81] studied the effect of metallic activators, such as Fe^{3+} and Ca^{2+}, on PFAS removal efficiency, and their results indicated that the valence of ions influences the removal efficiency of PFAS, for example, the highest PFOS removal efficiency of 99.5% was obtained when introducing Fe^{3+}. Nevertheless, although the high removal efficiency up to 99% was reported in the literature by employing foam fractionation, the challenge is to efficiently remove the short-chain PFAS, i.e., PFBS.[82,87,106] On the other hand, although many studies investigated the PFAS removal efficiency in the presence electrolytes, the systematic studies on the correlations between the PFAS foaming behavior and their interfacial properties in the presence of salts are still limited.

Despite reporting PFAS removal by using the foam fractionation, the air-water interfacial properties are also crucial to study when considering the effect of adding electrolytes since the PFAS foaming behavior is highly affected by their interfacial properties via influencing the film stability, as mentioned in the previous Chapter.[111,138] For example, the foam height, foam stability, and the length of Plateau Boader are influenced by the maximum rate of surface tension reduction, $(\frac{d\gamma_t}{dt})_{max}$.[107,108] Besides the surface tension, interfacial rheology is another important factor influencing the PFAS foaming properties as it was reported that the films tend to be more stable if they have a higher interfacial elasticity.[111] The interfacial elasticity at low frequencies governs the bubble Ostwald ripening, whereas the interfacial elasticity at high frequencies controls the bubble coalescence.[112] Additionally, the foam stability was reported to be governed by the viscoelastic modulus rather than molecular diffusion.[109]

Therefore, in this Chapter, the air-water interfacial properties including dynamic surface tension and dilatational interfacial rheology of PFAS are investigated in the presence of electrolytes (NaCl and $CaCl_2$) with various concentrations for better understanding the role of electrolytes on modifying the PFAS interfacial properties. Three typical PFAS anions of PFOS, PFOA and PFBS are used in this Chapter. Dynamic surface tensions of the PFAS aqueous solutions containing electrolytes are measured by using different tensiometers of Wilhelmy plate tensiometer, bubble pressure tensiometer and drop shape tensiometer, and the Gibbs and Extended Langmuir isotherms are employed to find the maximum concentration of PFAS at the air-water interface. In addition to the surface tensions, the diffusion coefficients of PFAS in the water are estimated to study the effect of electrolytes. Furthermore, the dilatational interfacial rheological properties of PFAS in the presence of electrolytes are explored for the first time. The interfacial dilatational moduli, E' and E'', of PFAS are calculated and the effect of salt concentrations on the moduli is discussed. This work advances the understanding of improved PFAS removal efficiency by using foam fractionation upon an addition of electrolytes. Additionally, our findings emphasize the importance of interfacial rheology on enhancing the PFAS removal efficiency via adding electrolytes.

4.2. Effect of electrolytes on the PFAS equilibrium surface tension

Figure 4.1 shows and summarizes the equilibrium surface tension of KPFOS, PFOA and KPFBS at various bulk concentrations with and without electrolytes in our work and from the literature work.[71,84,110,114,115,139–142] In our work, the *Equation (3.1)* is used to obtain the equilibrium surface tension by an extrapolation to $t^{-0.5} \rightarrow 0$ as mentioned in Chapter *3*.[93,117] Equilibrium surface tensions of 0.4 mM PFAS are summarized in **Table 4.1**. The surface tension of PFAS is reduced when introducing the electrolytes, and the divalent salts reduce the surface tension more.

Qazi et al.[143] also observed the surface tension reduction of cationic surfactant hexadecyltrimethylammonium bromide (CTAB) upon an addition of NaCl. The reduction of surface tension is useful in the Enhanced Oil Recovery (EOR) since it enhances the crude oil mobility within the reservoir, decreasing the capillary force, and ultimately improving the oil production.[144]

In addition to surface tension reduction, the electrolytes also influence the CMC of PFAS. One can see from **Figure 4.1A**, the CMC of KPFOS is not appearing even when approaching the solubility limit (around 1.1-1.2 mM). However, in the presence of electrolytes, the CMC of KPFOS shifts to the lower concentrations. It was reported that the CMC of KPFOS is around 7-8.5 mM,[31,122,126] which is far above its solubility limit. In the presence of 100 mM NaCl, the CMC is around 0.4 mM, while the CMC is around 0.2 mM if adding 100 mM $CaCl_2$. The concentration of electrolytes also affects KPFOS CMC, for example, higher CMC of around 1 mM is obtained if only adding 10 mM $CaCl_2$. For KPFBS, the CMC is still not appearing upon an addition of 100 mM $CaCl_2$.

The solubility limit of PFOA is found to be around 9.7 mM (4000 ppm), and the CMC of PFOA is exactly to be around 9.7 mM. Ning et al.[145] also reported the same CMC of PFOA according to ^{19}F NMR spectroscopy. Upon an addition of electrolytes, the PFOA CMC shifts to the lower concentrations (**Figure 4.1D**). A CMC of 7.3 mM is obtained when introducing 100 M NaCl into the PFOA aqueous solutions, whilst the CMC is 4.8 mM in the presence of 100 mM $CaCl_2$. If decreasing $CaCl_2$ concentration to 10 mM, the CMC is around 7.3 mM. It was also reported in the literature that the CMC is affected by adding the electrolytes, but only ionic surfactants are the cases.[123,143,146] Steffens et al.[146] evaluated the composition of 3M AFFF, and reported that high salinity reduces the CMC of the AFFF formulation, consequently, the mass

accumulation of certain PFAS in solutions increases. Their work explains the retention of PFAS in coastal environment and demonstrates that the PFOS and amine functionalized precursor compounds seem to drive the aggregation and surface behavior of PFAS mixture, whose aqueous behavior is substantially impacted in high salinity matrices. Furthermore, the shift of the CMC occurs up to a certain concentration of NaCl, after which the CMC remains a constant.[143]

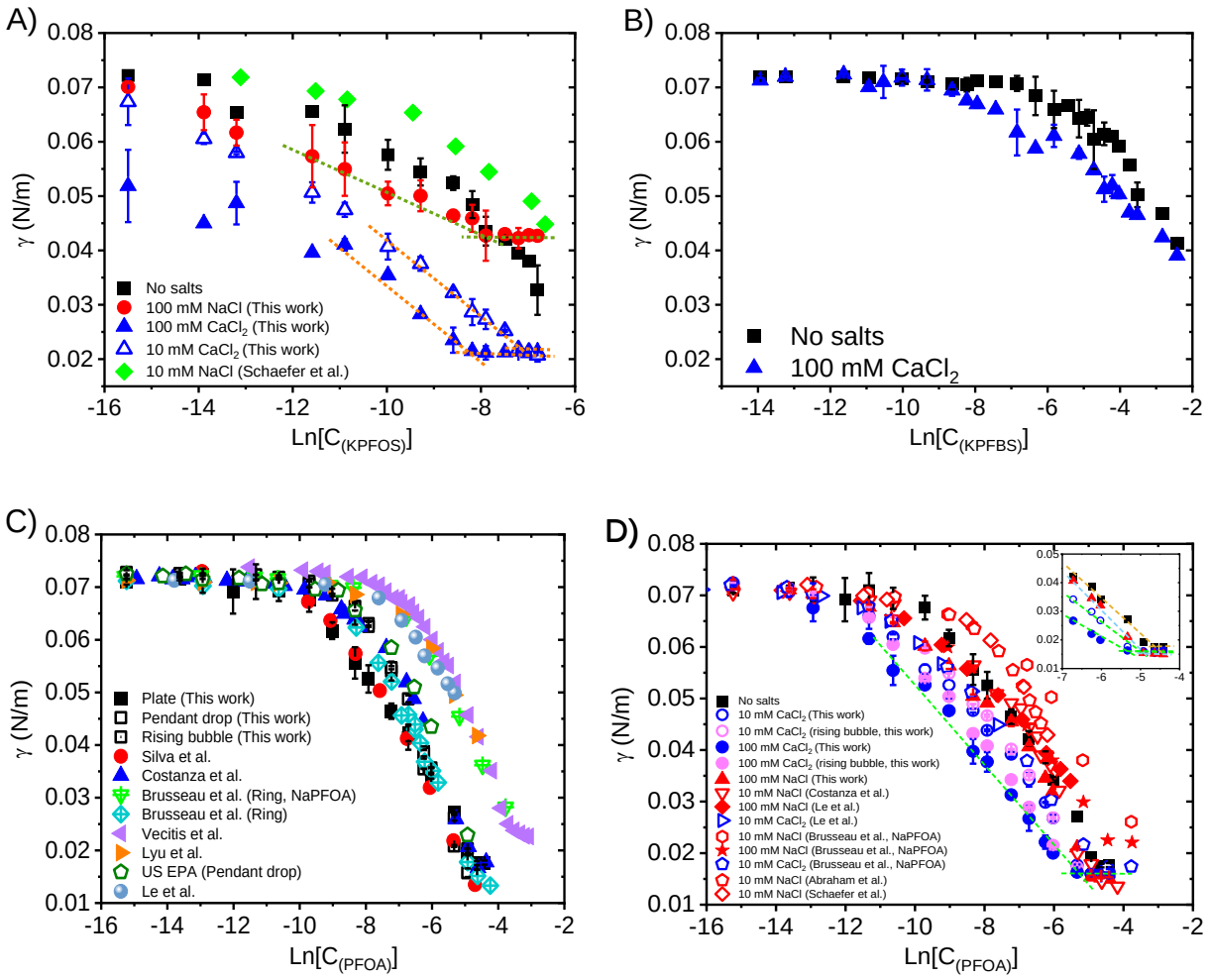

Figure 4.1 A) KPFOS surface tension versus concentration in the presence of 100 mM NaCl, 10 mM and 100 mM $CaCl_2$. The black solid square points are the samples without an addition of salts, and the green solid points are from Schaefer et al.[115], showing the surface tension of KPFOS in the presence of 10 mM NaCl. B) KPFBS surface tension versus concentration with and without adding 100 mM $CaCl_2$ as the background ions. C) PFOA (NaPFOA) surface tension versus concentration in this study and from the literature.[71,84,110,114,139–141] D) PFOA (NaPFOA) surface tension versus concentration in the presence of 10 mM and 100 mM NaCl, and 10 mM and 100 mM $CaCl_2$ conducted in this study and retrieved from the literature.[110,115,139,141,142] The inset shows the CMC of PFOA with and without adding electrolytes.

In addition to CMC, the micellization of PFAS in water is affected upon an addition of electrolytes. The Gibbs free energy of micellization (ΔG_{mic}) is the net free-energy gain for transferring a free surfactant molecule and its counterion from the bulk aqueous solution to a micelle. *Equation (4.1)* below shows the relationship between the CMC of ionic surfactants and ΔG_{mic}.[123]

$$\Delta G_{mic} = (2 - \alpha)RTln(X_{CMC}) \qquad \textit{Equation (4.1)}$$

where α is the degree of counterion dissociation, and X_{CMC} is the mole fraction of surfactants at the CMC. Corrin–Harkins equation, $ln(X_{CMC}) = A - \beta ln(X_C)$, can be used to obtain the α. X_C is the total concentration of free counterion (mole fraction) in the solution at the CMC, $\beta = 1 - \alpha$ is the degree of counterion binding. Without adding electrolytes, $X_{CMC} = X_C$ and $\Delta G_{mic}/RT = A = (1 + \beta)ln(X_{CMC})$. ΔG_{mic} becomes more negative after adding the electrolytes. The *Equation (4.2)* considers different contributions to the total ΔG_{mic}.[123]

$$\Delta G_{mic} = \Delta G_{tr} + \Delta G_{int} + \Delta G_{pack} + \Delta G_{st} + \Delta G_{elec} + \Delta G_{ent} - \beta kTln(X_c e) - kT$$

Equation (4.2)

where ΔG_{tr} is the transfer free energy, ΔG_{int} is the interfacial free energy, ΔG_{pack} is the packing free energy, ΔG_{st} is the steric free energy, ΔG_{elec} is the electrostatic free energy, ΔG_{ent} is the entropic free energy, k is the Boltzmann constant. ΔG_{pack} is associated with the formation of hydrophobic core in the micelles, whereas ΔG_{ent} is linked to the hydrophilic shell of the micelles.

In *Equation (4.2)*, $-\beta kTln(X_c e)$ is the translational entropy lost by the counterions upon binding onto the charged surface of micelles. Kancharla et al.[123] reported the CMC shifts for NaPFO and NaPFHx, which are PFOA and perfluorohexanoic acid (PFHxA) sodium salts, respectively, and have various chain lengths. The lower CMC of long-chain ones is due to the longer fluorinated chain, giving rise to a more negative ΔG_{tr}, lower ΔG_{int}, and lower ΔG_{pack}. The

micellization of long-chain ones is influenced more by adding NaCl compared to that of short-chain ones. It is due to the greater decrease in the entropy lost by binding the counterions onto the charged micelle surface after adding NaCl. Moreover, a greater increase in ΔG_{elec} with the addition of NaCl is obtained. Additionally, Small Angle Neutron Scattering (SANS) shows the growth of micelles in the presence of NaCl.

In addition to Wilhelmy plate method, drop shape profile methods including pendant drop and rising bubble methods were also used for measuring the dynamic surface tension of PFOA. Although du Noüy ring/Wilhelmy plate tensiometry has long been widely employed in surfactant-related industries as a traditional method, Venzmer[147] noted that drop shape tensiometry has been considered the pinnacle in surface tension measurement for many years across academic and industrial settings. This is because with each measurement, a fresh drop is formed, ensuring a well-defined surface age, and enabling the tracking of surface tension reduction kinetics.[147] **Figure 4.2** presents the pendant drop and rising bubble of 0.4 mM and 2.4 mM PFOA aqueous solutions with and without salts, respectively. Based on our results, Wilhelmy plate method gives rise to the smaller equilibrium surface tensions of PFOA in the surface tension drop regime compared to pendant drop and rising bubble methods. Nevertheless, in the lower and higher surface tension regimes, the effect of methods becomes less significant.

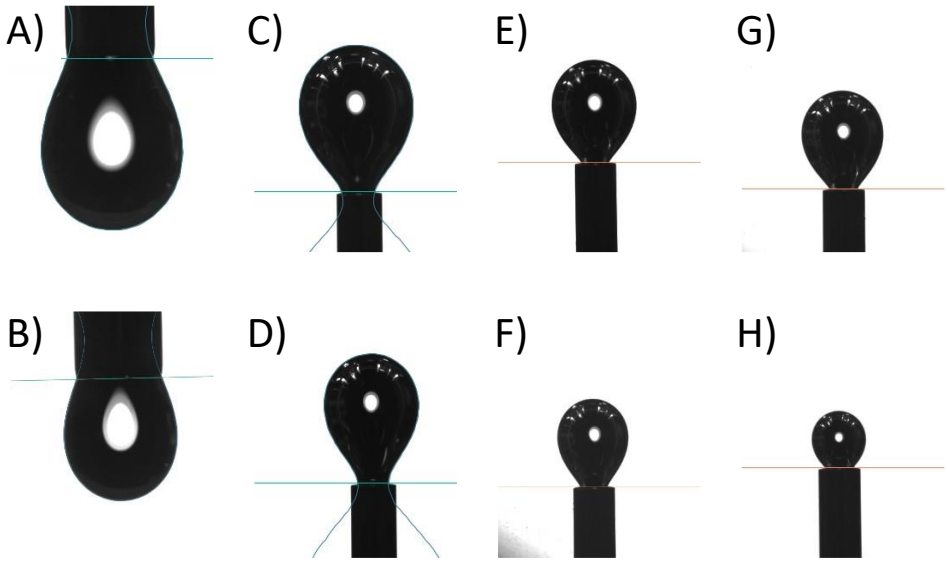

Figure 4.2 Pendant drops of A) 0.4 mM, and B) 2.4 mM PFOA aqueous solutions in the air. Rising bubbles of C) 0.4 mM, and D) 2.4 mM PFOA aqueous solutions in the air. Rising bubbles of E) 0.4 mM, and F) 2.4 mM PFOA aqueous solutions containing 10 mM $CaCl_2$ in the air. And rising bubbles of G) 0.4 mM, and H) 2.4 mM PFOA aqueous solutions containing 100 mM $CaCl_2$ in the air.

Figure 4.3 shows the concentration effect of electrolytes (NaCl and $CaCl_2$) on the equilibrium surface tension of PFAS. It reveals that, for KPFOS, the surface tension is independent of NaCl (monovalent salts) concentration, but it is decreasing with an increase in the concentration of $CaCl_2$ (divalent salts). For PFOA, the surface tension depends on both NaCl and $CaCl_2$ (monovalent and divalent salts) concentration. Nevertheless, only higher concentration of NaCl affects the surface tension of PFOA. Only $CaCl_2$ was tested for KPFBS, and it seems the surface tension of KPFBS is decreasing if the $CaCl_2$ concentration is high. Qazi et al.[143] studied the effect of NaCl concentration ranging from 0.005 M to 5.5 M on either the dynamic surface tension and equilibrium surface tension of cationic surfactant CTAB and nonionic surfactant Tween 80. The reduction in CTAB CMC upon the addition of NaCl was noted, with Qazi et al.[143] suggesting that this phenomenon arises from the salt anions effectively screening the electrostatic repulsion among the cationic head groups of CTAB molecules. This, in turn, promotes their aggregation into micelles. Additionally, the CMC of CTAB stops shifting to lower concentration when the NaCl

concentration reaches ~0.2 M, which is attributed to the fact that the maximum charge screening is approached by adding the counterions. However, the maximum surface excess concentration of CTAB is not affected by increasing the NaCl concentration according to the Gibbs isotherm calculation and sum frequency generation (SFG) spectroscopy results. On the country, the equilibrium surface tension as well as the CMC of Tween 80 are not influenced upon increasing the NaCl concentration.

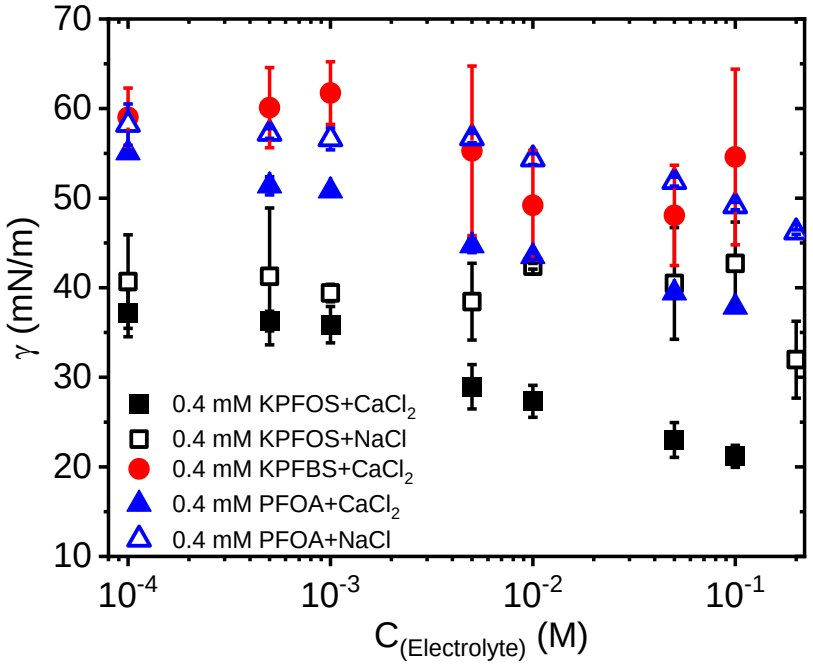

Figure 4.3 Effect of electrolyte concentration on the surface tension of PFAS.

Zhang et al.[148] studied the effect of NaCl concentration ranging from 1 mM to 200 mM on the surface activity of cationic surfactants CTAB and cetyltrimethylammonium chloride (CTAC). They claimed that the influence of adding electrolyte on dynamic adsorption of surfactants is dependent on the time. In their systems, the adsorption of surfactants is initially prevented by the salt ions because the salt ions present at the fresh air-water interface of subsurface, and thus, hindering the surfactant adsorption at a short timescale (less than 0.1 s). Nevertheless, the reports

focusing on the fundamental study of $CaCl_2$ effect on the adsorption behavior of surfactants, especially PFAS, are limited.

4.3. Effect of electrolytes on the surface excess of PFAS

The Gibbs isotherm is shown as *Equation (2.4)*, and it can be used to estimate the maximum surface excess concentration of PFAS. The concentration regime before the CMC is used to fit with the Gibbs isotherm (linear fit), **Figure 4.4** shows the fitting example of KPFOS in the presence of 100 mM $CaCl_2$. All the fitted parameters are shown in **Table B1**. An alternative approach to obtain the surface concentration at different bulk concentrations is to first fit the surface tesnion before the CMC with the polynomial to obtain the local slope,[91] and then apply the Gibbs isotherm to obtain the surface excess concentration. The dashed line in **Figure 4.4** shows the example of third-order polynomial fit to the KPFOS with 100 mM $CaCl_2$. **Table B2** summarizes all the fitted parameters. This method is suitable for the surfactants have no measurable CMC due to the limited solubility.

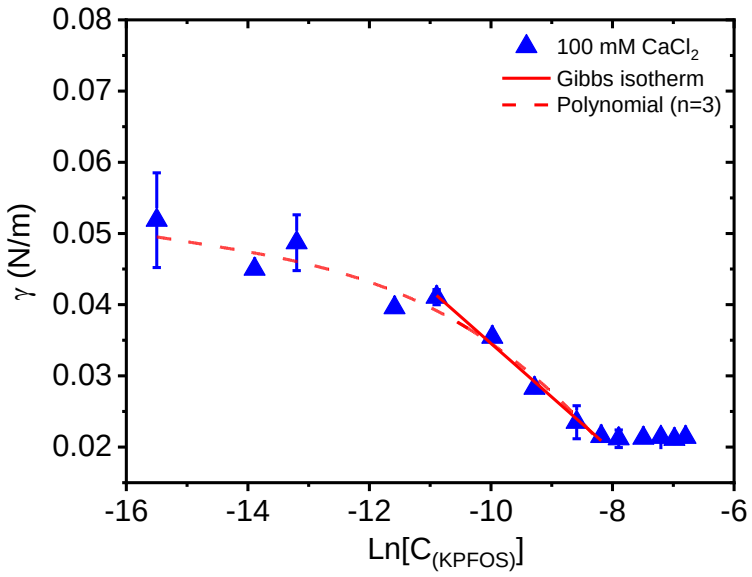

Figure 4.4 Gibbs isotherm fit and polynomial fit with the third-order to the surface tension of KPFOS in the presence of 100 mM $CaCl_2$.

Figure 4.5 presents the local surface excess concentrations of PFAS with and without the addition of electrolytes. As can be seen, the surface concentration of PFAS is enhenced upon an addition of electrolytes. At the same concentration, the divalent salts ($CaCl_2$) improve the surface excess more, and $CaCl_2$ concentration affects the PFAS surface excess. On the other hand, no significant improvement of KPFOS surface excess is obtained by using monovalent salt NaCl as shown in **Figure 4.5A**.

The Langmuir isotherm, shown as *Equation (2.5)*, is an empirical model based on the kinetic principles, that is the adsorption and desorption rates are equal with zero accumulation at the equilibrium conditions.[149] The assumptions of Langmuir model are 1) monolayer adsorption, 2) homogeneous sites, 3) constant adsorption energy, and 4) no lateral interactions between the adsorbed molecules. The adsorption curve of Langmuir isotherm is a L-shape, however, a S-shape adsorption isotherm was proposed, known as the Extended Langmuir isotherm as seen in *Equation (2.6)*.[95,96] Extended Langmuir isotherm combines the Freundlich and Langmuir models, and it is also called Sips isotherm.[149] Since the Extended Langmuir isotherm generates more accurate fits based on the R^2 (see previous Chapter),[149] only *Equation (2.6)* is used in this Chapter.

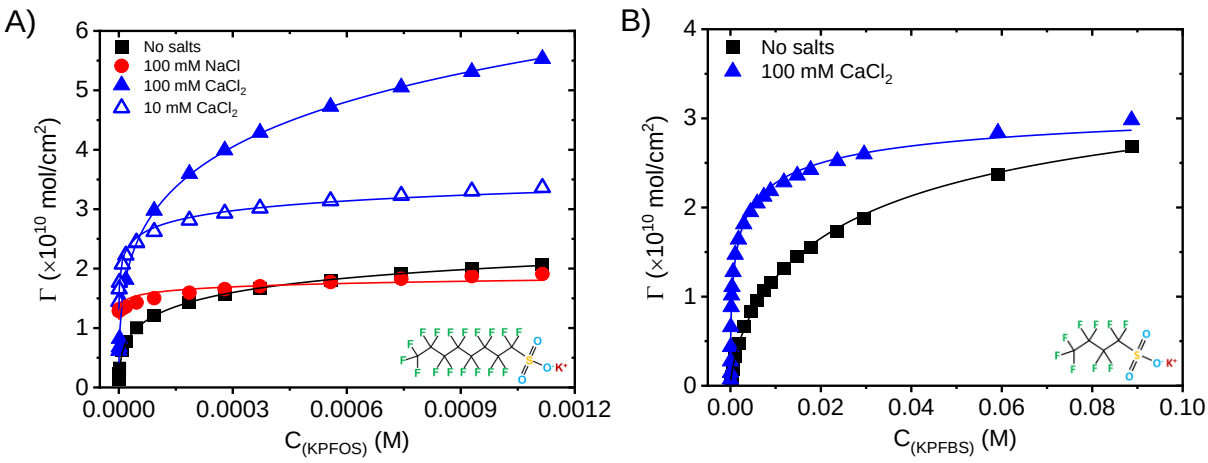

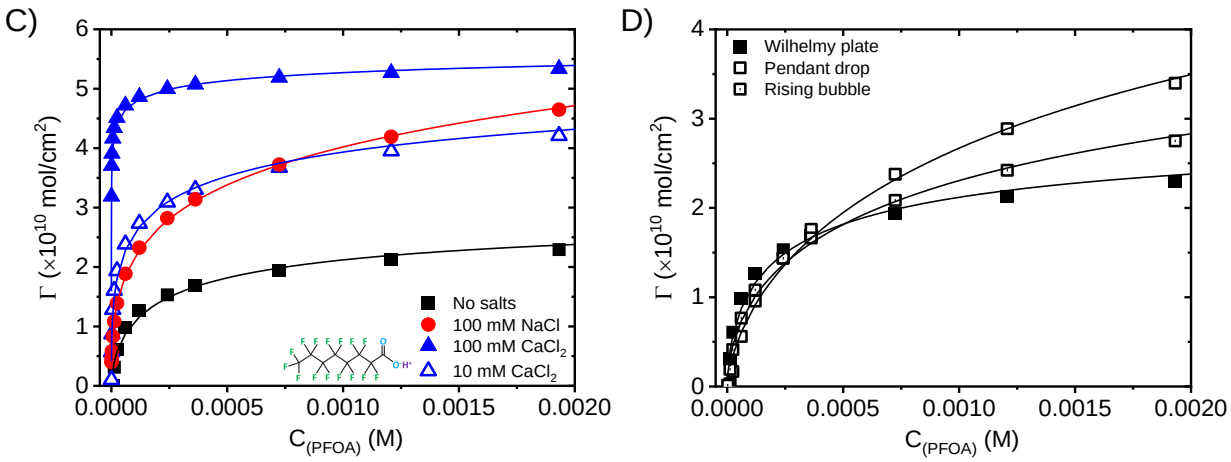

Figure 4.5 A) Surface excess concentration of KPFOS with and without adding electrolytes (NaCl and $CaCl_2$) as a function of KPFOS bulk concentration. B) Surface excess concentration of KPFBS with and without adding $CaCl_2$ as a function of KPFBS bulk concentration. C) Surface excess concentration of PFOA with and without adding electrolytes (NaCl and $CaCl_2$) as a function of PFOA bulk concentration. And D) comparison of PFOA surface excess concentrations obtained by using methods of Wilhelmy plate tensiometry, pendant drop tensiometry and rising bubble tensiometry. The solid lines are the Extended Langmuir isotherm fit.

The solid lines presented in **Figure 4.5** are the Extended Langmuir isotherm, and the fitted parameters are shown in **Table B3**. The Γ_ms of PFAS obtained by employing Gibbs and Extend Langmuir models are summarized as seen in **Table 4.1**, and it indicates that a higher value of Γ_m will be obtained if applying Extended Langmuir model. The Gibbs and Extend Langmuir fittings generally demonstrate that the Γ_ms of PFAS increase upon an addition of electrolytes, for example, the Γ_m of KPFOS is enhanced from 1.18 molecule/nm^2 to 1.83 molecule/nm^2 after adding 100 mM $CaCl_2$ according to the Gibbs model. However, no increase of Γ_m is observed for KPFBS by employing Extended Langmuir model. In addition, the results of Γ_m imply that monovalent salts are more effective in improving the adsorption of PFOA, whilst the surface excess of KPFOS is enhanced more by using the divalent salts. Furthermore, the PFOA Γ_ms obtained by using three tensiometries are different, indicating that the selection of tensiometers has an impact on finding the maximum surface concentration.

Table 4.1 Properties of PFAS (KPFOS, PFOA and KPFBS) in the absence and presence of salts.

PFAS	Salt	Molecular weight (g/mol)	Solubility in water (mM)	CMC (mM)	γ (mN/m) for 0.4 mM aqueous solution at 25˚C	$\Gamma_{m,G}$ (molecule/nm^2)	$\Gamma_{m,EL}$ (molecule/nm^2)
KPFOS	-	538.22	~1.1-1.2, 0.93[121], 1.06[31]	7[122], 8[31], 8.5[126]	44.82	1.18	1.98
	100 mM NaCl		-	~0.4	42.71	1.22	2.91
	10 mM $CaCl_2$		-	~0.9-1.0	27.32	1.59	3.15
	100 mM $CaCl_2$		-	~0.2	21.18	1.83	9.23
PFOA (P.d.*)	-	414.07	-	-	62.54	1.68	4.59
PFOA (R.b.&)	-		-	-	63.07	1.54	3.35
PFOA	-		~9.7	~9.7	52.56	1.16	1.88
	100 mM NaCl		-	~7.3	49.11	2.17	7.23
	10 mM $CaCl_2$		-	~7.3	43.81	2.09	3.88
	100 mM $CaCl_2$		-	~4.8	37.70	2.15	3.81
KPFBS	-	338.19	136.61[121]	22[122]	69.99	1.16	2.34
	100 mM $CaCl_2$		-	-	66.91	1.59	2.02

* Pendant drop tensiometry and pendant drop method.

& Rising bubble method.

4.4. Short-time adsorption of PFAS

The bubble pressure tensiometer is used to measure the dynamic surface tension in a very short time scale and to study the short-time adsorption behavior of PFAS. **Figure 4.6** presents the dynamic surface tension of KPFOS with various bulk concentrations in and not in the presence of electrolytes. The same as utilizing the Wilhelmy plate tensiometer, the surface tension of KPFOS decreases with increasing bulk concentration. In the presence of 100 mM NaCl, the KPFOS

dynamic surface tensions in the short-time scale are not reduced. However, the KPFOS dynamic surface tensions in the first 10 s are dramatically decreasing when 10 mM and 100 mM $CaCl_2$ are presenting as the background ions. Typical dynamic surface tension curves usually display four stages: 1) induction, 2) fast fall, 3) meso-equilibrium, and 4) equilibrium as shown in **Figure B1**.[150] The equation below was proposed by Hua et al.[150] for the first three stages:

$$\gamma - \gamma_m = \frac{\gamma_0 - \gamma_m}{1+(t/t^*)^n} \qquad \textit{Equation (4.3)}$$

where γ_m is the equilibrium surface tension in the stage of meso-equilibrium, γ_0 is the surface tension in the absence of surfactants, and t^* and n are fitted parameters. t^* has the same unit as time, and n being dimensionless. The γ_e, obtained from using *Equation (3.1)*, was taken as γ_m. The solid lines in **Figure 4.6** are the obtained lines by fitting with the *Equation (4.3)*. The fitted parameters are listed in **Tables B4** to **B7**.

It can be seen from **Figure 4.6A** that the fast fall stage is found for all concentrations, but the induction stage becomes shorter with increasing the KPFOS bulk concentrations. Additionally, the meso-equilibrium stage is not approaching yet. When the background ions are 100 mM NaCl, the induction stage becomes longer as seen from **Figure 4.6B**, even though the $\gamma_0 - \gamma_m$ remains the same. When adding 100 mM $CaCl_2$, the induction stage becomes shorter, the $\gamma_0 - \gamma_m$ becomes greater, and at higher concentrations (300-600 ppm), the meso-equilibrium stage is obtained (**Figure 4.6D**). Decreasing the concentration of $CaCl_2$ to 10 mM, the induction stage is not influenced too much, and the meso-equilibrium stage is still obtained. However, the $\gamma_0 - \gamma_m$ slightly decreases (**Figure 4.6C**).

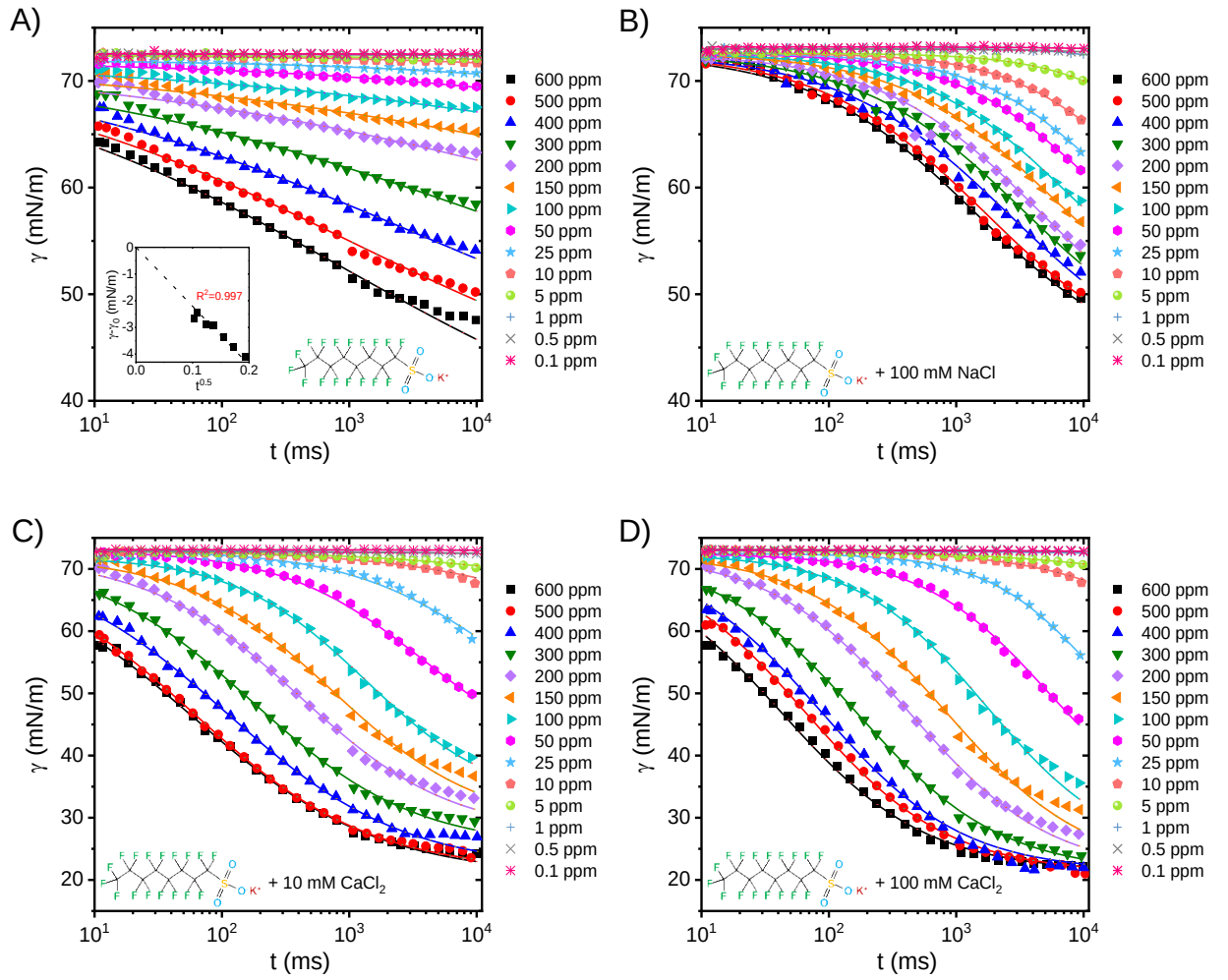

Figure 4.6 Dynamic surface tension of various concentrations of KPFOS A) in the absence of electrolytes, B) in the presence of 100 mM NaCl as the background ions, C) in the presence of 10 mM $CaCl_2$ as the background ions, and D) in the presence of 100 mM $CaCl_2$ as the background ions by using the bubble pressure tensiometer.

The actual Fickian diffusion coefficient can be approximated from *Equation (4.4)* if short enough times are used to measure the surface tension:[93,117]

$$\gamma - \gamma_0 = -2CRT\left(\frac{Dt}{\pi}\right)^{0.5} \qquad \textit{Equation (4.4)}$$

where D is the Fickian diffusion coefficient. The inset of **Figure 4.6A** shows the example of calculating the D when plotting $\gamma - \gamma_0$ vs $t^{0.5}$. The details about the values of D in the absence and presence of salts are discussed in the following Subchapter.

Figure 4.7 shows the dynamic surface tension of PFOA with various bulk concentrations in and not in the presence of electrolytes, and the solid lines are the model based on the *Equation (4.3)*. The fitted parameters are summarized in **Tables B8** to **B11**. Without adding electrolytes, the same as KPFOS, the induction stage becomes shorter as increasing the bulk concentration of PFOA. No further decrease of surface tension is observed when the PFOA concentration is around 9.7 mM (4000 ppm), indicating the CMC. The CMC shifts to lower concentrations when adding electrolytes. These results are in agreement with the Wilhelmy plate tensiometer results. Additionally, upon an addition of electrolytes regardless the valence, no significant change of induction stage time is observed, and the $\gamma_0 - \gamma_m$ increases. When adding 100 mM NaCl, it is earlier to reach the meso-equilibrium stage compared to adding 100 mM $CaCl_2$.

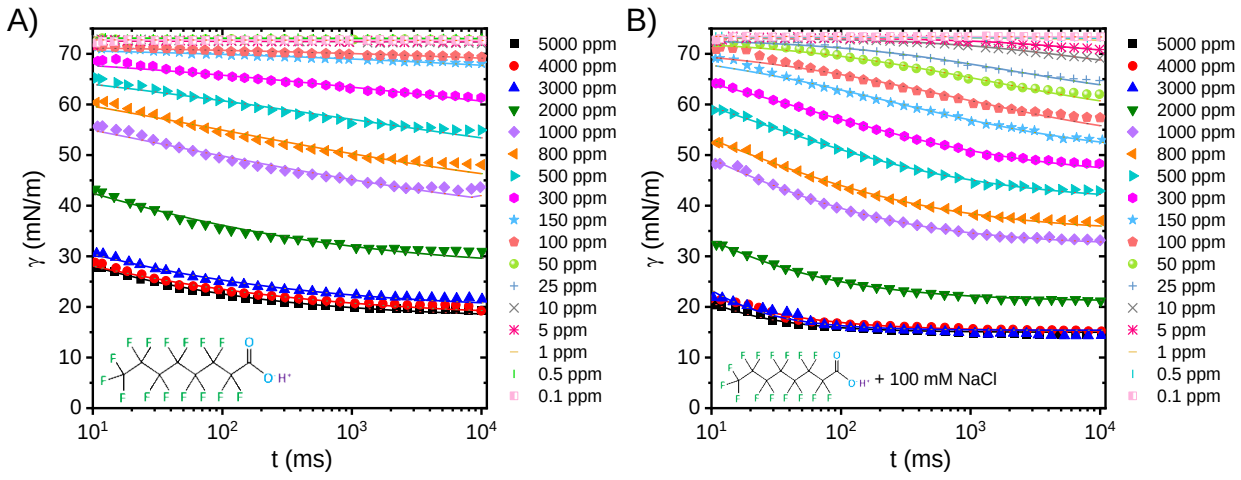

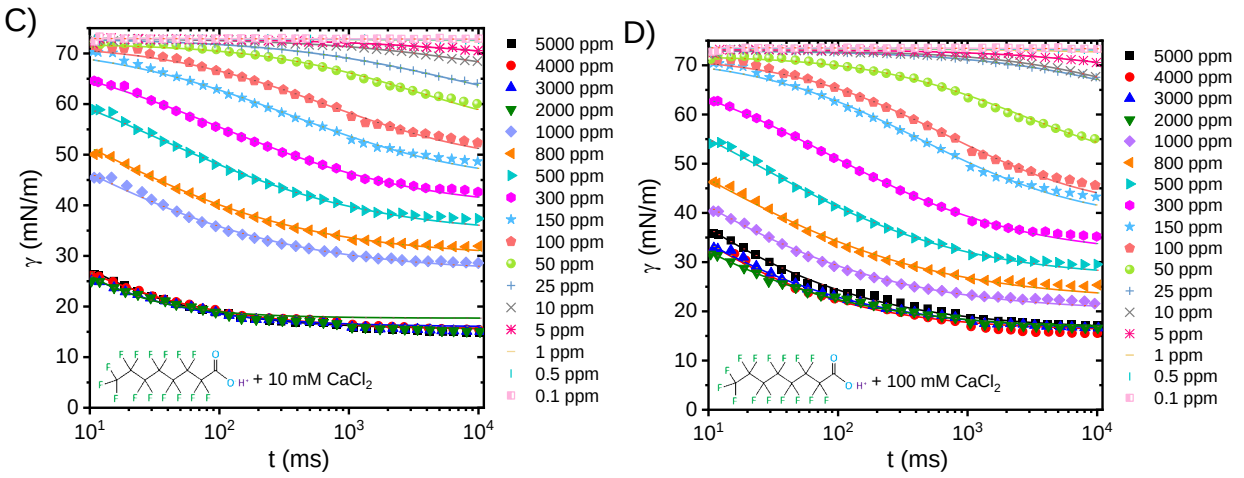

Figure 4.7 Dynamic surface tension of various concentrations of PFOA A) in the absence of electrolytes, B) in the presence of 100 mM NaCl as the background ions, C) in the presence of 10 mM $CaCl_2$ as the background ions, and D) in the presence of 100 mM $CaCl_2$ as the background ions by using the bubble pressure tensiometer.

The parameter t^* (characteristic time), obtained by the fitting with *Equation (4.3)*, can be used to approximately estimate the half-life of the fast fall stage (the time required to reduce half of the total γ decrease). **Figure 4.8** compares the t^* of KPFOS and PFOA, demonstrating that at lower concentrations, the characteristic time of KPFOS is less than that of PFOA. It indicates that the surface activity of KPFOS is higher than that of PFOA at the low concentration regime. Nevertheless, the t^* of KPFOS and of PFOA tend to become close with increasing their bulk concentrations. The t^* is independent of PFOA bulk concentration when the CMC is reached, indicating that the presence of PFAS micelles has no remarkable impact on the PFAS adsorption dynamics.[143] Moreover, at the lower bulk concentrations, the t^*s of PFOA are more independent of its bulk concentrations compared to those of KPFOS. Qazi et al.[143] calculated the characteristic time of CTAB according to Ward and Tordai model, revealing that the concentration-dependency of characteristic time of hydrocarbon surfactants. Additionally, two stages of characteristic time were observed, with the characteristic time rapidly decreasing with increasing the CTAB concentration followed by remaining the same once reaching the CMC. It is in agreement with the

change of t^* for PFOA in our work. However, the low concentration (i.e., below 10^{-4} M) of CTAB was not considered in Qazi et al.'s[143] work.

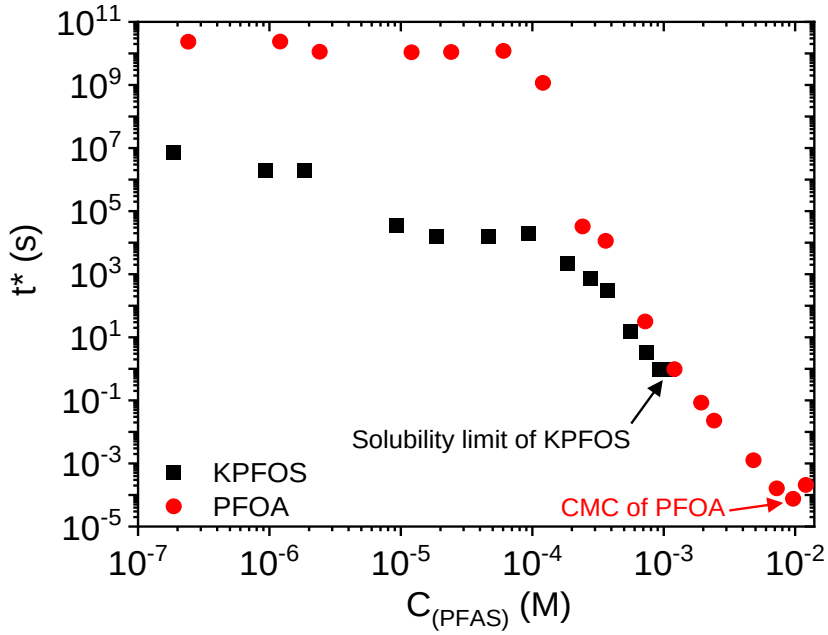

Figure 4.8 Comparison of characteristic time of KPFOS and PFOA at various bulk concentrations.

The same approach is used to deduce the characteristic time for PFAS in the presence of electrolytes and correlate the characteristic time with the PFAS concentration. **Figure 4.9** presents the effects of adding electrolytes on the half-life of the surface tension fast fall stage. **Figure 4.9A** reveals that adding NaCl significantly reduces the characteristic time of KPFOS and makes it less dependent on the KPFOS bulk concentration. In addition, $CaCl_2$ makes the characteristic time of KPFOS more dependent on its bulk concentration, in other words, in the presence of 10 mM and 100 mM $CaCl_2$, the t^* of KPFOS becomes greater at lower concentration regimes and becomes lower at higher concentration regimes. **Figure 4.9B** shows the trend of changes in characteristic time for PFOA systems, that is, in the presence of electrolytes regardless of valence and concentration, the t^* decreases until reaching the CMC. The change of slope suggests the change

of adsorption mechanism, as shown in **Figure 4.9A**.[143] The slope of -2 implies the diffusion-controlled mechanism according to the Ward and Tordai model, while the slope change suggests the appearance of adsorption barrier.[143] Although the CMC of KPFOS is observed when either NaCl or $CaCl_2$ present, the CMC appears to have negligible effect on the slope of characteristic time with respect to the KPFOS concentration. It suggests that the KPFOS micelle diffusion also plays an important role in determining the KPFOS adsorption dynamics.[143] In contrast, the appearance of PFOA CMC affects the slope, as depicted in **Figure 4.9B**, implying that the PFOA micelle diffusion has no remarkable effect on the PFOA adsorption dynamics. Additionally, the concentration of salts and type of salts do not significantly influence the slope of characteristic time as a function of PFOA concentration.

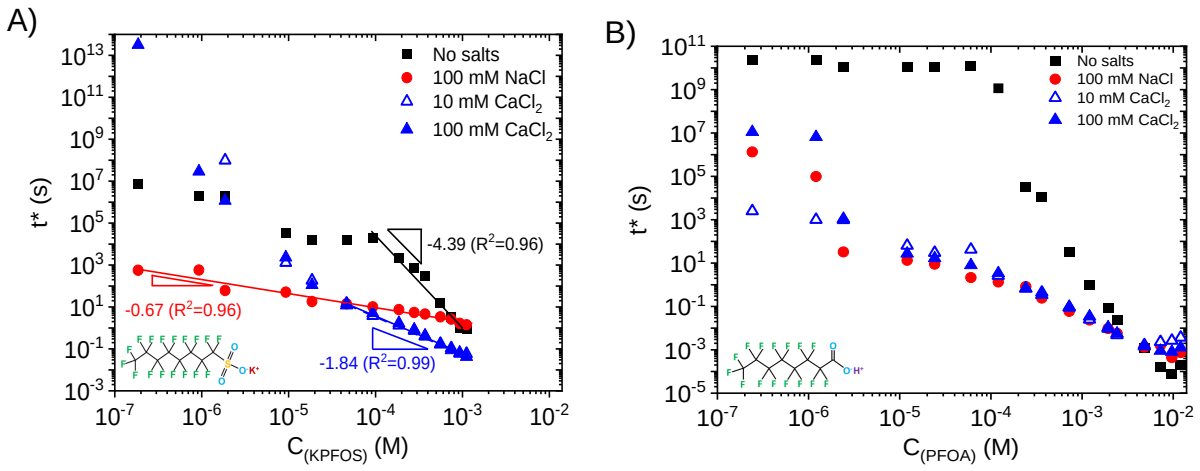

Figure 4.9 A) Effect of adding electrolytes (NaCl and $CaCl_2$) on the characteristic time of KPFOS aqueous solutions. B) Effect of adding electrolytes (NaCl and $CaCl_2$) on the characteristic time of PFOA aqueous solutions.

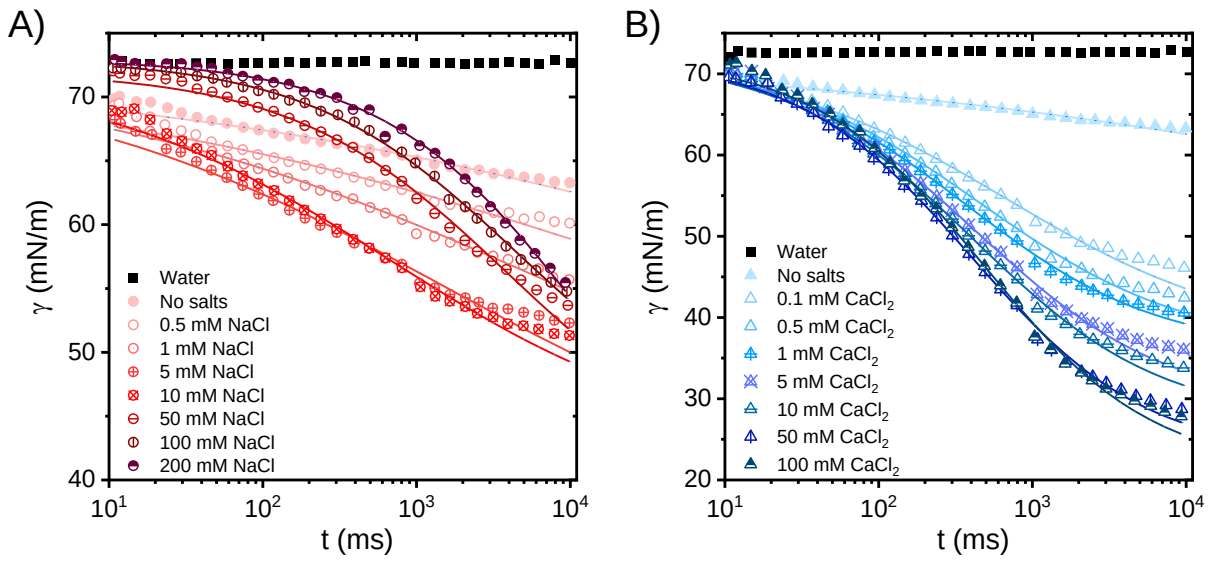

Figure 4.10 Dynamic surface tension of 0.4 mM KPFOS aqueous solutions A) with various concentrations of NaCl, and B) with various concentrations of $CaCl_2$.

Considering the effect of electrolyte concentrations on the dynamic surface tension of PFAS at a short timescale, **Figure 4.10A** shows the dynamic surface tension of 0.4 mM KPFOS in the presence of various concentrations of NaCl, and **Figure 4.10B** shows the influence of various concentrations of $CaCl_2$ on the dynamic surface tension of 0.4 mM KPFOS. Again, the solid lines presented in **Figure 4.10** are the model based on the *Equation (4.3)*, and the fitted parameters are listed in **Tables B12** to **B13**. It implies that there is a certain concentration of NaCl reducing the KPFOS dynamic surface tension at a short timescale the most, and this concentration is around 5-10 mM. Above 5-10 mM, the induction stage becomes longer again, in turn, the effect of reducing the dynamic surface tension of KPFOS at the short-time range is weaken, even though the equilibrium surface tensions of KPFOS are independent of NaCl concentrations (see **Figure 4.3**). According to Zhang et al.,[148] the slower decrease of surface tension of KPFOS in the presence of high concentration of NaCl is very likely due to the presence of NaCl at the air-water interface or subsurface, blocking the position for KPFOS. Eventually, the NaCl ions are pushed out by KPFOS molecules, giving rise to the independence of KPFOS equilibrium surface tension on the

NaCl concentration. Furthermore, the dynamic surface tension of KPFOS at the short-time range is also dependent on $CaCl_2$ concentrations. **Figure 4.10B** reveals that the fast fall stage is shorten and the $\gamma_0 - \gamma_m$ increases with increasing the $CaCl_2$ concentrations, it is in agreement with **Figure 4.3**.

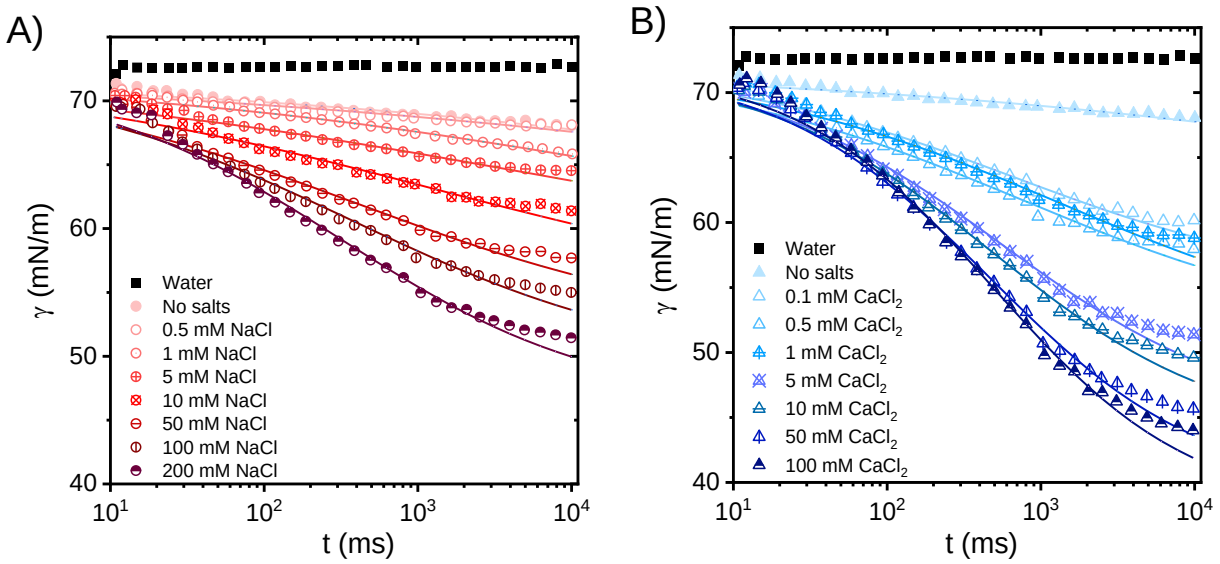

Figure 4.11 Dynamic surface tension of 0.4 mM PFOA aqueous solutions A) with various concentrations of NaCl, and B) with various concentrations of $CaCl_2$.

The effect of electrolyte concentrations on the dynamic surface tension of 0.4 mM PFOA can be found in **Figure 4.11**. The fitted parameters of the solid lines in **Figure 4.11**are presented in **Tables B14** to **B15**. Differing from KPFOS, the dynamic surface tension of PFOA decreases with increasing the NaCl concentrations. When the concentration of NaCl is 200 mM, the lowest surface tension is obtained, and the meso-equilibrium stage appears. The same trend is observed for the effect of various concentrations of $CaCl_2$, and **Figure 4.11B** indicates that the meso-equilibrium stage appears when the $CaCl_2$ concentration is above 10 mM. **Figure 4.12** considers the effect of various concentrations of $CaCl_2$ on the dynamic surface tension of 0.4 mM KPFBS, and the fitted parameters of *Equation (4.3)* are shown in **Table B16**. When a small amount of

$CaCl_2$ (0.1 mM to 1 mM) is presented in KPFBS aqueous solutions, the dynamic surface tension is slightly reduced, the induction stage is hard to be observed, and no meso-equilibrium stage is found. With increasing the $CaCl_2$ concentrations, the $\gamma_0 - \gamma_m$ increases, the induction stage is shortened, and the meso-equilibrium stage is still absent.

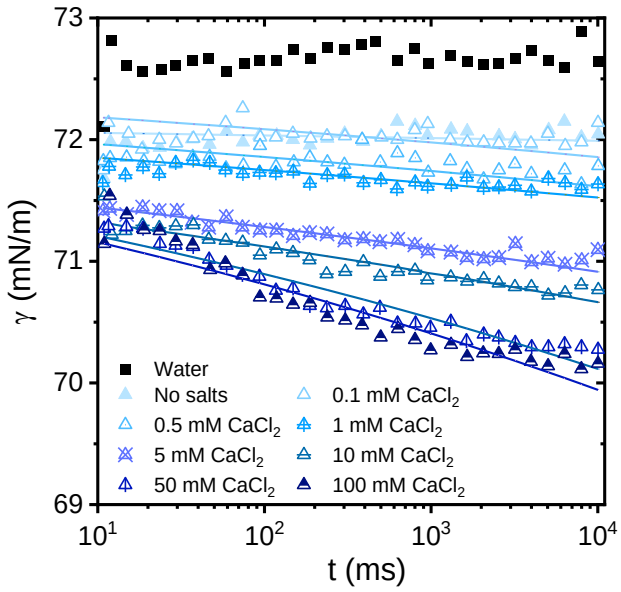

Figure 4.12 Dynamic surface tension of 0.4 mM KPFBS aqueous solutions with various concentrations of $CaCl_2$.

Figure 4.13 clearly presents the influence of electrolyte concentration on the characteristic time of 0.4 mM KPFOS, PFOA aqueous solutions, respectively. The $CaCl_2$ concentrations have no significant impact on the t^* of surface tension drop for both KPFOS and PFOA. Nevertheless, the NaCl concentrations has a meaningful effect on the t^*. A t^* minimal for KPFOS is observed when using 10 mM NaCl, indicating this concentration is the most effective one to reduce KPFOS dynamic surface tension in a short time scale (most effective for mass transport of molecules to the interface). While the dynamic surface tension of 0.4 mM PFOA keeps decreasing with an increase in NaCl concentration. Additionally, at higher electrolyte concentrations, monovalent salts faster decrease the dynamic surface tension of PFOA compared to divalent salts. Although

no significant influence of increasing $CaCl_2$ concentrations on the t^* is found for long-chain (C8) PFAS, the t^* of short-chain (C4) PFAS is decreasing by increasing the concentrations of $CaCl_2$ as seen in **Figure 4.14**.

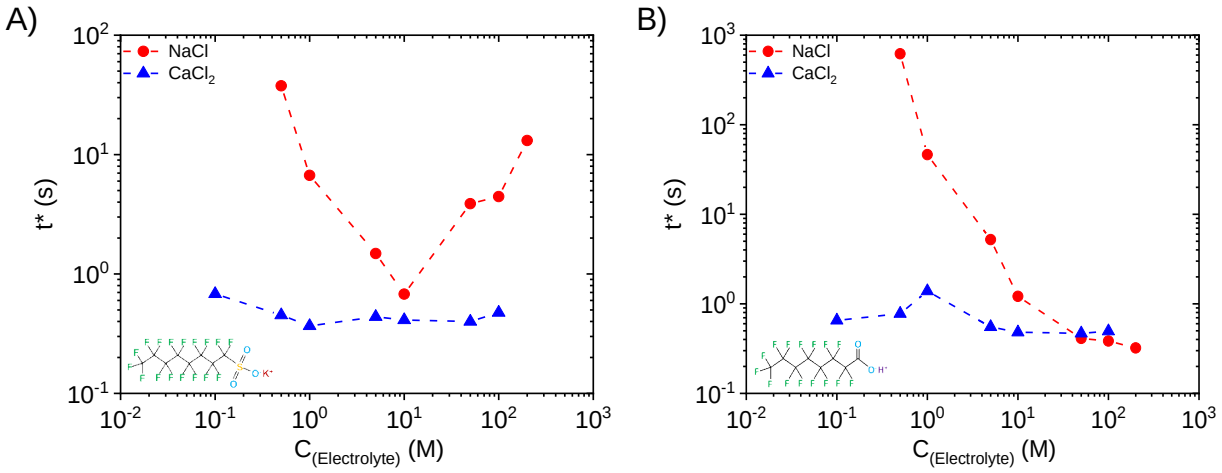

Figure 4.13 A) Effect of electrolyte (NaCl and $CaCl_2$) concentration on the characteristic time of 0.4 mM KPFOS aqueous solutions. B) Effect of electrolyte (NaCl and $CaCl_2$) concentration on the characteristic time of 0.4 mM PFOA aqueous solutions.

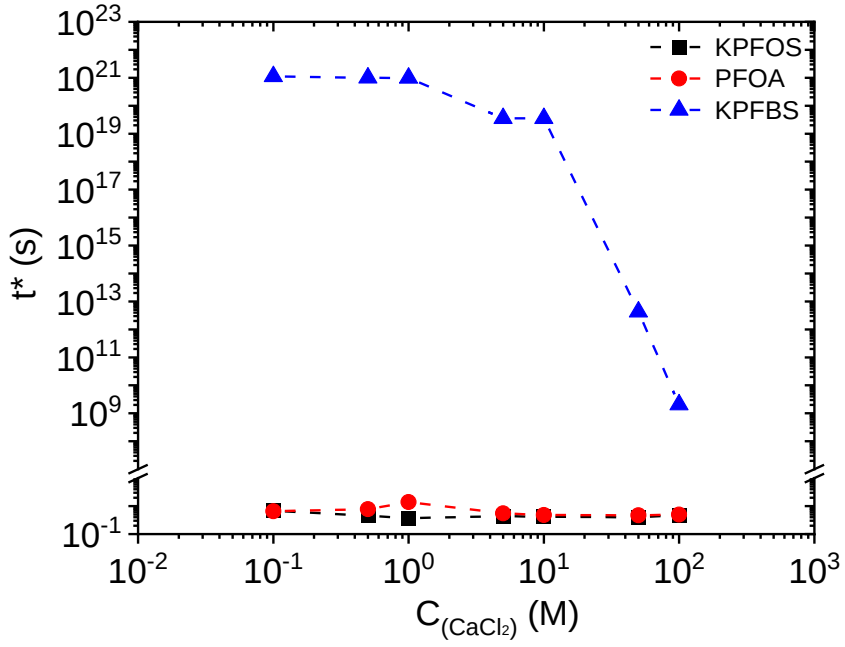

Figure 4.14 Comparison of influence of various concentrations of $CaCl_2$ on the characteristic time of 0.4 mM PFAS aqueous solutions.

4.5. Diffusion of PFAS

The adsorption mechanism of soluble surfactant molecules is illustrated in **Figure 4.15**, which introduces the concept of subsurface, a few molecular diameters below the interface. The adsorption-diffusion model involves two stages: first the molecules arrive at the subsurface from the bulk driven by the concentration gradient or hydrodynamic forces, followed by the directly adsorption at the interface.[31,93,117,151] *Equation (3.1)* and *Equation (4.4)*, the classic Ward-Tordai model, are usually used to approximately estimate the diffusion coefficient under the conditions where the diffusion rate of molecules from the bulk to subsurface governs the adsorption process or adsorption rate.[117] Effective diffusion coefficient (D_{eff}) is obtained by using *Equation (3.1)*, whereas Fickian diffusion coefficient (D) is presented in *Equation (4.4)*. It is assumed that the energy barrier is not presented when the molecules are transported from the subsurface to the interface.

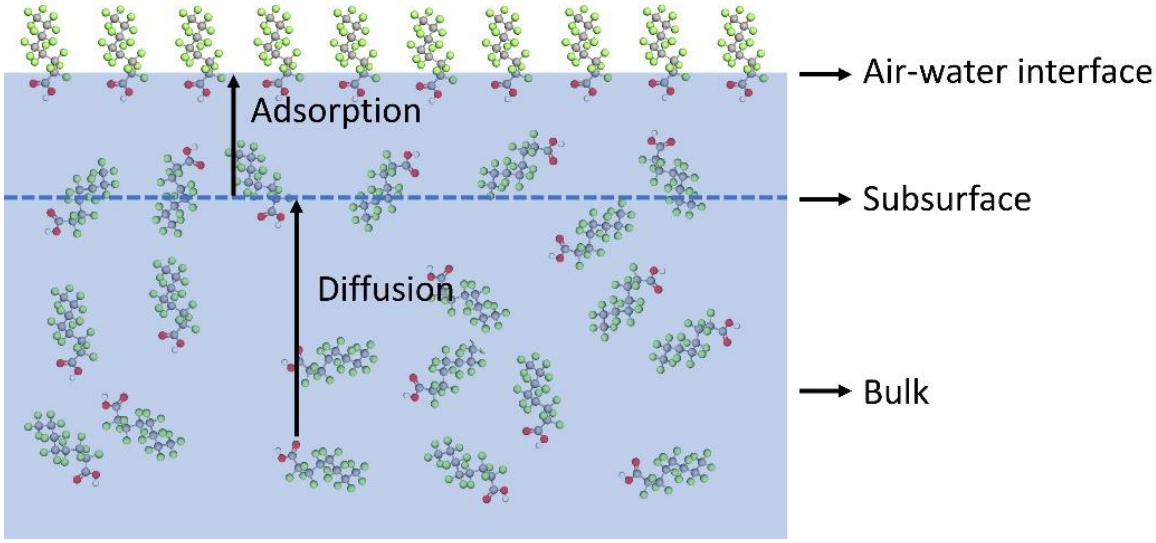

Figure 4.15 Adsorption-diffusion mechanism of PFAS molecules to the air-water interface.

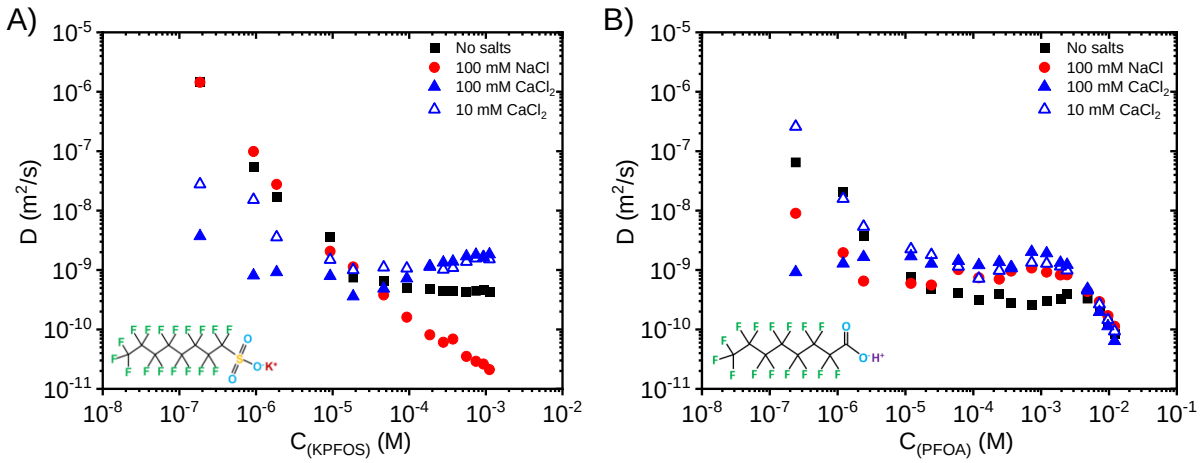

Figure 4.16 The estimated Fickian diffusion coefficient (*D*) of A) KPFOS and B) PFOA as a function of their bulk concentration with and without the addition of electrolytes (NaCl and $CaCl_2$).

The estimated *D* of KPFOS and PFOA with and without adding electrolytes calculated by using *Equation (4.4)* are presented in **Figure 4.16**. Typically, the change of *D* vs PFAS bulk concentrations has three stages. The first stage occurs within the lower concentration regime. In this stage, the *D* decreases when the PFAS bulk concentration increases, Mohammadi et al.[152] reported the reduction of *D* of asphaltenes with an increase in their bulk concentration, Stasiak et al.[153] reported the same trend of *D* for commercial surfactant Nafol 810D, and Yoshimura et al.[117] also used the Ward-Tordai model to study the diffusion of partially fluorinated surfactants, and their results also show that the diffusion rate is reduced by increasing the concentration. This trend suggests that when the system is dilute, PFAS molecules can more easily find open positions at the subsurface[154] or a slower migration of surfactant molecules occurs from the bulk to interface due to the increase of intermolecular interactions.[152] However, as approaching the second stage, the diffusion rate becomes slower as the surface coverage increases due to the difficulty of finding the available positions at the subsurface. At the second stage, the *D* is independent of the PFAS bulk concentrations. In addition, the diffusion of PFAS back from the subsurface to the bulk also occurs when the concentration is higher due to the Marangoni Effect. The third stage takes place

when reaching the CMC. In our study, the third stage is only found for PFOA as seen in **Figure 4.16B**.

For KPFOS systems, the influences of monovalent and divalent salts are quite different. In the presence of 100 mM NaCl, the D keeps decreasing in the studied KPFOS concentration range. However, upon adding 100 mM $CaCl_2$, the D becomes less dependent on the KPFOS concentration, and two stages are still observed. Differ from sole KPFOS systems (**Figure 4.16A**), the D decreases at the lower KPFOS concentrations, but it is slightly increasing in the second stage rather than the plateau. In addition, it seems the higher $CaCl_2$ concentration, the less dependency of D on KPFOS bulk concentrations. For PFOA systems, the addition of electrolytes makes the D less dependent on PFOA bulk concentrations (the shapes are flatter). Nonetheless, a further reduction of D is observed when reaching the CMC (**Figure 4.16B**), determining the third stage. According to Yoshimura et al.,[117] the further decrease in D is because the adsorption rate of PFOA at the air-water interface decreases due to the formation of micelles in the solutions.

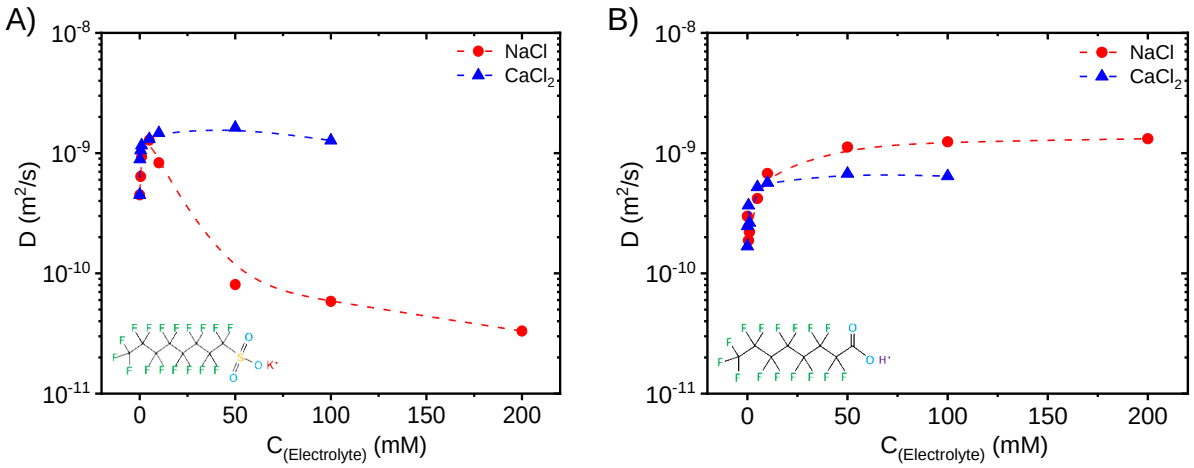

Figure 4.17 A) Effect of electrolyte (NaCl and $CaCl_2$) concentrations on the Fickian diffusion coefficient (D) of 0.4 mM KPFOS aqueous solutions. B) Effect of electrolyte (NaCl and $CaCl_2$) concentrations on the Fickian diffusion coefficient (D) of 0.4 mM PFOA aqueous solutions.

The effect of electrolyte concentrations can be seen in **Figure 4.17**. When increasing the electrolyte concentrations up to around 5-10 mM, the *D* of both KPFOS and PFOA is increasing. The highest diffusion rate of KPFOS is obtained when 5 mM NaCl is presented (**Figure 4.17A**), above 5 mM, the *D* decreases. In the case of adding $CaCl_2$, the *D* of KPFOS reaches a plateau when the $CaCl_2$ concentration is higher than 10 mM. Furthermore, the *D* of PFOA becomes independent of electrolyte concentrations when the electrolyte concentration is above 10 mM (**Figure 4.17B**). **Figure 4.18** compares the *D* of 0.4 mM KPFOS, PFOA, and KPFBS in the presence of $CaCl_2$ with various concentrations. It reveals that the *D* of KPFBS also depends on the $CaCl_2$ concentrations, and when the $CaCl_2$ concentration is greater than 10 mM, the *D* of KPFBS reaches to a plateau. Additionally, higher diffusion coefficient of long-chain (C8) PFAS gives rise to a reorientation of molecules at the interface/surface, hence, more adsorption sites will be provided for new incoming molecules to the interface.[154]

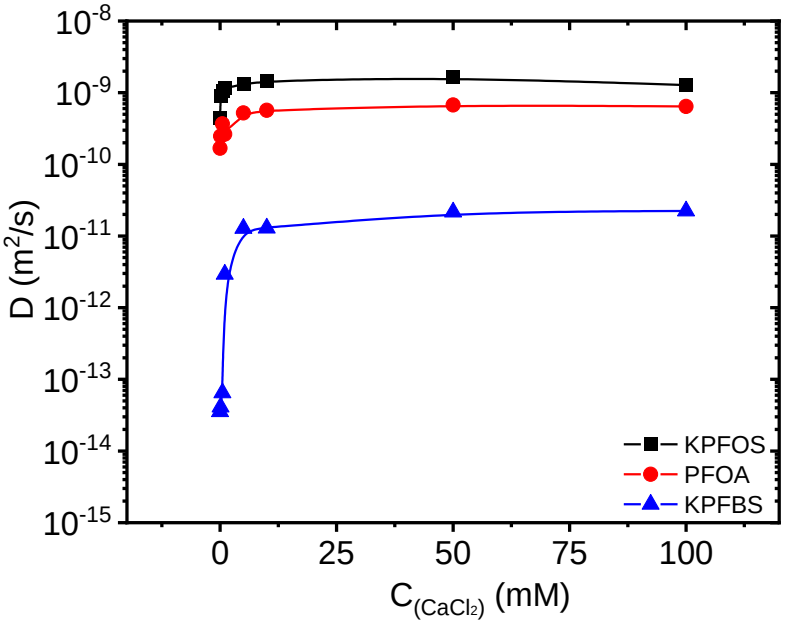

Figure 4.18 Comparison of Fickian diffusion coefficient (*D*) of 0.4 mM PFAS aqueous solutions in the presence of various concentrations of $CaCl_2$.

4.6. Interfacial dilatational rheology

Figure 4.19 shows the typical normalized oscillation curves of surface tension and surface area for sole 0.4 mM PFOA aqueous solutions, and for 0.4 mM PFAS aqueous solutions (KPFOS, PFOA and KPFBS, respectively) with 100 mM $CaCl_2$ as the background ions at 0.5 Hz. For 0.4 mM PFOA, the surface area oscillates with a phase lag with respect to the surface tension, indicating a viscoelastic interface.[130] For the long-chain (C8) PFAS, the addition of $CaCl_2$ qualitatively increases the interfacial viscoelasticity, for instance, 1) the $tan\,\delta$ of 0.4 mM PFOA increases from 0.30 ± 0.16 to 0.61 ± 0.12 after adding 100 mM $CaCl_2$, and 2) the shape of KPFOS pendant drop becomes more elongated after adding 100 mM $CaCl_2$ (**Figure 3.8A** and **Figure 4.19B**). In addition, the addition of 100 mM $CaCl_2$ enhances the adsorption capacity of KPFBS due to its air-water interface becoming elastic (**Figure 4.19D**). It suggests that there are more KPFBS molecules being adsorbed at the air-water interface, giving rise to surface tension oscillations.

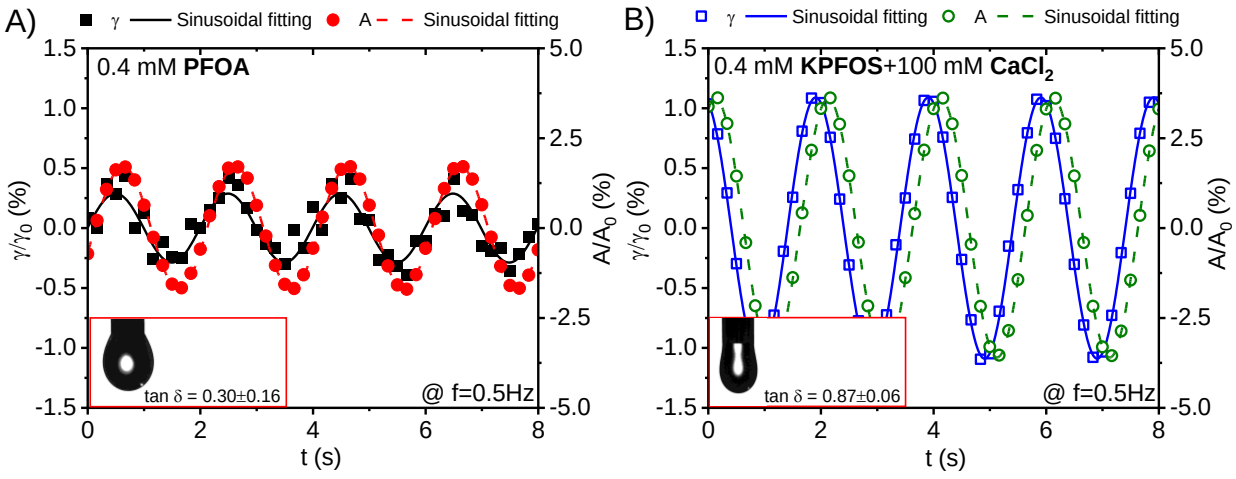

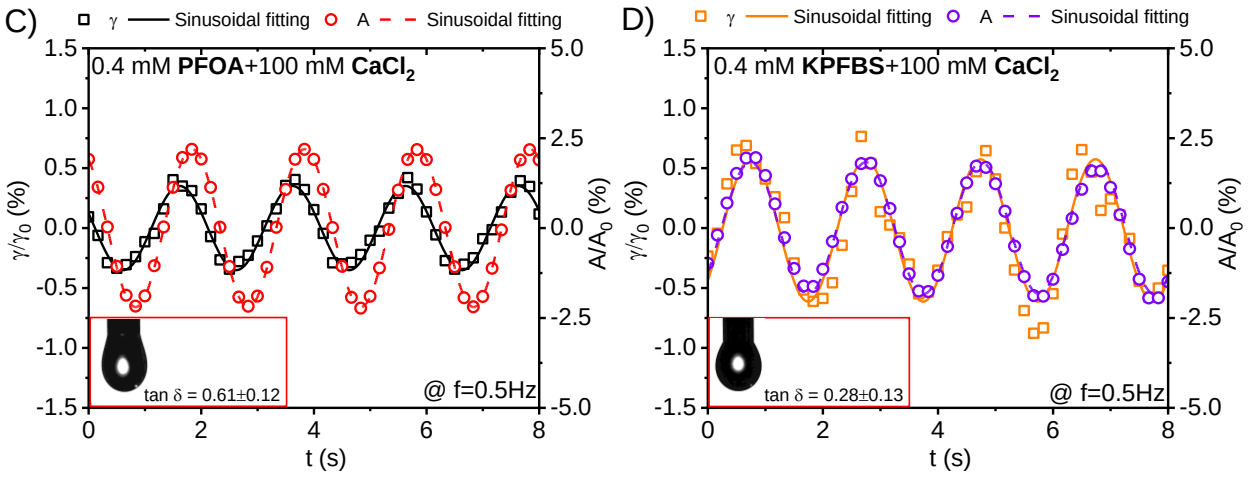

Figure 4.19 Normalized surface tension and surface area oscillations of 0.4 mM A) PFOA-adsorbed air-water interface, B) KPFBS-adsorbed air-water interface in the presence of 100 mM $CaCl_2$, C) PFOA-adsorbed air-water interface in the presence of 100 mM $CaCl_2$, and D) KPFBS-adsorbed air-water interface in the presence of 100 mM $CaCl_2$ obtained by performing the dilatational interfacial rheology at 0.5 Hz. Inset: the pendant drop shape along with the value of $tan\,\delta$ showing different degrees of dilatational interfacial viscoelasticity.

4.6.1. Interfacial dilatational rheology of PFOA

The interfacial dilatational rheology of PFAS with sulfonic acid headgroups is discussed in Chapter 3. In this Subchapter, the interfacial dilatational rheology of PFAS with carboxylic acid headgroups is demonstrated. The dilatational interfacial modulus is defined in Chapter 2 according to *Equation (2.8)*:[75,97,98] The E' and E'' can be calculated according to *Equation (2.9)*.[75,97,99,100]

The same as KPFOS (see Chapter 3), maximums of E' and E'' are also observed for PFOA when its bulk concentration is around 0.24 mM at both 0.5 Hz and 0.1 Hz, as seen in **Figure 4.20**. The decrease in E' at the higher concentration regime suggests that the PFOA molecules are subject to be compressible within the studied concentration range.[133] As seen in **Figure 4.20**, two distinct stages are associated with the change of E' and E'' of PFOA within the studied concentration range due to the maximum in E' and E'' of PFOA. At the first stage, the dilatational interfacial moduli increase with an increase in PFOA bulk concentration since the dominated mechanism in this regime is the Gibbs adsorption (molecular adsorption).[102] Even though the

desorption of PFOA molecules occurs due to the increasing surface pressure, the adsorbed PFOA molecules at the maximum of dilatational modulus are in a more compact state compared to those with a lower dilatational modulus.[133] Moreover, at the maximum of dilatational modulus, the rate of molecular adsorption and molecular exchange is equal. At the second stage, the dominant factor is the molecular exchange between the bulk/subsurface and the air-water interface.[102] In addition, the Marangoni Effect becomes more significant at this stage because the molecular adsorption cannot compensate the molecular exchange anymore due to a faster mass transfer. Moreover, the PFOA interface is gel-like at the CMC due to $E' \approx E''$ (i.e., $tan\,\delta = 1.01 \pm 0.48$ at 0.5 Hz).

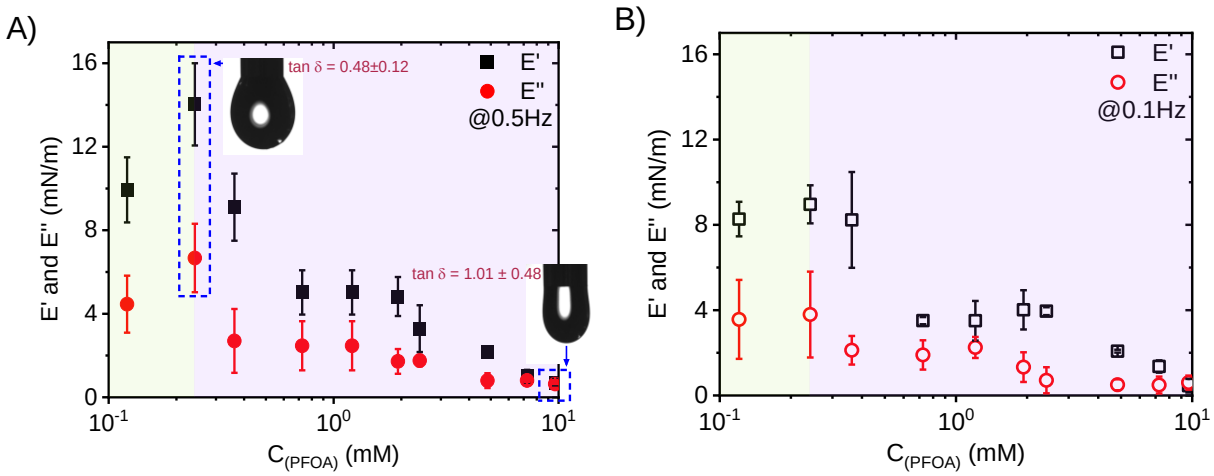

Figure 4.20 E' and E'' of PFOA-adsorbed air-water interface as a function of PFOA bulk concentration at a fixed frequency of A) 0.5 Hz and B) 0.1 Hz. The pendant drops of 0.24 mM and 9.7 mM of PFOA aqueous solutions are shown in the A) along with the $tan\,\delta$ value.

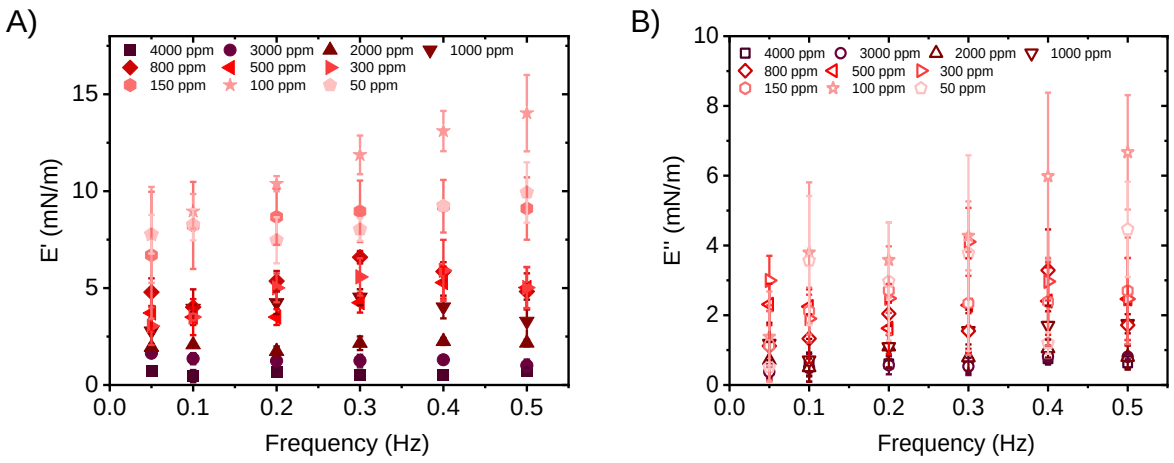

Figure 4.21 A) E' and B) E'' of PFOA-adsorbed air-water interfaces vs frequency at various PFOA bulk concentrations.

The frequency-dependency of dilatational interfacial modulus of PFOA at different PFOA bulk concentrations is shown in **Figure 4.21**. As can be seen, the frequency-dependency of E changes with PFOA bulk concentrations. At higher concentrations (>4.8 mM), oscillation frequency has no effect on both E' and E''. However, when the concentration is around 0.24 mM, the E' and E'' show the highly dependency on the frequency. Interestingly, when the PFOA concentrations are below 0.24 mM, the E' and E'' become less dependent on the frequency. In addition, the maximums of E' and E'' appear at 0.24 mM as mentioned above. The dependency of E on the frequency is also reported in the literature.[100,130,133,155] For example, Kotsmar et al.[100] found the maximum of E'' of 0.001 mM β-casein protein at 0.01 Hz, which is called characteristic frequency (ω_D).[102,103] **Figure 4.22** compares the E' and E'' of 0.4 mM KPFOS and PFOA at different frequencies, and our results suggest that at the same concentration, the PFAS with the sulfonic acid group tend to have the higher dilatational interfacial modulus.

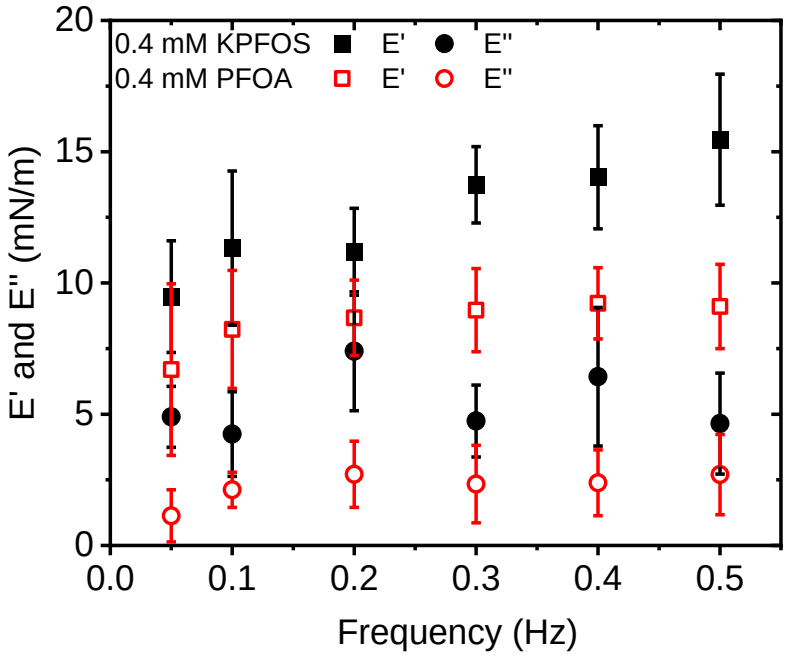

Figure 4.22 Comparison of E' and E'' of 0.4 mM KPFOS and PFOA as a function of frequency.

4.6.2. Effect of electrolytes on the interfacial dilatational rheology of PFAS

When adding the electrolytes, **Figure 4.23** shows the concentration effect of NaCl on the E' and E'' of 0.4 mM KPFOS-adsorbed air-water interface. Out of our expectation, both E' and E'' first decrease and then increase with increasing the NaCl concentration. The smallest E' and E'' are obtained when the NaCl concentration is around 5-10 mM (purple and orange points in **Figure 4.23**), where the largest D and the smallest t^* of KPFOS are obtained as mentioned in the previous Chapter. Furthermore, in the relatively high salinity environment, 200 mM NaCl in our study, the KPFOS shows highest E' and E'', and both of them highly depends on the frequency.

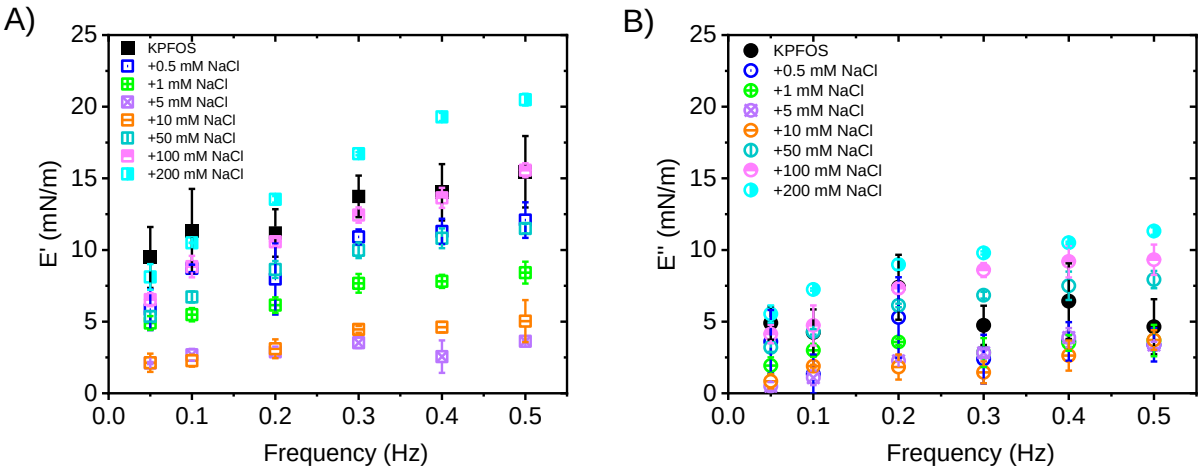

Figure 4.23 A) E' and B) E'' of 0.4 mM KPFOS-adsorbed air-water interface with and without an addition of various concentrations of NaCl.

On the other hand, the divalent salt $CaCl_2$ has a quite different effect on the E' and E'' of 0.4 mM KPFOS, as seen in **Figure 4.24**. Upon an addition of $CaCl_2$, the E' of KPFOS is qualitatively reduced, and it seems that the $CaCl_2$ concentrations barely influence the KPFOS interfacial elasticity. However, the insets in **Figure 4.24A** show that apparently, the E' is also dependent on the $CaCl_2$ concentration, with the E' decreasing first then increasing with increasing the $CaCl_2$ concentration. Compared to NaCl, the variation of KPFOS interfacial elasticity with an increase in $CaCl_2$ concentration occurs within a smaller magnitude. Moreover, the E'' of KPFOS slightly decreases after introducing $CaCl_2$. The insets of **Figure 4.24B** imply that the change of KPFOS E'' does not follow the trend of decreasing and increasing. Both E' and E'' of KPFOS increase with increasing the frequency. The $\tan\delta$ values at different $CaCl_2$ concentrations are compared, and no significant difference is observed, implying the effect of $CaCl_2$ concentrations on KPFOS E' and E'' is smaller than that of NaCl concentrations.

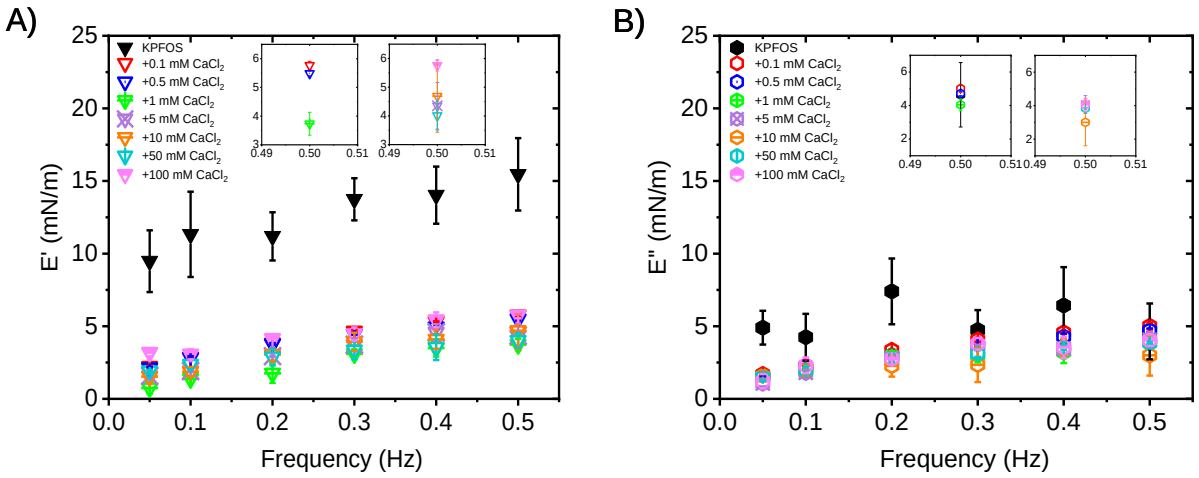

Figure 4.24 A) E′ and B) E′′ of 0.4 mM KPFOS-adsorbed air-water interface with and without an addition of various concentrations of $CaCl_2$.

The effect of NaCl and $CaCl_2$ concentrations on the E' and E'' of 0.4 mM PFOA-adsorbed air-water interface is also examined, as seen in **Figure 4.25** and **Figure 4.26**. In terms of NaCl, the E' and E'' of PFOA decrease with increasing the NaCl concentration. The smallest moduli are obtained when the NaCl concentration is 200 mM. Compared to the same amount of KPFOS (0.4 mM), the moduli of PFOA in the presence of NaCl are less dependent on the frequency. Furthermore, the addition of $CaCl_2$ also reduces the E' of PFOA as seen in **Figure 4.26A**. The dependency of E' reduction for PFOA on $CaCl_2$ concentration is not significant, which is similar to the case of KPFOS. Additionally, no significant impact on E'' of PFOA is observed after adding $CaCl_2$ with various concentrations.

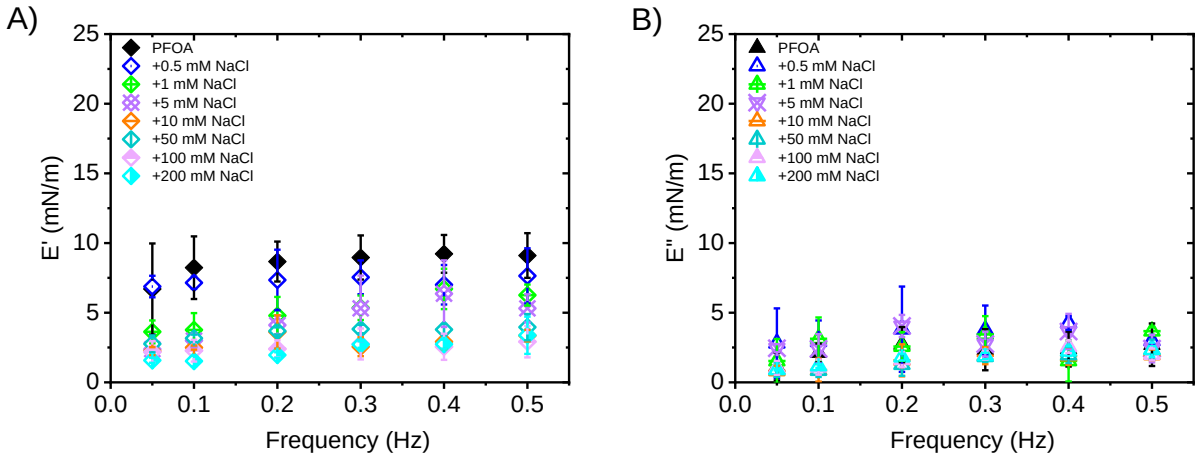

Figure 4.25 A) E' and B) E'' of 0.4 mM PFOA-adsorbed air-water interface with and without an addition of various concentrations of NaCl.

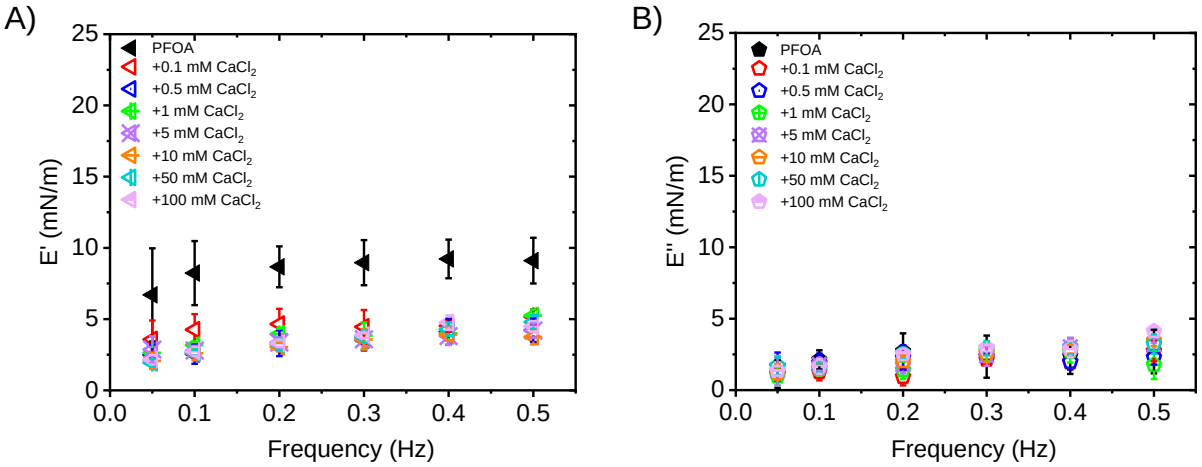

Figure 4.26 A) E' and B) E'' of 0.4 mM PFOA-adsorbed air-water interface with and without an addition of various concentrations of $CaCl_2$.

Taking into account the chain length, **Figure 4.27** compares the E' and E'' of 0.4 mM KPFOS and 0.4 mM KPFBS in the presence of 100 mM $CaCl_2$ since the surface tension oscillation of sole KPFBS-adsorbed interface cannot be obtained according to the previous Chapter. The addition of $CaCl_2$ makes KPFBS-adsorbed air-water interface have the moduli, suggesting that the adsorption capacity of short-chain PFAS is enhanced upon adding the divalent salts. Comparing KPFOS and KPFBS, $CaCl_2$ increases the viscoelasticity of KPFOS-adsorbed interface, while the

KPFBS-adsorbed interface has a higher surface elasticity when adding 100 mM $CaCl_2$. The waiting time of 30 mins were applied prior to the pendant drop volume oscillation (the pendant drop volume was kept a constant manually), and as seen in **Figure 4.27**, the E' of KPFBS is further enhanced. It suggests that more KPFBS molecules are being adsorbed at the air-water interface in the presence of $CaCl_2$ over the time.

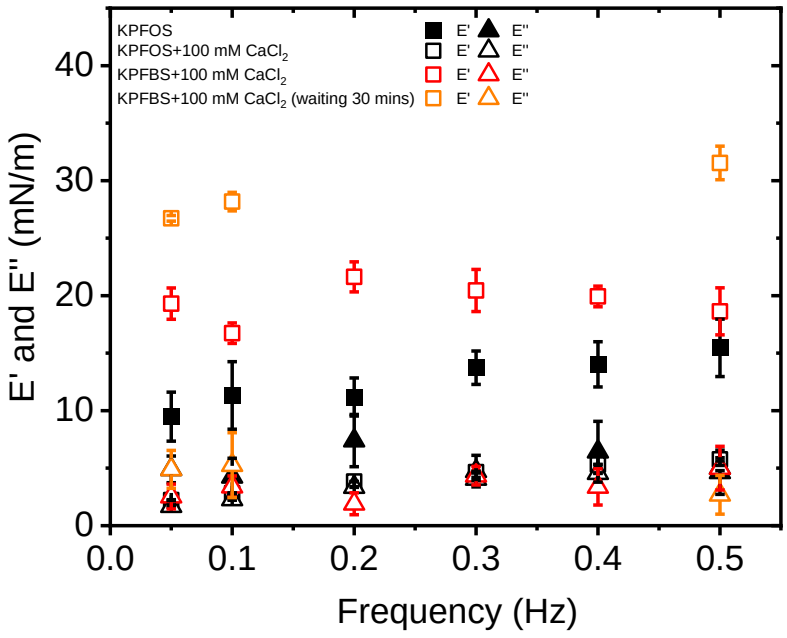

Figure 4.27 Comparison of E' and E'' of 0.4 mM KPFOS-adsorbed and 0.4 mM KPFBS-adsorbed air-water interfaces with and without an addition of 100 mM $CaCl_2$.

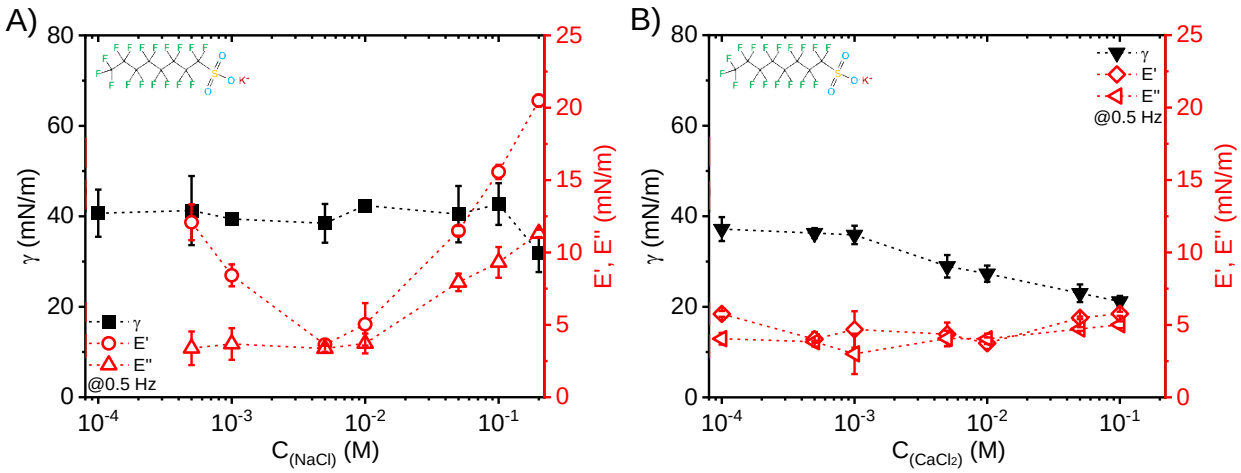

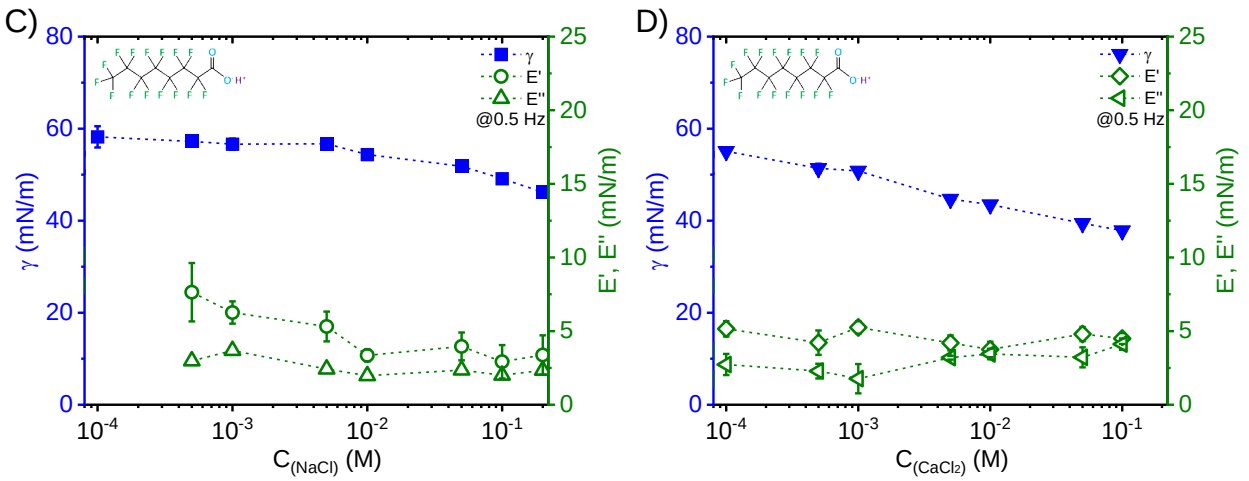

Figure 4.28 Surface tension and surface moduli change of 0.4 mM KPFOS-adsorbed air-water interface as a function of A) NaCl and B) $CaCl_2$. Surface tension and surface moduli change of 0.4 mM PFOA-adsorbed air-water interface as a function of C) NaCl and D) $CaCl_2$. The lines are just for guidance.

Figure 4.28 presents the change of surface tension and dilatational interfacial moduli at 0.5 Hz of 0.4 mM KPFOS and PFOA as a function of electrolyte concentrations. NaCl effect on KPFOS is special because a minimum of dilatational modulus is obtained when the NaCl concentration is 5 mM, at which the largest D and the smallest t^* of KPFOS appear. However, the addition of NaCl has no effect on KPFOS equilibrium surface tension. Upon adding $CaCl_2$, the moduli of KPFOS remain almost the same with increasing the $CaCl_2$ concentrations, but a slight increase is observed at higher concentrations of $CaCl_2$. Additionally, the equilibrium surface tension keeps decreasing when increasing the $CaCl_2$ concentrations. Furthermore, the equilibrium surface tension of 0.4 mM PFOA is decreasing when increasing the concentration of electrolytes including both NaCl and $CaCl_2$. The E' of PFOA decreases with increasing the NaCl concentrations, but the interfacial elasticity is being dominated all the time for PFOA in the presence of NaCl within the studied concentrations. Nevertheless, the PFOA interface tends to be dominated by the interfacial viscosity when increasing the $CaCl_2$ concentrations as seen in **Figure 4.28D**.

4.7. Conclusions

In this study, dynamic surface tensions of PFAS aqueous solutions in the absence and presence of electrolytes were examined by using different tensiometries including Wilhelmy plate tensiometer, pendant drop tensiometer and bubble pressure tensiometer. Three typical PFAS, which are KPFOS, PFOA and KPFBS, were selected in this study. PFOA showed a CMC (~9.7 mM) within the studied concentrations. At a specific concentration, 0.4 mM in our case, the equilibrium surface tension of PFAS follows the order of: KPFOS < PFOA < KPFBS. The equilibrium surface tensions at varied PFAS bulk concentrations were fitted with Gibbs, and Extended Langmuir isotherms, and our results suggest that the polar headgroups of PFAS, which have the same carbon number, have no significant effect on the maximum surface concentrations of PFAS. Nevertheless, the different tensiometries affect the estimation of maximum surface excess concentrations.

In the presence of electrolytes, the surface tension is reduced for all PFAS studied. The CMC shifts to the lower concentration regime upon an addition of salts, but it is not the case for short-chain PFAS (KPFBS). Electrolyte concentrations affect the CMC shift for long-chain (C8) PFAS, for example, a smaller CMC of KPFOS is obtained when adding 100 mM $CaCl_2$ compared to adding 10 mM $CaCl_2$. Furthermore, the addition of electrolytes enhances the adsorption of PFAS due to the increased maximum surface excess concentration according to the isotherm fitting. Moreover, our studies show that different tensiometry methods influence the equilibrium surface tension of PFAS, especially their surface excess concentrations.

The short-time adsorption behavior of PFAS was studied through estimating the diffusion coefficient based on the surface tension data acquired by using the bubble pressure tensiometer. According to the classic Ward-Tordai model, the diffusion coefficient of long-chain (C8) PFAS is

dependent on their bulk concentration, and three stages of diffusion coefficients were observed. At the first stage, the diffusion coefficient decreases with an increase in the bulk concentration. When entering the second stage, the diffusion coefficient is independent of the bulk concentration. Once the CMC is reached, the diffusion coefficient is instantly reduced. Keeping the bulk concentration same, the diffusion coefficient of PFAS follows the order of: KPFBS < PFOA < KPFOS. In terms of the electrolyte effect, the diffusion coefficient of all PFAS tested in this work increases in the presence of $CaCl_2$, and the increase rate becomes slower until approaching the plateau with increasing the $CaCl_2$ concentrations. However, a maximum diffusion coefficient of KPFOS was observed at a specific NaCl concentration (5 mM), above which the diffusion coefficient of KPFOS is decreasing.

Lastly, the interfacial dilatational rheology was studied. The same as KPFOS as mentioned in the previous Chapter, the dilatational surface elasticity (E') of PFOA is also greater than its dilatational loss modulus (E''), suggesting that a viscoelastic interface but the elasticity is being dominated. In addition, both E' and E'' of PFOA are not only dependent on their bulk concentrations but also dependent on the oscillation frequency. Nevertheless, the dependency of frequency disappears when approaching the CMC of PFOA. A maximum of dilatational modulus vs. concentration was also observed for PFOA, further implying the competition of molecular adsorption and molecular exchange for long-chain (C8) PFAS adsorption at the air-water interface. When adding electrolytes, the interfacial dilatational rheology becomes more complicated. Upon adding NaCl, the E' and E'' of KPFOS first decrease followed by an increase, while the dependency of E' and E'' on NaCl concentrations for PFOA is not significant. The E' of both KPFOS and PFOA is dramatically reduced when introducing $CaCl_2$ regardless of the $CaCl_2$ concentration. The E'' of KPFOS is also significantly reduced after adding $CaCl_2$ compared to that

of PFOA. Furthermore, when introducing the $CaCl_2$, even the short-chain PFAS (i.e., KPFBS) to some extent show the interfacial dilatational rheology, suggesting the addition of $CaCl_2$ promotes the adsorption of short-chain PFAS at the air-water interface. But differ from long-chain (C8) PFAS (i.e., KPFOS), the interface containing short-chain (C4) PFAS is more elastic in the presence of $CaCl_2$.

Chapter 5. Intermolecular Interaction between Per- and Polyfluoroalkyl Substances (PFAS) and Salt Ions*

5.1. Introduction

As mentioned in the previous Chapters, the addition of salts allows the CMC of KPFOS, and shifts the CMC of PFOA, suggesting the formation of micelles. Some techniques are useful to study the properties of micelles, such as SANS, SAXS, Molecular Dynamics (MD) simulations, NMR spectroscopy, and etc.[123,145,156–162]

The process of surfactant micelle formation has been a subject of debate for a long time, primarily focused on two models: the mass-action and the pseudophase transition models.[160,161] The former views micellization as a multi-step event, accounting for the smooth change in the system's physical properties near the CMC. While the latter treats micelle formation as a single process. Cui et al.[161] believe in the former, which is the premicellar aggregation, and they performed ^{1}H NMR and NMR self-diffusion measurement to study the micellization of anionic surfactant SDS, cationic surfactant n-hexyldecyltrimethylammoniumbromide (CTAB), and nonionic surfactant Triton X-100. For CTAB and Triton X-100, the resonance peaks shift when the concentration is below CMC, indicating the surfactant molecules are aggregating into the oligomers. Double peaks of phenyl protons begin to merge before reaching CMC for Triton X-100, implying the environment of the monomer is varied. The result of self-diffusion coefficients of SDS shows the same trend.

The ^{19}F NMR spectroscopy can be used to monitor the exchange between fluorinated surfactant micelles and monomers. In addition, the diffusion NMR and T1, T2 relaxation

* This Chapter is in preparation for submission to peer-reviewed journals. **Zhou, M.**, Akhmedov, NG., Foudazi, R.

measurements are a powerful tool to study the interaction in host-guest systems, such as poly(amidoamine) dendrimers (PAMAM)-PFOA system. The ^{19}F NMR spectra for PFOA with different concentrations was the first time analyzed by Ning et al.,[145] and two signals were observed for the terminal -CF_3 group when the concentration is higher than 4000 ppm, and the second smaller peak (-83 ppm) was subject to the PFOA micelles. It was reported that the ^{19}F NMR chemical shift of the -CF_3 group is influenced by intermolecular interactions, which gives rise to shifting of the peak upfield. The ^{19}F NMR was also performed and analyzed for different ratios of PFOA and -NH_3^+, and the results reveal that the addition of -NH_3^+ promotes the formation of PFOA micelles, and the exchange between PFOA monomers and PFOA micelles is slow. In addition, the upfield shifts of terminal -CF_3 (F8) and F7 of PFOA suggest complexation formation, contributing an enhanced shielding, and micellization.

Besides NMR spectra, SAXS stands as an additional instrumental technique for examining the structure of surfactant micelles. The significance of the small-angle scattering method lies in its ability to investigate the dimensions significant to surfactant micelles, offering insights into their overall shape, size, and the micelle cross-sectional profile.[160] Jensen et al.[160] utilized synchrotron SAXS alongside stopped-flow mixing to study the entire micelle formation process from single surfactants to equilibrium micelles. Their findings revealed that surfactant micelles form via a gradual process of individual surfactant molecules being added or removed. Ochoa et al.[157] used SAXS to investigate the effect of increasing SDS concentrations on micellar dimensions and intermicellar interactions vis applying core-shell ellipsoid form factor and Hayter-Penfold structure factor models. The SAXS spectra for surfactant micellar solutions follows $I(q) \propto \phi P(q) S(q)$, where ϕ is the micelle volume fraction, $P(q)$ is the form factor, and $S(q)$ is the

structure factor, corresponding to the scattering contributions from individual micelles and the spatial correlations between them.

Numerous studies have focused on analyzing the structure and intermolecular interactions of hydrocarbon surfactants. However, investigations into the structure and intermolecular dynamics of fluorinated surfactants, particularly PFAS, remain scarce to our knowledge. This Chapter highlights ongoing investigations into PFAS molecules, utilizing techniques such as SAXS and NMR to examine the properties of PFAS micelles and the nature of their intermolecular and intermicellar interactions.

5.2. NMR spectroscopy of PFAS solutions

5.2.1. KPFOS aqueous solutions

Figure 5.1 shows the ^{19}F NMR spectra of 1.1 mM KPFOS D_2O solutions with and without adding 100 mM $CaCl_2$. All NMR spectra were already calibrated by using the reference peak of haxafluorobenzene (-164.9 ppm). Regarding KPFOS, as indicated by the black line in **Figure 5.1**, the prominent peak at -82.56 ppm (purple area) originates from the terminal -CF_3 group in the linear chain.[163–165] Although the reports on the ^{19}F NMR spectra of KPFOS is limited, the concordance between our ^{19}F NMR spectrum for KPFOS and those documented in the literature reveals that the KPFOS molecules in D_2O retain their monomeric form at a concentration of 1.1 mM, which falls below the CMC. The spectrum for the seven -CF_2 groups is distributed between -110 to -130 ppm, with three CF_2 signals converging in the middle of this spectrum, consistent with existing literature reports.[163,164] **Table C1** lists the chemical shift of the eight peaks assigned to KPFOS. According to Moody et al.,[163] the peak at -116.17 ppm is assigned to the -CF_2 near the sulfonic acid group, the pink area in **Figure 5.1**.

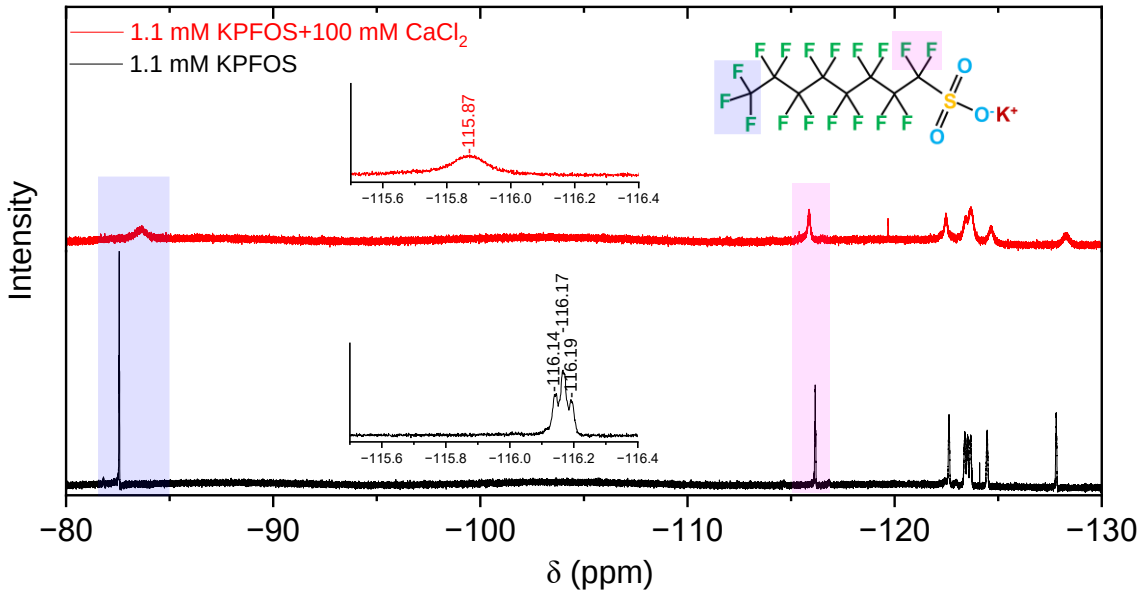

Figure 5.1 ^{19}F NMR spectra of 1.1 mM (600 ppm) KPFOS in D_2O in the absence and presence of 100 mM $CaCl_2$. The temperature was room temperature. The insets are the ^{19}F NMR spectra -CF_2-SO_3- regime (pink area).

The chemical shift stands as the most responsive and commonly utilized parameter in NMR spectroscopy for identifying intramolecular interactions, including the measurement of the CMC in surfactants.[145,158] For KPFOS with 100 mM $CaCl_2$, clear chemical shifts are observed (red line in **Figure 5.1**). First, the chemical shift of resonance peak for the terminal -CF_3 group moves to a higher field upon adding $CaCl_2$. Additionally, the split triplet resonance peaks merge together, changing from sharp and narrow to smooth and wide (the half-line width becomes wider). Shifting to a higher field for chemical shift implies that the chemical environment of the monomer molecules, herein KPFOS, is varied. In Cui et al.'s work,[166] they demonstrated that the upfield shifting of resonance peak for phenyl protons is because the phenyl ring current effect resulting from the association of Triton X 100 monomers as the phenyl rings come close together, and thus, attributing to the premicellization of Triton X 100 monomers. Therefore, the upfield shifting of resonance peak for the terminal -CF_3 group of KPFOS clearly indicates the micellization of KPFOS monomers. In addition, the merging and broadening of resonance peak also result from

aggregating of KPFOS monomers and exchange of monomers in between micelles and in bulk solution.[166] Additionally, when increasing the concentration of Ca^{2+}, as seen in **Figure 5.2** (blue line), the higher upfield shifting for terminal -CF_3 group suggests the stronger aggregation of KPFOS monomers. Compared to 100 mM Ca^{2+}, the resonance peak of terminal -CF_3 is not subject to shift in the presence of Na^+, but the triplet peaks merge. It might suggest that the KPFOS monomers are aggregating when introducing Na^+, but the electron distribution of C-F is not significantly affected.

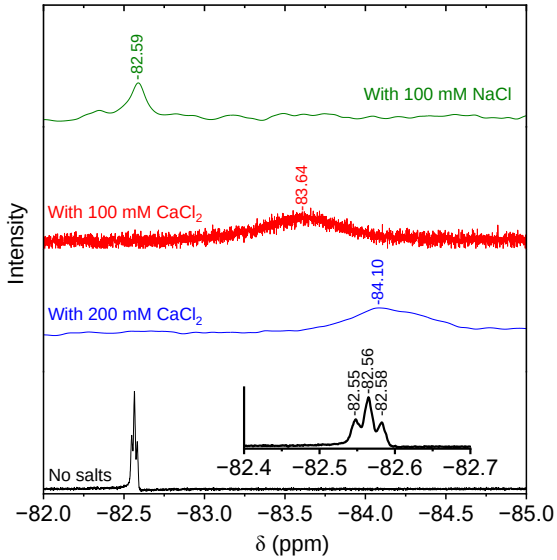

Figure 5.2 ^{19}F NMR spectra CF_3 regime of 1.1 mM (600 ppm) KPFOS in D_2O in the absence and presence of electrolytes. The inset shows the triplet peaks for sole KPFOS system.

In addition to the chemical shift of resonance peak for terminal -CF_3 group, the resonance peak for -CF_2 group closest to the headgroup is also subject to shift (inset of **Figure 5.1**). This signal assigned to the -CF_2 group closest to the headgroup is sensitive to the chemical environment of the polar head, and thus, it can be treated as the indicator to track the interaction between the headgroup and ions.[158] The downfield shifting suggests that the chemical environment of the sulfonic acid shell of KPFOS micelles is changed. Moreover, apparently the split triplet resonance

peaks of -CF_2-SO_3- merge in the presence of $CaCl_2$, changing from sharp and narrow to smooth and wide. The ^{19}F NMR spectra provide strong evidence about the interactions between the sulfonic acid group of KPFOS and the Ca^{2+}. Besides the ending -CF_3 and the -CF_2 near the polar head, the resonance peaks for the rest -CF_2 are also affected as seen in **Figure 5.1**, indicating the polarity of these C-F is varied when having the Ca^{2+} in the KPFOS solutions.

5.2.2. PFOA aqueous solutions

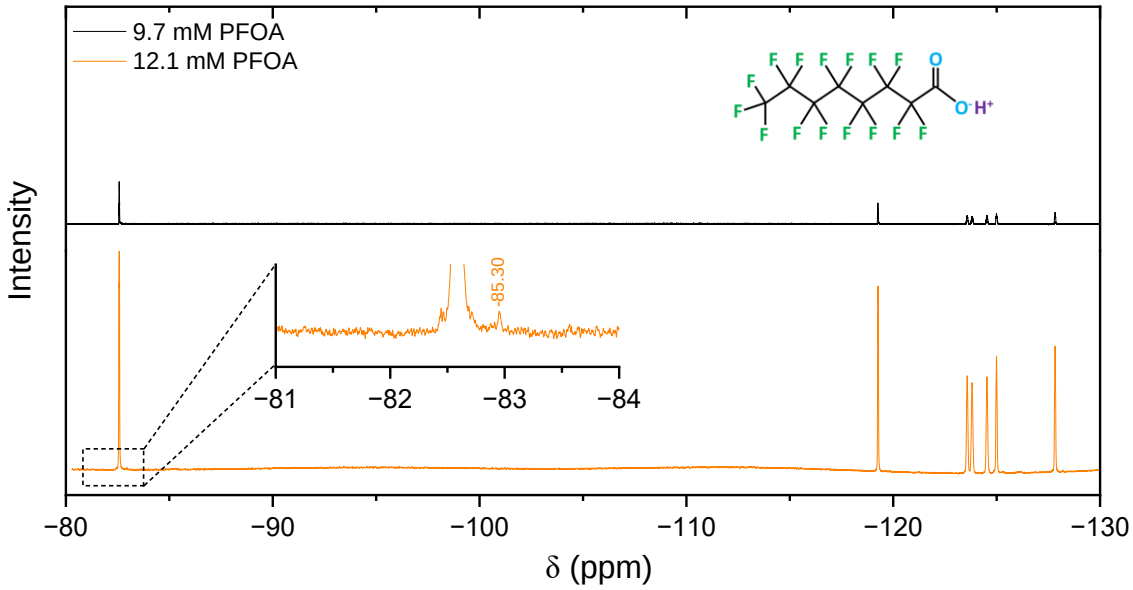

Figure 5.3 ^{19}F NMR spectra of 9.7 mM (4000 ppm) and 12.1 mM (5000 ppm) PFOA in D_2O. The inset shows a small peak corresponding to the formation of micelles.

The ^{19}F NMR spectra of PFOA at two different concentrations in D_2O at the room temperature is shown in **Figure 5.3**. As seen, seven resonance peaks are detected corresponding to the seven types of fluorine in PFOA, the same as the literature.[145,158] The same as KPFOS, the resonance peak at -82.58 ppm is assigned to the terminal -CF_3 group, of which the ^{19}F NMR chemical shift is influenced by the intermolecular interactions. **Table C2** lists the chemical shift of the seven peaks assigned to PFOA. Compared to 9.7 mM (~4000 ppm, CMC, see Chapter 3), an additional resonance peak at -85.30 ppm is observed as seen in the inset of **Figure 5.3**. It is

attributed to the micelle formation of PFOA monomers, which was also observed by Ning et al.[145] This signal assigned to the formation of PFOA micelles is increasing with increasing the bulk concentration. Our ^{19}F NMR spectra of PFOA confirms the CMC of PFOA in water is around 9.7 mM.

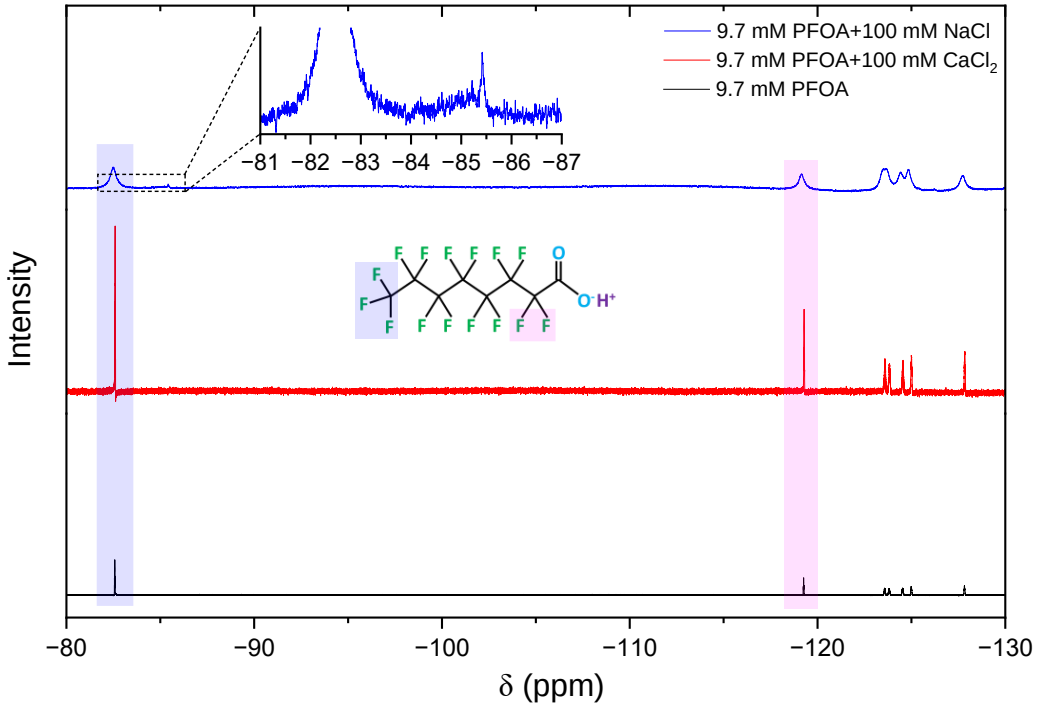

Figure 5.4 ^{19}F NMR spectra of 9.7 mM (4000 ppm) PFOA in D_2O in the absence and presence of 100 mM NaCl and $CaCl_2$, respectively. The temperature was room temperature. The inset shows a small peak corresponding to the formation of micelles after adding NaCl.

With respect to the salt effect, both NaCl and $CaCl_2$ were added to 9.7 mM PFOA in D_2O, respectively. **Figure 5.4** shows the ^{19}F NMR spectra of 1 CMC PFOA in D_2O in the absence and presence of 100 mM NaCl and $CaCl_2$, respectively. One can see that after introducing the Na^+, the half-line width of all resonance peaks becomes wider. The resonance peaks distributed between -120 to -126 ppm, assigned to the third to sixth fluorine from the one closest to the headgroup, are merging together. Furthermore, an additional resonance peak appears near the ending $-CF_3$ group peak (inset in **Figure 5.4**), implying the aggregation of PFOA monomers in the presence of Na^+.

On the other hand, introducing Ca^{2+} to PFOA systems does not apparently affect the chemical shifts. **Figure 5.5** clearly shows the details of two ^{19}F NMR spectra regimes corresponding to the terminal -CF_3 group and -CF_2 closest to carboxylic acid headgroup, respectively. No resonance peak shift is observed upon adding $CaCl_2$, whereas the downfield shifting is observed for both signals assigned to the -CF_3 group and -CF_2 closest to the polar head of PFOA monomer when introducing NaCl. Moreover, the split triplet resonance peaks merge to form a wider and smoother peak for both fluorine at the end and head. The same as KPFOS with Ca^{2+}, the chemical shift towards the lower field for -CF_3 group of PFOA also strongly indicates the aggregates of PFOA monomers when having the Na^+. Additionally, the chemical environment variation of -CF_2-COO- evidenced by the downfield shifting of resonance peak (**Figure 5.5B**) strongly implies the interaction between the carboxylic acid headgroup of PFOA and the Na^+ as the proton is easily kicked out by Na^+.

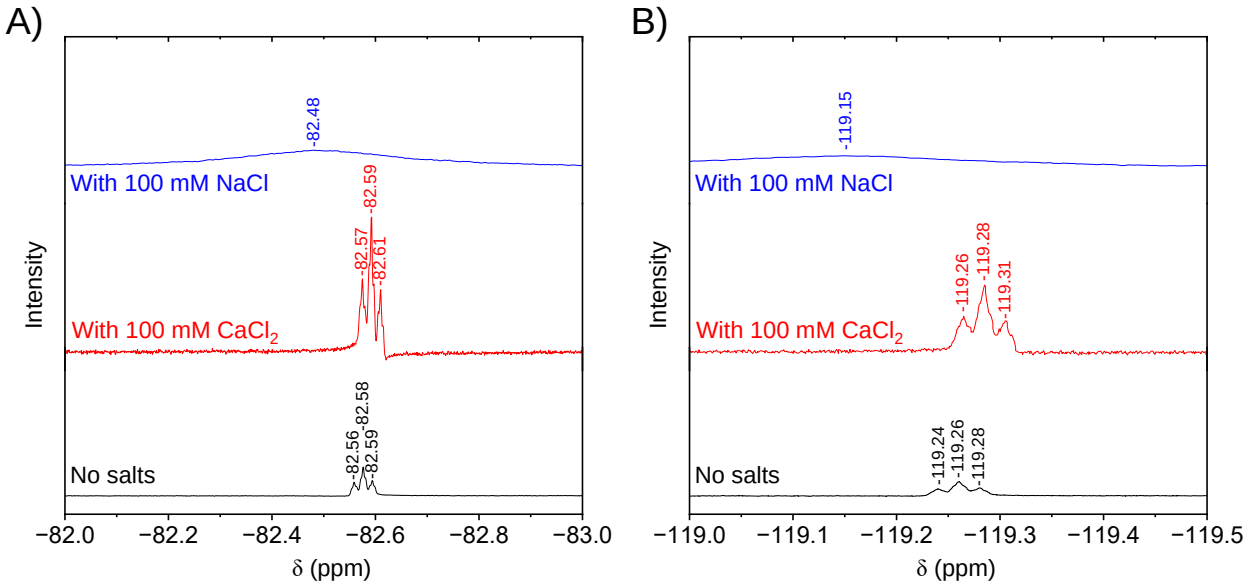

Figure 5.5 Specific regimes of ^{19}F NMR spectra for 9.7 mM (4000 ppm) PFOA in D_2O in the absence and presence of 100 mM NaCl and $CaCl_2$, respectively. A) ^{19}F NMR spectra -CF_3 regime, and B) ^{19}F NMR spectra -CF_2-COO- regime.

5.3. SAXS of PFAS solutions

As ongoing research, SAXS was performed to the PFAS aqueous solutions to further study the microstructure of PFAS aggregates in the bulk phase. The surfactant sodium dodecyl sulfate (SDS) solutions were performed with SAXS for the purpose of study as the SDS is well explored in the literature. **Figure 5.6** shows the 2D-SAXS patterns of SDS solutions with concentrations of 1 CMC and 10 CMC, respectively. **Figure 5.7** shows the 1D-SAXS profiles for 1 CMC and 10 CMC SDS solutions. The intensity is plotted as a function of scattering vector q in the range of q_{min} to q_{max}, as determined by the experimental setup and typically constrained by geometric factors. Typically, the q range is divided into three regimes: the low q domain, the intermediary q domain, and the high q domain. In the low q domain, where the observation scale is broadest, it is possible to derive the structure factor $S(q)$, which provides insights into the system's interactions. In our case, this low q domain can be used to determine if the PFAS micelles aggregate to form complex structure. The intermediate q domain allows for the determination of the form factor $P(q)$, related to the dimensions, shape, and internal makeup of an individual particle. Herein, the size and shape of PFAS micelles can be obtained based on the measurement in this regime. The high q domain, known as Porod's region, offers details about the surface at a small observational scale. Thus, this high q regime reflects the aspect of PFAS molecules.

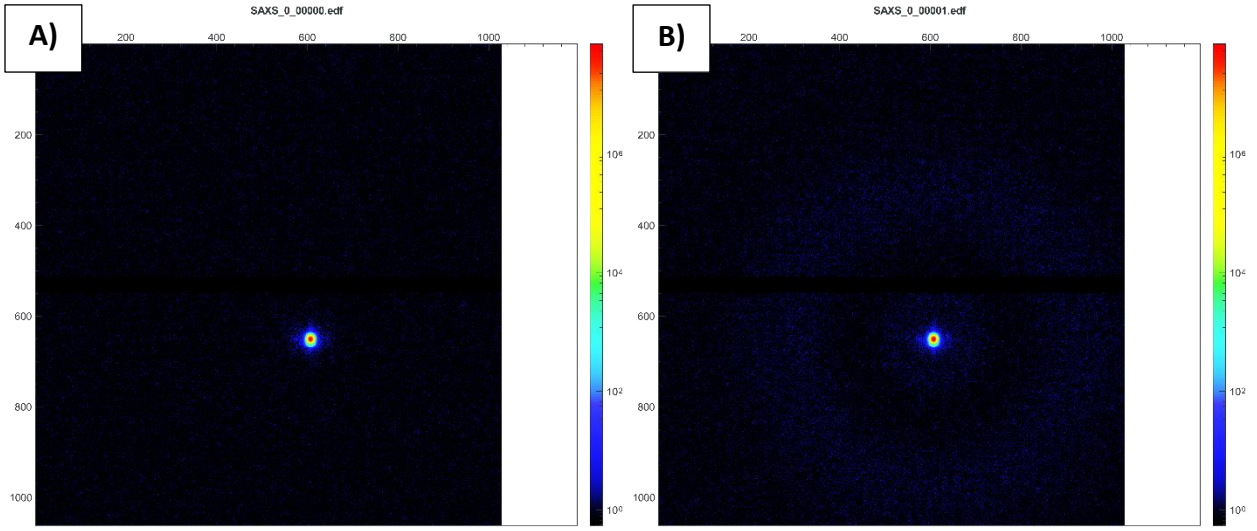

Figure 5.6 2D-SAXS patterns of A) 1 CMC SDS, and B) 10 CMC SDS.

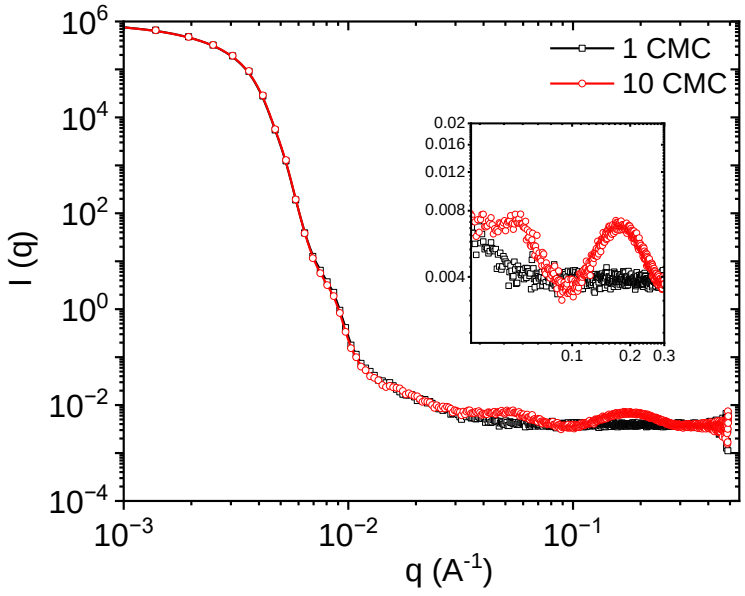

Figure 5.7 SAXS profiles for SDS solutions with two different concentrations of 1 CMC and 10 CMC. The lines are for guidance.

The overall scattering intensity, $I(q)$, as a function of scattering vector q, can be described as $I(q) \propto \phi P(q) S(q)$. According to Ochoa et al.,[167] the combined influence of $P(q)$, $S(q)$, and the scattering length density differences between solvent and shell and between shell and core

create distinct peaks and valleys in the SAXS profiles of SDS solutions. The inset in **Figure 5.7** clearly shows two peaks for 10 CMC (~82 mM) SDS solutions. The intensity peak in the q range of 0.03 to 0.1 A^{-1} is attributed to the $S(q)$, whereas the intensity peak in the q range of 0.1 to 0.3 A^{-1} is due to the $P(q)$. The former peak indicates the interaction of the SDS micelles, which will shift to higher q range with increasing the SDS concentrations.[167] This peak also implies the intermicellar distance. The latter peak indicates the SDS micelle size, which will remain the same with increasing the SDS concentration.[167] According to the $S(q)$ model proposed by Hayter and Penfold, and $P(q)$ model of oblate ellipsoidal core–shell micelles, the shell of SDS micelles is 0.75 nm, and the micelle diameter is between 1.3 to 2.0 nm.[167]

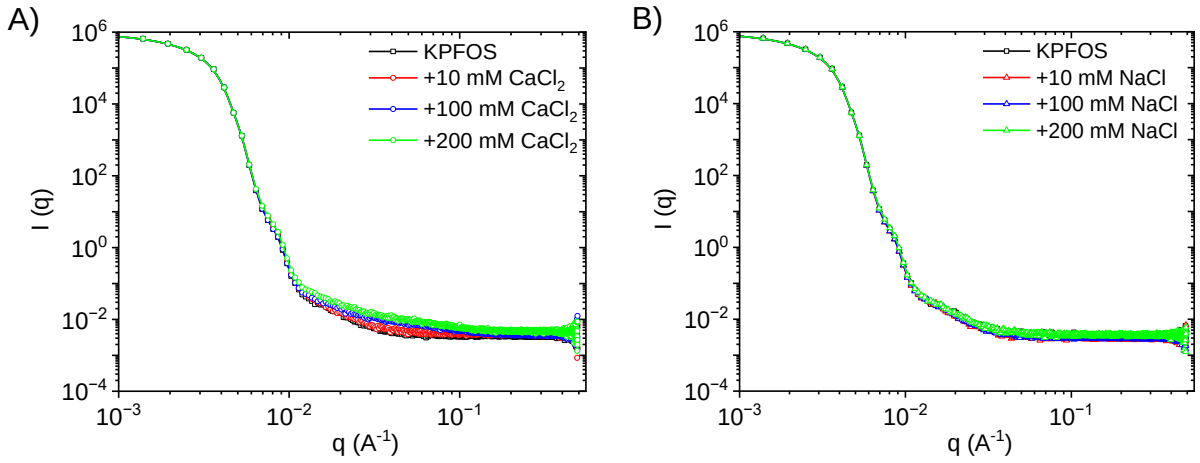

Figure 5.8 SAXS profiles for 1.1 mM KPFOS solutions with A) three different concentrations of $CaCl_2$, and B) with three different concentrations of NaCl. The lines are for guidance.

Figure 5.8 shows the 1D-SAXS profiles for 1.1 mM KPFOS solutions containing varied concentrations of electrolytes. Apparently, increasing the concentration of $CaCl_2$ affects the $P(q)$ of KPFOS aggregates since the $I(q)$ is increasing within the intermediate q domain. Therefore, addition of $CaCl_2$ qualitatively influences the KPFOS micelle size and shape; however, the intermicellar interaction is not affected upon adding the $CaCl_2$. On the other hand, the addition of NaCl does not significantly affect the KPFOS micelle size and shape, as well as the intermicellar

interaction. Interestingly, PFOA shows different trends. **Figure 5.9A** shows the 1D-SAXS profiles for 1 CMC PFOA solutions containing 10 mM and 100 mM $CaCl_2$. As seen, the divalent salts have no significant effect on PFOA micelle size and shape, which is different from KPFOS. Nevertheless, monovalent salts, i.e., NaCl, have an impact on PFOA micelle size and shape as seen in **Figure 5.9B**, and $I(q)$ change is dependent on NaCl concentration. Moreover, in the presence of 100 mM NaCl, increasing PFOA concentration dramatically increases the $I(q)$ within the intermediate q domain (light blue points in **Figure 5.9B**). The 2D-SAXS patterns of KPFOS and PFOA solutions in the absence and presence of electrolytes are shown in **Figures C1** and **C2**.

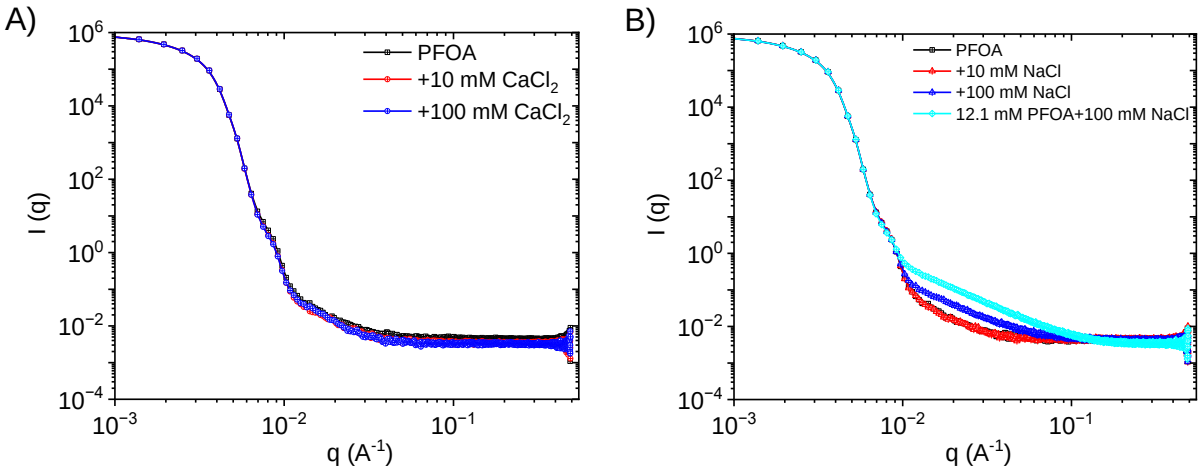

Figure 5.9 SAXS profiles A) for 9.7 mM PFOA solutions with two different concentrations of $CaCl_2$, and B) for 9.7 mM PFOA solutions with two different concentrations of NaCl, and for 12.1 mM PFOA solutions with 100 mM NaCl. The lines are for guidance.

5.4. Conclusions

In this Chapter, the ^{19}F NMR, and SAXS were utilized to further investigate the interactions between polar headgroups of PFAS and ions, and PFAS micelles. Our initial results confirm the formation of KPFOS micelles when introducing $CaCl_2$, as well as the interaction between sulfonic acid headgroups and Ca^{2+} ions. For PFOA, the monomers tend to interact with Na^+ ions instead of Ca^{2+} ions. In addition, an additional resonance peak was observed when increasing PFOA bulk

concentration from 9.7 mM (1 CMC) to 12.1 mM, demonstrating the formation of PFOA micelles. Furthermore, the SAXS results show evidence that the Ca^{2+} ions affect the KPFOS micelles, whilst the PFOA micelles are influenced by Na^{+} ions.

Chapter 6. Foam Formation of Per- and Polyfluoroalkyl Substances (PFAS)*

6.1. Introduction

The previous Chapters demonstrate the interfacial properties, such as surface tension and interfacial viscoelasticity, of PFAS in the absence and presence of electrolytes since they were reported to significantly influence the foaming behavior of PFAS.[72,73,99,107–109,113] For example, Gibbs stability ($E > \frac{\gamma}{2}$) was introduced as the criteria for determining the stability of interface stabilized by particles, and thus, the foam stability.[112,113,168,169] Georgieva et al.[112] emphasized the importance of dilatational elastic modulus, demonstrating that Ostwald ripening is controlled by the low frequency elasticity, and bubble coalescence is dominated by high frequency elasticity. Brown et al.[113] also investigated the relationship between the interfacial rheology and stability of Pickering foams, revealing that a higher critical shear strain contributes to the enhanced foam stability against liquid drainage.

The employment of aeration for removing PFAS from contaminated water with a promising removal efficiency is also demonstrated in the previous Chapters.[69–71,82,106,170–173] Dimensional analysis is a powerful tool in various fields of science and engineering, including the study of foaming process. Beyond the studies focused directly on foaming,[72,73,113,168,169,171–173,81,82,99,106–109,112] dimensional analysis can be applied to investigate and understand foaming process more comprehensively. For instance, optimization of foaming process, scale-up and scale-down studies, comparative studies, model validation, and parameter sensitivity analysis. Despite its significance, a limited number of research endeavors have been devoted to exploring the

* This Chapter is in preparation for submission to peer-reviewed journals. **Zhou, M.**, Foudazi, R.

dimensional analysis of foaming process induced by mechanical stirring. To the extent of our knowledge, the dimensional analysis concerning aeration remains unreported. Bois et al.[85] applied dimensional analysis to surfactant solutions (sodium laureth sulfate (SLES), Tween 20, and Brij L23) to study the influence of processing parameters on their foamability. The $\frac{H_f}{H_l}$ (expansion rate of foaming, defined in Chapter 2) was used to characterize the foaming behavior of surfactant solutions, and it was found that the dimensionless numbers of Reynolds number (Re) and mixing time number control the foaming process occurring in a mechanically agitated vessel. However, the effect of interfacial properties was not taken into account for different surfactants. Mary et al.[86] used dimensional analysis to predict the bubble size of the surfactant solutions, and they demonstrated that the bubble size of foams is mainly controlled but not limited by Capillary number (Ca). They also suggested that the impact of more parameters, such as interfacial rheology and kinetic diffusion of surfactants to the interfaces, needs to be investigated. Chapter 2 demonstrates the dimensional analysis used in this dissertation.

This Chapter aims to investigate the foaming behavior (foamability) of PFAS aqueous solutions and correlations between the foaming capacity of PFAS and their interfacial properties. PFAS with different headgroups and with different chain lengths are used in the present work. Electrolytes, NaCl and $CaCl_2$, are introduced to explore their impact on the foaming behavior of PFAS. The foaming behavior characterized by $\frac{H_f}{H_l}$, $\dot{H}_f = \frac{dH_f}{dt}$ (foaming kinetics), and ε (liquid content across the foams) is systematically analyzed for different types of PFAS by carrying out the dimensionless analysis of a lab-scale foaming column. This theoretical methodology is reinforced by conducting experiments where process parameters are altered, and the progression of foam height with foaming time is observed. This is done to confirm the semi-empirical correlations derived from the theory. The factors that affect the PFAS foaming behavior are

considered and discussed in this present Chapter, including interfacial parameters such as γ and E. The objective of this study is to enhance our understanding of the primary physical phenomena that predominantly influence foam formation in the foam aeration process of PFAS.

6.2. Foaming capacity of PFAS aqueous solutions

6.2.1. Comparison of different PFAS

Foaming capacity, or foamability, and foam stability are two important characteristics of foams. In this Chapter, only foamability is discussed. Various aeration times (t_f) of 30 s, 60 s, 120s, and 300 s were used to foam the PFAS aqueous solutions. **Figure 6.1A** shows the H_f of KPFOS aqueous foams during the 30 s of aeration by using three Q_{air}s of 0.2, 0.4, and 0.6 L/min, and two D_fs of 40-100 and 16-40 μm, respectively. The H_f increases with an increase of Q_{air}. Additionally, the use of the filter with a smaller D_f has no significant impact on the H_f, while the $\dot{H}_f$ (green triangle in **Figure 6.1A**) is slightly affected, for example, lower $\dot{H}_f$ is obtained at the beginning of foaming by using the Q_{air} of 0.2 L/min and smaller D_f. Furthermore, the H_f does not approach the equilibrium status at 30 s for KPFOS. The system can be considered to have reached equilibrium once the H_f measurements show that the changes fall below a predetermined threshold, and the corresponding time is noted as the equilibrium time t_e. The equation below is used to define the H_f change:

$$\left|\Delta H_f\right| = \frac{H_{f,t+\Delta t} - H_{f,t}}{H_{f,t+\Delta t}} \times 100\% \qquad \textit{Equation (6.1)}$$

If the $\left|\Delta H_f\right|$ is smaller than 1.5 % for the next 10 s, then the first time is used as the equilibrium time t_e. It can be seen in **Figure 6.1B**, the H_f approaches the equilibrium status at around 89 s for KPFOS. After the equilibrium (at around 100 s), H_f drops a little bit and undergoes a small oscillation (graph is now shown here) because the foam structure is separated by some

large air bubbles. According to Amani and Firouzi,[174] the flow regime in a vertical tube/pipe during the aeration includes 1) bubble, 2) foamy bubble, 3) slug flow, 4) churn flow, and 5) annular flow depending on the Q_{air}. Our result suggests that the KPFOS foaming flow regime transits from foamy bubble to slug flow and churn flow when the H_f reaches to the steady state (constant Q_{air} of 0.2 L/min). When the Q_{air} is higher than 0.2 L/min, the equilibrium status of KPFOS foams cannot be reached by using *DFA 100* due to the overflow alarm, for instance, the increasing H_f reached to the overflow alarm height at 36 s when the Q_{air} was 0.4 L/min, yet the equilibrium status was not approaching.

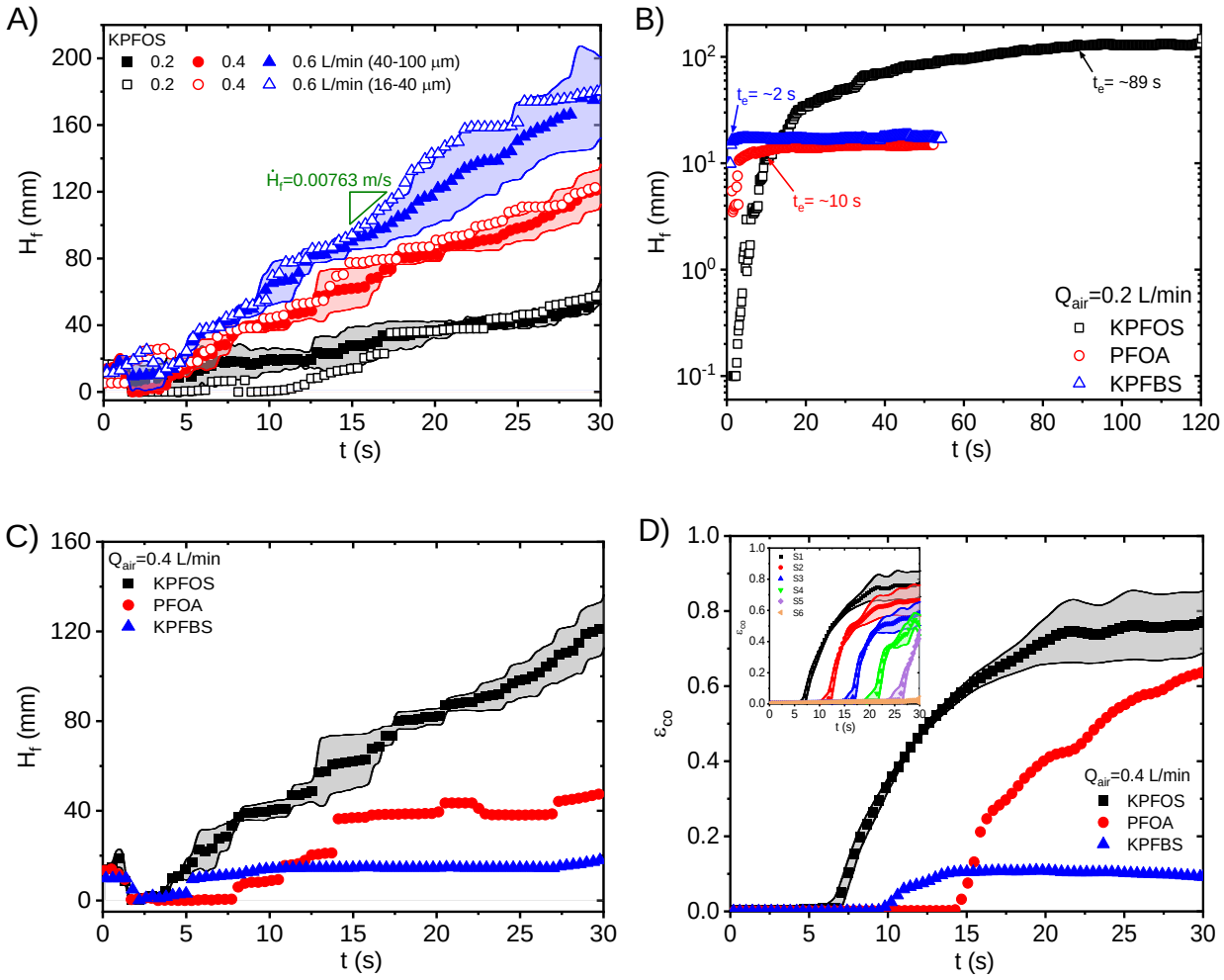

Figure 6.1 A) Foam height of 0.4 mM KPFOS aqueous foams during 30 s of aeration by using various air flow rates of 0.2, 0.4, and 0.6 L/min, and two filters with different pore size ranges of 16-40 and 40-100 µm, respectively. The

green triangle represents the kinetics of foaming. B) Foam height of 0.4 mM KPFOS, PFOA, and KPFBS aqueous foams as a function of aeration time, showing the various times used to approach the equilibrium status. The air flow rate was 0.2 L/min, and the filter size was 40-100 μm. C) Foam height of 0.4 mM KPFOS, PFOA, and KPFBS aqueous foams during 30 s of aeration, indicating that the foaming capacity follows the order: KPFOS>PFOA>KPFBS. The pore size range of filter was 40-100 μm, and the air flow rate was 0.4 L/min. And D) corrected liquid content of 0.4 mM KPFOS, PFOA, and KPFBS aqueous foams during 30 s of aeration based on the values provided by the first sensor. The inset is the corrected liquid content of 0.4 mM KPFOS at various heights of foams.

Compared to KPFOS, it takes less time for PFOA and KPFBS to reach equilibrium status. The t_e for PFOA is around 10 s, and a shorter t_e of around 2 s is obtained for KPFBS, when use the Q_{air} of 0.2 L/min (**Figure 6.1B**). While using 0.2 L/min, PFOA and KPFBS only have a thin layer of bubbles on the top of bulk solutions. **Figure 6.1C** shows the H_f of 0.4 mM KPFOS, PFOA, and KPFBS aqueous foams within the 30 s of aeration when use the Q_{air} of 0.4 L/min, implying that the KPFOS have the best foamability. When increase the Q_{air} to 0.6 L/min, the KPFOS still have the best foaming capacity as seen in **Figure 6.2**. Furthermore, the ε of the foams is another crucial concept, defined as:

$$\varepsilon = \frac{V_{liquid}}{V_{foam}} \qquad \textit{Equation (6.2)}$$

where V_{liquid} is the volume of liquid in the foams with a volume of V_{foam}.[138] ε determines the structure of foams.[73,138] Bubble deformation is no longer observed as jamming transition is approached when $\varepsilon \sim 0.36$, whilst the bubbly liquid is formed if $\varepsilon > 0.36$.[73,138] On the other hand, the foams have polyhedral bubbles if $\varepsilon \leq 0.05$.[73] As mentioned in Chapter 2, two liquid content sensors were used to directly measure the liquid content and resistance across the foams. For 0.4 mM of KPFOS aqueous solutions (D_f was 40-100 μm and the Q_{air} was 0.2 L/min), only the first two sensor chips had the reading if foaming for 30 s, whereas all sensor chips had the reading if increasing the aeration time to 120 s. The volume fraction of liquid in the foams can be correlated with the conductivity as follows:[73,113,175]

$$\varepsilon_{co} = \frac{3\sigma(1+11\sigma)}{1+25\sigma+10\sigma^2} \qquad \textit{Equation (6.3)}$$

where σ is the ratio of $\sigma_{foam}/\sigma_{reference}$, called relative conductivity. **Figure 6.1D** is the ε_{co_1} of 0.4 mM KPFOS, PFOA, and KPFBS aqueous foams (the lowest sensor chip position), indicating that the KPFOS foams contain more continuous phase (water), whereas the KPFBS foams are relatively dry. Additionally, the ε_{co_1} of PFOA foams are still increasing even if the foams are already approaching the equilibrium status. When the Q_{air} was 0.4 L/min, the foams only hit the first sensor chip for PFOA and KPFBS, but for KPFOS, six sensor chips had the readings as shown in the inset of **Figure 6.1D**.

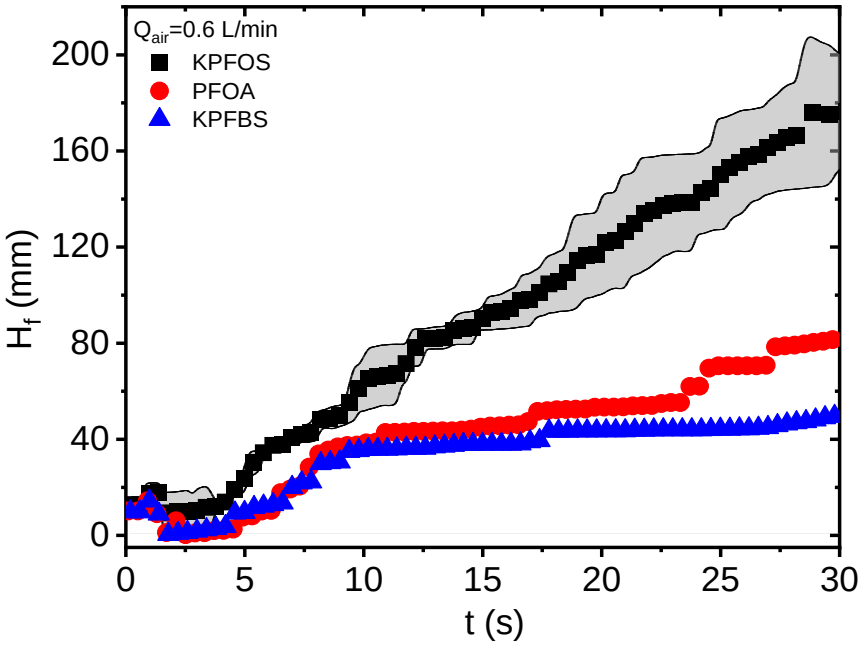

Figure 6.2 Foam height of 0.4 mM KPFOS, PFOA, and KPFBS aqueous foams during 30 s of aeration. The pore size range of filter was 40-100 μm, and the air flow rate was 0.6 L/min.

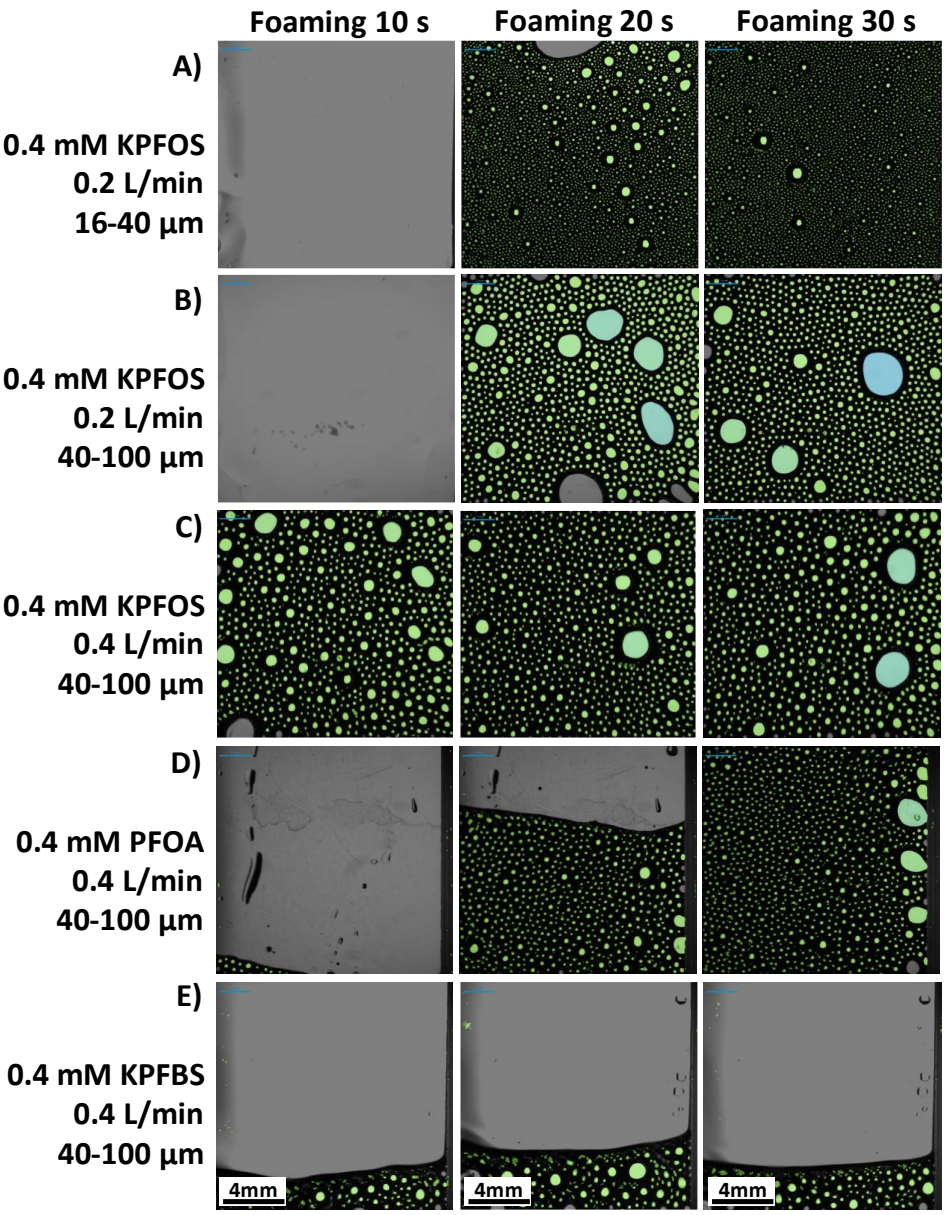

Figure 6.3 Foam structure at 10 s, 20 s and 30 s during 30 s of foaming for different PFAS with the same bulk concentration of 0.4 mM by using different aeration conditions. The scale bar is 4 mm. Bubbles of 0.4 mM KPFOS aqueous foams by using the air flow rate of 0.2 L/min, and sparged by the filter with a pore size range of A) 40-100 µm, and B) 16-40 µm. Bubbles of 0.4 mM C) KPFOS aqueous foams, D) PFOA aqueous foams, and E) KPFBS aqueous foams by using the air flow rate of 0.4 L/min, and the pore size range of the filter is 40-100 µm.

Figure 6.3 shows the foam bubble morphology at aeration times of 10 s, 20 s and 30 s from left to right for different PFAS foams created by using different conditions. As the foam was creating, the camera captured the bubbles at 13-15 s for 0.4 mM KPFOS aqueous foams when the

Q_{air} was 0.2 L/min. Different types of bubble radius were obtained from *DFA 100*, **Figure 6.4A** shows the average bubble radius and Sauter mean bubble radius of 0.4 mM KPFOS foams sparged by using the 40-100 µm filter and the Q_{air} of 0.2 L/min. The average bubble size becomes smaller as aerating. **Figure 6.4B** shows the bubble count per mm^2. In addition, the D_f has an impact on the bubble size of PFAS foams. Smaller bubble size was obtained by using the filters with a smaller D_f of 16-40 µm as shown in **Figures 6.3A** to **6.3B** at the foaming times of 20 s and 30 s. However, when the steady state was reached, the foams sparged by the filters with a smaller D_f have a greater Sauter mean bubble radius as seen in **Table 6.1**. In this study, the Sauter mean bubble radius is used for discussion, and the last 10 data points before stopping the aeration were used to obtain the final value of bubble radius as R.

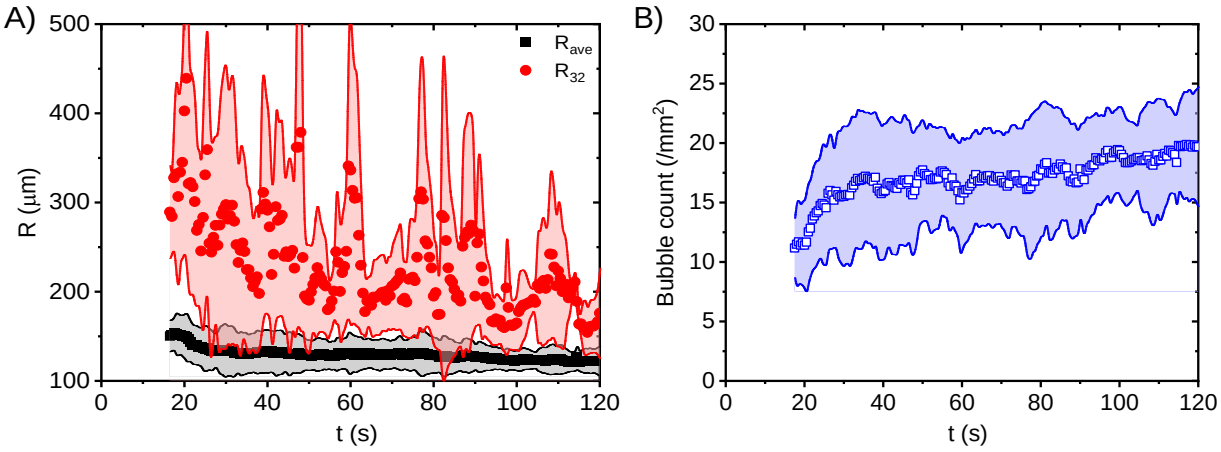

Figure 6.4 A) Average bubble radius including average bubble radius and Sauter mean bubble radius, and B) bubble count per area of 0.4 mM KPFOS aqueous foams during foaming process by using 0.2 L/min air flow rate. The filter size was 40-100 µm.

For 0.4 mM PFOA and KPFBS aqueous solutions, the bubbles were not captured by the camera since the H_f was not high enough if using 0.2 L/min. When Q_{air} is 0.4 L/min and D_f is 40-100 µm, as seen in **Figures 6.3C** to **6.3E**, PFOA have smaller bubble size, while KPFOS have larger bubble size. While using 0.4 L/min, for PFOA, the foam approaches the equilibrium status

at around 15-18 s, whereas the t_e is around 7-10 s for KPFBS. The t_e increases to around 30 s for PFOA foams while increasing the Q_{air} to 0.6 L/min, whilst it takes around 12-18 s to get to the equilibrium status for KPFBS foams. In other words, the t_e becomes larger when increasing the Q_{air}. Furthermore, Q_{air} in the tested range has no significant effect on the bubble size of PFAS foams including the ones already in steady state and the ones not in the equilibrium status.

Table 6.1 Average bubble radius and Sauter mean bubble radius of KPFOS aqueous foams in steady state sparged by using filters with different pore size range.

Average bubble radius	
D_f=40-100 µm	122.33±0.30
D_f=16-40 µm	84.10±2.37
Sauter mean bubble radius	
D_f=40-100 µm	162.73±5.34
D_f=16-40 µm	380.70±109.70

6.2.2. Effect of PFAS bulk concentration

The concentration of PFAS also influences the foam structure. Taking the example of KPFOS, the foamability is not linearly correlated with the bulk concentrations. **Figure 6.5** depicts the foam structure of KPFOS foams with various bulk concentrations, ranging from 0.05 mM to 0.8 mM. A layer of bubbles is obtained when the KPFOS bulk concentrations are 0.01 and 0.02 mM. Nevertheless, the H_f is too short to be recorded. Below 0.01 mM, the KPFOS solutions cannot be foamed. Ranging from 0.01 to 0.4 mM, the foamability is enhanced due to the increased H_f with increasing the concentration. It is attributed to the increased KPFOS concentration at the air-water interface.[111,176] Additionally, the bubble size of KPFOS foams becomes more uniform and smaller with an increase in concentration. Increasing the KPFOS concentration from 0.4 mM to higher molarity, the bubble size further becomes smaller and more monodispersed. Nonetheless, the H_f is reduced as seen in **Figure 6.5F**. Above 0.8 mM, the foam bubbles are not able to be

recorded due to the short H_f. Only a thin layer of bubbles is obtained when the concentration is near the KPFOS solubility limit (1.1-1.2 mM) in water. The increase in foam collapse rate with increasing the concentration of surfactant mixture sodium dodecyl benzenesulfonate (DOBS) and sodium lauryl ether sulfate (SLES) was reported by Behara et al.,[111] attributing to the reduction in Gibbs elasticity of the Plateau Borders (PBs).

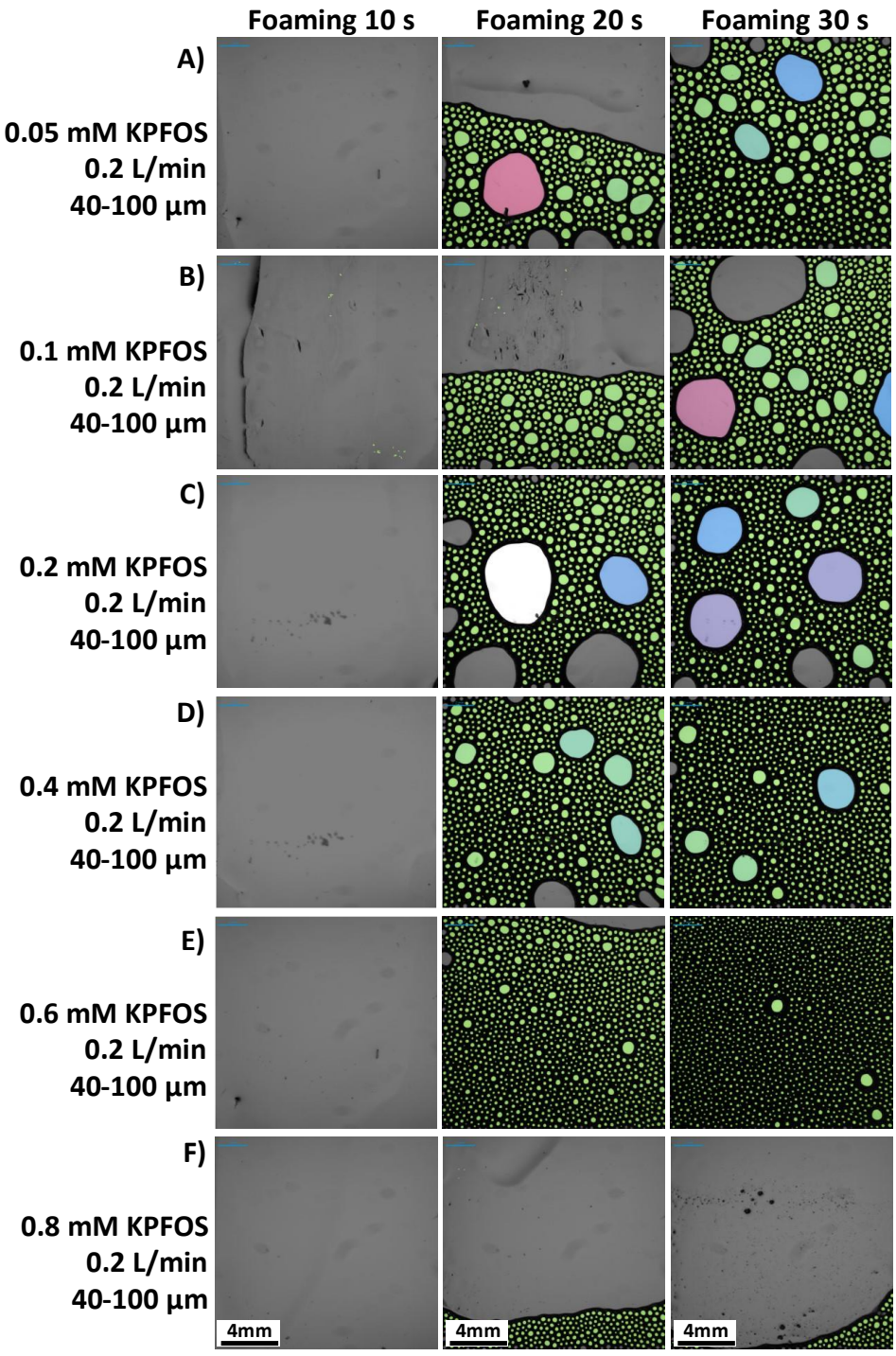

Figure 6.5 Foam structure at 10 s, 20 s and 30 s during 30 s of foaming process for A) 0.05 mM, B) 0.1 mM, C) 0.2 mM, D) 0.4 mM, E) 0.6 mM, and F) 0.8 mM KPFOS aqueous foams by using the same air flow rate of 0.2 L/min and the same glass filter with the pore size range of 40-100 µm. The scale bar is 4 mm. Below 0.05 mM and above 0.8 mM, the foamability is worse and the foam height is not high enough to be captured by the camara.

6.3. Dimensional analysis of expansion rate of foaming

6.3.1. KPFOS aqueous solutions

The foamability was tested for KPFOS aqueous solutions at various bulk concentrations by varying the processing parameters of t_f, and Q_{air}. As a result, various t_e were obtained. We used t_e instead of t_f for the dimensional analysis since the equilibrium status is considered. The KPFOS samples involved in the dimensional analysis of $\frac{H_f}{H_{l0}}$ have no salts added because the steady state cannot be achieved due to the overflow. **Figures 6.6A** to **6.6G** show the effect of various dimensionless numbers on the expansion rate of foaming.

As can be seen in **Figure 6.6A**, $\frac{H_f}{H_{l0}}$ is clearly correlated with Re_b. The correlation of $\frac{H_f}{H_{l0}}$ with Re_b follows Freundlich model (lines in **Figure 6.6A**), and the fitted equations are shown in **Table D1**. The Re_b represents the ratio of inertial force and viscous force. The low Re_bs shown in **Figure 6.6A** indicate the flows are laminar flow, where the viscous force is the dominant force. It can explain the spherical bubble shape shown in **Figures 6.3** and **6.5** as the bubbles will become non-spherical in the case of high Re_b (>500).[104] A significant increase of $\frac{H_f}{H_{l0}}$ with a decrease of Re_b is observed for various Q_{air}s. In Bois et al.'s work, they claimed that the lower expansion rate of foaming in the high Re_b regime is due to the transition from intermediate flow to turbulent, where the bubble breakup is easier to take place.[85] If at the same Re_b, one can see from **Figure 6.6A** that higher Q_{air} gives rise to higher expansion rate of foaming.

The Ca measures the effect of viscous force versus surface tension across the gas-liquid interface. It was reported that the increase of Ca is associated with the change of bubble size and shape. Mary et al.[86] used the Ca to predict the Sauter mean diameter of bubbles and found the inverse relationship between the bubble size and the Ca. Drenckhan et al.[105] pointed out that the

elongation of bubbles is associated with larger Ca. **Figure 6.7** shows the R as a function of Ca. A valley of R is observed for all three Q_{air}s. Additionally, a peak is also observed regarding the relationship between the $\frac{H_f}{H_{l0}}$ and Ca. From our previous work (see Chapter 3), the highlighted areas in **Figure 6.6B** and **Figure 6.7** have the highest E, which occurs in the concentration range of 0.2-0.4 mM. Hence, the appearance of $\frac{H_f}{H_{l0}}$ peak and R valley versus Ca is coinciding with the maximum of E. On the left side of E maximum, the interfacial force is dominated compared to the viscous force due to the relatively smaller Ca. In addition, the dominant mechanism in terms of PFAS adsorption is the Gibbs adsorption (see Chapter 3).[102] On the right side of E maximum, where the effect of viscous force becomes more dominant, the molecular exchange of PFAS between the interface and bulk is dominated.[102] Thus, for each Q_{air}, the correlation between the $\frac{H_f}{H_{l0}}$ of KPFOS and Ca has regime I and regime II determined by the peak. In surface tension-dominating regime I, the foamability is increasing and the bubble size is decreasing with increasing the Ca, whereas in the viscous force-dominating regime II, the foaming behavior becomes worse as increasing the Ca. The equation $y = e^{(ax^2+bx+c)}$ is used to fit the $\frac{H_f}{H_{l0}}$ as a function of Ca, with the fitted equations showing in **Table D1**. Noting the $\frac{H_f}{H_{l0}}$ increases with increasing the air injection rates, therefore, some data points are not considered for fitting to correctly show the trend. For example, the highlighted points for 0.2 L/min are excluded since these concentrations are not shown for 0.4 and 0.6 L/min in **Figure 6.6B** due to the overflow occurrence before reaching the steady state.

The variation of foam expansion rate over the We_b also follows the Freundlich model as seen in **Figure 6.6C**, and the fitted equations are shown in **Table D1**. The We_b is used to determine the significance of fluid's inertia in comparison to its surface tension. At a lower Q_{air}, the

dependency of $\frac{H_f}{H_{l0}}$ on the We_b is not very significant, whilst the foamability increases with a decrease on the We_b when using higher Q_{air} of 0.6 L/min. Our results reveal that once the foamability is improved, in turn, the effect of surface tension becomes more important. The rate of foam expansion is linearly related to Fr_b as seen in **Figure 6.6D**. The linear relationships of $\frac{H_f}{H_{l0}}$ as a function of Fr_b for various Q_{air}s are shown in **Table D1**. The Fr_b refers to the ratio of inertial force and gravitational force. In our case, the foaming capacity of KPFOS increases with increasing the effect of inertial force compared to the gravitational force, with this trend being clearer in the case of higher Q_{air} (blue line in **Figure 6.6D**).

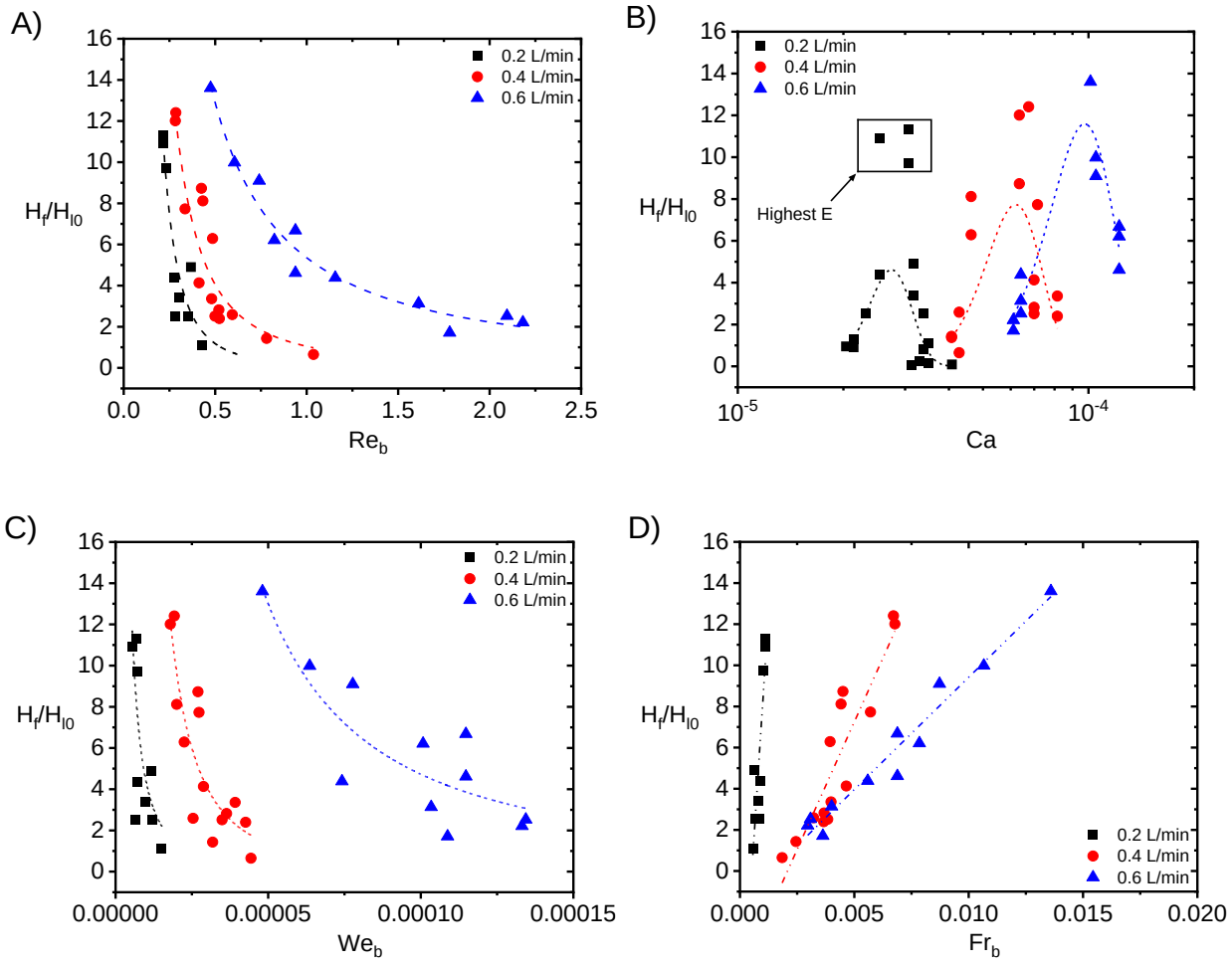

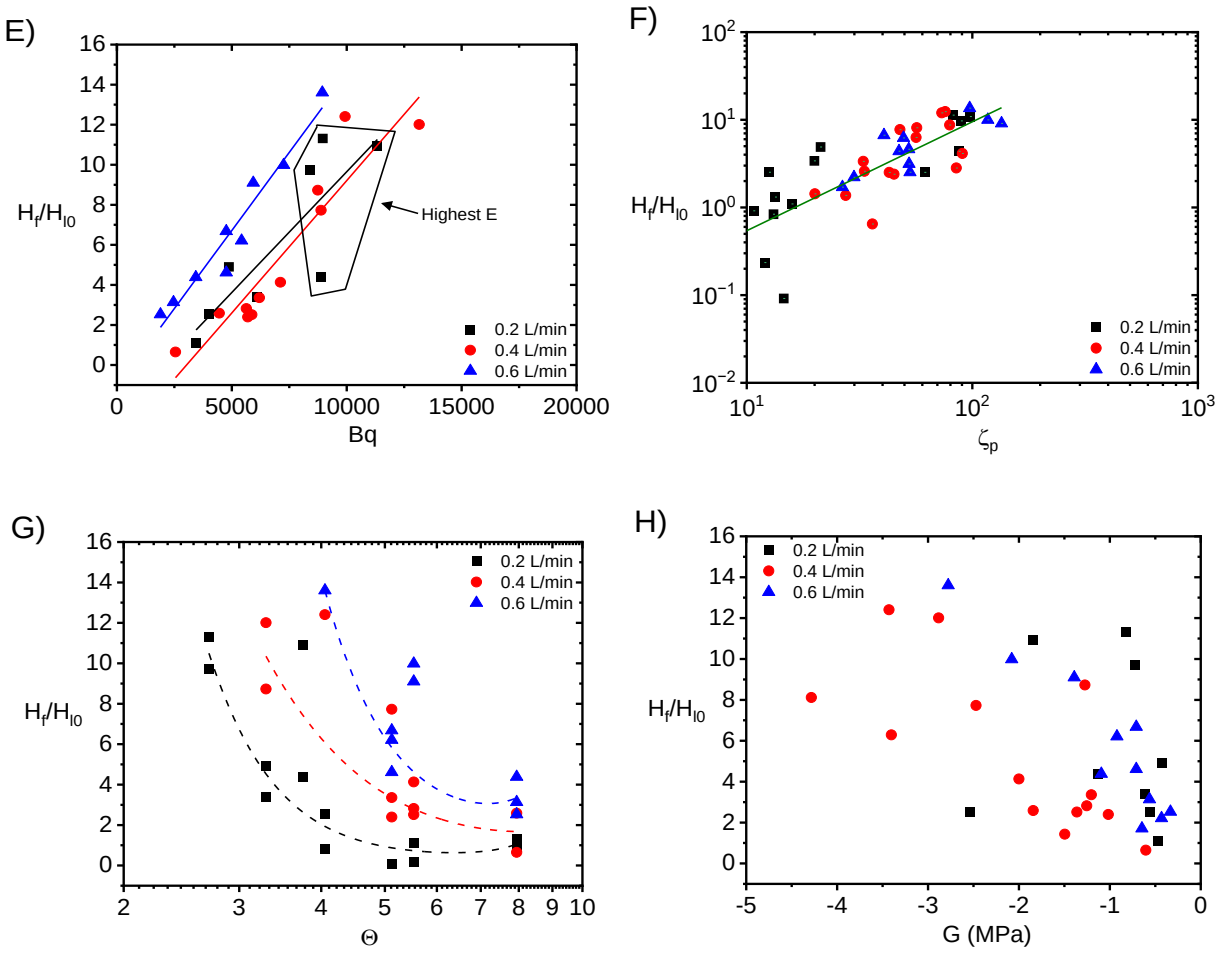

Figure 6.6 Evolution of foam expansion rate for KPFOS aqueous solutions with the A) Reynolds number, B) Capillary number, C) Weber number, D) Froude number, E) Boussinesq number, F) processing number, G) interface number, and H) Gibbs stability.

The same as Fr_b, $\frac{H_f}{H_{l0}}$ is also linearly correlated with Bq as seen in **Figure 6.6E** and **Table D1**. The importance of the surface-to-bulk viscous forces is given by the Bq when the Reynolds numbers are small.[177] It was reported that the liquid drainage velocity is correlated with the interfacial shear viscosity represented by Bq.[178,179] The Bq can also represent the surface mobility since the η_s is the effective parameter to characterize the surface mobility.[180] We used the dilatational interfacial viscosity to calculate the Bq since the shear interfacial rheology is not suitable for the soluble surfactants. The dilatational interfacial elasticity and viscosity are reported

to influence the surface mobility, as a consequence, the surfactant flows in the Plateau Borders are regulated by the adsorption behavior occurring at the surface of node.[180] One can see from **Figure 6.6E**, the expansion rate of foaming increases with increasing the Bq. For 0.2 L/min, as pointed in **Figure 6.6E**, the samples having greater values of Bq have highest E, corresponding to the highest E''. It suggests that the effect of η_s on the foaming behavior of KPFOS is significant. The lower $\frac{H_f}{H_{l0}}$ is obtained in the situation of lower η_s, correlating with the increased mobility of molecules at the air-water interface, and thus, the foamability is reduced.

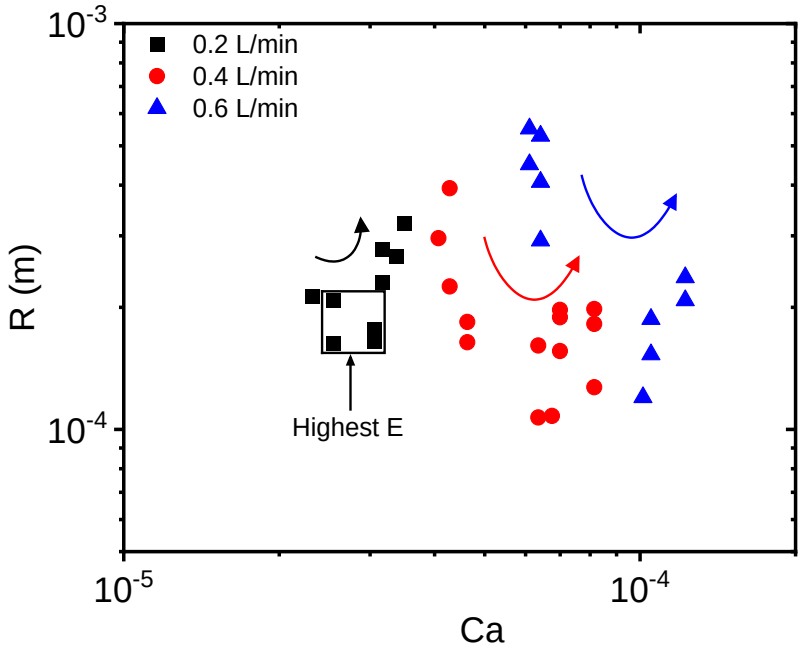

Figure 6.7 Sauter mean radius of KPFOS aqueous foams with the Capillary number.

As for ζ_p, the rate of foam expansion increases with an increase of ζ_p because of the increased t_e (**Figure 6.6F** and **Table D1**). The correlation between $\frac{H_f}{H_{l0}}$ and Θ was fitted with equation $y = e^{(ax^2+bx+c)}$, shown as the dashed lines in **Figure 6.6G**. The fitted equations are shown in **Table D1**. Decreasing Θ indicates the higher impact of E, in this situation, the higher $\frac{H_f}{H_{l0}}$

suggests the significance of dilatational modulus on the KPFOS foamability. The dimensionless numbers that can be analyzed are not limited to the ones mentioned above, for example, the $\frac{H_f}{H_{l0}}$ is also affected by Ga_b as seen in **Figure 6.8**. But more details will not be discussed in this study.

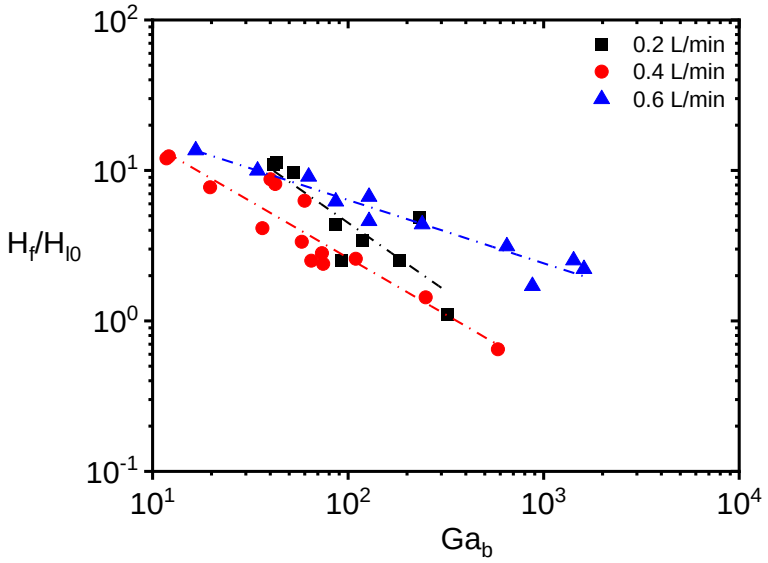

Figure 6.8 Evolution of foam expansion rate for KPFOS aqueous solutions with the Galilei number.

Gibbs stability can be used as the criterion to determine the stability of air-water interfaces involved in the Pickering foams.[112,113,168,169] The *Equation (6.4)* is originally used to determine the occurrence of bubble coarsening if it is fulfilled:[181]

$$\frac{dP}{dR} = -\frac{2\gamma}{R^2} < 0 \qquad \textit{Equation (6.4)}$$

where P is the bubble capillary pressure. For the surfactant solutions, *Equation (6.4)* is always true since γ is independent on the R. This destabilization is to some extent counteracted by introducing the E.[181] Therefore, the *Equation (6.4)* becomes:

$$\frac{dP}{dR} = -\frac{2\gamma}{R^2} + \frac{4E}{R^2} = G \qquad \textit{Equation (6.5)}$$

where G is Gibbs stability, and $E > \frac{\gamma}{2}$ is known as the Gibbs stability criterion.[181,182] Once the Gibbs stability criterion is fulfilled, the Laplace pressure increases with the bubble size increasing,

thereby the bubble coarsening slows down.[181] **Figure 6.6H** shows the expansion rate of foaming versus Gibbs stability for KPFOS aqueous foams. The Gibbs stability criterion is not fulfilled for KPFOS aqueous foams because of negative G. The $\frac{H_f}{H_{l0}}$ is not dependent on the G when the Q_{air} is 0.2 L/min. However, the foamability decreases as the system is approaching the Gibbs stability criterion when using higher Q_{air}s of 0.4 and 0.6 L/min. Hence, the foaming capacity is reduced as the E becomes closer to $\frac{\gamma}{2}$, at least for KPFOS aqueous foams without any additives. It was pointed out by Maestro et al.[181] that the Gibbs stability criterion is essential to prevent the bubble coarsening, but it is not sufficient to determine the bubble stability. The interface needs to be strong enough to resist the breakup.

6.3.2. PFOA aqueous solutions

Given a concentration of PFOA, various concentrations of NaCl were tested, as shown in **Table 2.2**. Different t_es were obtained as the processing parameters t_f and Q_{air} were varied. The same as KPFOS, the steady state is taken into account for PFOA foams. **Figures 6.9A** to **6.9G** are the dependency of expansion rate of foaming on the dimensionless numbers.

The expansion rate of foaming is negatively correlated with the Re_b as shown in **Figure 6.9A**. Linear relationships can be used to describe their correlation, and the fitted parameters are shown in **Table D2**. The Re_bs shown in **Figure 6.9A** are smaller than 1.5, suggesting the laminar flow. The hollow points in **Figure 6.9A** are the PFOA foams without adding NaCl, and they tend to have low foamability. Nonetheless, the foamability is not linearly increasing with increasing the NaCl concentration. For example, the highest foamability of PFOA is obtained for both Q_{air}s of 0.4 and 0.6 L/min when the concentration range of NaCl is between 5-50 mM as seen in **Figure 6.9A**, the data points in the dashed line box. The γ and E are slowly decreasing with an increase of NaCl concentration. The details of interfacial properties of PFAS in the presence of salts are

discussed separately. Ndiritu et al.[183] studied the effect of NaCl on the foamability of cricket proteins, and they found that there is a certain NaCl concentration at which the highest foamability is obtained. It was claimed that the initial increasing foamability is due to the enhanced protein solubility, and the further decrease of the foaming capacity is because the charge-screening occurs, and thus, hydrophobic interaction and intermolecular cohesion between protein molecules are improved, leading to the reduction in flexibility of the protein surfactant molecules.[183,184]

The same as KPFOS, the peak of $\frac{H_f}{H_{l0}}$ as a function of Ca is also found for PFOA as seen in **Figure 6.9B**. The fitting equations for different Q_{air}s are shown in **Table D2**. The Ca is dependent on the NaCl concentration, and the NaCl concentration ranges where the $\frac{H_f}{H_{l0}}$ peak appears are coinciding with the those in **Figure 6.9A**. The linear relationship was also used to fit with the $\frac{H_f}{H_{l0}}$ as a function of the We_b, and the fitted equations are shown in **Table D2**. Similar with Re_b, when the NaCl concentration is between 5-50 mM, smaller We_bs and higher $\frac{H_f}{H_{l0}}$s are obtained. This NaCl concentration range is called the optimized NaCl concentrations in order to obtain the higher foamability of PFOA.

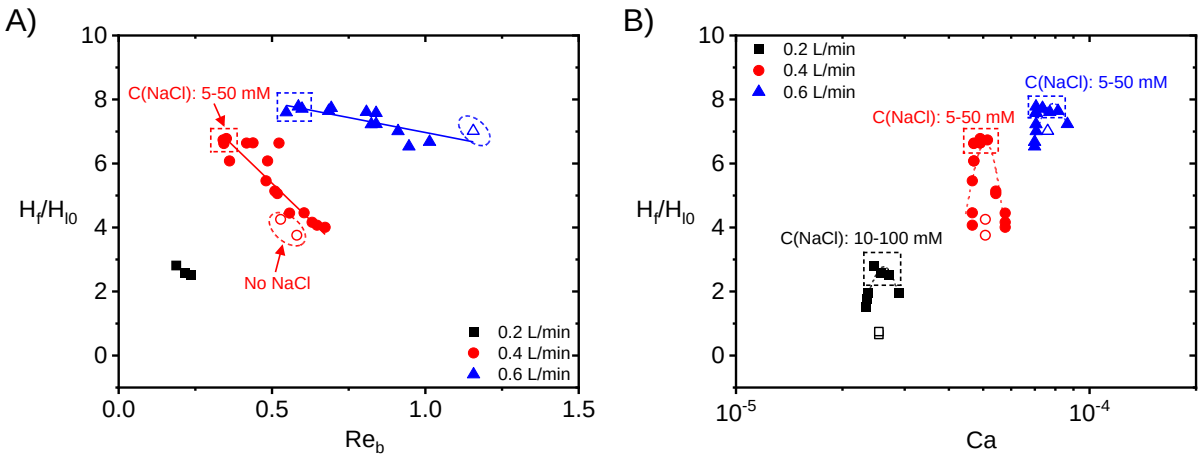

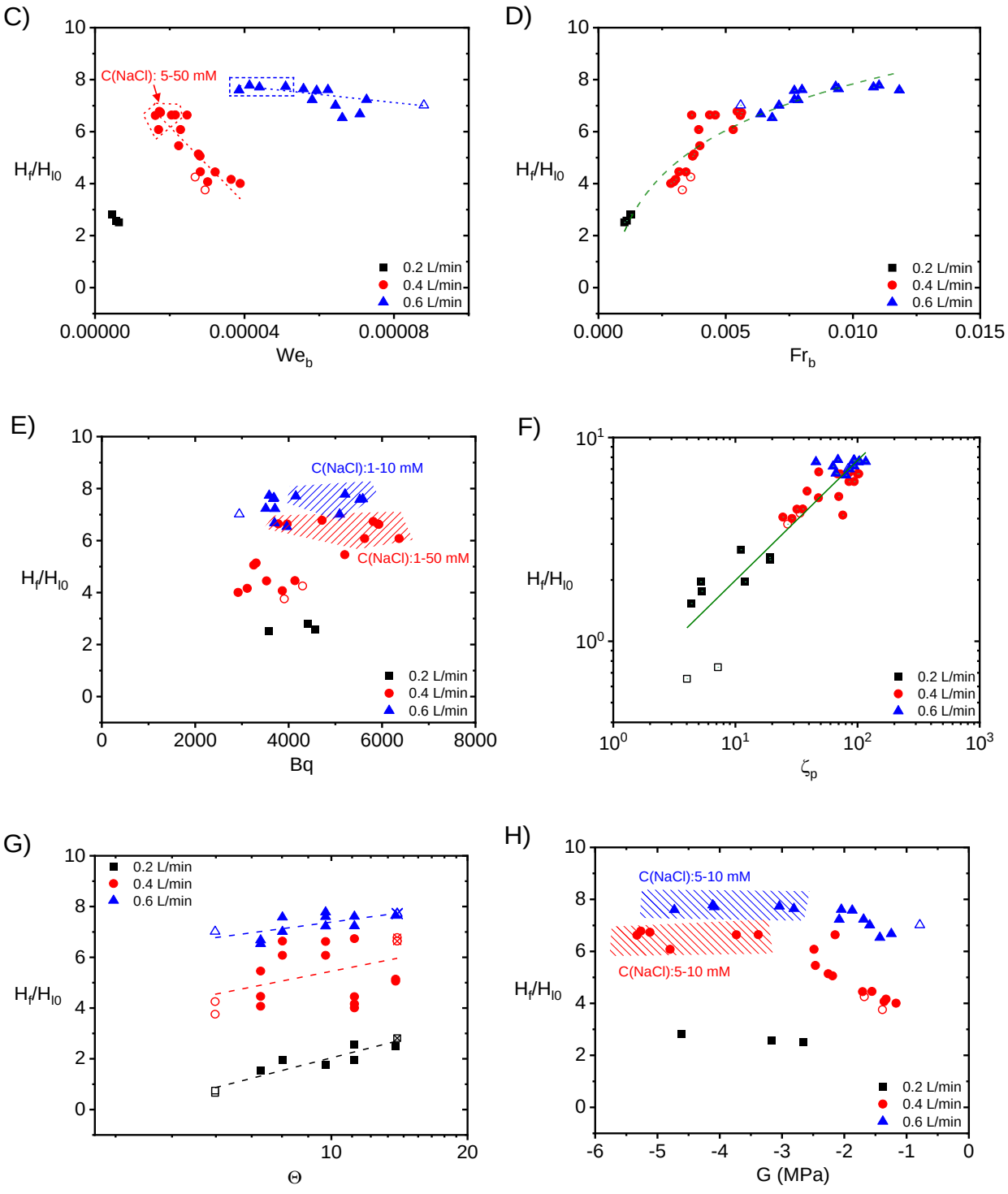

Figure 6.9 Evolution of foam expansion rate for PFOA aqueous solutions with the A) Reynolds number, B) Capillary number, C) Weber number, D) Froude number, E) Boussinesq number, F) processing number, G) interface number, and H) Gibbs stability. The hollow points are the foams solely containing PFOA.

One equation can be used for describing the relationship between the $\frac{H_f}{H_{l0}}$ and Fr_b as seen in **Figure 6.9D**, which is $\frac{H_f}{H_{l0}} = 66.9518Fr_b^{0.0493} - 45.51554$. One can see from **Figure 6.9D**, at a certain point, the effect of inertial force on the foamability of PFOA is no longer significant since a plateau of $\frac{H_f}{H_{l0}}$ is obtained. The dependance of $\frac{H_f}{H_{l0}}$ on the Bq seems less dependent compared to that of KPFOS (**Figure 6.9E**). But the $\frac{H_f}{H_{l0}}$ increases a little bit as the Bq increases. The optimized NaCl concentrations enhance the Bq, and thus, the η_s is increased. Addition of NaCl increases the ζ_p (**Figure 6.9F**) due to the enhanced t_e. However, differ from KPFOS, the dependency of $\frac{H_f}{H_{l0}}$ on the ζ_p becomes less significant in the case of using higher Q_{air}, for example, 0.6 L/min.

As for the Θ, the $\frac{H_f}{H_{l0}}$ increases with an increase of Θ in the range of 6-14, while the $\frac{H_f}{H_{l0}}$ of KPFOS decreases when increase the Θ in the range of 2.5-8. The crossed points in **Figure 6.9F** have the NaCl concentration of 10 mM, above which the effect of γ decreases as the Θ is decreasing, and consequently, the expansion rate of foaming decreases. The dimensionless number Ga_b also influences the $\frac{H_f}{H_{l0}}$ of PFOA systems as seen in **Figure 6.10**. The linear relationships of $\frac{H_f}{H_{l0}}$ as a function of Ga_b for different Q_{air}s are shown in **Table D2**.

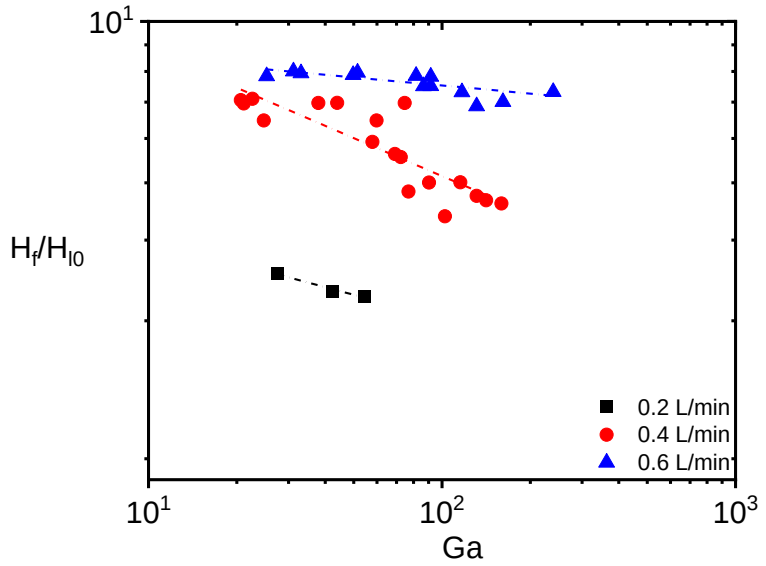

Figure 6.10 Evolution of foam expansion rate for PFOA aqueous solutions with the Galilei number.

Figure 6.9H is the correlation between the $\frac{H_f}{H_{l0}}$ and the G. The Gs are still negative for PFOA foams with and without NaCl. Therefore, the Gibbs stability criterion is not fulfilled for PFOA aqueous foams. Generally, adding the NaCl reduces the G, but the foamability of PFOA foams is independent of the G within the optimized NaCl concentrations as highlighted in **Figure 6.9H**. Additionally, in the case of non-optimized NaCl concentrations, as the E is getting closer to $\frac{\gamma}{2}$, the foaming capacity is somewhat hindered.

6.3.3. KPFBS aqueous solutions

0.4 mM of KPFBS was used to study the foaming behavior of KPFBS aqueous foams as shown in **Table 2.2** as well. As mentioned earlier, the foaming capacity of KPFBS is weaker compared to the same molarity of KPFOS and PFOA (**Figure 6.3**), even for using the Q_{air} of 0.4 L/min, only top part of the foams was recorded by the camera. Therefore, for the dimensional analysis which needs the data of bubble size, the KPFBS aqueous foams sparged by the Q_{air}s of 0.6, 0.8 and 1.0 L/min are studied. The KPFBS foams in steady state are discussed here. The

processing parameters t_f and Q_{air} were adjusted, so different t_es were obtained. Salt $CaCl_2$ was added to the KPFBS foams, and only two concentrations of $CaCl_2$ were tested to qualitatively compare the effect of high and low concentrations of $CaCl_2$. The effect of $CaCl_2$ on the foaming behavior of KPFBS aqueous foams is studied because the addition of $CaCl_2$ qualitatively improves the foaming capacity of KPFOS regardless of the $CaCl_2$ concentration and enhances the stability of KPFOS foams. However, the steady state of 0.4 mM KPFOS foams with $CaCl_2$ was not achieved by using even the smallest Q_{air}. Therefore, the cases of adding $CaCl_2$ are only discussed for KPFBS in terms of $\frac{H_f}{H_{l0}}$. **Figures 6.11A** to **11F** are the dependency of $\frac{H_f}{H_{l0}}$ on various dimensionless numbers.

In terms of Re_b, Ca, We_b, Fr_b, and ζ_p, the correlations between the $\frac{H_f}{H_{l0}}$ and them for KPFBS are similar to those for KPFOS and PFOA. One can see from **Figure 6.11A**, the $\frac{H_f}{H_{l0}}$ decreases when the effect of inertial force becomes more significant as well as KPFOS and PFOA. However, the data points are to some extent superimposed, and thus, the equation for $\frac{H_f}{H_{l0}}$ as a function of Re_b for KPFBS is $\frac{H_f}{H_{l0}} = (1.31495 - 0.12052Re_b)^{\frac{1}{0.09908}}$ ($R^2 = 0.70942$). Additionally, the introduction of $CaCl_2$ does not remarkably enhance the foamability of KPFBS. However, higher concentrations of $CaCl_2$, such as 100 mM, tend to weaken the foaming capacity of KPFBS, coinciding with increasing the Re_b.

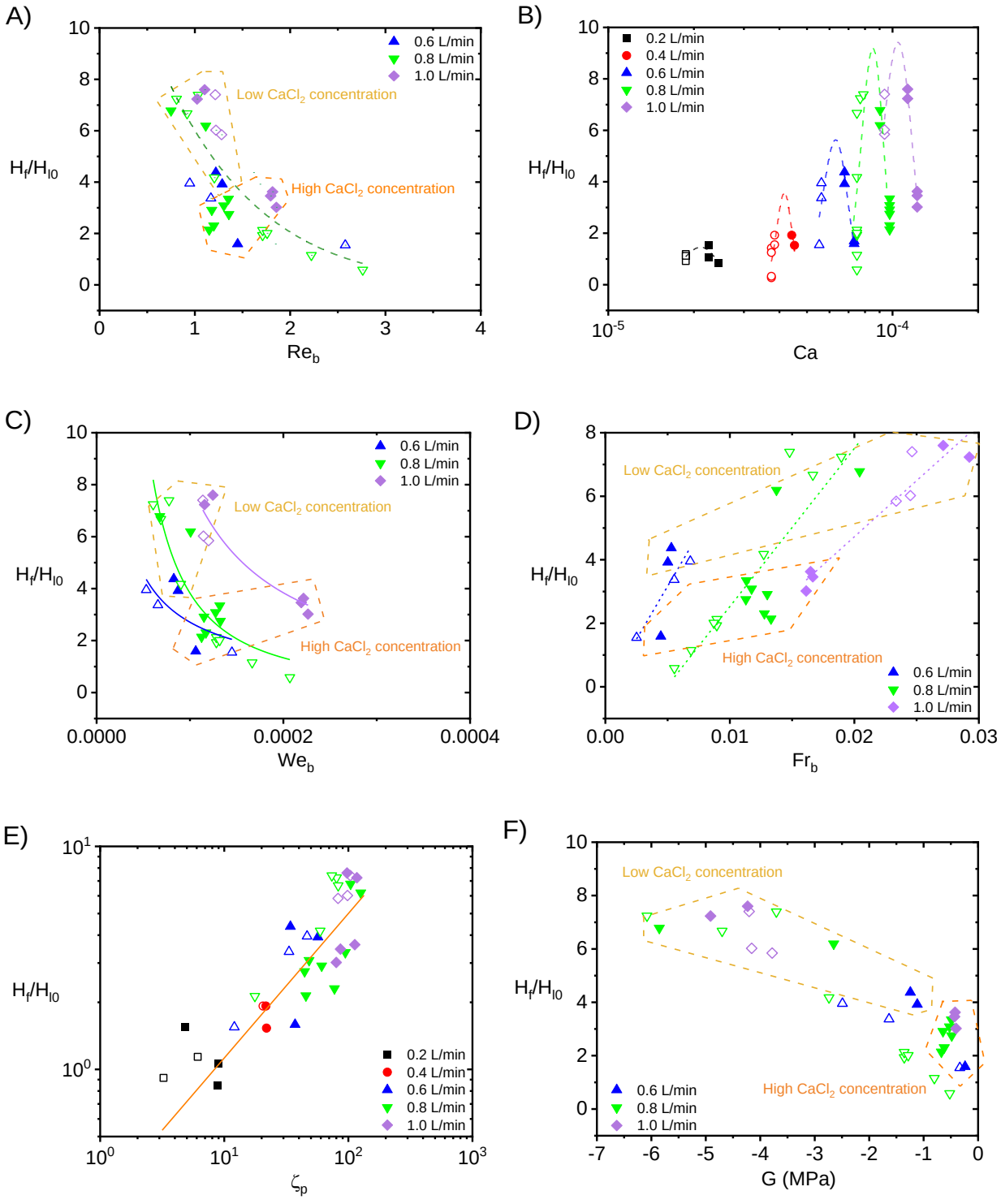

Figure 6.11 Evolution of foam expansion rate for KPFBS aqueous solutions with the A) Reynolds number, B) Capillary number, C) Weber number, D) Froude number, E) processing number, and F) Gibbs stability. The hollow points are the KPFBS foams without adding $CaCl_2$.

In **Figure 6.11B**, 0.2 and 0.4 L/min were also added to determine the relationship between the $\frac{H_f}{H_{l0}}$ and Ca since bubble size is not required. The fitted euqations are shown in **Table D3**. Due to the limited concentrations of either KPFBS or $CaCl_2$, the R^2 is reduced. However, the peaks of $\frac{H_f}{H_{l0}}$ are still appearing. Moreover, the addition of $CaCl_2$ increases the Ca for KPFBS foams, revealing that the viscous force effect becomes more important. The Freundlich model was used to describe the correlation between the $\frac{H_f}{H_{l0}}$ and We_b (**Figure 6.11C**), the equations are shown in **Table D3**. The linear relationships between the $\frac{H_f}{H_{l0}}$ and Fr_b for 0.6, 0.8, and 1.0 L/min are shown in **Table D3** and **Figure 6.11D**. The foaming capacity decreases with increasing the We_b and Fr_b. Furthermore, higher concentration of $CaCl_2$ tend to enhance the We_b and reduce the Fr_b, and at the same time, the foamability is hindered.

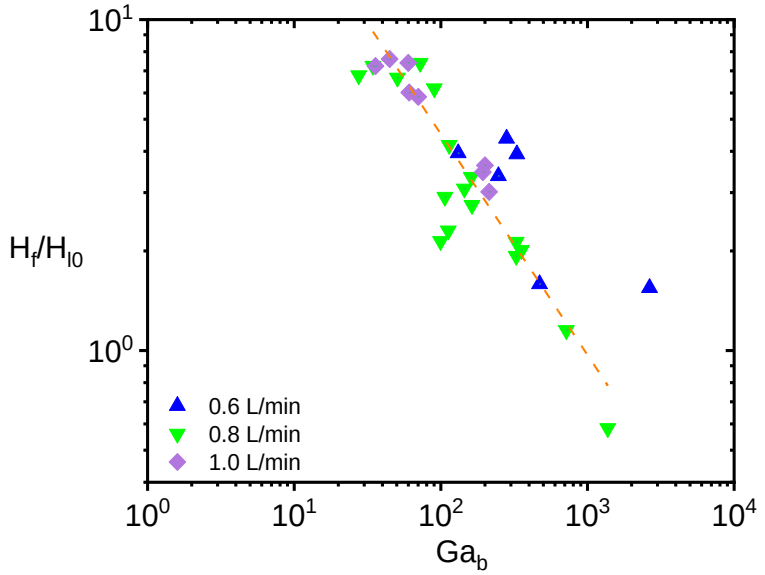

Figure 6.12 Evolution of foam expansion rate for KPFBS aqueous solutions with the Galilei number.

From our previous work (see Chapter 3), 0.4 mM of KPFBS do not have any dilatational interfacial rheological properties, and thus, the E is missing for solely KPFBS foams. Hence, the

dimensionless numbers Bq and Θ are not discussed for KPFBS. No significant influence of adding $CaCl_2$ on ζ_p is observed according to **Figure 6.11E**, although the expansion rate of foaming increases with increasing the ζ_p. **Figure 6.12** shows the dependency of $\frac{H_f}{H_{l0}}$ on the Ga_b. One equation, $\frac{H_f}{H_{l0}} = -0.66788Ga_b - 1.99023$, can be used to describe the function of $\frac{H_f}{H_{l0}}$ versus Ga_b due to the superimposed data points. Considering the G, in general the KPFBS foamability decreases with an increase of G. In addition, adding $CaCl_2$ does not dramatically enhance or decrease the G as shown in **Figure 6.11F**. Nonetheless, only considering the KPFBS foams with $CaCl_2$, higher $CaCl_2$ concentrations (100 mM) qualitatively make the systems approach the Gibbs stability criterion, and the same as KPFOS and PFOA, the $\frac{H_f}{H_{l0}}$ is reduced as reaching the Gibbs stability criterion.

6.3.4. Prediction of foaming expansion rate

The concentration of PFAS aqueous solutions is far below than their CMC, therefore, ρ and η were taken as the values of pure water, remaining constants. In addition, D_c and H_{l0} were also taken as the constants as well as D_f, therefore, $\frac{D_c}{H_{l0}}$ and $\frac{D_f}{H_{l0}}$ were kept as constants. Generally, the dimensionless numbers of Re_b, Fr_b, ζ_p, Ga_b, and $\frac{R}{H_{l0}}$ represent the processing parameters, while Ca, We_b, Bq, and Θ indicate the effect of interfacial properties. Consequently, the *Equations (2.17-18)* can be simplified as follows:

$$\frac{H_f}{H_{l0}} = f_6(Re_b, Ca, We_b, Fr_b, Bq, \Theta, \zeta_p, \frac{R}{H_{l0}}) \qquad \textit{Equation (6.6)}$$

$$\frac{H_f}{H_{l0}} = f_7(Ca, We_b, Ga_b, Bq, \Theta, \zeta_p, \frac{R}{H_{l0}}) \qquad \textit{Equation (6.7)}$$

The *Equations (6.6-6.7)* can be written, for example, as the monomial form as shown below:

$$\frac{H_f}{H_{l0}} = Const * Re_b^a * e^{(b1*Ca^2+b2*Ca)} * We_b^c * Fr_b^d * Bq^e * e^{(f1*\Theta^2+f2*\Theta)} * \zeta_p^g * (\frac{R}{H_{l0}})^h$$

Equation (6.8)

where $const$, a, $b1$, $b2$, c, d, e, $f1$, $f2$, g, and h are constants. The data were fitted to obtain the constants. **Table D4** was used to fit the *Equation (6.8)* and identify the proper coefficients for KPFOS solutions. The fitted values for *Equation (6.8)* are in a good agreement with the experimental values as shown in **Figure 6.13**, obtaining:

$$\frac{H_f}{H_{l0}} = 1587.63 * Re_b^{-1.72} * e^{(-9.00\times10^7*Ca^2+2.00\times10^4*Ca)} * We_b^{-0.44} * Fr_b^{1.02} * Bq^{0.72} *$$

$$e^{(0.097*\Theta^2-1.07*\Theta)} * \zeta_p^{0.45} * (\frac{R}{H_{l0}})^{2.85}$$ *Equation (6.9)*

with a R^2 of 0.86605, suggesting that the experimental values are well fitted with the model.

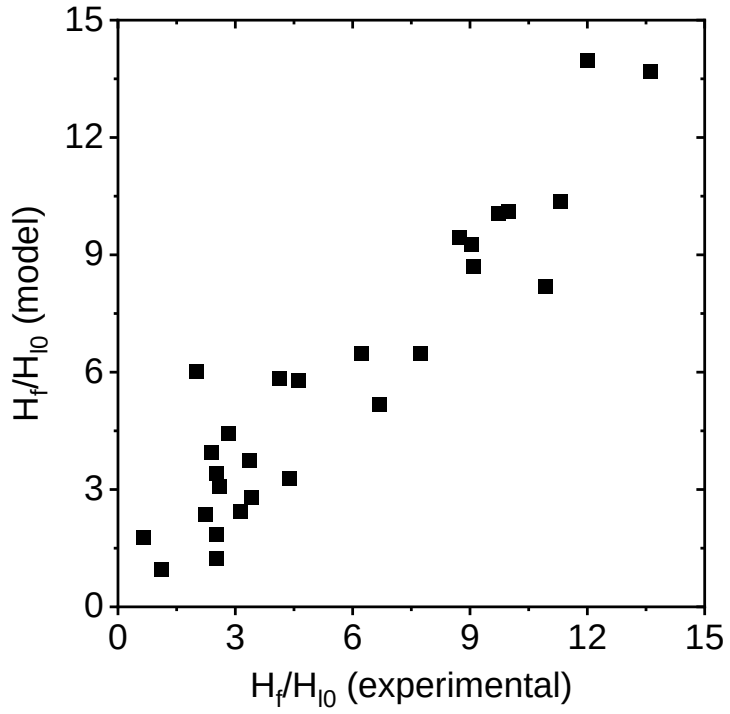

Figure 6.13 Predicted expansion rate of foaming for KPFOS aqueous solutions by using *Equation (6.9)*, compared to the experimental expansion rate of foaming for KPFOS aqueous solutions.

One should notice that the relatively larger power coefficients of Re_b and $\frac{R}{H_{l0}}$ in *Equation (6.9)*, suggesting the huge influence of these two dimensionless numbers on the expansion rate of foaming for KPFOS solutions in the studied experimental regime. The Q_{air} and R have the major effects on the expansion rate of KPFOS foams, and both Q_{air} and R influence the Re_b. Additionally, the dimensionless numbers We_b and Fr_b also contain Q_{air} and R, and higher coefficients for Re_b and Fr_b suggest that the inertial force effect is significant for KPFOS foamability. Moreover, comparing We_b and Bq, higher coefficient for Bq suggests that the interfacial viscosity affects the KPFOS foamability much more than expected. The marks in **Table 6.2** indicate whether the dimensionless number contributes to the foaming behavior. Given the range of dimensionless numbers according to **Figure 6.6**, it is allowed to further estimate the influence of each number on the KPFOS foamability. For example, the Re_b ranges from 0.2 to 2.2, giving the $Re_b^{-1.85}$ range between 0.23 and 19.64. If it is close to 1, it suggests the negligible effect. The numbers (significance) in **Table 6.2** rank the effect of each dimensionless number.

Considering the Ga_b, the monomial form of *Equation (6.7)* is shown as *Equation (6.10)*, and **Figure D1** shows the model values are in a good agreement with the experimental values. The lower coefficient of Ga_b in *Equation (6.10)* indicates the importance of inertial force (Q_{air}) since the inertial force effect is removed by replacing Re_b and Fr_b with Ga_b. Again, the coefficient of $\frac{R}{H_{l0}}$ in *Equation (6.10)* is still 2.85.

$$\frac{H_f}{H_{l0}} = 3229.23 * e^{\left(-1.00\times10^{7}*Ca^{2}+2.00\times10^{4}*Ca\right)} * We_b^{-0.32} * Ga_b^{-0.95} * Bq^{0.72} * e^{\left(0.098*\Theta^{2}-1.07*\Theta\right)} * \zeta_p^{0.45} * \left(\frac{R}{H_{l0}}\right)^{2.85} \quad \textit{Equation (6.10)}$$

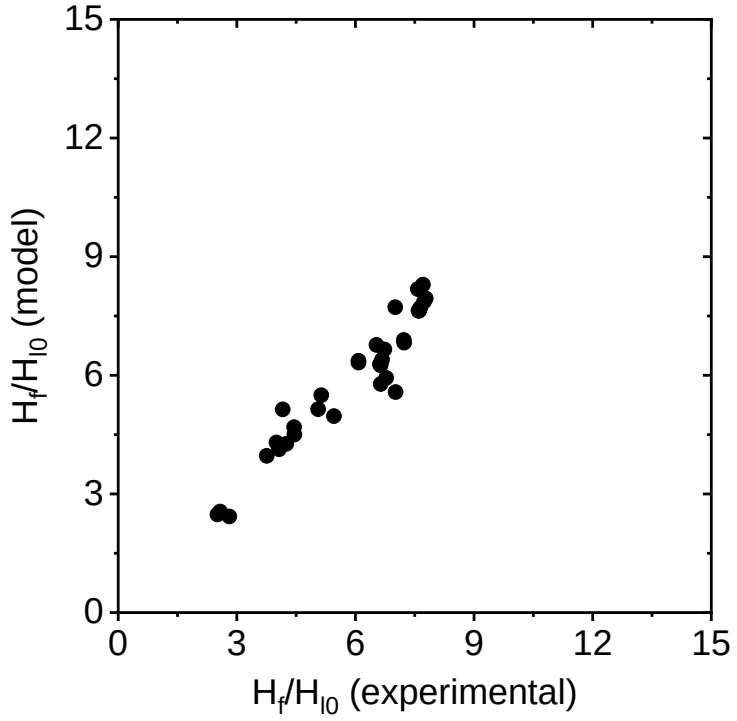

Figure 6.14 Predicted expansion rate of foaming for PFOA aqueous solutions by using *Equation (6.11)*, compared to the experimental expansion rate of foaming for PFOA aqueous solutions.

For PFOA, as shown in **Figure 6.14**, the R^2 of the fit ($R^2 = 0.96797$) to *Equation (6.8)* based on **Table D5** implies good agreement between the model values and experimental values of $\frac{H_f}{H_{l0}}$, obtaining:

$$\frac{H_f}{H_{l0}} = 3.06 * e^{(-1.00\times10^8 * Ca^2 + 1.00\times10^4 * Ca)} * Fr_b^{0.41} * Bq^{0.38} * \Theta^{0.26} * \zeta_p^{0.16} * (\frac{R}{H_{l0}})^{0.42}$$

Equation (6.11)

The coefficients of Re_b and We_b are small and can be estimated as zero without affecting the R^2 of the fit. *Equation (6.12)* is the monomial form of *Equation (6.7)* for PFOA after fitting, and the comparison of predicted values to experimental values is shown in **Figure D2**. The greater coefficients of Fr_b and $\frac{R}{H_{l0}}$ in *Equation (6.11)* reveal that the foamability of PFOA in the presence

of NaCl highly depends on the Q_{air} and R. **Table 6.2** shows that the addition of NaCl improves the foamability of PFOA through affecting the interfacial properties, representing by Bq. In *Equation (6.12)*, the effects of R and Bq on the PFOA foamability in the presence of NaCl becomes dominated.

$$\frac{H_f}{H_{lo}} = 1.12 * e^{(-9.00\times10^6*Ca^2+1.00\times10^4*Ca)} * Ga_b^{-0.18} * Bq^{0.31} * \zeta_p^{0.23} * (\frac{R}{H_{lo}})^{0.38}$$

Equation (6.12)

Figure 6.15 shows the prediction of expansion rate of foaming for KPFBS solutions with a R^2 of 0.73937 for *Equation (6.13)*. The monomial equation based on *Equation (6.6)* is showing below:

$$\frac{H_f}{H_{lo}} = 12.30 * e^{(-4.00\times10^7*Ca^2)} * Fr_b^{0.51} * \zeta_p^{0.37}$$ *Equation (6.13)*

The case of KPFBS is simple, and the foamability only depends on three dimensionless numbers of Ca, Fr_b, and ζ_p. The dependency of bubble size in this study for KPFBS is not significant. If replacing Fr_b by Ga_b, as seen in **Figure D3**, the foaming behavior prediction is also good. The related monomial equation is *Equation (6.14)*.

$$\frac{H_f}{H_{lo}} = 2.50 * e^{(-4.00\times10^7*Ca^2)} * Ga_b^{-0.3} * \zeta_p^{0.55}$$ *Equation (6.14)*

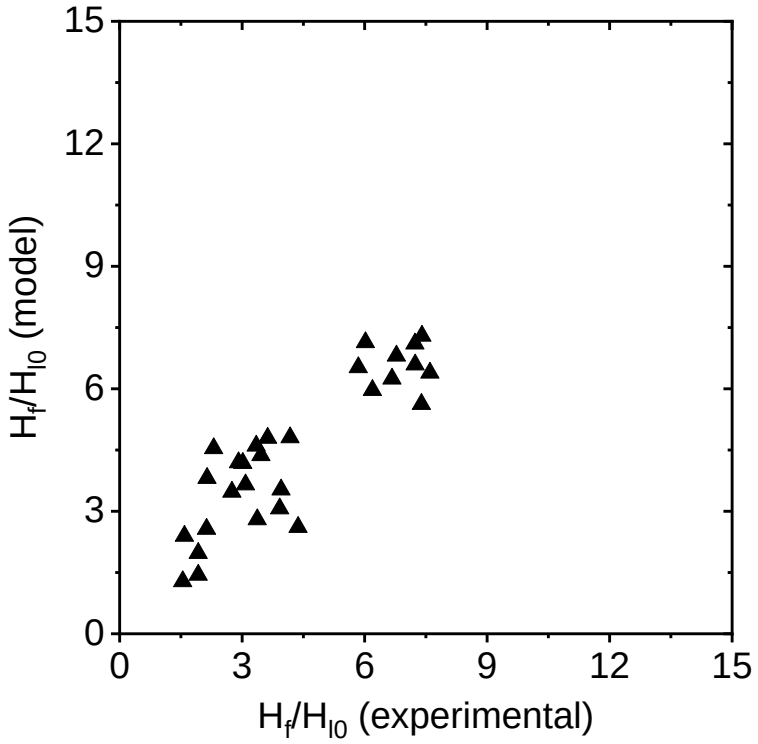

Figure 6.15 Predicted expansion rate of foaming for KPFBS aqueous solutions by using *Equation (6.13)* compared to the experimental expansion rate of foaming for KPFBS aqueous solutions.

Table 6.2 Correlation between the PFAS foaming behavior and dimensionless numbers.

KPFOS aqueous foams						
	Foaming expansion rate	Significance	Foaming kinetics	Significance	Liquid content	Significance
Re_b	✓	5	✓	5	✓	4
Ca	✓	6	✓	**1**	✓	**1**
We_b	✓	**3**	✓	**3**	✓	**2**
Fr_b	✓	**2**	✓	**2**	✓	**3**
Bq	✓	**1**	✓	4	✕	-
Θ	✓	4	✓	6	✕	-
ζ_p	✓	7	✓	7	✓	5
$\frac{R}{H_{l0}}$	✓	-	✓	-	✓	-
PFOA aqueous foams						
	Foaming expansion rate	Significance	Foaming kinetics	Significance	Liquid content	Significance
Re_b	✕	-	✓	4	✕	-

Ca	✓	5	✓	5	✓	**1**
We_b	✗	-	✓	**2**	✓	**3**
Fr_b	✓	**1**	✓	**3**	✓	**2**
Bq	✓	**2**	✓	**1**	✓	4
Θ	✓	4	✗	-	✓	5
ζ_p	✓	**3**	✗	-	✗	-
$\frac{R}{H_{l0}}$	✓	-	✓	-	✓	-
KPFBS aqueous foams						
	Foaming expansion rate		Foaming kinetics		Liquid content	
Re_b	✗		✗		✗	
Ca	✓		✗		✗	
We_b	✗		✗		✗	
Fr_b	✓		✗		✓	
Bq	✗		✗		✗	
Θ	✗		✗		✗	
ζ_p	✓		✗		✓	
$\frac{R}{H_{l0}}$	✗		✗		✗	

6.4. Dimensional analysis of foaming kinetics

As shown in **Figure 6.1A**, $\dot{H}_f = \frac{dH_f}{dt}$ can be used to study the kinetics of foaming before the steady state. Similar to the dimensional analysis for expansion rate of foaming (see Chapter 2), the *Equations (6.15-16)* below are used to study the kinetics of foaming for different PFAS. Because of unstable bubble size during the unsteady state, the R involved in this Subchapter is still the Sauter mean radius of bubbles in the steady state. Again, only 40-100 μm as the D_f is considered in the dimensional analysis for $\dot{H}_f$. $\frac{D_c^2 * \dot{H}_f}{Q_{air}}$ is used instead of $\dot{H}_f$ for nondimensionalization.

$$\frac{D_c^2 * \dot{H}_f}{Q_{air}} = f_1(Re_b, Ca, We_b, Fr_b, Bq, \Theta, \zeta_p, \frac{R}{H_{l0}}) \qquad \textit{Equation (6.15)}$$

$$\frac{D_c^2 * \dot{H}_f}{Q_{air}} = f_2(Ca, We_b, Ga_b, Bq, \Theta, \zeta_p, \frac{R}{H_{l0}}) \qquad \textit{Equation (6.16)}$$

6.4.1. KPFOS solutions

Figure 6.16 presents the correlations between $\frac{D_c^2 * \dot{H}_f}{Q_{air}}$ and various dimensionless numbers, respectively, for KPFOS aqueous solutions. It should be mentioned that the cases of adding NaCl and $CaCl_2$ are considered for discussing the dependency of $\frac{D_c^2 * \dot{H}_f}{Q_{air}}$ on the Ca and Θ since the R is not required for calculating Ca and Θ. Similar to $\frac{H_f}{H_{l0}}$ of KPFOS, the $\frac{D_c^2 * \dot{H}_f}{Q_{air}}$ of KPFOS correlates with Re_b, We_b, Fr_b, Bq and ζ_p as well. The foaming speed becomes faster as the Re_b and We_b decrease, seen in **Figures 6.16A** and **6.16C**. On the other hand, the foaming kinetics is slower with a decrease in Fr_b, Bq, and ζ_p as seen in **Figures 6.16D** to **6.16F**. Therefore, if the Q_{air} remains the same, in order to obtain the higher foaming kinetics, the inertial force is dominated compared to gravitational force. However, the effects of viscous force and interfacial force on the foaming kinetics become more dominated compared to inertial force. In addition, the $\frac{D_c^2 * \dot{H}_f}{Q_{air}}$ depends more on μ_s compared to $\frac{H_f}{H_{l0}}$ since the data points are more superimposed as seen in **Figure 6.16E**, saying higher μ_s, faster foaming.

Considering Ca and Θ, as seen in **Figures 6.16B** and **6.16G**, the situations become complicated. Without adding salts, as increasing the KPFOS bulk concentration, the Ca increases, in turn, the foaming kinetics increases until the peak of $\frac{D_c^2 * \dot{H}_f}{Q_{air}}$. The appearance of $\frac{D_c^2 * \dot{H}_f}{Q_{air}}$ peaks for three Q_{air}s is also coinciding with the appearance of peak of E. Once approached the peak, the foaming kinetics decreases with increasing Ca as well as the bulk concentration. Moreover, if keeping the bulk concentration same (0.4 mM, at which the E peak appears), the addition of salts

increases both Ca and $\frac{D_c^2 * \dot{H}_f}{Q_{air}}$, as seen in the crossed and dotted areas in **Figure 6.16B**, and the effect of divalent salts, $CaCl_2$, on increasing Ca and $\frac{D_c^2 * \dot{H}_f}{Q_{air}}$ is more effective, as comparing black dotted area ($CaCl_2$) to black crossed area (NaCl). For Θ, similar to **Figure 6.6G**, the $\frac{D_c^2 * \dot{H}_f}{Q_{air}}$ decreases with increasing the Θ for the cases without adding salts. When adding salts, the $\frac{D_c^2 * \dot{H}_f}{Q_{air}}$ is generally enhanced, and thus, two regimes are shown in **Figure 6.16G**. Additionally, **Figure 6.17** shows the dependency of foaming speed on the Ga_b. The $\frac{D_c^2 * \dot{H}_f}{Q_{air}}$ slightly decreases with increasing the Ga_b. However, the $\frac{D_c^2 * \dot{H}_f}{Q_{air}}$ is less dependent on G compared to the dependency of $\frac{H_f}{H_{l0}}$ on G. One can see from **Figure 6.16H**, the foaming kinetics only depends on G when using 0.6 L/min.

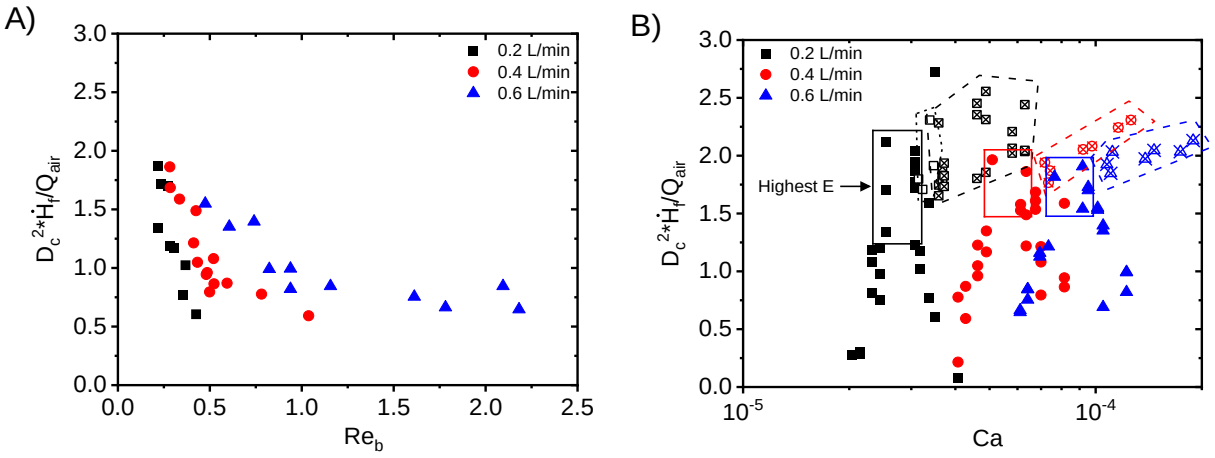

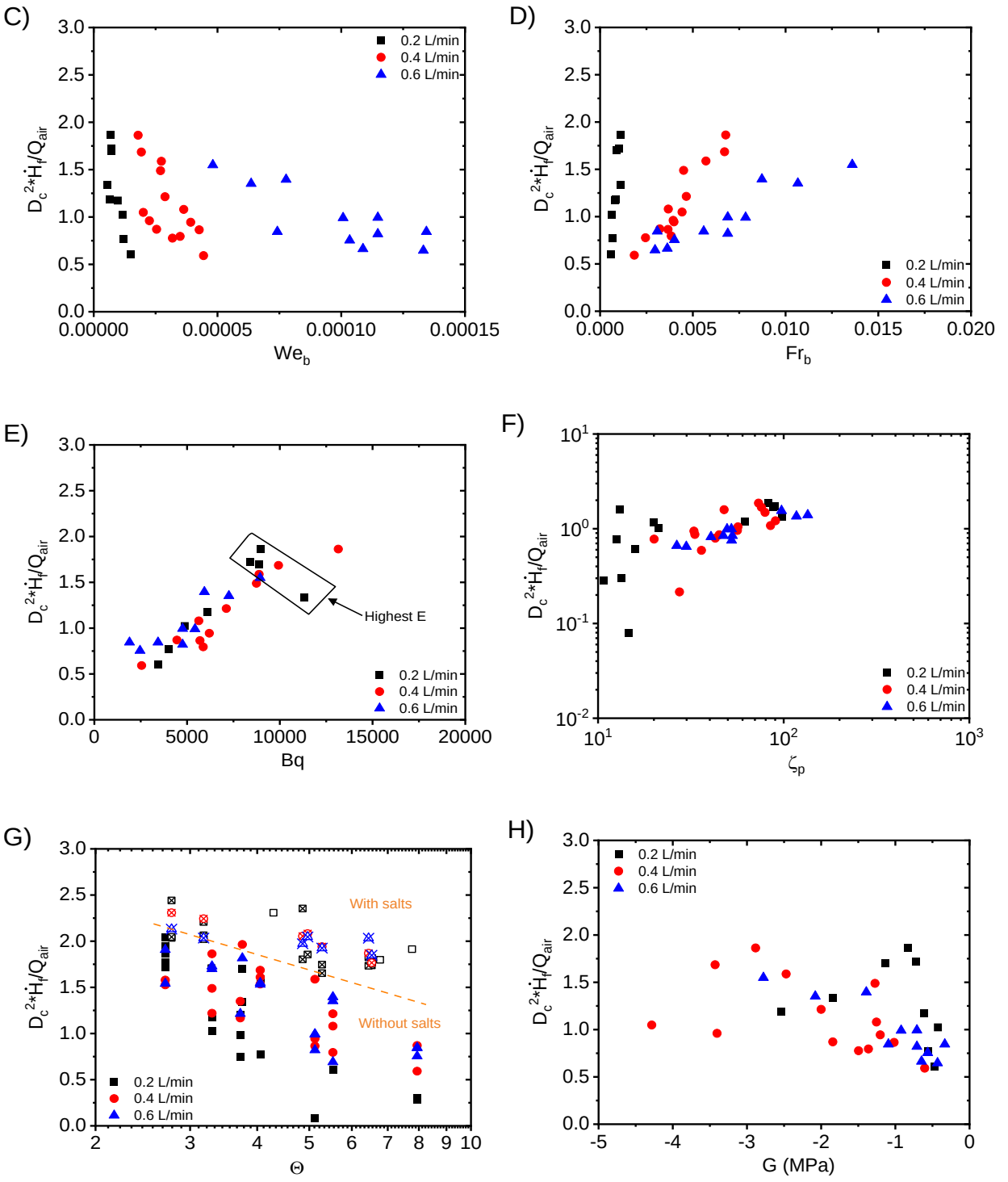

Figure 6.16 Change of foaming kinetics for various concentration KPFOS aqueous solutions with changing A) Reynolds number, C) Weber number, D) Froude number, E) Boussinesq number, F) processing number, and H) Gibbs stability. Foaming kinetics of KPFOS aqueous solutions in the absence and presence of salts as a function of B) Capillary number, and G) interface number. The hollow points are the KPFOS foams containing NaCl, and the hollow points with a cross are the KPFOS foams containing $CaCl_2$.

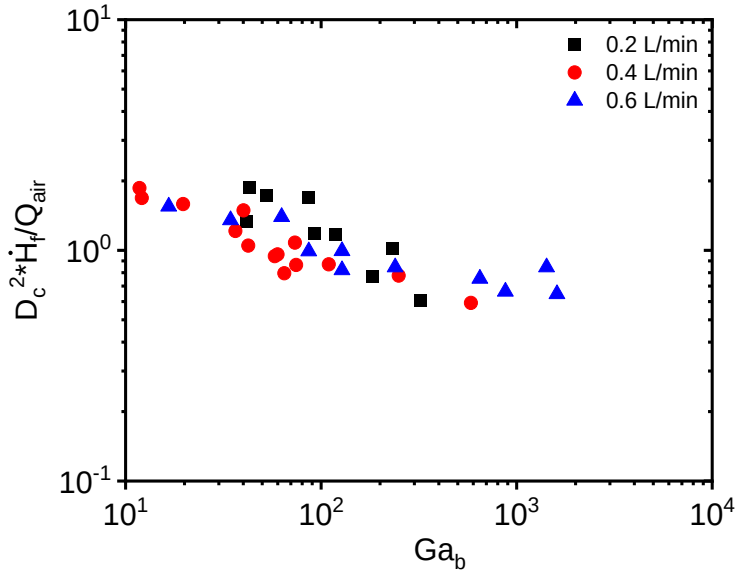

Figure 6.17 Kinetics of foaming for KPFOS aqueous foams with the Galilei number.

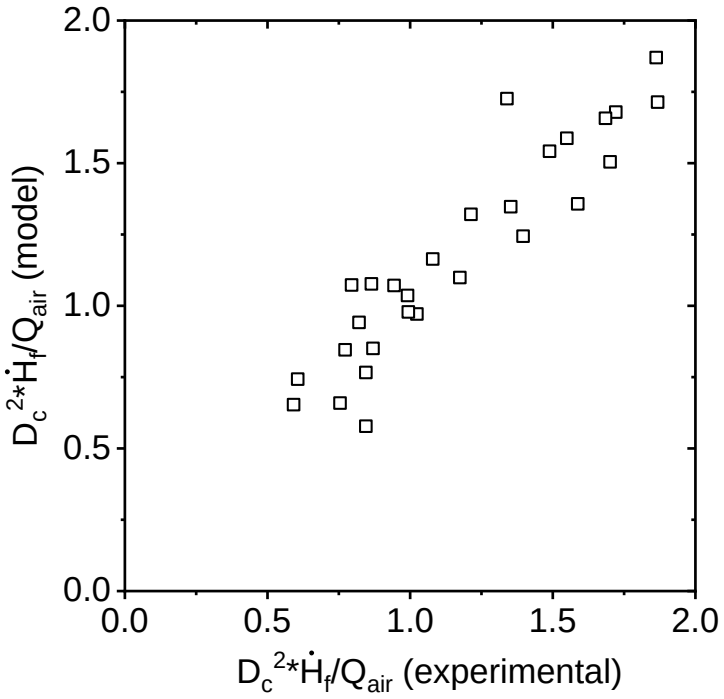

Figure 6.18 Predicted kinetics of foaming for KPFOS aqueous foams by using *Equation (6.17)*, compared to the experimental kinetics of foaming for KPFOS aqueous foams.

The fitting for the monomial form of *Equation (6.15)* is carried out, obtaining *Equation (6.17)* shown below.

$$\frac{D_c^2 * \dot{H}_f}{Q_{air}} = 37797.57 * Re_b^{-1.13} * Ca^{0.5} * We_b^{-0.52} * Fr_b^{0.8} * Bq^{0.25} * \Theta^{-0.25} * \zeta_p^{0.15} * (\frac{R}{H_{l0}})^{2.2}$$

Equation (6.17)

Figure 6.18 ($R^2 = 0.90685$) appears good agreement between the predicted values of $\frac{D_c^2 * \dot{H}_f}{Q_{air}}$ obtained from *Equation (6.17)* and the experimental values of $\frac{D_c^2 * \dot{H}_f}{Q_{air}}$. Considering both salt effect and KPFOS bulk concentration effect, power law is used for Ca to qualitatively determining the influence of Ca on the $\frac{D_c^2 * \dot{H}_f}{Q_{air}}$. The higher power coefficients of Re_b and $\frac{R}{H_{l0}}$ imply the large influence of these two dimensionless numbers on the KPFOS foaming speed I the studied regime. Additionally, the smaller coefficient of ζ_p suggests that the t_e has slight effect on the foaming kinetics for KPFOS aqueous solutions. Considering the range of dimensionless numbers, **Table 6.2** indicates that Ca, Fr_b, and We_b significantly contribute to the foaming speed of KPFOS. If replacing Re_b and Fr_b by Ga_b, **Figure D4** shows the agreement between the between the predicted values and the experimental values according to *Equation (6.18)*, where the $\frac{D_c^2 * \dot{H}_f}{Q_{air}}$ is still highly correlated with the $\frac{R}{H_{l0}}$.

$$\frac{D_c^2 * \dot{H}_f}{Q_{air}} = 221904 * Ca^{0.6} * We_b^{-0.38} * Ga_b^{-0.69} * Bq^{0.2} * \Theta^{-0.25} * \zeta_p^{0.22} * (\frac{R}{H_{l0}})^{2.2}$$

Equation (6.18)

6.4.2. PFOA solutions

Interestingly, the correlation between $\frac{D_c^2 * \dot{H}_f}{Q_{air}}$ and various dimensionless numbers for PFOA solutions with and without NaCl seems to be less correlated. As seen in **Figure 6.19B**, the $\frac{D_c^2 * \dot{H}_f}{Q_{air}}$

is only highly dependent on the Ca. The open points in **Figure 6.19B** represent the ones without NaCl. Differ from $\frac{H_f}{H_{l0}}$, the foaming kinetics is not improved upon adding NaCl. **Figure 6.19E** indicates that the foaming kinetics of PFOA solutions containing NaCl is slightly dependent on the Bq, with the $\frac{D_c^2 * \dot{H}_f}{Q_{air}}$ slightly increasing with increasing the Bq (green arrow shows the trend). Furthermore, increasing NaCl concentration increases the Θ until reaching 10 mM, which are the crossed points shown in **Figure 6.19F**. However, the Θ has no significant effect on PFOA foaming kinetics in studied regime. Additionally, the dependency of foaming speed on the G is not noteworthy, even though the G is reduced upon adding NaCl as seen in **Figure 6.19H**. The Ga_b also has no impact on the PFOA foaming kinetics (**Figure 6.20**).

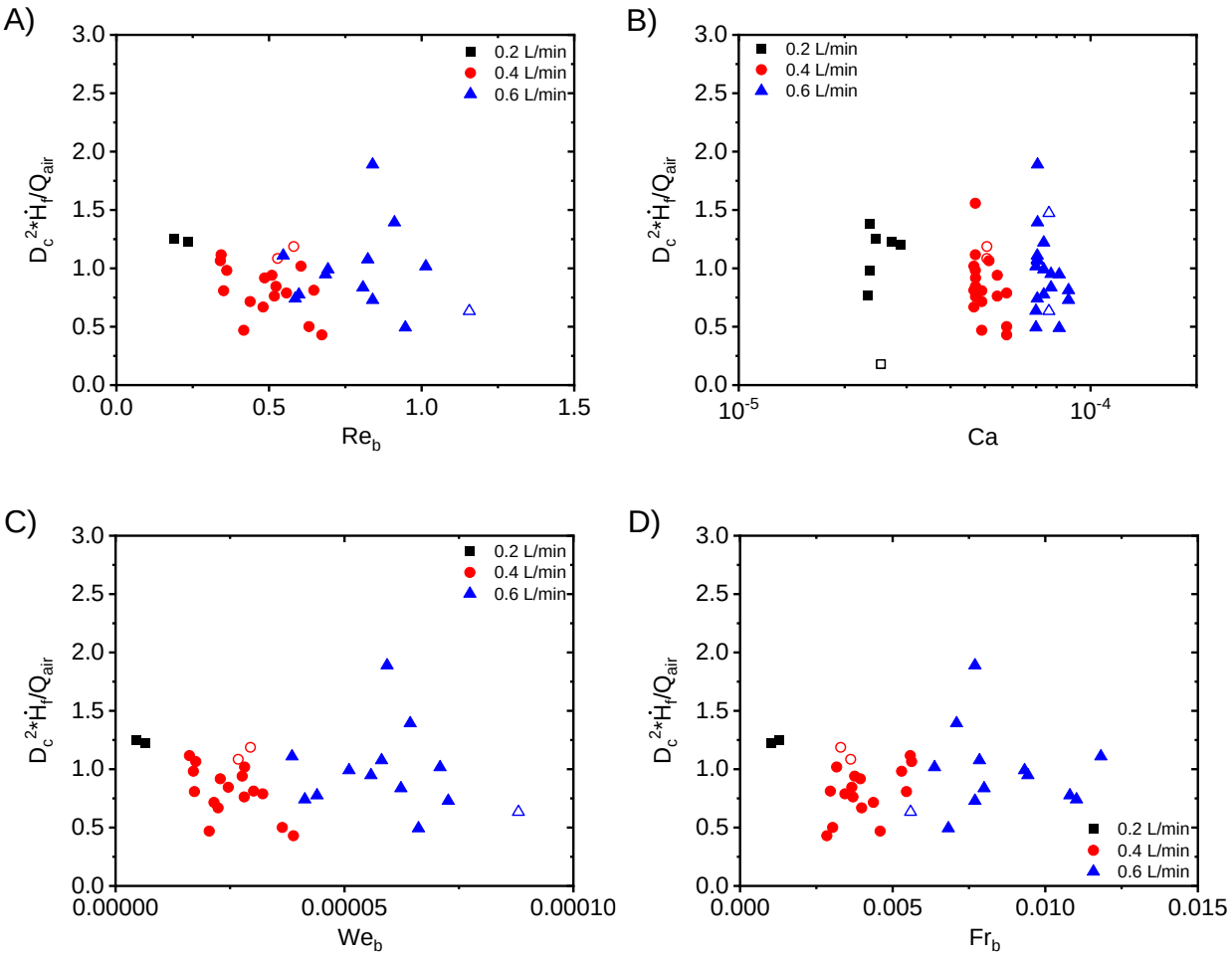

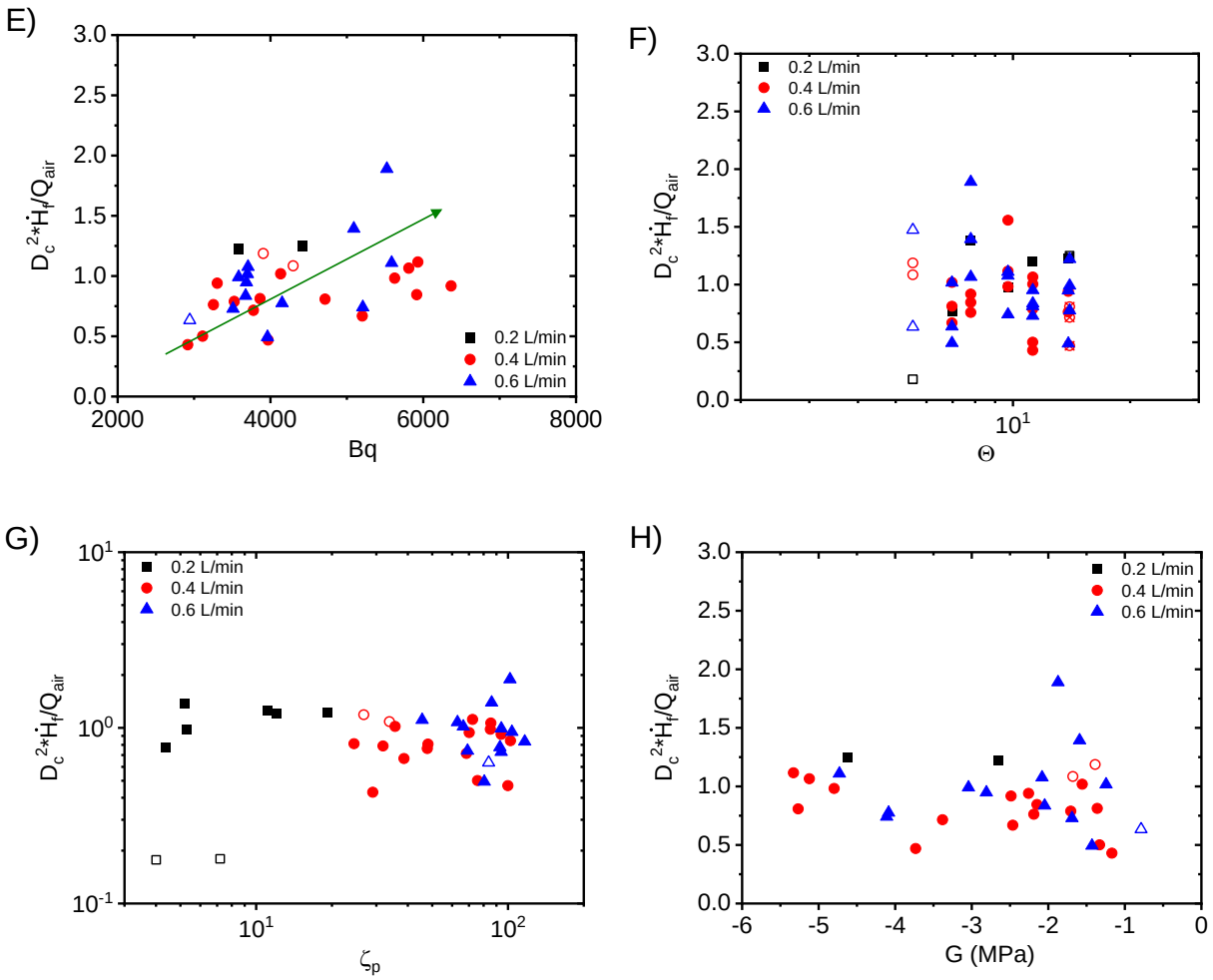

Figure 6.19 Change of foaming kinetics for PFOA aqueous solutions containing NaCl with changing A) Reynolds number, B) Capillary number, C) Weber number, D) Froude number, E) Boussinesq number, F) processing number, G) interface number, and H) Gibbs stability. The hollow points are the foams solely containing PFOA.

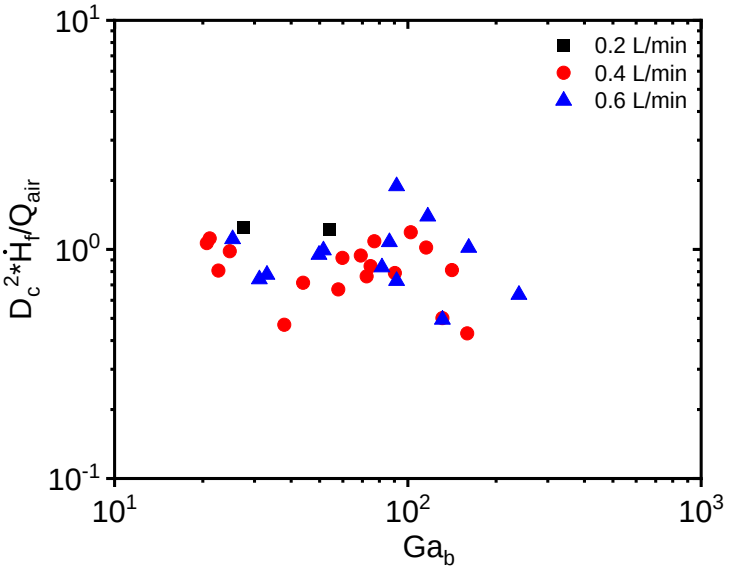

Figure 6.20 Kinetics of foaming for PFOA aqueous foams with the Galilei number.

After simplification, *Equation (6.19)* below is obtained for predicting the foaming kinetics of PFOA aqueous solutions with and without NaCl.

$$\frac{D_c^2*\dot{H}_f}{Q_{air}} = 1.63 * Re_b^{-1} * e^{(1.00\times10^8*Ca^2+3.00\times10^3*Ca)} * We_b^{-0.52} * Fr_b^{0.63} * Bq^{0.85} * (\frac{R}{H_{l0}})^{2.45}$$

Equation (6.19)

The influences of Re_b and $\frac{R}{H_{l0}}$ on the $\frac{D_c^2*\dot{H}_f}{Q_{air}}$ are significant due to the relatively greater power coefficients. In addition, for PFOA systems investigated in this study, the effect of Bq on the $\frac{D_c^2*\dot{H}_f}{Q_{air}}$ is high, implying that the foaming speed of PFOA foams containing various levels of NaCl is higher linked to the μ_s. **Table 6.2** also suggests that the PFOA foamability is remarkably affected by the μ_s upon adding the NaCl. Nevertheless, the fitting shown in **Figure 6.21** is scattering (0.44028 is the R^2). If using Ga_b, as shown in *Equation (6.20)*, the dominated dimensionless numbers are Bq and $\frac{R}{H_{l0}}$. However, the predictions are still scattering as seen in **Figure D5**.

$$\frac{D_c^2 * \dot{H}_f}{Q_{air}} = 8.50 * e^{(1.00\times10^8 * Ca^2 + 3.00\times10^4 * Ca)} * We_b^{-1.1} * Ga_b^{-1.1} * Bq^{1.3} * (\frac{R}{H_{l0}})^5$$

Equation (6.20)

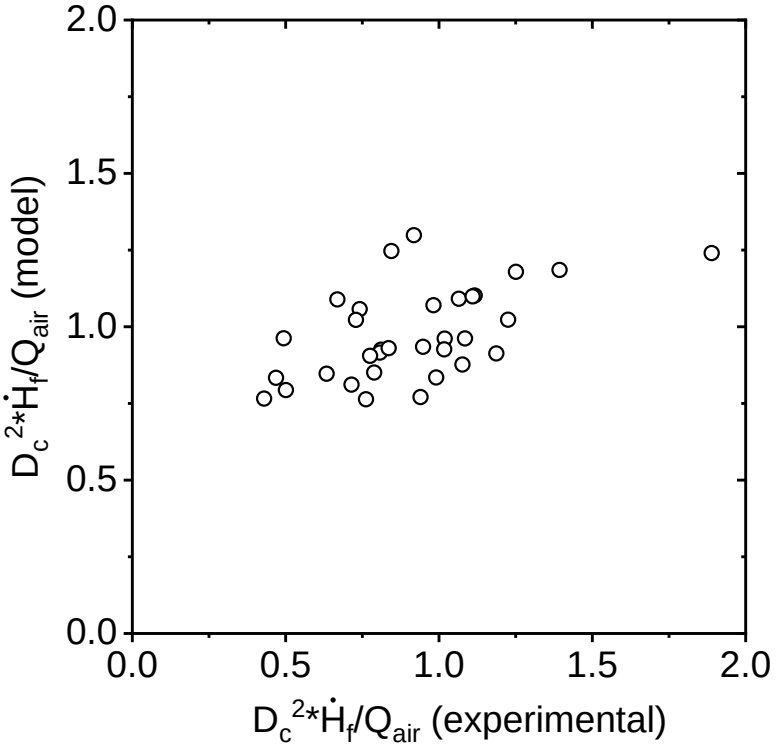

Figure 6.21 Predicted kinetics of foaming for PFOA aqueous foams by using *Equation (6.19)*, compared to the experimental kinetics of foaming for PFOA aqueous foams.

6.4.3. KPFBS solutions

The situation for KPFBS aqueous solutions is much simpler. As seen in **Figures 6.22** and **6.23**, the KPFBS foaming kinetics is not correlated with any studied dimensionless numbers and G. Recalling expansion rate of foaming for KPFBS, see *Equation (6.13)*, the $\frac{H_f}{H_{l0}}$ is at least correlated with Ca, Fr_b, and ζ_p, and the R^2 is around 0.81090 for the prediction. However, the $\frac{D_c^2 * \dot{H}_f}{Q_{air}}$ for KPFBS systems is not dependent on any studied dimensionless numbers and G. The fitting of the monomial form of *Equation (6.15)* is also failed as seen in **Figure 6.24**, the predicted

$\frac{D_c^2 * \dot{H}_f}{Q_{air}}$ remains the same as changing the experimental values. One of the possible reasons for that could be the absence of Θ and Bq, which might play an important role in predicting the foaming kinetics of PFAS foams, as least for KPFBS foams. It might also be due to the weak adsorption activity of KPFBS.

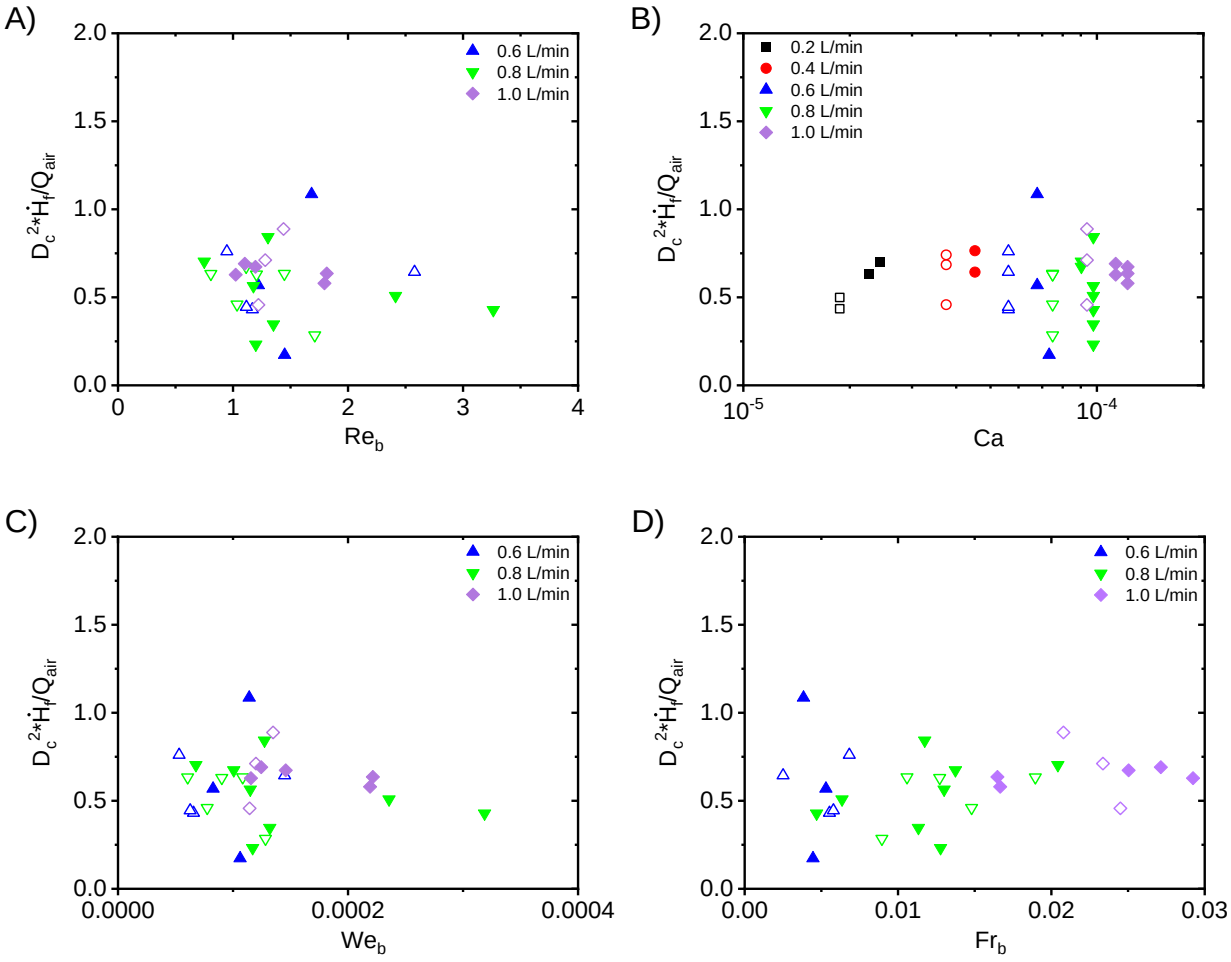

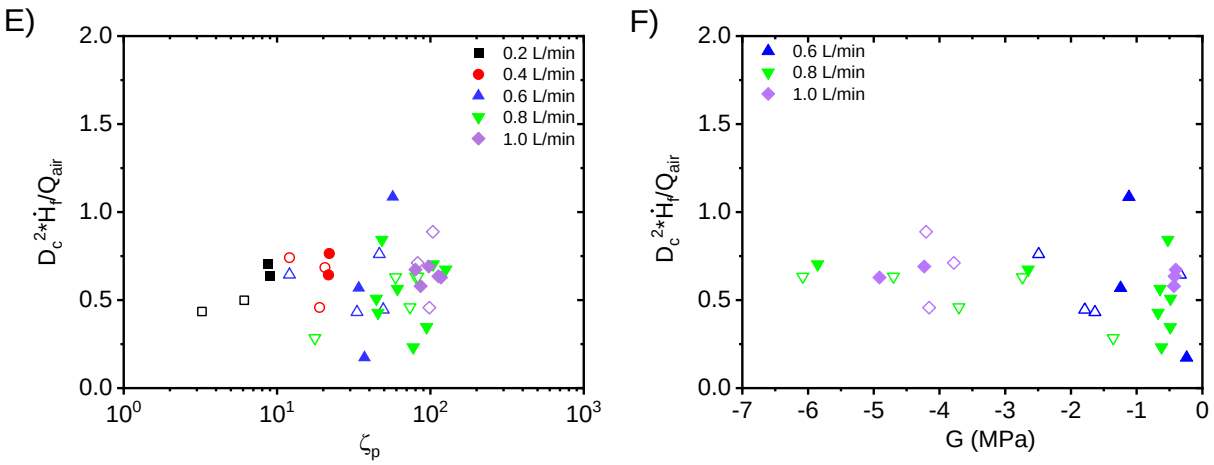

Figure 6.22 Kinetics of foaming for KPFBS aqueous solutions with the A) Reynolds number, B) Capillary number, C) Weber number, D) Froude number, E) processing number, and F) Gibbs stability. The hollow points are the foams solely containing KPFBS.

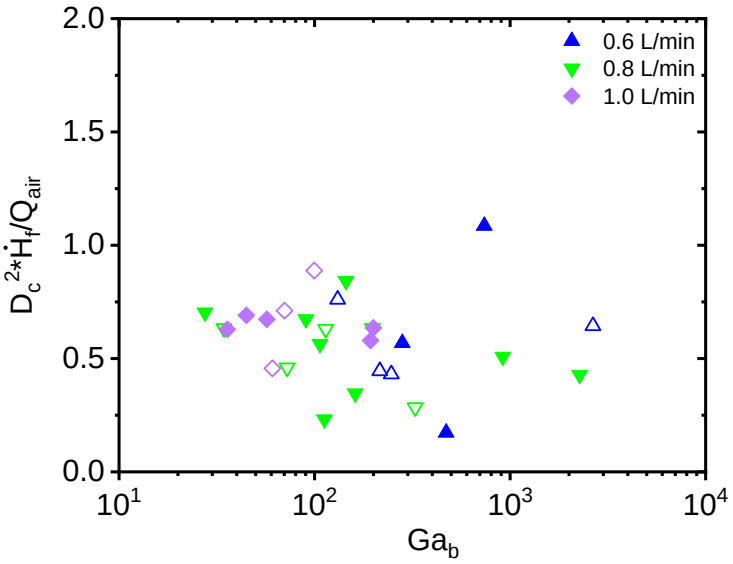

Figure 6.23 Kinetics of foaming for KPFBS aqueous foams with the Galilei number.

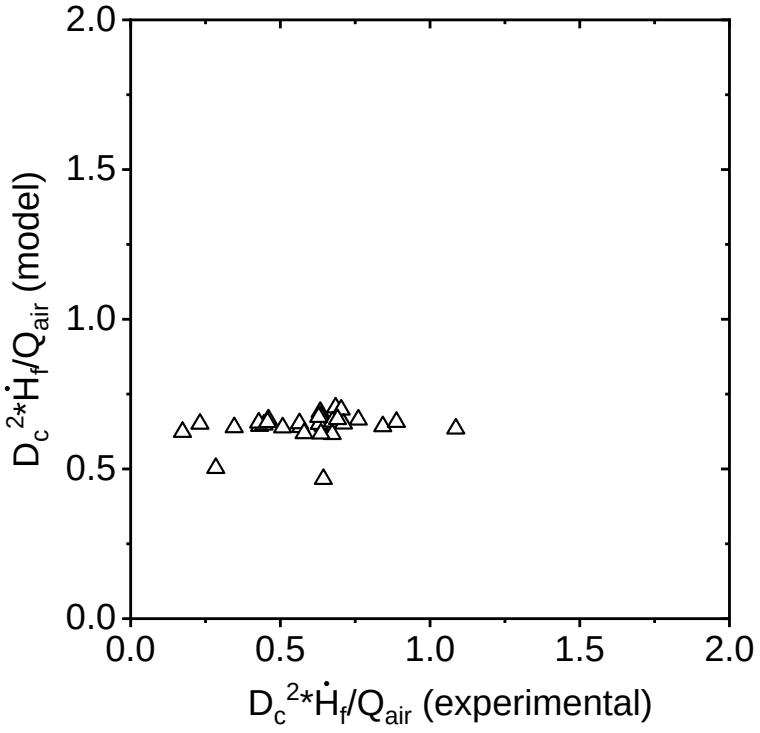

Figure 6.24 Predicted kinetics of foaming for KPFBS aqueous foams based on *Equation (6.16)*, compared to the experimental kinetics of foaming for KPFBS aqueous foams.

6.5. Dimensional analysis of liquid content

The *Equation (6.3)* was used to correct the liquid fraction of PFAS foams as depicted in **Figure 6.1D**. The ε_{co} in the steady state at the bottom part of PFAS foams was used to perform the dimensional analysis according to the *Equations (6.21-22)* shown as follows, using the same method as mentioned in Chapter 2.

$$\varepsilon_{co} = f_1(Re_b, Ca, We_b, Fr_b, Bq, \Theta, \zeta_p, \frac{R}{H_{lo}}) \qquad \textit{Equation (6.21)}$$

$$\varepsilon_{co} = f_2(Ca, We_b, Ga_b, Bq, \Theta, \zeta_p, \frac{R}{H_{lo}}) \qquad \textit{Equation (6.22)}$$

The R used in this Subchapter is the Sauter mean radius of bubbles in the steady state. Again, only 40-100 μm as the D_f is considered in the dimensional analysis for ε_{co}.

6.5.1. KPFOS aqueous foams

Similar to $\frac{H_f}{H_{l0}}$ and $\frac{D_c^2 * \dot{H}_f}{Q_{air}}$, the ε_{co}, identified as ε_{co_1}, at the first sensor chip location for KPFOS aqueous foams is also correlated with several dimensionless numbers as seen in **Figure 6.25**. According to **Figures 6.25A** to **6.25D**, the higher Q_{air}s tend to result in a stronger correlation between the ε_{co_1} and dimensionless numbers of Re_b, Ca, We_b, and Fr_b. For instance, the change of ε_{co_1} over the Re_b is small when using 0.2 L/min, however, the ε_{co_1} is apparently decreasing with increasing the Re_b if using higher Q_{air} of 0.6 L/min. The same trend was observed for We_b and Fr_b. As seen in **Figure 6.25B**, it seems that the ε_{co_1} of KPFOS foams also shows a maximum value when increasing Ca, and the two points at the peak position for the Q_{air} of 0.2 L/min exactly refer to the KPFOS concentrations where the interfacial dilatational modulus is the highest or is near the highest value (see Chapter 3).

Figure 6.25E shows the ε_{co_1} varies with the Bq, and the green arrow indicates the trend which is the water holding capacity of KPFOS foams is increasing with increasing the Bq. Besides the Bq, the positive correlation is also applied to the change of ε_{co_1} as a function of ζ_p (**Figure 6.25F**). For another dimensionless number Θ, characterizing the interfacial properties, the KPFOS foams tend to be drier as the effect of surface tension becomes more significant as seen in **Figure 6.25G**. In addition, the Ga_b influence the ε_{co_1} of KPFOS foams, and the general trend is the ε_{co_1} decreases with an increase in Ga_b (**Figure 6.25H**).

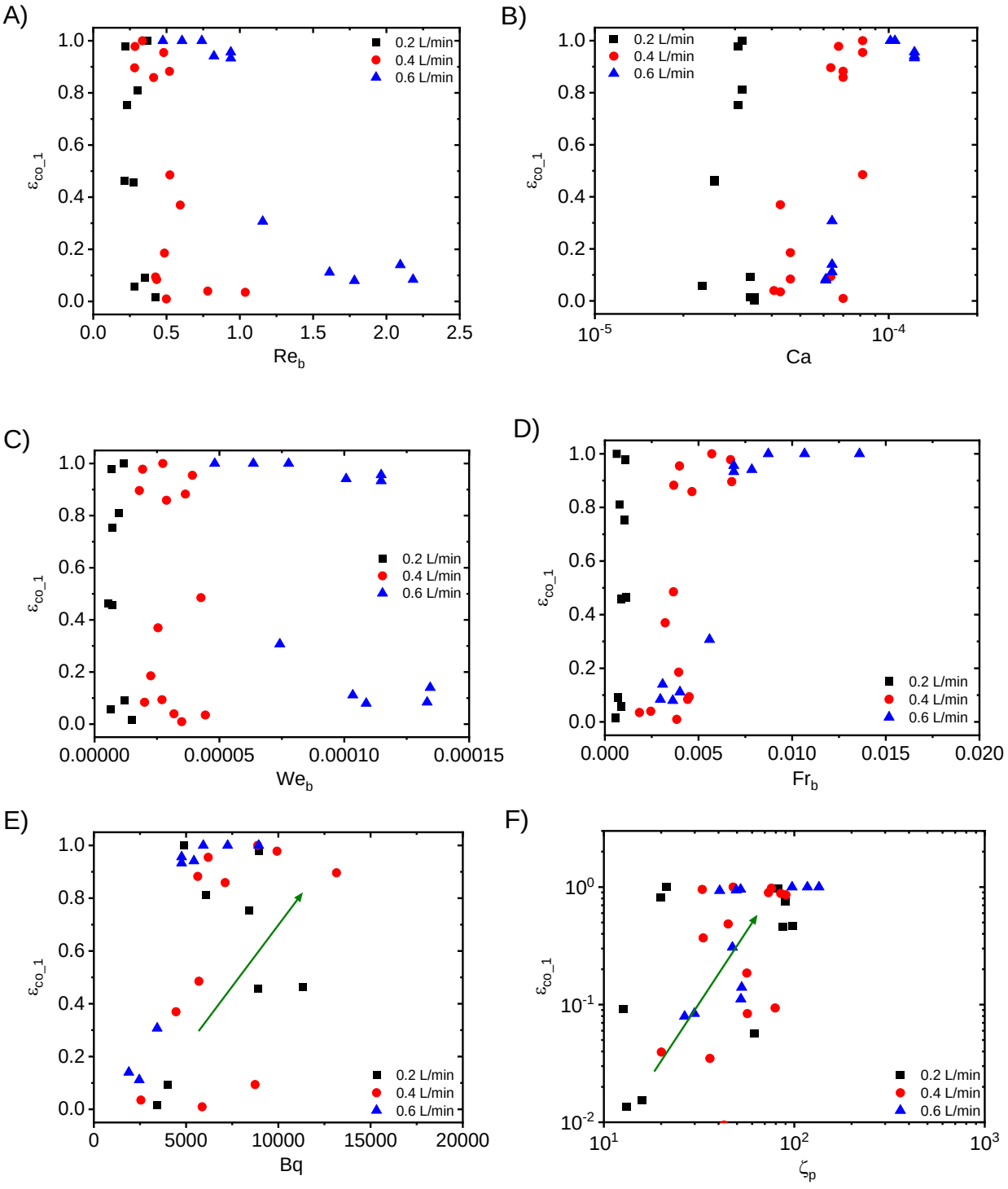
A)
B)
C)
D)
E)
F)
0.2 L/min
0.4 L/min
0.6 L/min
ε_{co_1}
Re_b
Ca
We_b
Fr_b
Bq
ζ_p

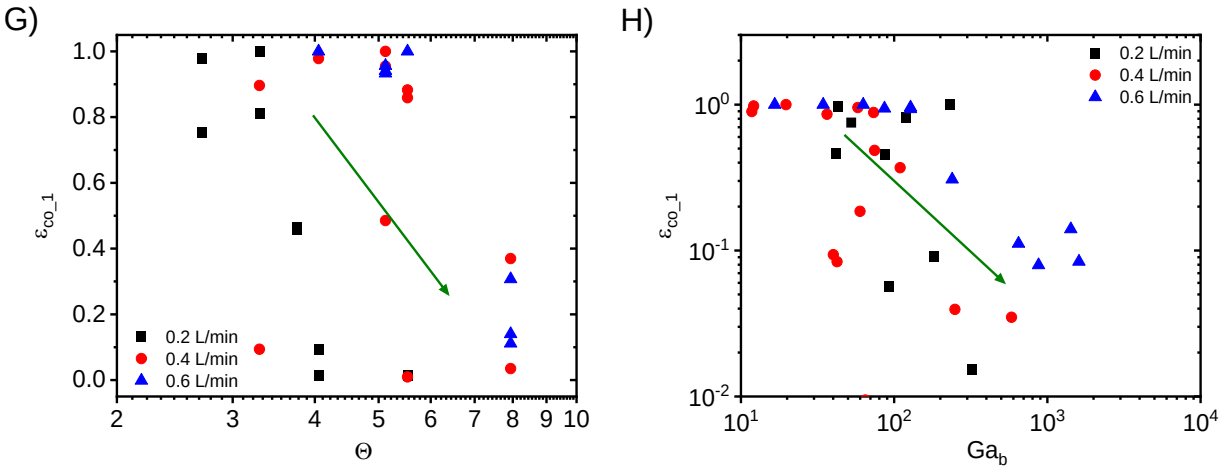

Figure 6.25 The corrected liquid content, which was calculated based on the values provided by the first sensor chips, for KPFOS aqueous solutions as a function of A) Reynolds number, B) Capillary number, C) Weber number, D) Froude number, E) Boussinesq number, F) processing number, G) interface number, and H) Galilei number.

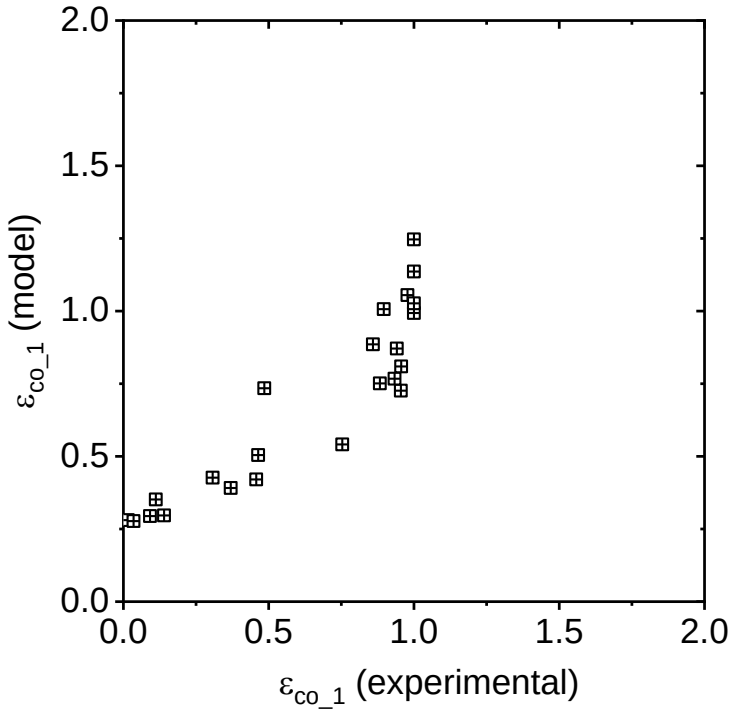

Figure 6.26 Model values of liquid content for KPFOS aqueous foams through the use of *Equation (6.23)*, compared to the experimental values of liquid content for KPFOS aqueous foams.

The same approach of modeling was then conducted for ε_{co_1}. **Figure 6.26** ($R^2 = 0.67897$) points out the correlation between the model values and the experimental values by using the

monomial equation below. As seen, the coefficients of Re_b, Ca, and $\frac{R}{H_{l0}}$ are greater than 1.0, indicating the water holding capacity of KPFOS foams is strongly correlated with the velocity of injected air, the surface tension, and bubble size. **Table 6.2** also shows that the water fraction of KPFOS foams is strongly related to the Ca.

$$\varepsilon_{co\_1} = 965112.5 * Re_b^{-1.04} * Ca^{1.11} * We_b^{-0.36} * Fr_b^{0.55} * \zeta_p^{0.21} * (\frac{R}{H_{l0}})^{1.3} \quad \textit{Equation (6.23)}$$

6.5.2. PFOA aqueous foams

Unlike the study of KPFOS bulk concentration effect on its aqueous foams, the NaCl effect on PFOA foams was studied. Again, the effect of Q_{air} on the water holding capacity of PFOA is significant, for example, as seen in **Figure 6.27A**, low Q_{air} of 0.2 L/min gives rise to smaller ε_{co_1}, whereas the higher Q_{air}, i.e., 0.4 and 0.6 L/min, tends to result in wet foams. However, the liquid fraction becomes less dependent on the Q_{air} in the high air velocity regime. But the trend is the ε_{co_1} increases with an increase in Re_b in the low Re_b regime. The similar trend can also be applied to We_b, Fr_b, and ζ_p as seen in **Figures 6.27C**, **6.27D** and **6.27F**. The special case belongs to Ca, and a very clear trend can be seen in **Figure 5.29B**. Although the ε_{co_1} increases with increasing the Ca at different Q_{air}s, the change of ε_{co_1} over the Ca follows the power law rule for each Q_{air}.

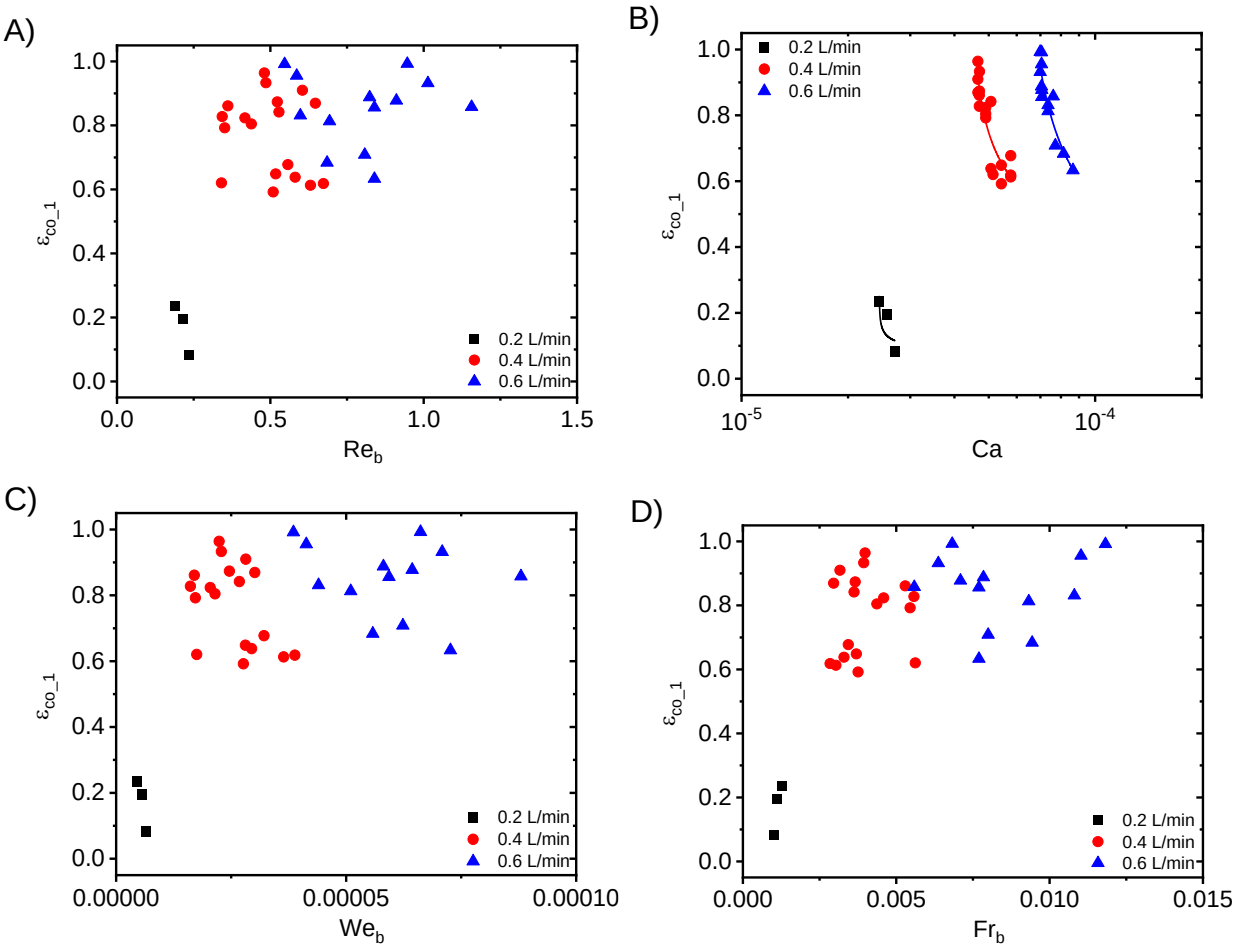
A)
B)
C)
D)
ε_{co_1}
Re_b
Ca
We_b
Fr_b
0.2 L/min
0.4 L/min
0.6 L/min

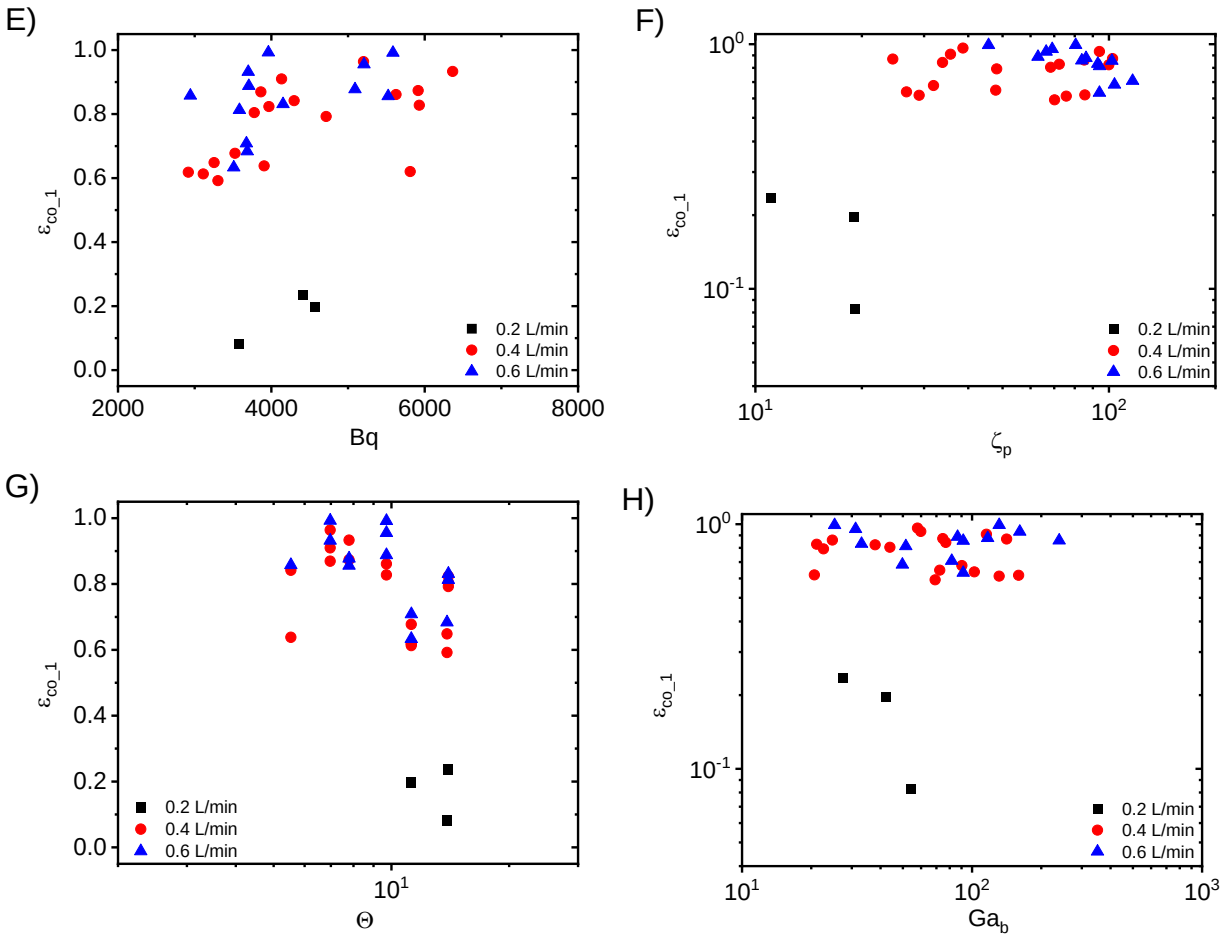

Figure 6.27 The corrected liquid content, which was calculated based on the values provided by the first sensor chips, for PFOA aqueous foams as a function of A) Reynolds number, B) Capillary number, C) Weber number, D) Froude number, E) Boussinesq number, F) processing number, G) interface number, and H) Galilei number.

In terms of the correlation between ε_{co_1} and the dimensionless numbers Bq, Θ, and Ga_b, higher Q_{air} increases the ε_{co_1} rather than shifting the ε_{co_1} to the right, for example, to the greater Bq regime. However, the ε_{co_1} slightly increases when the Bq becomes larger. Furthermore, the dependency of ε_{co_1} on Θ and Ga_b for PFOA foams containing NaCl with various concentrations cannot be determined according to **Figures 6.27G** and **6.27H**. **Figure 6.28** ($R^2 = 0.71484$ for model prediction) shows the predicted ε_{co_1} of PFOA aqueous foams over the experimental values by using the *Equation (6.24)* shown below. One can see that the effect of Ca on the ε_{co_1} of PFOA aqueous foams is significant, considering the effect of adding NaCl with different concentrations.

Besides the surface tension effect, the effect of Fr_b is also important for the water holding capacity of PFOA foams containing NaCl. **Table 6.2** show good agreement that the Ca highly influences the water holding capacity.

$$\varepsilon_{co\_1} = 0.0000663876 * Ca^{-2} * We_b^{0.36} * Fr_b^{0.9} * Bq^{0.1} * \Theta^{-0.15} * (\frac{R}{H_{lo}})^{0.5}$$

Equation (6.24)

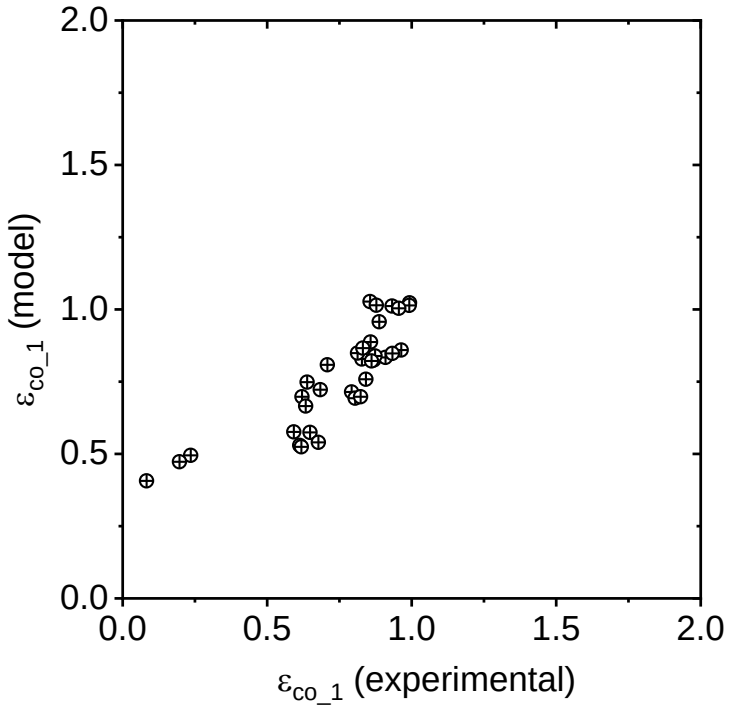

Figure 6.28 Model values of liquid content for PFOA aqueous foams through the use of *Equation (6.24)*, compared to the experimental values of liquid content for PFOA aqueous foams.

6.5.3. KPFBS aqueous foams

The ε_{co_1} of KPFBS aqueous foams is also plotted as a function of different dimensionless numbers as depicted in **Figure 6.29**. Despite the limited sample composition for KPFBS samples, our results show that the water fraction of KPFBS aqueous foams is highly correlated with the Ca, Fr_b, ζ_p, and Ga_b. The same as PFOA, the water fraction increases with increasing the Ca, and higher Q_{air} contributes to higher Ca. But it should be mentioned that for KPFOS, even the Q_{air} is

low, i.e., 0.2 L/min, the high content of water trapped in the foams can be achieved. **Figure 6.30** ($R^2 = 0.82850$ for model prediction) shows the predicted ε_{co_1} of KPFBS aqueous foams over the experimental values by using the *Equation (6.25)* shown below. It reveals the water holding capacity for KPFBS foams containing $CaCl_2$ is only dependent on the Fr_b and ζ_p.

$$\varepsilon_{co\_1} = 0.786628 * Fr_b^{0.38} * \zeta_p^{0.29} \qquad \textit{Equation (6.25)}$$

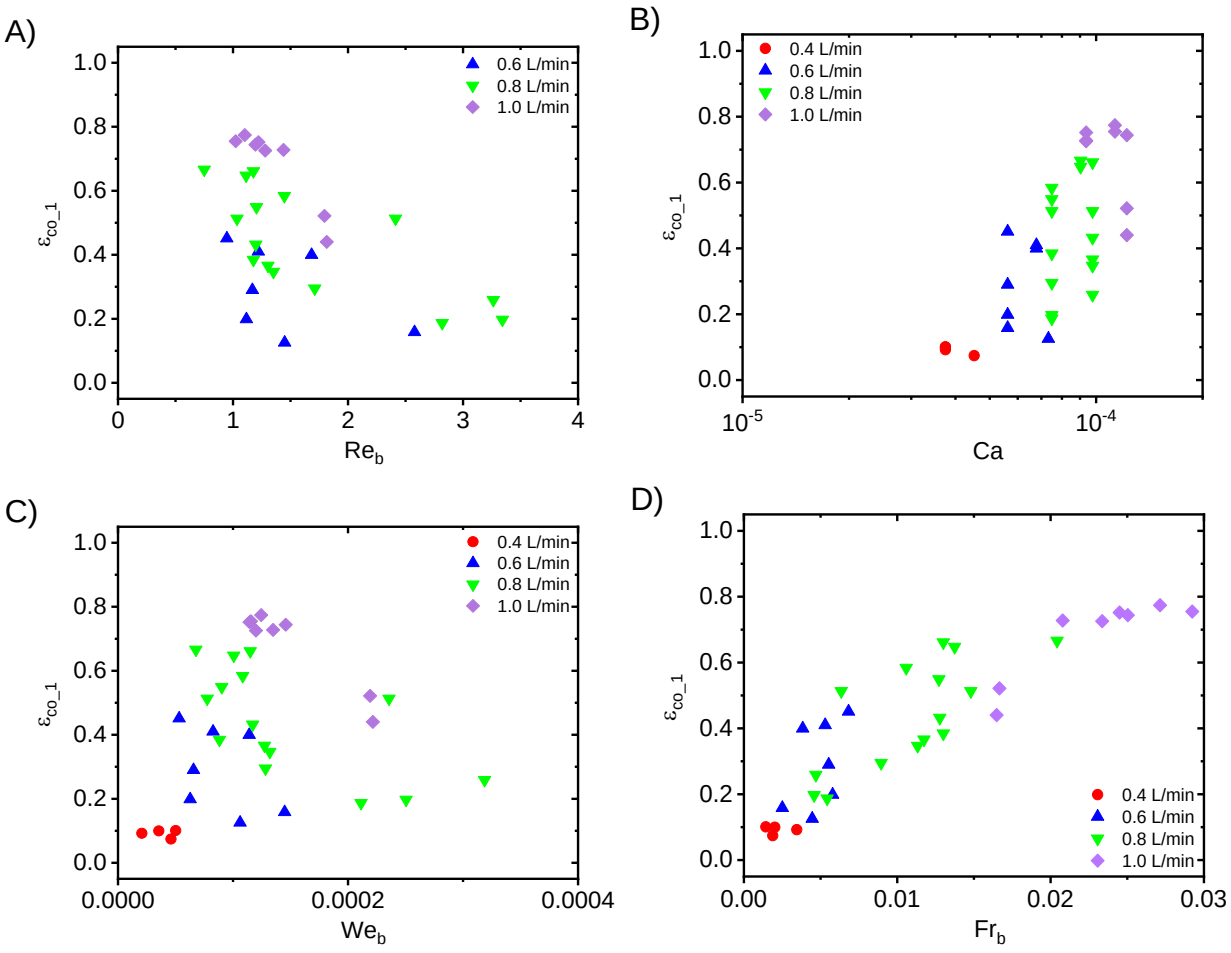

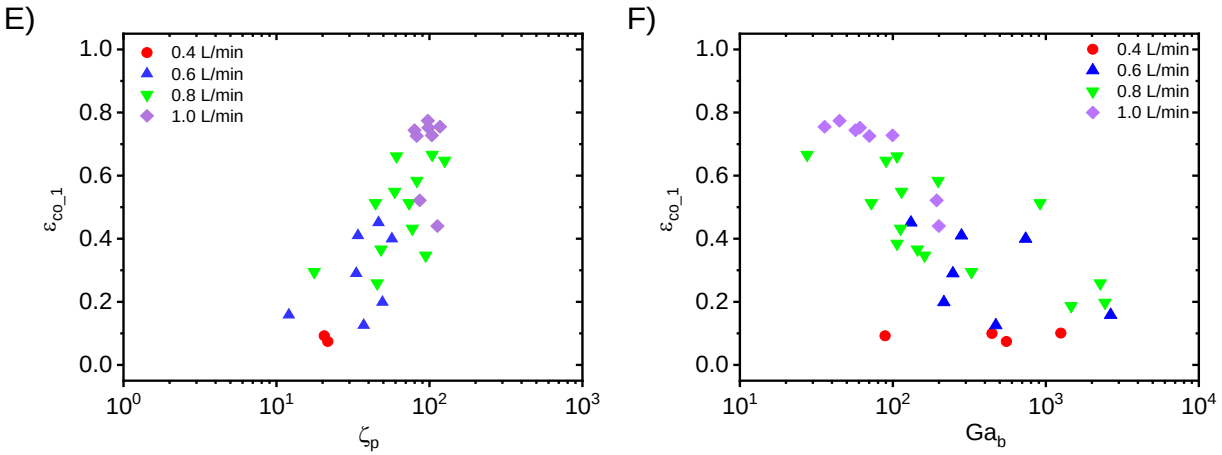

Figure 6.29 The corrected liquid content, which was calculated based on the values provided by the first sensor chips, for KPFBS aqueous foams as a function of A) Reynolds number, B) Capillary number, C) Weber number, D) Froude number, E) processing number, and F) Galilei number.

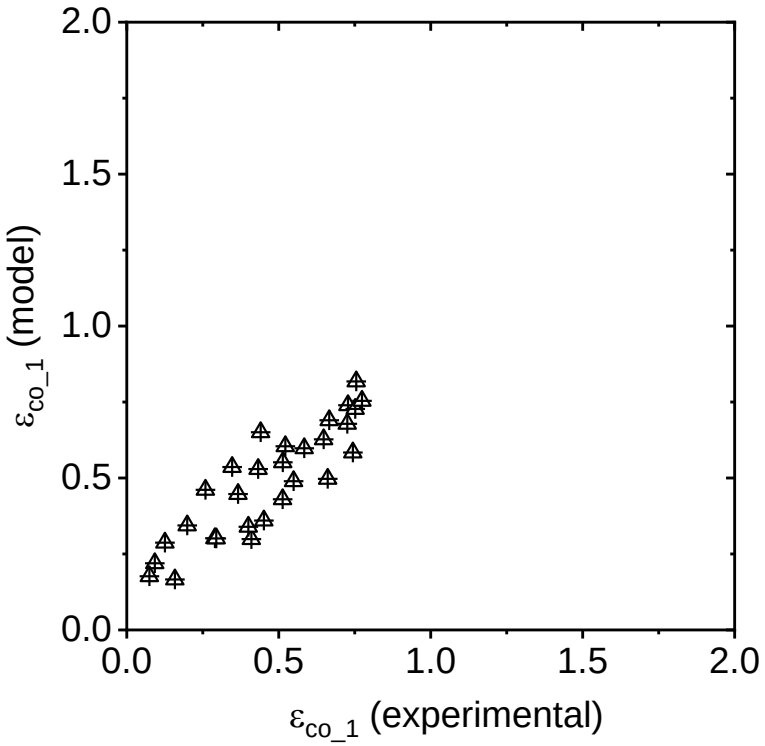

Figure 6.30 Model values of liquid content for KPFBS aqueous foams through the use of *Equation (6.25)*, compared to the experimental values of liquid content for KPFBS aqueous foams.

6.6. Conclusions

In this present study, the foaming behavior of three PFAS, which are KPFOS, PFOA and KPFBS, is studied by aerating their aqueous solutions with varied process parameters of air flow rate, foaming time and pore size range of glass filters. Generally, the foaming capacity follows the order of KPFOS>PFOA>KPFBS. The foaming capacity of KPFOS, PFOA and KPFBS is further investigated by using dimensional analysis approach to correlate the expansion rate of foaming, foaming kinetics, and liquid content with several different dimensionless numbers.

PFAS bulk concentration affects their foaming behavior. Taking example of KPFOS, there is a concentration (around 0.4 mM) at which the highest foam height is obtained. However, the bubble size continuously decreases with increasing the bulk concentration. Both process and interfacial parameters influence KPFOS foamability. In the studied regime, the Boussinesq number affects the expansion rate of foaming the most, the Capillary number influences the foaming kinetics and liquid content the most during the aeration. Furthermore, the addition of salts (NaCl and $CaCl_2$) enhances the KPFOS foaming kinetics through affecting the Capillary number and interface number. The predictions of foaming expansion rate, foaming kinetics and liquid content for KPFOS solutions have the R^2 of 0.96, 0.99 and 0.95, respectively.

Given a concentration of PFOA (0.4 mM), the NaCl concentration affects PFOA foaming behavior. A NaCl concentration range of 5-50 mM improves PFOA foaming capacity by influencing the Boussinesq number. Interestingly, the maximum value of foam height with changing the Capillary number and interface number appear around this NaCl concentration range. Additionally, the liquid content of PFOA foams containing NaCl is highly correlated with the Capillary number. The model works good for predicting the foaming expansion rate and liquid

content for PFOA with a R^2 of 0.99 and 0.98, respectively. However, the data are more scattering for the prediction of foaming kinetics (R^2 is 0.94).

The situation of KPFBS is much simpler. According to our previous study, 0.4 mM KPFBS has no dilatational interfacial modulus. Therefore, Boussinesq and interface numbers are not considered for KPFBS. The foaming expansion rate as well as the liquid content for KPFBS are governed by the Froude number, and the prediction of its foaming expansion rate along with the liquid content is in an agreement with the experimental values (R^2 is 0.96 for both). Our study suggests that lower $CaCl_2$ concentration is helpful to obtain the relatively higher foaming expansion rate for short-chain PFAS, coinciding with lower Reynolds and Weber numbers, as well as Gibbs stability. Nevertheless, the foaming kinetics of KPFBS is not dependent on any dimensionless numbers studied for it, leading to a failure of predicting the foaming kinetics.

Comparing to the process parameters, our study demonstrates the significant impact of interfacial properties, representing by Capillary, Weber, Boussinesq and interface numbers, on PFAS foaming behavior. A maximum PFAS foaming capacity with changing the Capillary number is observed, coinciding with the appearance of highest dilatational interfacial modulus. Moreover, the Gibbs criterion is not fulfilled for PFAS aqueous foams, implying the PFAS foams are relatively unstable. On the other hand, the Froude number, referring to the air injection process, significantly contributes to the PFAS foaming behavior.

*Chapter 7. Collapse of Per- and Polyfluoroalkyl Substances (PFAS) Aqueous Foams**

7.1. Introduction

Previous Chapters have explored the ability of PFAS to create foam, highlighting the significance of foamability in employing foam fractionation for the removal of these "forever chemicals". Equally important is the process of defoaming PFAS-laden foams, as the effectiveness of foam collection is contingent upon our ability to destabilize and subsequently eliminate PFAS from the foam. The challenge arises with highly stable PFAS foams, which are difficult to break down, complicating the collection and disposal of PFAS. Thus, the stability of foams is another foam property that needs to be considered. Given that all foams are inherently thermodynamically unstable, characterized by high interfacial free energy, they can be categorized into two distinct types: 1) transient foams, which dissipate within seconds, and 2) so-called permanent foams, which can persist for days.[185] Typically, unstable foams are produced by low molecular weight alcohols and fatty acids, while detergents, proteins, long-chain fatty acids, and particulate matter tend to form more stable foams.

The stability of foams is significantly affected by their composition. Manyala et al.[186] conducted research on the foam formation capacity and stability in binary surfactant mixtures, specifically combining polyoxyethylene cholesteryl ether ($ChEO_{30}$) with either hexadecyltrimethylammonium bromide (CTAB) or sodium dodecylbenzenesulfonate (SDBS). Their findings revealed that the presence of these surfactant combinations notably enhances both the creation and persistence of foam with $ChEO_{30}$, as evidenced by increased foam heights. This

* This Chapter is in preparation for submission to peer-reviewed journals. **Zhou, M.**, Foudazi, R.

improvement is attributed to the synergistic actions within the $ChEO_{30}$/CTAB and $ChEO_{30}$/SDBS mixtures, alongside the elevated disjoining pressures in the films, which contribute to the stabilization of the thin films over those formed by single surfactants. The same trend of increasing foamability and foam stability upon using surfactant mixtures was also reported in the literature.[187] Besides surfactant mixtures, the addition of (nano)particles also effectively improves the foam stability, creating Pickering foams.[188,189] Particle-stabilized foams, owing to their higher desorption energy compared to surfactant-based foams, exhibit a largely irreversible desorption process, enhancing stability.[188] On the other hands, when both surfactants and nanoparticle present in the systems, partial of surfactant molecules tend to be adsorbed at the surface of nanoparticles to modify the hydrophobicity (wettability) of nanoparticles, consequently, the stability of foams is enhanced. Compared to hydrocarbon-based surfactants, fluorinated surfactants are noted for producing more stable foams, despite their lower foam-forming capabilities.[187] Furthermore, the small molecular weight alcohol, such as ethanol, acts as a defoamer and lead to decrease in foaming tendencies.[190]

Beyond the nature of surfactants, several other factors also play crucial roles in determining foam stability, including but not limited to temperature, pH levels, additives, and processing conditions.[85,87,187–189,191–193] It has been extensively reported that the introduction of salts enhances the foamability and foam stability of PFAS, as well as the PFAS removal efficiency.[81,82,87,88] This improvement is primarily attributed to the increased adsorption of surfactants and the consequent reduction in surface tension. Nonetheless, the comprehensive investigations into the studies on the correlation between the PFAS foam stability/foam lamellar stability and their interfacial properties in the presence of electrolytes is very limited. Thus, herein, we use the foam analyzer to create the

PFAS aqueous foams in the absence and presence of electrolytes and examine the foam properties during the collapse of foam structures.

7.2. PFAS foam stability and liquid content

Different air-sparging times were used to create the PFAS aqueous foams by using the *DFA 100*. **Figure 7.1** typically shows the H_f, H_l, and foam + liquid height (H_t) of KPFOS aqueous foams created by sparging the solutions for 30 s, 60 s, 120 s and 300 s, respectively, as a function observation time. The Q_{air} was 0.2 L/min, and the glass filter has a D_f of 40-100 µm. As reported in the previous Chapter, the KPFOS aqueous foams reach a steady state within 100 s, therefore, the initial foam heights in **Figures 7.1C** and **7.1D** remain almost the same. The bubbles of 0.4 mM KPFOS foams corresponding to **Figure 7.1A** at various times are shown in **Figure 7.2B**. It can be seen that the bubble size increases as the foam collapses. Apparently, liquid drainage occurs over time as the edge of bubbles becomes thinner and the bubbles become polyhedral. **Figures 7.2A** and **7.2B** show the effect of D_f on the foam structure change during the foam collapse. They imply that the D_f determines the initial bubble size for KPFOS foams, and the KPFOS foams tend to have a smaller bubble size if the prior solutions are sparged by using the filter with a smaller D_f. Nevertheless, a greater bubble size increasing rate belongs to the smaller bubbles since the bubble sizes at 180 s and 420 s are the same if comparing **Figures 7.2A** to **7.2B**. However, 0.2 L/min was not a suitable Q_{air} to prepare PFOA and KPFBS foams, of which the bubbles barely can be captured by the camera.

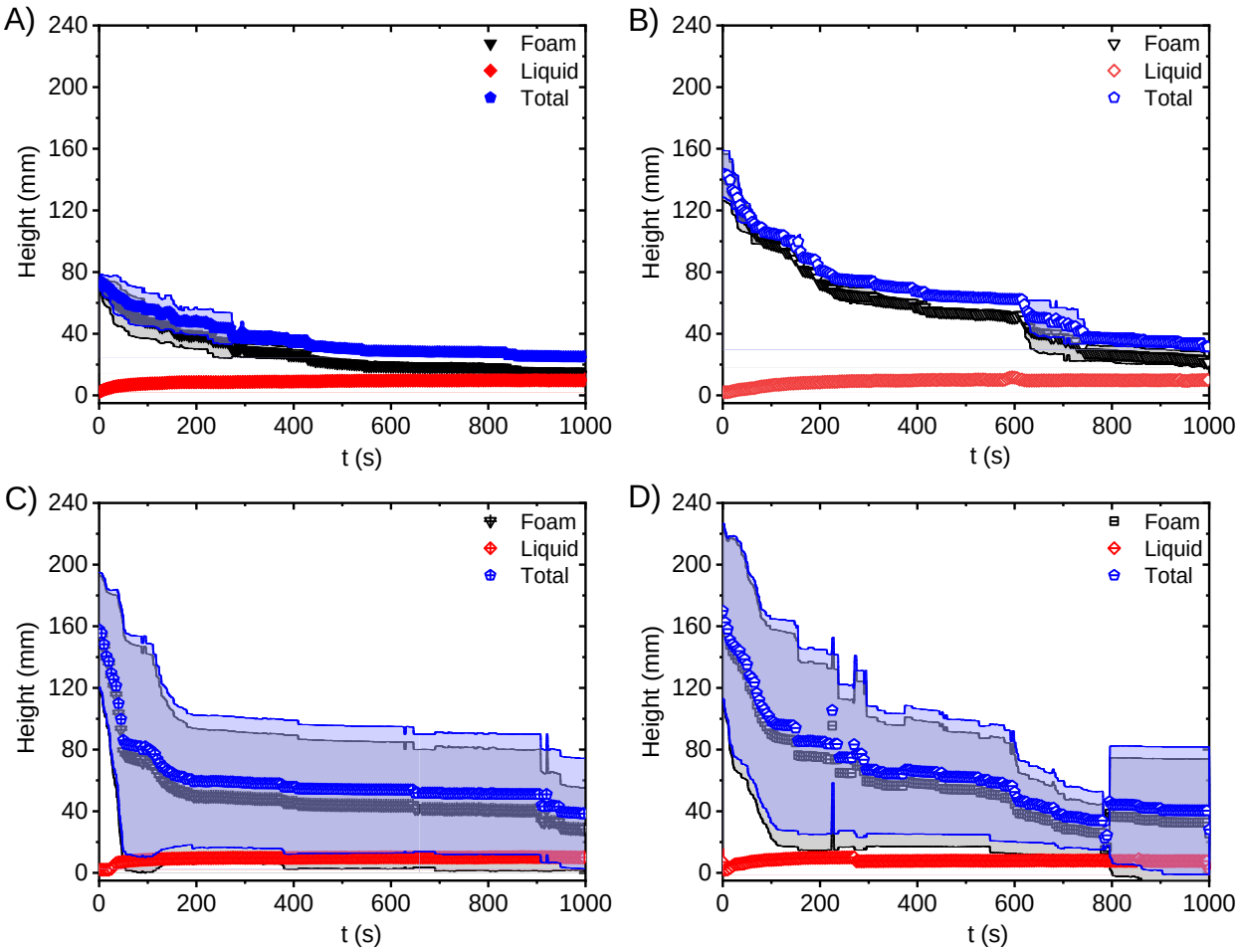

Figure 7.1 Height of KPFOS aqueous foams, KPFOS solutions, and KPFOS aqueous foams + KPFOS solutions, which were created with the aeration duration of A) 30 s, B) 60 s, C) 120 s, and D) 300 s prior to the bubble collapse, as a function of time during the bubble collapse. Note that 300 s of aeration was not finished for some of the samples in D) due to overflow alarm, however, the time was normalized. The concentration of KPFOS is 0.4 mM.

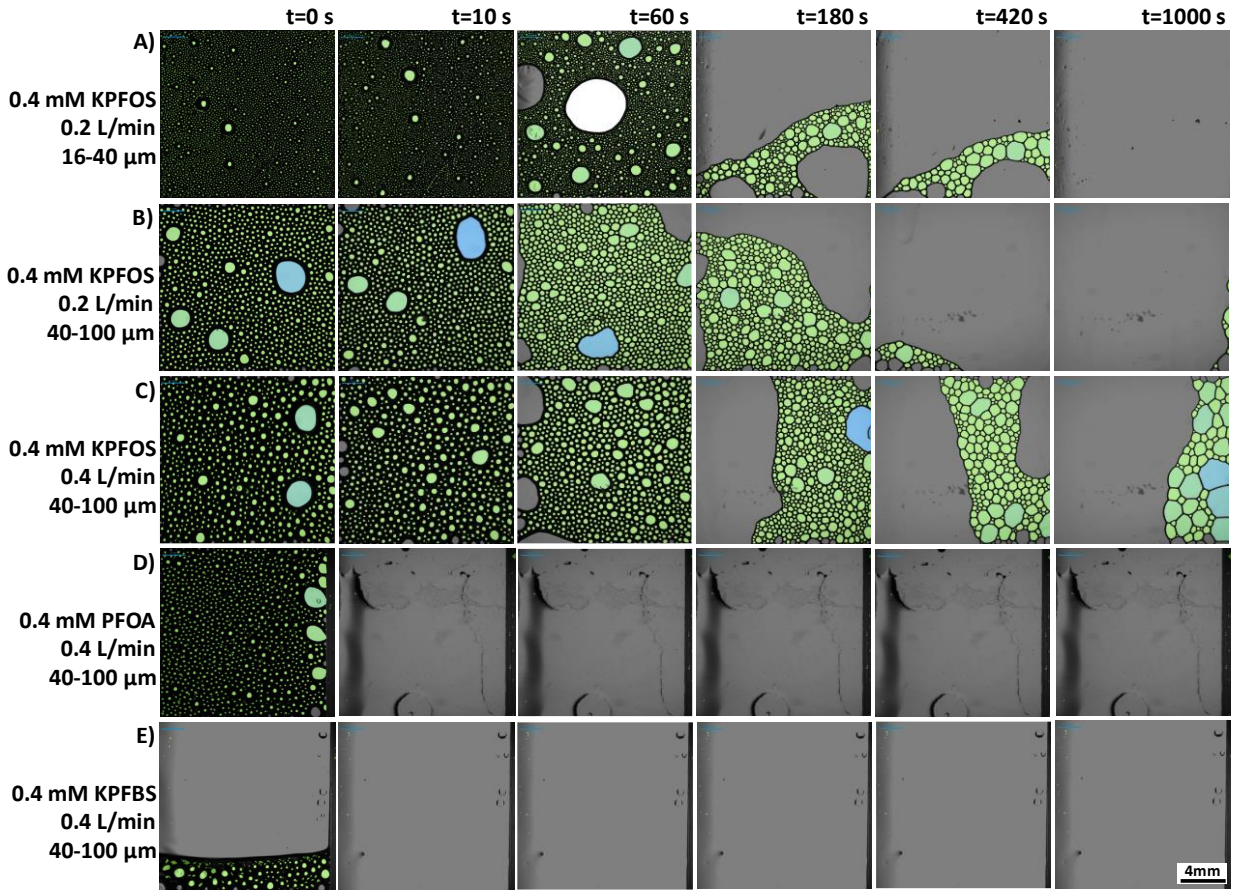

Figure 7.2 Foam structure at various times during 1000 s of bubble collapse for different PFAS with the same bulk concentration of 0.4 mM. The scale bar is 4 mm. The foam was created under different aeration conditions. Bubbles of 0.4 mM KPFOS aqueous foams by using the air flow rate of 0.2 L/min, and sparged by using the filter with a pore size range of A) 40-100 µm, and B) 16-40 µm. Bubbles of 0.4 mM C) KPFOS aqueous foams, D) PFOA aqueous foams, and E) KPFBS aqueous foams by using the air flow rate of 0.4 L/min, and the pore size range of the filter is 40-100 µm. For all, the air-sparging time was 30 s.

A Q_{air} of 0.4 L/min was used to sparge 0.4 mM PFAS solutions, and their bubbles during the 1000 s of foam collapse can be found in **Figures 7.2C**-**7.2E**. As seen, PFOA and KPFBS foams collapse quickly, all bubbles disappear within 10 s. Higher Q_{air} makes the KPFOS foams wetter, it can also be seen if comparing **Figures 7.2B** to **7.2C**. **Figure 7.3A** presents the H_f of 0.4 mM KPFOS, PFOA, and KPFBS aqueous foams, which were sparged by using three different Q_{air}s, during the foam collapse. Due to the insufficient H_f, only KPFOS foams prepared by using low Q_{air} of 0.2 L/min are shown in **Figure 7.3A**, and two D_fs are also compared with respect to the

foam evolution (solid black square and open black square with a dot inside). As seen, the foams prepared by using larger D_f have a lower initial H_f, and the bubbles start to collapse earlier. Nevertheless, the KPFOS foams with a smaller initial bubble size have a top-down foam collapse at around 100 s, since then the effect of initial bubble size is negligible. The initial H_f of PFAS foams increases when using higher Q_{air}s. However, the top-down collapse occurs faster in the case of sparging KPFOS solutions by using higher Q_{air}s, and thus, no significant difference in H_f is observed after 300 s no matter what Q_{air} was using to create the foams. In the case of using 0.4 L/min, the KPFOS foams are the most stable, and the PFOA and KPFBS foams completely collapse at 10 s. In the case of using 0.6 L/min, the KPFOS foams are still the most stable one, however, the PFOA foams become more stable compared to KPFBS foams since the former completely collapses at 20 s, but the structure of the latter is completely gone at 10 s.

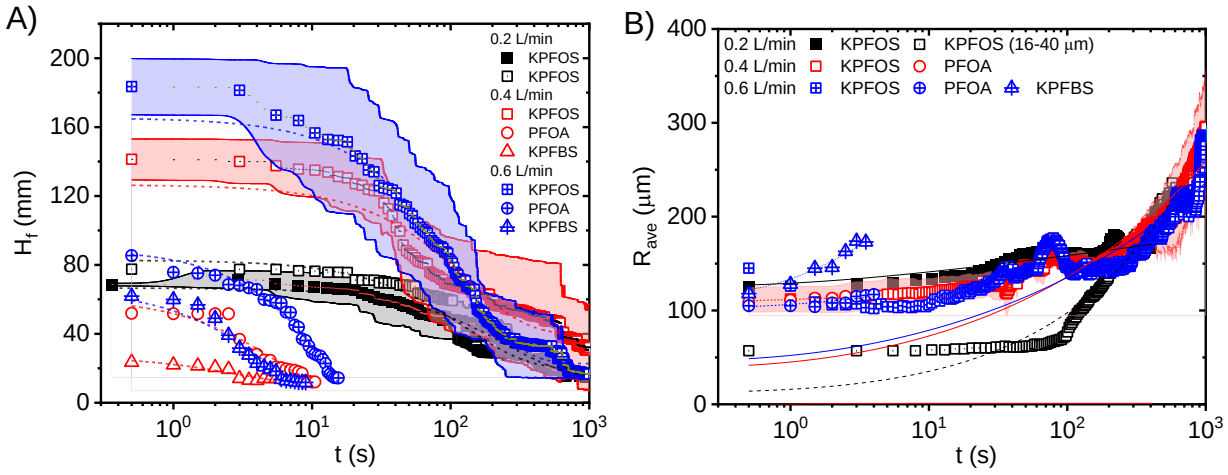

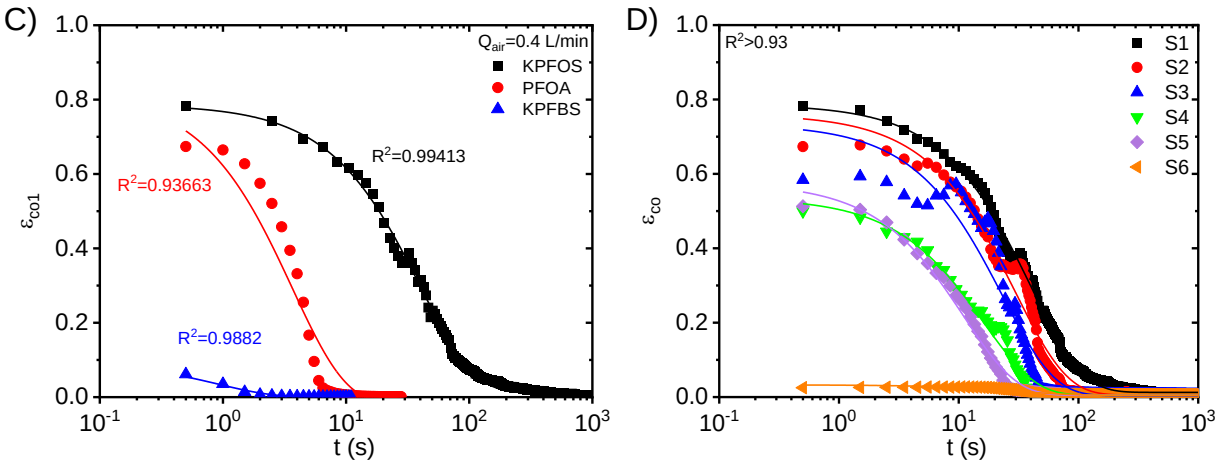

Figure 7.3 A) Foam height and B) average bubble radius of 0.4 mM KPFOS, PFOA, and KPFBS aqueous foams, created by 30 s of aeration, during 1000 s of bubble collapse. Air flow rates were 0.2, 0.4, and 0.6 L/min, respectively. For KPFOS aqueous foams, a filter with an average pore size range of 16-40 µm was also used, shown as the black hollow square with a dot inside. For the rest, the filter has an average pore size range of 40-100 µm. C) Corrected liquid content of 0.4 mM KPFOS, PFOA, and KPFBS aqueous foams with the air sparging time of 30 s during 1000 s of bubble collapse based on the values provided by the first sensor (S1). And D) corrected liquid content of 0.4 mM KPFOS at various heights of foams during 1000 s of bubble collapse. The air sparging time is 30 s. For C) and D), the air flow rate was 0.4 L/min.

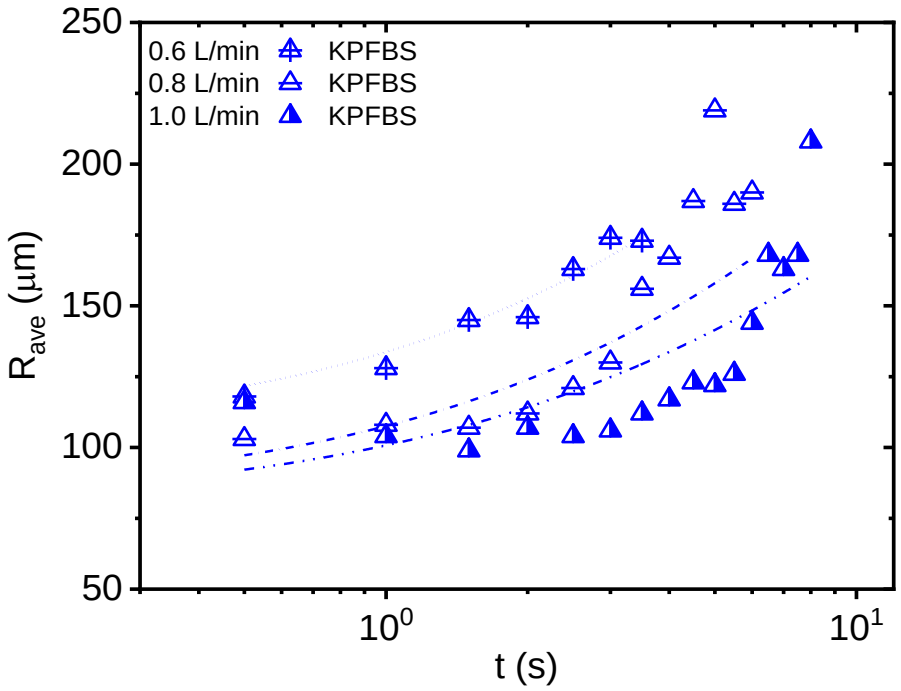

Figure 7.4 Average bubble radius of 0.4 mM KPFBS aqueous foams, prepared by 30 s of aeration using various air flow rates of 0.6, 0.8, and 1.0 L/min, respectively, during bubble collapse.

The average diameter of the foam bubbles offers valuable insights into the foam's characteristics at any given moment. **Figure 7.3B** shows the average bubble radius (R_{ave}) of PFAS foams during the structure collapse. As shown, the bubbles are growing during the foam collapse. The similar trend was also reported by Kamal and Guo.[187,194] For KPFOS foams sparged by using 0.2 L/min, the smaller D_f results in a smaller R_{ave} at the beginning of collapse, which is in agreement with **Figure 7.2**. However, a greater bubble growth rate is obtained at around 100 s and eventually the R_{ave} tends to be the same depending on the nature of foam film. Additionally, an increase in Q_{air} has no significant effect on the R_{ave} evolution during the collapse stage. Due to the very fast foam collapse, limited data points of R_{ave} were obtained for PFOA and KPFBS foams. Nevertheless, we can still find that the Q_{air} has no apparent influence on the R_{ave} of PFOA foams, but it affects the R_{ave} of KPFBS foams as seen in **Figure 7.4**.

The lines in **Figures 7.3B** and **7.4** are the fits of Power-law model $R_{ave} = a * (1 + t)^b$, and the fitted parameters can be found in **Table E1**. The power of t can be used to determine the bubble instability mechanism: Ostwald ripening and coalescence according to Zowada et al.'s work.[195] As seen, the D_f affects the bubble instability mechanism, with the power being equal to 0.05 when using the filter with a larger pore size and the power being equal to 0.46 when using smaller D_f. The latter indicates that the dominant mechanism for KPFOS foam bubble coarsening is coalescence. However, the Q_{air} also influences the mechanism of bubble coarsening. The power decreases from 0.46 to 0.24 with increasing the Q_{air}, implying that the mechanism of bubble coarsening changes to Ostwald ripening for KPFOS foams if sparging the solutions with higher air injection rate. Additionally, Ostwald ripening also governs the bubble instability for KPFBS foams.

As mentioned earlier, two liquid content sensors were used to directly measure the ε and resistance across the foams. The liquid volume fraction in the foams can be correlated with the conductivity as shown in *Equation (6.3)* in the Chapter 6.[73,113,175] **Figures 7.3C** and **7.3D** depict the ε_{co} of 0.4 mM PFAS aqueous foams during 1000 s of foam collapse, based on the resistance values provided by the first sensor chips at the bottom of foams. The Q_{air} used to prepare the foams was 0.4 L/min. Since the foams collapse faster, the ε_{co} of PFOA and KPFBS foams reaches zero faster than that of KPFOS foams. The exponential decay function shown below can be used to determine the liquid content characteristic time, at which the ε_{co} has reduced to 50 % of its initial value.

$$f(t) = A + Be^{Ct} \qquad \textit{Equation (7.1)}$$

where $\tau = -1/C$. As seen in **Figure 7.3C**, the fits (solid lines) to *Equation (7.1)* have the $R^2 > 0.93$. For 0.4 mM KPFOS foams, $\tau_{\varepsilon_{co1}} = 40.08$ s, for 0.4 mM PFOA, the $\tau_{\varepsilon_{co1}} = 3.67$ s, and for 0.4 mM KPFBS, the $\tau_{\varepsilon_{co1}} = 0.93$ s. For PFOA and KPFBS foams, only the first sensor chip had the reading. **Figure 7.3D** shows the ε_{co} at different foam heights for KPFOS foams, and the solid lines are the fit to *Equation (7.1)*. We obtain that $\tau_{\varepsilon_{co2}} = 29.60$ s, $\tau_{\varepsilon_{co3}} = 23.20$ s, $\tau_{\varepsilon_{co4}} = 16.15$ s, $\tau_{\varepsilon_{co5}} = 11.12$ s, and $\tau_{\varepsilon_{co6}} = 32.39$ s. It indicates that for KPFOS foams, the dryness of foams depends on the H_f, and the higher position, the water drains faster due to the gravity.

The *Equation (7.1)* can also be used to estimate the half-life of the foams, called τ_f. As seen in **Figure 7.3A**, the dashed lines are the fit to *Equation (7.1)* to determine the τ_f, and the fitted parameters can be found in **Table E2**. For KPFOS, the $\tau_f = 250.00$ s if the foams were sparged by using the Q_{air} of 0.2 L/min. The τ_f of KPFOS foams decreases with increasing the air-sparging flow rates, for example, the τ_f decreases to 115.61 s in the case of using 0.6 L/min to aerate the solutions. The same trend is applied to the foams sparged by using a smaller D_f, however,

the τ_f is dramatically reduced if using a smaller D_f, for instance, a τ_f of 131.58 s is obtained compared to 250.00 s when using 0.2 L/min to sparge the foams. Furthermore, the foam stability of PFOA and KPFBS foams is lower compared to that of KPFOS since the τ_fs of PFOA and KPFBS foams are only 6.00 s and 2.91 s, respectively, compared to 131.06 s for KPFOS foams when using 0.4 L/min to inject the air. However, increasing the Q_{air} to 0.6 L/min allows the enhancement of τ_f for PFOA and KPFBS foams, and the τ_fs are 9.24 s and 4.42 s, respectively, which is an opposite trend compared to KPFOS foams. Higher Q_{air}s of 0.8 and 1.0 L/min were also tested for KPFBS foams, and the τ_fs are 4.55 s and 5.10 s, respectively.

7.3. Effect of electrolytes on PFAS foams

7.3.1. PFAS foam stability

The electrolytes of NaCl and $CaCl_2$ with varied concentrations were added to the PFAS aqueous solutions to study the electrolyte effect on PFAS foam stability. It has been reported that the addition of electrolytes increases both foaming capacity and foam stability.[81,82,87,88] **Figure 7.5** shows the effect of introducing $CaCl_2$ with varied concentrations on the foam structure of 0.4 mM KPFOS foams prepared by injecting the air with a speed of 0.2 L/min for 30 s. It can be seen that the higher concentrations of $CaCl_2$ slightly increases the initial bubble size. In addition, upon adding $CaCl_2$, the KPFOS foam stability is improved due to the decreasing rate of bubble coalescence. Also, the foam stability is positively linked to $CaCl_2$ concentrations within the studied $CaCl_2$ concentrations.

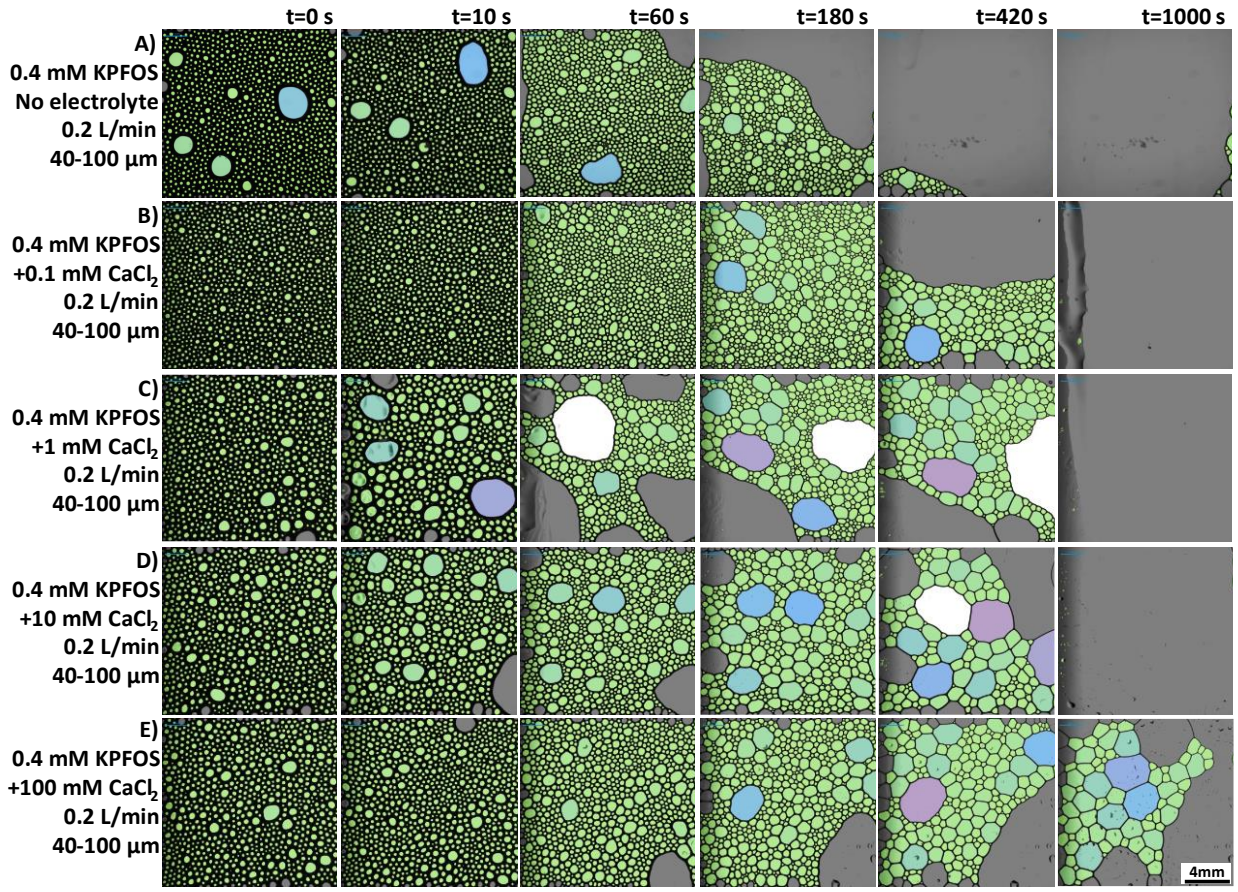

Figure 7.5 Effect of $CaCl_2$ concentrations on KPFOS foam structure at various times during 1000 s of bubble collapse. The scale bar is 4 mm. A) Bubbles of 0.4 mM KPFOS aqueous foams. Bubbles of 0.4 mM KPFOS aqueous foams containing B) 0.1 mM, C) 1 mM, D) 10 mM, and E) 100 mM $CaCl_2$. The air flow rate used to create the foams was 0.2 L/min, and the pore size range of the filter is 40-100 µm.

The tendency of a separation of gas and aqueous phases of the foams due to the gravity and capillary effects, which are related to liquid fraction gradient, leads to liquid drainage.[73] In other words, the liquid trapped in the foams tends to become uniform to form the dry foams since the gravity and capillary effects are balanced through viscous dissipation happening within the liquid network. As seen in **Figure 7.5**, the water is drained out of the films over the time in the KPFOS foams containing $CaCl_2$ because the films become thinner, and consequently, the bubbles become more polyhedron over the time. Moreover, the films become more stable and viscoelastic upon an addition of $CaCl_2$, enabling a reduced rate of bubble coalescence. Without adding $CaCl_2$, the thin

film of liquid raptures relatively faster, inducing bubble coalescence. If bubble coalescence rate is fast, the liquid drainage to the lower height of foams tends to occur faster.[188] In addition, the bubbles continuously grow due to the bubble coarsening, which appears owing to the differences in Laplace pressure between thin liquid films, making the gas diffuse between the bubbles, and thus, the increased bubble size.

Figure 7.6A shows the R_{ave} evolution of KPFOS foams containing various concentrations of $CaCl_2$ during the bubble collapse. The air injection rate was 0.2 L/min. Apparently, the addition of $CaCl_2$ results in a larger initial R_{ave}, and after 200 s, the bubble growth rate of KPFOS foams containing $CaCl_2$ is visually greater than that of sole KPFOS foams until the bubbles disappear in the camera. The solid lines in **Figure 7.6A** are the *Equation (7.1)* fittings, and the fitted parameters are shown in **Table E3**. Compared to the power-law fitting, the exponential fitting has a higher R^2. The bubble growth rate is defined as the *Equation (7.2)*.

$$\dot{R}_{ave} = \frac{dR_{ave}}{dt} \qquad \textit{Equation (7.2)}$$

Therefore, the bubble growth rate equations can be obtained by taking the derivative of *Equation (7.1)* as also summarized in **Table E3**. The influence of $CaCl_2$ on the H_f of KPFOS foams is shown in **Figure 7.6B**. Upon an addition of $CaCl_2$, the H_f decreases slower especially at the high $CaCl_2$ concentrations, implying the top-down collapse is effectively reduced. However, a small-scale top-down collapse is observed as pointed out in **Figure 7.6B** when the $CaCl_2$ concentration is high. In terms of the foamability, the concentration of $CaCl_2$ has no significant impact on the KPFOS H_f (graph is not included here).

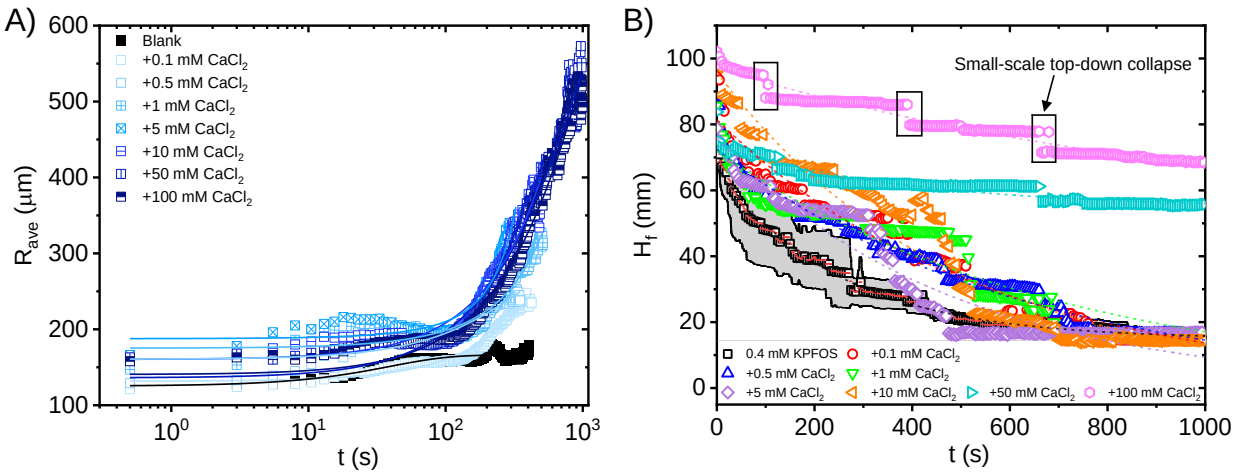

Figure 7.6 A) Average bubble radius, and B) foam height evolution of 0.4 mM KPFOS aqueous foams containing different $CaCl_2$ concentrations during bubble collapse. The foams were created by sparging the KPFOS aqueous solutions with 30 s. Air flow rate was 0.2 L/min. And the pore size range of the filter was 40-100 μm. The solid lines shown in A) represent the fitting with the *Equation (7.1)*.

In addition to the divalent salt $CaCl_2$, monovalent salt NaCl was also tested to study its effect on the H_f evolution of KPFOS foams as depicted in **Figure 7.7B**. Our results show that the high salinity destabilizes the KPFOS foams as seen in **Figure 7.7A**. In the range of 0.5-10 mM, the addition of NaCl enhances the foamability of KPFOS, in turn, higher H_f s are obtained. However, the KPFOS foaming capacity is hindered when further increasing the NaCl concentrations up to 100 mM. Considering foam stability, 0.5 and 1.0 mM NaCl contribute to improve KPFOS foam stability, however, 5.0 and 10.0 mM NaCl increase the foam collapse rate, and the foams completely collapse after 150 s. Again, the *Equation (7.1)* is used to estimate the τ_f of KPFOS foams with and without adding electrolytes, and the dashed lines in **Figures 7.3A**, **7.6B** and **7.7B** represent the fittings to *Equation (7.1)*. The fitted parameters can be found in **Table E2**.

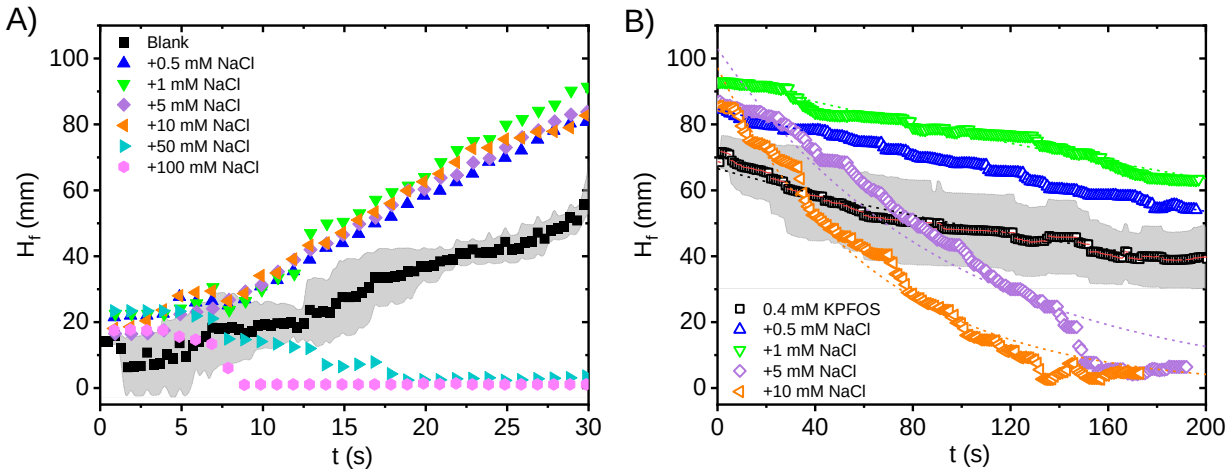

Figure 7.7 A) Foam height of 0.4 mM KPFOS aqueous foams with different NaCl concentrations during the 30 s of air-sparging process by using the air flow rate of 0.2 L/min and the filter with a pore size range of 40-100 µm. B) After the 30 s of aeration, foam height evolution during 200 s of foam collapse.

As well as KPFOS foams, the addition of electrolytes influences the H_f of PFOA foams, which have the same bulk concentration as KPFOS foams. Unlike KPFOS, monovalent salt NaCl is more effective on improving both foaming capacity and foam stability for 0.4 mM PFOA, and **Figure 7.8A** shows the PFOA foam stability in the absence and presence of NaCl with various concentrations. Nevertheless, high salinity, such as 100 and 200 mM, has a negative effect on PFOA foam stability compared to low salinity environment. Even though the high salinity starts to destabilize PFOA foams, their stability is still enhanced compared to sole PFOA foams. The effect of divalent salt $CaCl_2$ on PFOA foam stability can be found in **Figure 7.8B**. Lower $CaCl_2$ concentrations (0.1-1 mM) favor the PFOA foam stability, however, the foams collapse faster in the environment with a higher $CaCl_2$ concentration, for instance, 100 mM.

The same as KPFOS, τ_fs of PFOA foams with and without electrolytes are calculated based on the *Equation (7.1),* (the dashed lines in **Figure 7.3A** and **Figure 7.8**), and the fitted parameters are shown in **Table E2**. In addition, the τ_fs of sole KPFBS foams and KPFBS foams containing 100 mM $CaCl_2$ are also estimated and summarized in **Table E2**. It can be seen that high

$CaCl_2$ concentrations to some extent destabilize the KPFBS foams since the τ_f is reduced to 1.35 s from 4.55 s (for the foams prepared by using a Q_{air} of 0.8 L/min). In summary, the effect of monovalent and divalent salts on the H_f and τ_f of KPFOS foams and PFOA foams are to some extent opposite as depicted in **Figure 7.9**. In order to have more stable KPFOS foams, lower concentrations of monovalent salts (NaCl) are favorable, whereas the addition of monovalent salts (NaCl) qualitatively enhances the stability of PFOA foams within the studied NaCl concentrations. Furthermore, lower concentrations of divalent salts ($CaCl_2$) are effective to improve PFOA foam stability, while the KPFOS foam stability remains relatively higher within the investigated $CaCl_2$ concentrations.

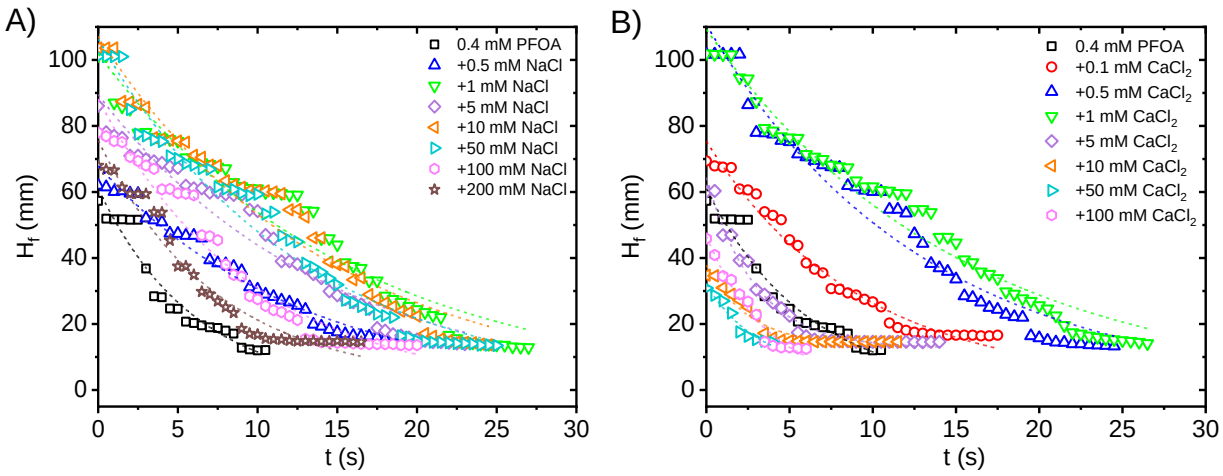

Figure 7.8 Foam height of 0.4 mM PFOA aqueous foams A) in the presence of various concentrations of NaCl during bubble collapse, and B) in the presence of different concentrations of $CaCl_2$ during bubble collapse. The filter used to sparge the KPFOS solutions was the one with 40-100 µm pore size. The air flow rate was 0.4 L/min.

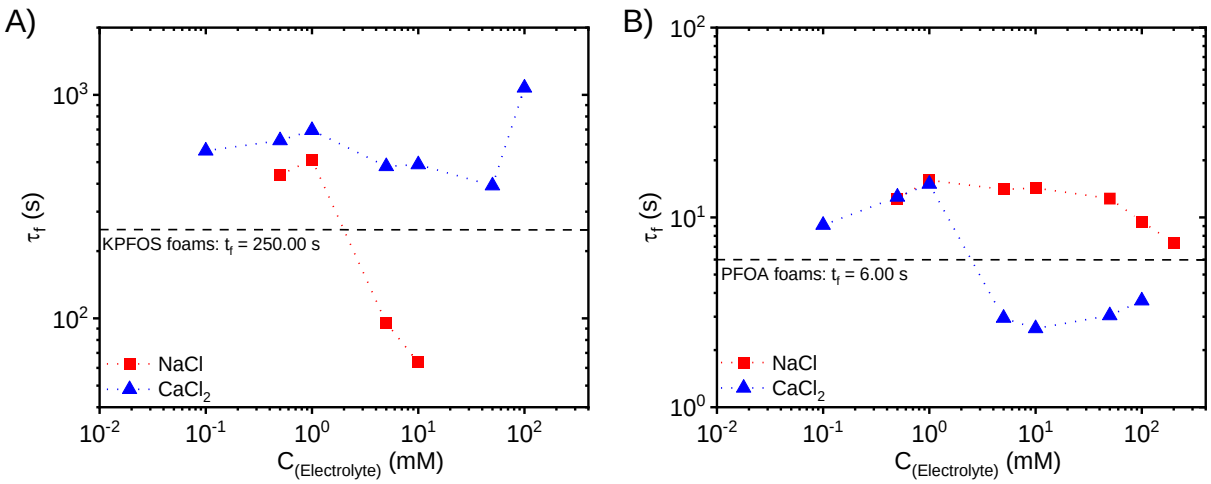

Figure 7.9 A) The half-life of 0.4 mM KPFOS aqueous foams containing electrolytes with varied concentrations. The dashed line is the half-life of 0.4 mM KPFOS aqueous foams without electrolytes. The air flow rate used to sparge the solutions was 0.2 L/min. The filter has the pore size range of 40-100 µm. B) The half-life of 0.4 mM PFOA aqueous foams containing electrolytes with varied concentrations. The dashed line is the half-life of 0.4 mM PFOA aqueous foams without electrolytes. The air flow rate used to sparge the solutions was 0.4 L/min. The filter has the pore size range of 40-100 µm.

7.3.2. Liquid content across the PFAS foams

Figure 7.10A compares the ε_{co} at the bottom of the foams in the presence of $CaCl_2$ with concentration ranging from 0.1 to 100 mM. As seen, the liquid fraction of KPFOS foams is dependent on the $CaCl_2$ concentration, and the ε_{co1} is increasing when the $CaCl_2$ concentrations are in the range of 0.1 to 5 mM. When the $CaCl_2$ concentration is higher than 5 mM, the ε_{co1} is apparently reduced. The *Equation (7.1)* is used to estimate the $\tau_{\varepsilon_{co1}}$, and the solid lines in **Figure 7.10A** are the fitting lines. The $\tau_{\varepsilon_{co1}}$ for 0.4 mM KPFOS foams sparged by using the Q_{air} of 0.2 L/min is 32.45 ± 12.09 s, and the $\tau_{\varepsilon_{co1}}$s are 32.30 ± 1.61 s, 25.07 ± 8.13 s, 24.71 ± 2.37 s, 17.26 ± 4.90 s, 23.84 ± 6.99 s, 56.01 ± 40.43 s and 93.27 ± 59.40 s, respectively, in the presence of 0.1 mM to 100 mM $CaCl_2$. The $\tau_{\varepsilon_{co1}}$ as a function of $CaCl_2$ concentrations is shown in **Figure 7.11A**, indicating that the liquid drainage velocity at the bottom of KPFOS foams

becomes faster when it contains 0.1-10 mM $CaCl_2$. In the higher $CaCl_2$ concentration regime, higher $\tau_{\varepsilon_{co1}}$s are obtained, suggesting a lower liquid drainage velocity.

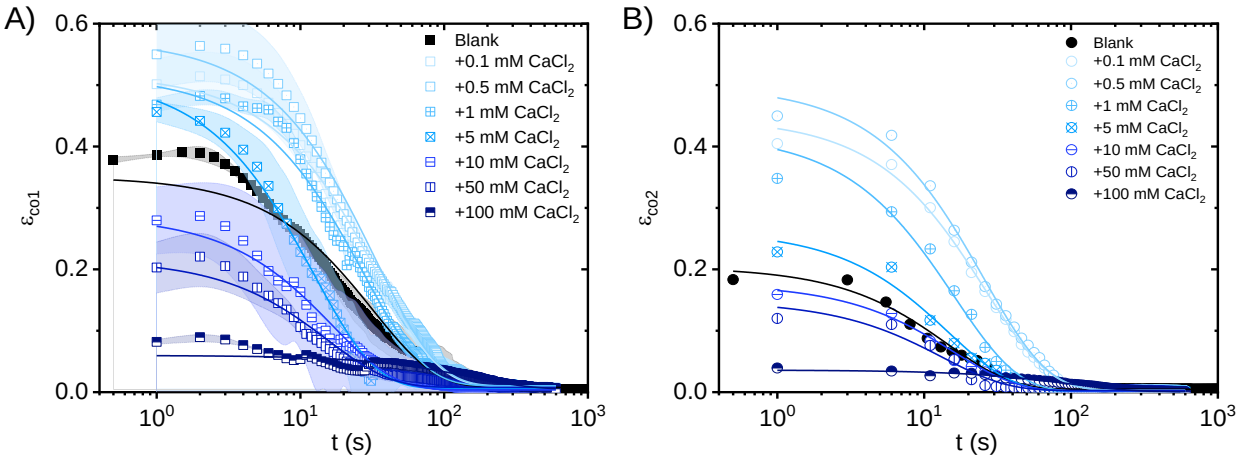

Figure 7.10 A) corrected liquid content (values based on the first sensor chip), and B) corrected liquid content (values based on the second sensor chip) evolution of 0.4 mM KPFOS aqueous foams containing different $CaCl_2$ concentrations during bubble collapse. The foams were created by sparging the KPFOS aqueous solutions with 30 s. Air flow rate was 0.2 L/min. And the pore size range of the filter was 40-100 µm. The solid lines represent the fitting with the *Equation (7.1)*. The error bar in B) is skipped for a clear view.

Figure 7.10B shows the ε_{co2} of KPFOS foams in the absence and presence of $CaCl_2$. The same as ε_{co1}, the ε_{co2} also increases first and then decreases with increasing the $CaCl_2$ concentrations. For both ε_{co1} and ε_{co2}, the highest liquid content is obtained when the $CaCl_2$ concentration is 0.5 mM, above which the corrected liquid content starts to be decreasing with adding more $CaCl_2$ until it becomes lower than that of sole KPFOS foams. **Figure 7.11A** shows the change of $\tau_{\varepsilon_{co2}}$ over the $CaCl_2$ concentrations, and the relatively lower $CaCl_2$ concentrations of 0.1-5 mM have no significant effect on liquid drainage velocity in the middle part of the KPFOS foams since no large change of $\tau_{\varepsilon_{co2}}$ is observed. However, the liquid drainage velocity decreases when further increasing the $CaCl_2$ concentrations. In addition, the $\tau_{\varepsilon_{co3}}$s of KPFOS foams containing $CaCl_2$ are also compared in **Figure 7.11A**, but $\tau_{\varepsilon_{co3}}$ of KPFOS foams without $CaCl_2$ is missing due to the insufficient H_f. Although the control line is absent, one can still see that the

$CaCl_2$ concentration affects the $\tau_{\varepsilon_{co3}}$, and its trend is the same as that of $\tau_{\varepsilon_{co1}}$ and $\tau_{\varepsilon_{co2}}$. In addition to $CaCl_2$ concentrations, the $\tau_{\varepsilon_{co}}$ is also correlated with the initial liquid fraction across the foams as presented in **Figure 7.11B**. It reveals that the slower liquid drainage velocity can be attributed to the lower content of liquid at the beginning of foam collapse. Moreover, the higher position across the KPFOS foams, the liquid drains faster due to gravity.

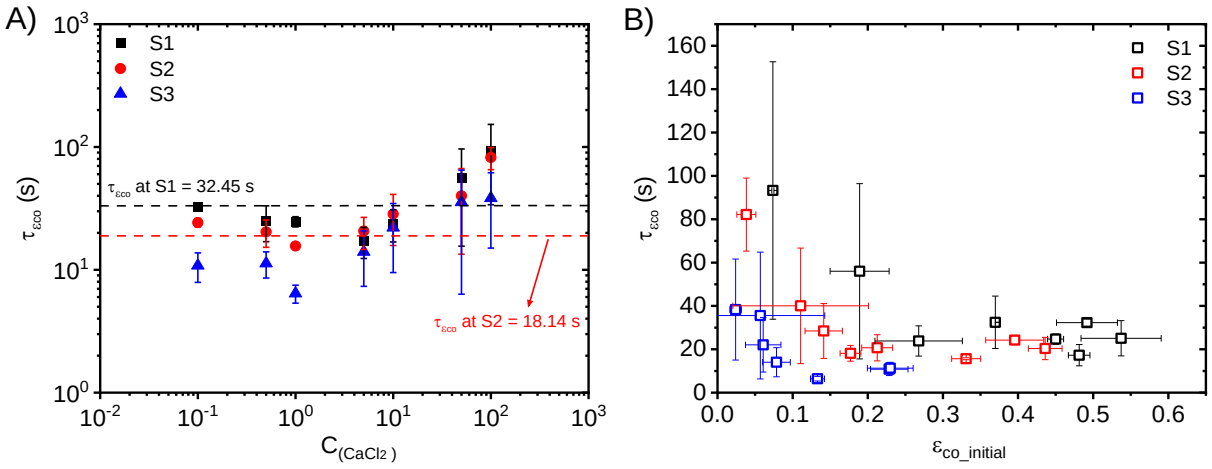

Figure 7.11 A) Comparison of the liquid content characteristic time, at which the liquid content has been reduced to half of its initial value, across the 0.4 mM KPFOS foams containing $CaCl_2$ with varied concentrations. The dashed lines are the liquid content characteristic time for KPFOS foams in the absence of $CaCl_2$. B) Liquid content characteristic time at different foam heights of 0.4 mM KPFOS foams with various $CaCl_2$ concentrations as a function of the initial corrected liquid content at this position.

7.4. Osmotic pressure across the PFAS foams

In the foam or emulsion systems, the pressure between the individual bubbles or droplets and continuous phase is different due to the surface/interfacial tension, and it governs the thickness of liquid films.[196] When the bubbles are spherical, the systems have the minimum interfacial energy state, and when the bubble shape becomes polyhedral due to the liquid drainage, the osmotic pressure (Π) occurs to regain the sphericity by flowing the continuous phase back in between the jammed bubbles. In the foam column, a mechanical equilibrium is developing based on the balance between the buoyancy force of bubbles and the Π.[113] Therefore, the liquid drainage

across the PFAS foams can be studied through calculating the Π at different foam heights throughout the PFAS foams over the time. The *Equation (7.3)* below is used to calculate the Π across the PFAS aqueous foams in the foam column.[197,198]

$$\Pi = k\frac{2\gamma}{d_{32}}\frac{(\varepsilon_c-\varepsilon)^2}{\sqrt{\varepsilon}} \qquad \textit{Equation (7.3)}$$

where k is a constant of 7.3 for the monodispersed bubbles, and 3.2 for the polydispersed bubbles, γ is the surface tension, d_{32} is the Sauter mean diameter of bubbles, and ε_c is the critical volume fraction of the foams, and $\varepsilon_c = 0.26$ is for the foams with an ordered structure (monodispersed bubbles), whereas $\varepsilon_c = 0.36$ for the foams with a disordered structure (polydispersed bubbles). The Π can be scaled with $2\gamma/d_{32}$, giving the normalized osmotic pressure $\widetilde{\Pi}$.

As can be seen in **Figure 7.12**, apparently, the $\widetilde{\Pi}$ is correlated with the foam height for KPFOS foams, which were prepared by injecting the air with a speed of 0.2 L/min. For example, at 20 s of foam collapse, the $\widetilde{\Pi}$ reaches 0.69 at the position of 33 mm, which is the level of the first sensor chip, while the $\widetilde{\Pi}$ is 2.87 at the position of 53 mm, which is the location of the second sensor chip. It is attributed to liquid drainage, taking place from the top to the bottom of the foams. In addition, the $\widetilde{\Pi}$ increases with the KPFOS foam collapse, indicating that the KPFOS has negligible effect on stabilizing the foams against liquid drainage.[113] Moreover, the inset of **Figure 7.12** shows the change of $\widetilde{\Pi}$ at the position of first sensor ship as a function of liquid fraction, showing the decrease in $\widetilde{\Pi}$ with increasing the liquid fraction. This decreasing trend was also reported in the literature.[196]

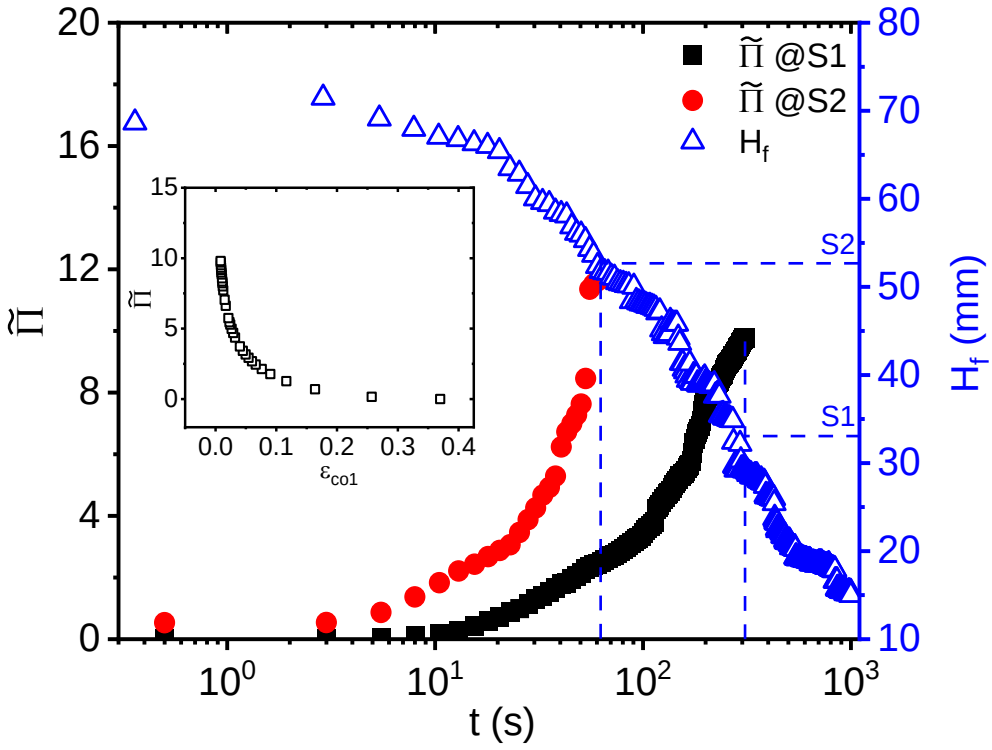

Figure 7.12 The change of normalized osmotic pressure (left y-axis) at different foam heights and KPFOS foam height evolution (right y-axis) during foam collapse. The air flow rate used to sparge the solutions was 0.2 L/min. The filter has the pore size range of 40-100 µm. Inset: dependence of normalized osmotic pressure on the corrected liquid content at the first sensor chip.

The effect of electrolyte concentrations is also taken into account. **Figure 7.13** shows the variation of Π and $\tilde{\Pi}$ at the first sensor chip location for 0.4 mM KPFOS foams containing varied concentrations of $CaCl_2$ at 50 s and 200 s of foam collapse. The dashed lines are the Π and $\tilde{\Pi}$ of KPFOS foams without $CaCl_2$. One can see that at 50 s of foam collapse, both Π and $\tilde{\Pi}$ slightly increase with increasing the $CaCl_2$ concentrations, however, they reach the plateau when the $CaCl_2$ concentration is above 10 mM. Allow the KPFOS foams to continue collapse, when at 200 s, the Π at the bottom of the foams containing $CaCl_2$ is smaller than that of KPFOS foams without $CaCl_2$, and the Π slightly decreases with increasing the $CaCl_2$ concentration. Nevertheless, after scaling with Laplace pressure, the $\tilde{\Pi}$ is no longer dependent on the $CaCl_2$ concentration. In other words,

the addition of $CaCl_2$ influences the $\tilde{\Pi}$ of KPFOS foams at the early stage of foam collapse, but over the time, this effect of $CaCl_2$ becomes negligible.

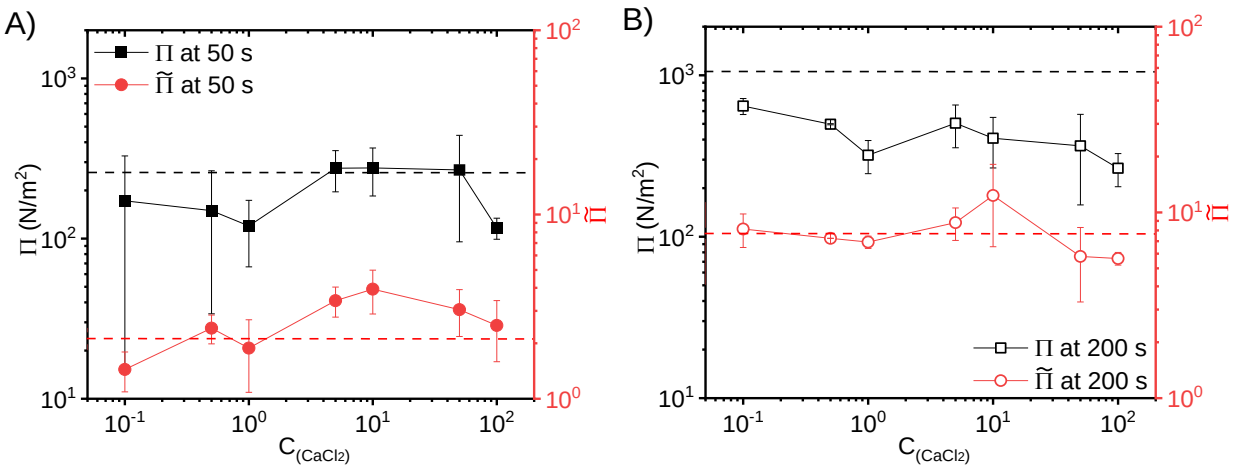

Figure 7.13 Effect of $CaCl_2$ concentrations on the osmotic pressure (left y-axis) and normalized osmotic pressure (right y-axis) at the bottom of 0.4 mM KFPOS foams containing different $CaCl_2$ concentrations at A) 50 s, and B) 200 s of defoaming process. The dashed lines in both A) and B) refer to the level without adding $CaCl_2$.

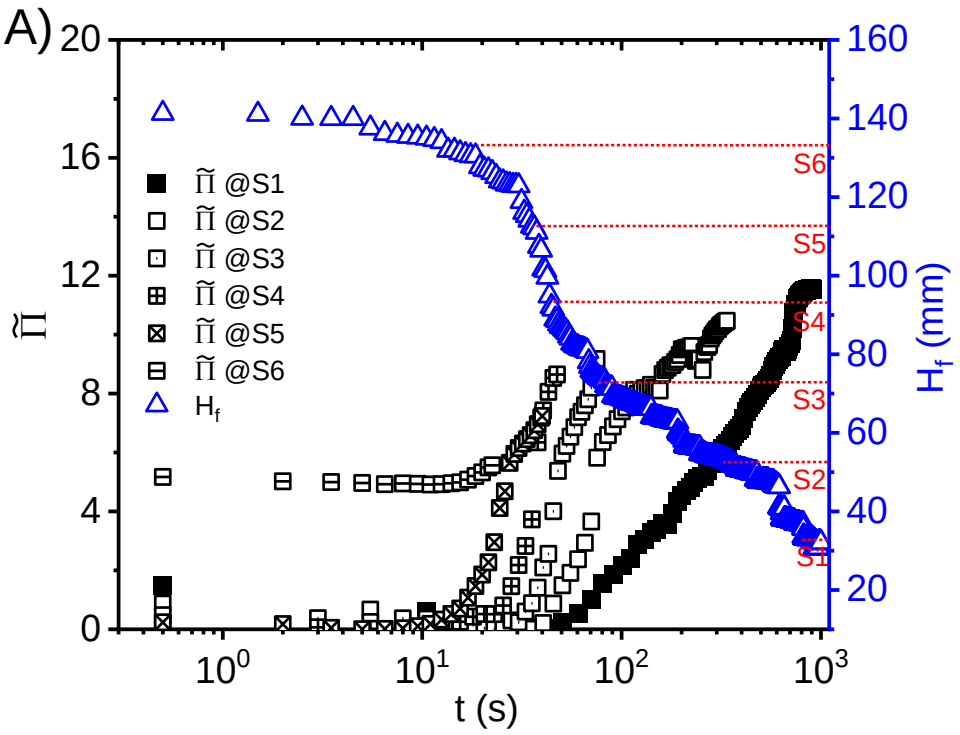

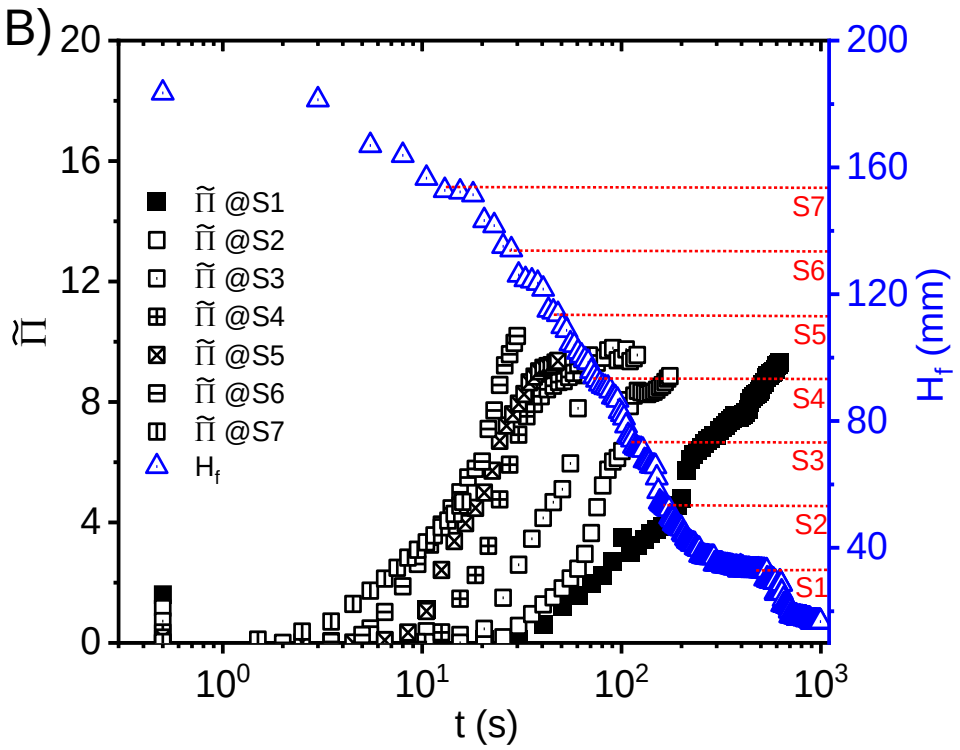

Figure 7.14 The change of normalized osmotic pressure (left y-axis) at different foam heights and KPFOS foam height evolution (right y-axis) during the foam collapse. The air flow rate used to sparge the solutions was A) 0.4 L/min, and B) 0.6 L/min, respectively. The filter has the pore size range of 40-100 μm.

The effect of higher Q_{air}s, used to sparge the solutions, on the $\tilde{\Pi}$ of KPFOS foams was also studied as seen in **Figure 7.14**. It can be seen that as the H_f increasing, more sensor chips had the reading, and for each location, the $\tilde{\Pi}$ increases as the foam structure is collapsing. However, the time, at which the $\tilde{\Pi}$ suddenly rise sharply, is delayed compared to the KPFOS foams prepared by gently injecting the air. In addition, greater $\tilde{\Pi}$s are obtained at the higher positions of foams, and they are earlier to increase sharply compared to those of the lower positions, suggesting that the top part of KPFOS foams is relatively unstable. Furthermore, the $\tilde{\Pi}$s of bottom part of KPFOS, PFOA and KPFBS foams at the first 4 s of foam collapse are compared as shown in **Figure 7.15**. It reveals that long-chain PFAS is assigned a higher $\tilde{\Pi}$.

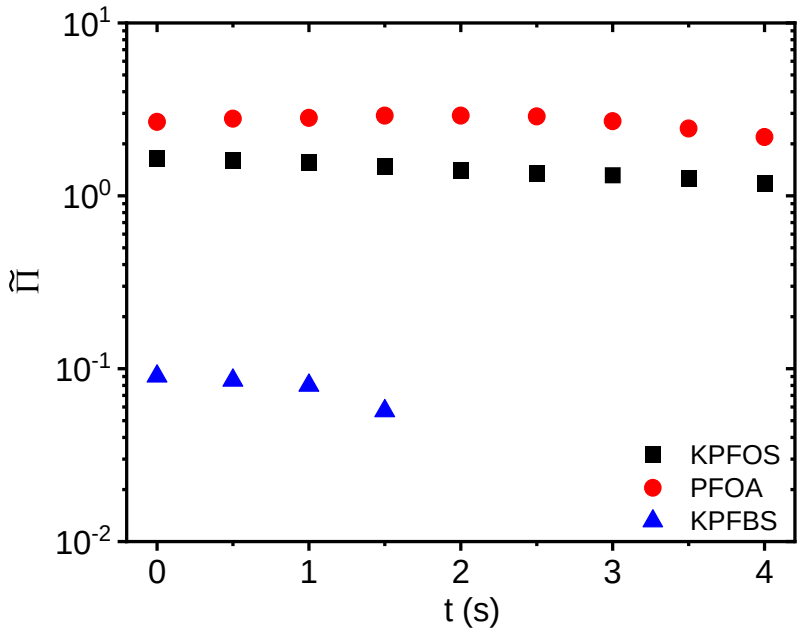

Figure 7.15 Comparison of normalized osmotic pressure of 0.4 mM PFAS aqueous foams at the first 4 s of foam collapse. The foams were sparged by the air flow rate of 0.6 L/min for 30 s. The filter has the pore size range of 40-100 μm.

7.5. Influence of interfacial properties on the PFAS foams

The same as the Chapter 7, some dimensionless numbers correlating with the interfacial properties are calculated in order to study the effect of interfacial properties on the PFAS foam stability. At small Reynolds numbers, the relative importance of the surface-to-bulk viscous stresses is given by the Boussinesq number $Bq = \eta_s/(\eta \cdot l)$, where l is the characteristic length scale.[177] However, in our case, the surface shear viscosity is difficult to measure since the PFAS are soluble in the water. Therefore, we define $Bq = \eta_s/(\eta \cdot R)$ as mentioned in previous Chapter. Θ', defined as the ratio of surface tension to interfacial dilatational elasticity, is equal to γ/E', and the Capillary number $Ca = (Q_{air} \cdot \eta)/(\gamma \cdot {D_c}^2)$. The $\Theta'' = \gamma/E''$ is introduced here to compare the effect of surface tension and dilatational viscosity. Due to the change of Sauter mean radius of bubbles in the defoaming process, the initial radius is used for studying the trend.

The 0.4 mM KPFOS foams containing various concentration of $CaCl_2$ are used, and **Figure 7.16** shows the dependency of τ_f on Bq, Θ', Θ'', and Ca. As mentioned in Chapter 5, the Bq corresponds to the surface mobility because the η_s is the effective parameter to characterize the surface mobility.[180] As seen in **Figure 7.16A**, the foam τ_f increases with an increase in Bq, suggesting the KPFOS foam stability is hindered by the high surface mobility (low η_s). The τ_f is also correlated with the Θ' (**Figure 7.16B**), and the foam stability is improved with increasing theΘ'. Therefore, in the case of adding electrolytes, i.e., $CaCl_2$, the KPFOS foams tend to become more stable when the effect of surface tension becomes dominated compared to the surface elasticity. If using monovalent salts, such as NaCl, the trend will probably vary, but it is not discussed here. In addition to Θ', the τ_f also varies with increasing Θ'', as depicted in **Figure 7.16C**. One can see that compared to the interfacial dilatational viscosity, representing by E'', the KPFOS foam stability is still governed by the surface tension in the case of increasing the concentration of $CaCl_2$.

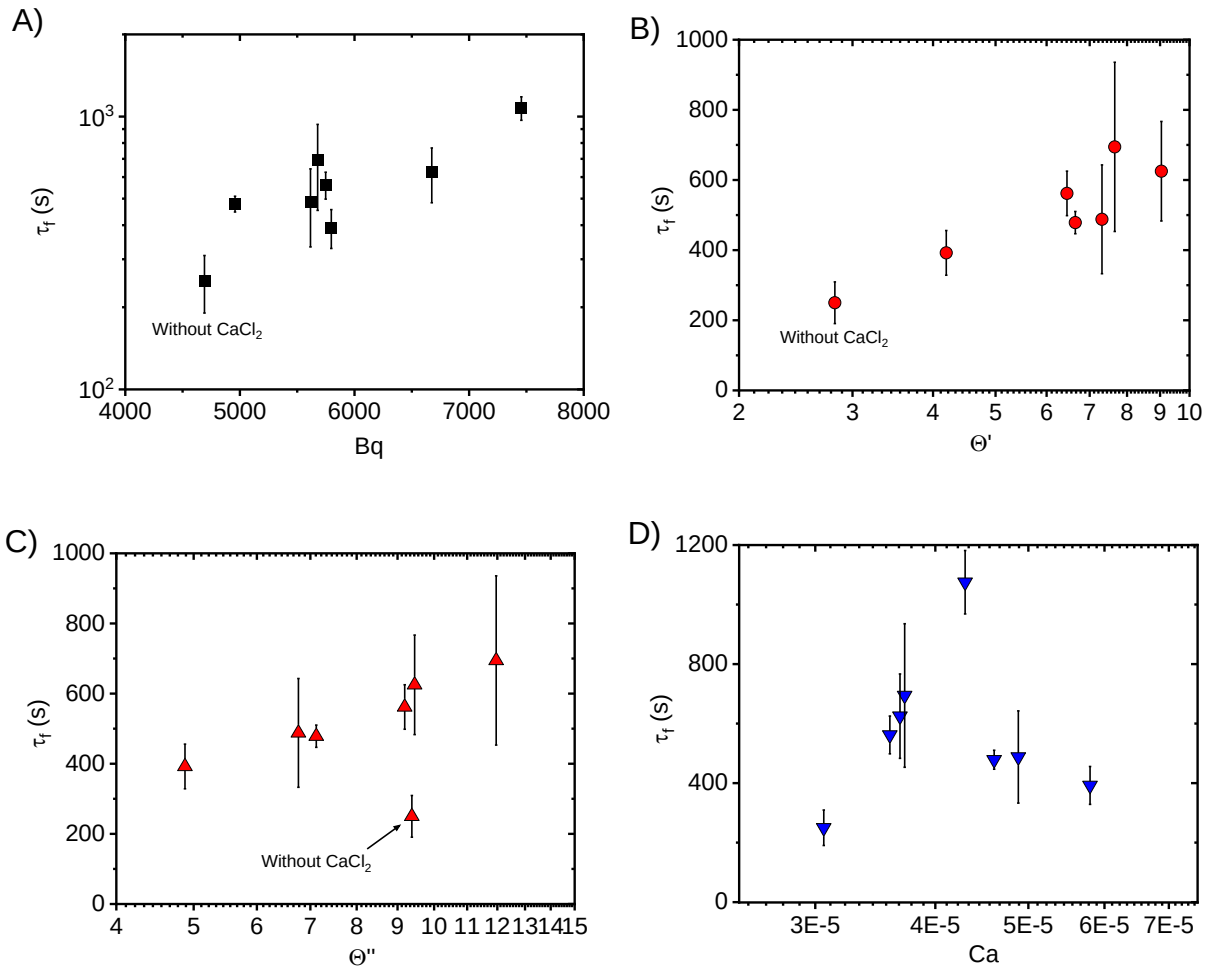

Figure 7.16 The dependency of foam half-life on the A) Boussinesq number, B) ratio of surface tension to interfacial dilatational elasticity, C) ratio of surface tension to dilatational loss modulus, and D) Capillary number for 0.4 mM KPFOS aqueous foams in the absence and presence of $CaCl_2$ with various concentrations. The air flow rate of 0.2 L/min was used to sparge the solutions for 30 s, and the filter has the pore size range of 40-100 μm.

Furthermore, the effect of surface tension, representing by Ca, is taken into account as seen in **Figure 7.16D**. It reveals that, despite the ratio of surface tension to either surface elasticity or surface viscosity, the stability of KPFOS foams is also corresponding to the sole factor of surface tension. When we talked about the foamability of KPFOS with various bulk concentrations in the Chapter 6, a maximum of $\frac{Hf}{Hl0}$ is obtained with increasing the Ca. Similar to it, the τ_f of KPFOS foams containing various $CaCl_2$ concentrations also shows a peak when increasing the Ca.

Moreover, **Figure 7.17** shows the change of Bq and Ca as a function of $CaCl_2$ concentrations. As seen, the increase in $CaCl_2$ concentration slightly affect the Bq, giving rise to a slightly increase of Bq. While increasing the concentration of $CaCl_2$ significantly increases the Ca for KPFOS foams.

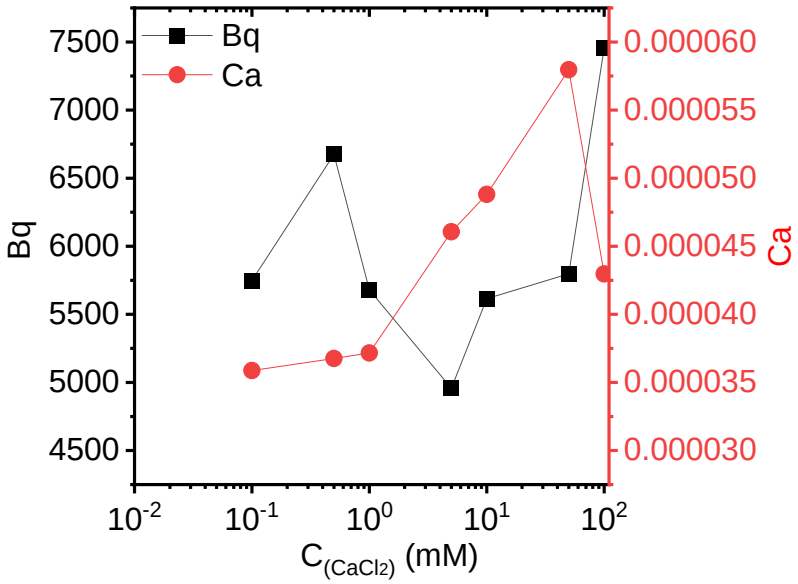

Figure 7.17 The variation of Boussinesq number (left y-axis) and Capillary number (right y-axis) of 0.4 mM KPFOS aqueous foams as a function of $CaCl_2$ concentrations.

7.6. Conclusions

In this present Chapter, three types of PFAS are used, including KPFOS, PFOA, and KPFBS to examine the defoaming process of PFAS aqueous foams by using the dynamic foam analyzer (*DFA 100*). The foam stability in terms of foam half-life, τ_f, is evaluated. In addition to the τ_f, the bubble size during the defoaming process is also monitored by using the *DFA 100*. The liquid content is modified based on the resistance provided by the liquid content sensors. The electrolytes including NaCl and $CaCl_2$ are introduced to further study the effect of salts on the stability of PFAS aqueous foams.

Our results show that KPFOS, PFOA and KPFBS aqueous foams have different foam stabilities. In terms of foam lifetime, KPFOS foams have the longest lifetime, followed by PFOA foams and KPFBS foams. The air injection rates not only influence the initial foam heights, but also affect the foam lifetime. For KPFOS, use of lower air injection rates results in a more stable foams, while increasing the air flow rate leads to a top-down foam collapse, and thus, the lifetime of foams decreases. This trend is also true if switching the glass filter with the one has a smaller pore size. However, for PFOA and KPFBS, the higher air injection rates improve the foam stability due to the longer τ_f. Furthermore, the bubble size is increasing along the foam structure collapse for KPFOS foams regardless of the initial foam heights (air injection rates). For PFOA and KPFBS, the trend of bubble size change is not yet clear since their foams completely collapse within 3 s. But if increasing the air injection rates, for example, the bubble size of KPFBS foams is increasing as the foams collapse. Additionally, the greater air flow rates tend to lower the bubble size. Comparing the liquid content, the same as the liquid content during the foam formation (see Chapter 5), KPFOS foams have the strongest ability to hold the water, followed by PFOA and KPFBS. The liquid content across the PFAS foams is different, less liquid content is associated with the higher foam height. The liquid content variation during the foam collapse follows the exponential decay function.

The addition of electrolytes remarkedly increases the foam stability, but it strongly depends on the salt concentration. For monovalent salt, i.e., NaCl, there is an optimized concentration where both foamability and foam stability of KPFOS approach the maximum, and the foamability and foam stability decreases until completely disappear when further increasing the NaCl concentration. However, the addition of NaCl qualitatively increases the PFOA foam stability as well as its foamability within the studied concentrations. Interestingly, upon addition divalent salts,

i.e., $CaCl_2$, the KPFOS foam stability is qualitatively enhanced, and it is positively correlated with the $CaCl_2$ concentrations, although the foaming capacity remains similar to the samples without adding $CaCl_2$. Nevertheless, the effect of adding $CaCl_2$ on PFOA foam properties is similar to the effect of NaCl on KPFOS, that is both foamability and foam stability reach the maximum when introducing 1 mM $CaCl_2$, followed by decreasing with an increase in $CaCl_2$ concentrations.

Lastly, the normalized osmotic pressure of KPFOS aqueous foams is increasing during the defoaming process, indicating that the PFAS aqueous foams are relatively unstable. Additionally, the top part of PFAS foams tends to have higher osmotic pressure due to the fast liquid drainage. We also found that the PFAS defoaming properties are strongly correlated with their interfacial properties. The evidence is that the lifetime of KPFOS foams containing $CaCl_2$ increases when increasing the Boussinesq number, or the effect of surface tension compared to the interfacial dilatational modulus.

Chapter 8. Summary and Future Work

8.1. Summary

The environmental and health impacts of PFAS have been well-documented, highlighting their persistent contamination over the years. Foam fractionation is proposed herein as a promising approach to separate PFAS from contaminated water sources. A critical component of this process involves analyzing the physicochemical properties of PFAS. The dissertation delves into the interfacial characteristics of PFAS, including their dynamic surface tension, interfacial dilatational rheology, and foam formation and collapse properties. Based on our investigative results, several primary conclusions are outlined:

- The surface tension of KPFOS and KPFBS as a function of their bulk concentration is measured, there is an absence of CMC identification up to their solubility limits. If defining KPFOS as C8 PFAS, KPFHxS as C6 PFAS, and KPFBS as C4 PFAS, the order of equilibrium surface tension for these sulfonated PFAS at a fixed concentration below the solubility limit is established as C8 < C8+C4 < C6 < C4. Also, C4 PFAS show a decreased adsorption coefficient at the air-water interface compared to C8 PFAS, indicating divergent adsorption dynamics between long-chain and short-chain PFAS. Based on the Gibbs and Langmuir adsorption isotherms, C4 PFAS exhibit a slightly higher maximum surface excess concentration compared to C8 PFAS.
- At low bulk concentration, C4 PFAS molecules at the air-water interface are insufficient to induce surface tension fluctuations during oscillation of a pendant drop at frequencies ranging from 0.05 Hz to 0.5 Hz. Consequently, comparisons should be made using the same surface tension instead of the same bulk concentration. In the case of C8 PFAS, i.e., KPFOS and PFOA,

E' was observed to be greater than E'', and both are influenced by the concentration and the oscillation rate. The change in modulus with frequency disappears when approaching the CMC (example: PFOA).

- A peak in both E' and E'' as a function of bulk concentration is noted for C8 PFAS (this part is for C8 PFAS due to the absence of surface tension oscillation for C4 PFAS), and this peak reflects the competitive dynamics between the adsorption and exchange of molecules. Applying the Lucassen and van den Tempel model allows for the fitting of the E' and E'' from which the diffusion coefficient (D_{L-T}) was calculated. A similar maximum for both E' and E'' as predicted by the model underscores the complex interactions governing interface behavior.
- When examining anionic PFAS with an equivalent carbon chain length but different acid head groups, i.e., KPFOS and PFOA (PFOA used in this dissertation was its acid form due to the unavailability of its potassium salts), it is observed that PFOA exhibits a higher solubility limit and increased surface tension. Importantly, PFOA presents a CMC at approximately 9.7 mM. According to our findings, the nature of the polar head groups of anionic PFAS does not significantly influence the maximum surface concentration of PFAS.
- According to the traditional Ward-Tordai model, for PFAS with longer chains, the diffusion coefficients are contingent upon their concentrations in the bulk, unveiling three distinct phases of diffusion behavior. When the bulk concentration is the same, the diffusion constant follows the order KPFBS < PFOA < KPFOS.
- The NaCl effect on C8 PFAS (KPFOS and PFOA) is studied. Upon an addition of NaCl, a reduction in surface tension is observed for C8 PFAS under study, indicative of an increased maximum surface excess concentration. NaCl addition leads to a downward shift in the CMC

towards lower concentration for C8 PFAS. With respect to diffusion coefficient, the KPFOS demonstrates a peak of diffusion coefficient at a NaCl concentration of 5 mM.

- The $CaCl_2$ effect on both C8 and C4 PFAS is studied. The introduction of $CaCl_2$ results in a decreased surface tension across the PFAS being examined, suggesting a rise in the maximum surface excess concentration. Additionally, this $CaCl_2$ addition results in a decrease in the CMC for C8 PFAS, moving to lower concentrations, an effect not observed in C4 PFAS, such as KPFBS studied herein. Additionally, $CaCl_2$ leads to an increase in the diffusion coefficients for all PFAS analyzed, with the rate of increase approaching a plateau at higher $CaCl_2$ levels.
- The addition of electrolytes to the PFAS system intricately affects interfacial dilatational rheology. When NaCl is added, there is a significant decrease followed by an increase in both the E' and E'' of KPFOS, a pattern not replicated in PFOA. $CaCl_2$ causes a pronounced reduction in E' for both KPFOS and PFOA, however, the change in E' with $CaCl_2$ concentration is in a smaller magnitude compared to the change with NaCl concentration. The $CaCl_2$ addition also lowers E'', but a reduction in E'' for KPFOS is more significant than that for PFOA. Furthermore, $CaCl_2$ addition induces measurable interfacial dilatational rheology in KPFBS, hinting at $CaCl_2$'s role in promoting the air-water interface adsorption of C4 PFAS.
- ^{19}F NMR spectra show the evidence of interaction between sulfonic acid headgroups in KPFOS and Ca^{2+} ions, with no interaction detected for Na^+ ions. Conversely, the carboxylic acid headgroups in PFOA interact with Na^+ ions rather than with Ca^{2+} ions. In addition to the interaction between the PFAS headgroups and salt ions, the formation of PFAS micelles is confirmed based on the ^{19}F NMR spectra. Furthermore, SAXS results show evidence that the Ca^{2+} ions affect the KPFOS micelles without any influence by Na^+ ions, while the reverse is true for PFOA micelles.

- KPFOS demonstrates the highest foaming capacity, followed by PFOA, and KPFBS showing the lowest.
- Exploring foaming capacity through dimensional analysis allows for the correlation of expansion rate of foaming (defined as the ratio of foam height and initial liquid height), foaming kinetics (defined as the slope of foam height during the early stage of foaming process), and liquid content to a set of dimensionless numbers. The expansion rate of KPFOS foams is closely linked to the Reynolds number (laminar) and Froude number, with its foaming kinetics being notably influenced by the Reynolds number. Furthermore, the liquid content in KPFOS foams is determined by the Reynolds number and capillary number. For PFOA, influences on the foaming expansion rate come from the Froude number, and its foaming velocity is subject to change by the Reynolds number and Boussinesq number, with water retention capacity linked to the capillary number. Conversely, the expansion rate and liquid content of KPFBS foams, is primarily affected by the Froude number, with the foaming kinetics showing no dependence on any of the dimensionless numbers studied here.
- The bubble size also contributes to the foaming behavior of C8 PFAS. The foaming expansion rate and liquid content of KPFOS is influenced by the foam bubble size. Additionally, the bubble size affects the foaming expansion rate and foaming kinetics of PFOA in the presence of NaCl. However, the effect of bubble size on the C4 PFAS, KPFBS in our study, is not significant.
- At a concentration of 0.4 mM, KPFOS exhibits the highest foam height found in this study, correlating with the peak in foaming expansion rate over the capillary number as well as the highest dilatational interfacial modulus. In the case of PFOA, the foaming expansion rate is greatly improved by adding NaCl at concentrations between 5-50 mM, where the maximal

foaming expansion rate is noted with changing the capillary number. The maximal foaming expansion rate also corresponds to a maximum in the ratio of surface tension to dilatational interfacial moudulus. This dissertation also illustrates the importance of interfacial rheology on the foaming speed of PFAS.

- The foam stability of PFAS aqueous foams varies across different PFAS compounds, with KPFOS foams showing the longest lifetime, followed by PFOA and KPFBS foams. The initial heights and the lifetime are directly affected by the rates of air injection. KPFOS foams exhibit bubble growth during foam collapse. In terms of liquid content, KPFOS foams demonstrate the highest liquid content, followed by PFOA and KPFBS foams. This study also notes a rise in normalized osmotic pressure to Laplace pressure in KPFOS foams during defoaming, indicating the instability of PFAS foams. A strong correlation between PFAS defoaming properties and their interfacial properties is observed with respect to the Boussinesq number, the ratio of surface tension to dilatational interfacial elasticity, the ratio of surface tension to dilatational interfacial viscosity, as well as the capillary number.
- The introduction of electrolytes markedly boosts foam stability, albeit with a pronounced dependency on salt concentration. In the case of introducing NaCl, there is a specific concentration at which KPFOS foamability and stability are optimized. On the other hand, $CaCl_2$ enhances KPFOS foam stability in a monotonic manner with improvements directly proportional to the $CaCl_2$ concentration. Nonetheless, the addition of NaCl effectively improves the stability of PFOA foams, while an optimized concentration range of $CaCl_2$ exists to increase the foam stability for PFAS.

8.2. Future work

As previously discussed in the literature,[81,82,87,88] the introduction of electrolytes has been shown to improve the efficiency of PFAS removal through foam fractionation. However, the underlying mechanisms, particularly in relation to divalent and trivalent salt ions, have not been extensively investigated. Upon the addition of various concentrations of electrolytes, the dynamics—such as the behavior of PFAS molecules or micelle structures, along with interfacial rheology—become more complex, a point we have detailed in earlier Chapters. Our findings in Chapter 5 suggest a pronounced likelihood of interaction between KPFOS molecules and divalent salts, specifically $CaCl_2$, while PFOA molecules exhibit a preference for monovalent salts like NaCl. To elucidate the specific interactions between salt ions and the polar head groups of PFAS molecules, including their fluorinated chains, additional characterization techniques, such as dynamic light scattering (DLS) and ultraviolet-visible spectroscopy (UV-vis), are imperative. Moreover, investigating a broader range of electrolyte concentrations and short-chain PFAS types, such as KPFBS, is essential for a more comprehensive understanding of the intermolecular interactions between PFAS compounds and ions.

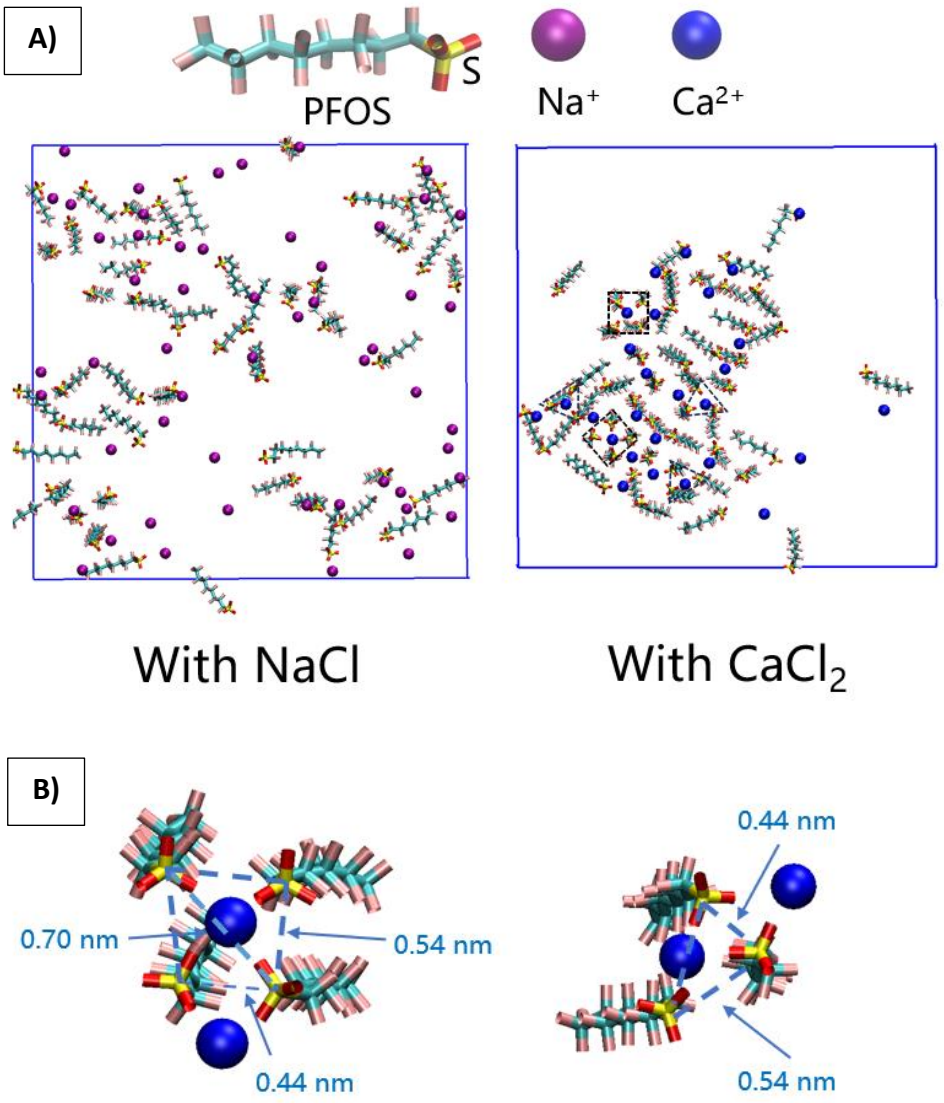

Figure 8.1 A) PFOS molecules at the air-water interface in the presence of Na^+ and Ca^{2+}, respectively, based on the MD simulations. B) Two predicted complex structures of KPFOS when introducing the Ca^{2+}. (Provided by Dr. Zhehui Jin's group at the University of Alberta)

Researchers at the University of Alberta are currently collaborating with us and employing Molecular Dynamics (MD) simulations to examine the structural transformations of KPFOS and PFOA at the air-water interface, influenced by the presence of NaCl and $CaCl_2$. The initial findings from Dr. Zhehui Jin's group are depicted in **Figure 8.1** (top view), highlighting the emergence of a complex structure of KPFOS molecules at the air-water interface following the introduction of

$CaCl_2$. No complex strucrure observed with the addition of NaCl. Additionally, **Figure 8.1B** reveals two potential configurations of the KPFOS complex when $CaCl_2$ is present, one has the rhombus structure, another one has the triangle structure.

Future research directions include, but are not limited to, examining the effects of additives such as co-surfactants and Fe_3O_4 nanoparticles on 1) the properties of PFAS foams, such as film and foam stability, 2) variations in micelle structure, and 3) interfacial rheological properties. The small-angle neutron scattering (SANS) results suggest micelle growth following NaCl addition, as illustrated in **Figure 8.2**.[123] However, this study was limited to a single concentration of NaCl and only explored the behavior of sodium perfluorohexanoate (NaPFHx) and sodium perfluorooctanoate (NaPFO). To comprehensively understand PFAS micellization, it is recommended to extend investigations to include electrolytes, co-surfactants, solvents, other organic compounds, and their combinations. Additionally, given that PFAS mixtures are prevalent in natural environments and previous reports indicate changes in micelle shape with the presence of two surfactants, a deeper understanding of micelle configurations within PFAS mixture systems remains a critical gap in current knowledge.

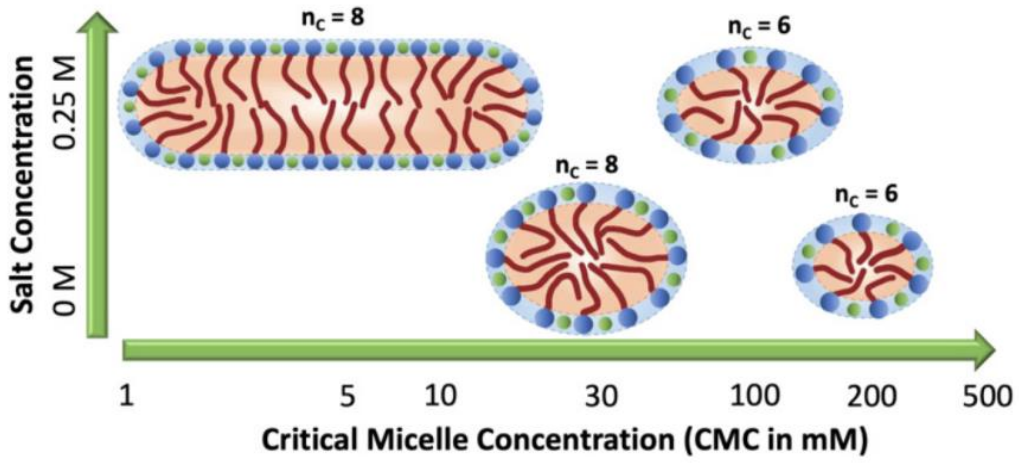

Figure 8.2 Effects of NaCl addition and PFAS chain length on PFAS micelle shape.[123]

The inclusion of co-surfactants, such as the cationic surfactant cetrimonium bromide (CTAB), in PFAS solutions offers a unique opportunity to investigate adsorption and foaming behaviors.[54,89,90] **Figure 8.3** demonstrates that the incorporation of dodecyltrimethylammonium bromide (DTAB), another cationic surfactant, significantly enhances the foaming capacity of short-chain KPFBS. As discussed in Chapter 5, achieving measurable foam heights with 0.4 mM KPFBS proved challenging when aerating the solutions at a rate of 0.2 L/min. While DTAB has been shown to improve PFAS removal efficiency via foam flotation, the mechanisms behind its impact on interfacial properties, micelle behavior, and foam stability have yet to be explored in depth.[54] Moreover, the study of ternary systems, comprising PFAS, a co-surfactant, and salts, presents a promising research avenue, albeit one that is currently underexplored.

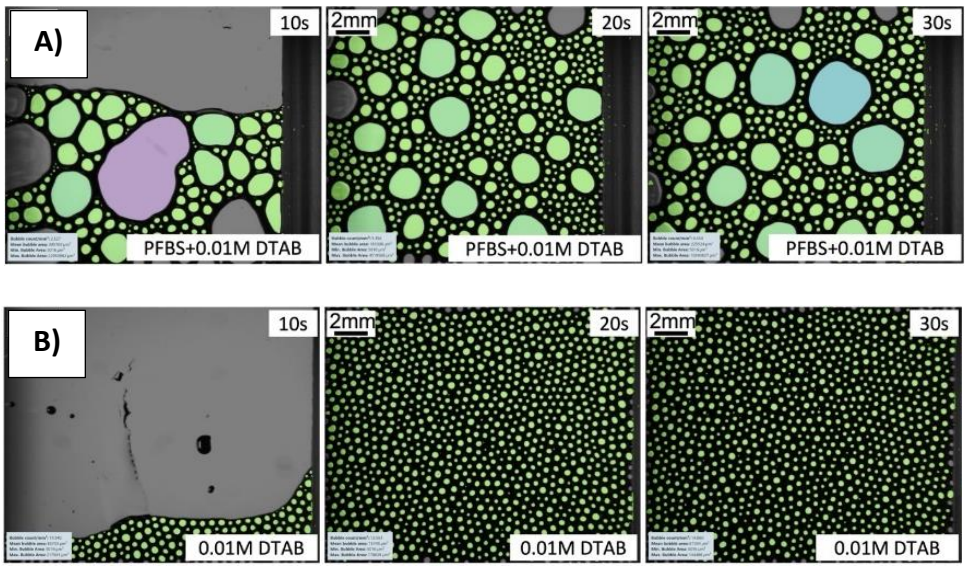

Figure 8.3 Foam structure at 10 s, 20 s, and 30 s during foaming process by using the air flow rate of 0.2 L/min for A) 0.4 mM KPFBS aqueous foams containing 10 mM DTAB, and B) 10 mM DTAB aqueous foams. The filter has the pore size of 40-100 µm.

Nanoparticles, such as Fe_3O_4 nanoparticles, are versatile additives for stabilizing foams, notably in the formation of Pickering foams.[199] We synthesized the neat Fe_3O_4 nanoparticles as well as the oleic acid-coated Fe_3O_4 nanoparticles, the latter is for tuning their wettability. **Figures**

8.4A and **8.4B** are the scanning electron microscopy (SEM) and transmission electron microscopy (TEM) images of synthesized neat Fe_3O_4 nanoparticles, showing the morphology. **Figure 8.5** is the DLS results of the hydrophilic Fe_3O_4 nanoparticle suspensions, showing their particle size. Even though the Fe_3O_4 nanoparticles are hydrophilic, they can also be used to stabilize the foams. However, the stabilization mechanism is different for hydrophilic particles compared to that for hydrophobic particles.[188] The myriad factors influencing foam dynamics include particle size, concentration, wettability, shape, and type. It is noteworthy that salt addition modifies the electrostatic interactions between nanoparticles by altering surfactant micelle charges, thus affecting Pickering foam properties.[188] Future investigations should elucidate the impact of varying Fe_3O_4 nanoparticle concentrations and their wettability on the foaming and defoaming properties of PFAS, encompassing foamability, drainage velocity, and the rate of thin film rupture.

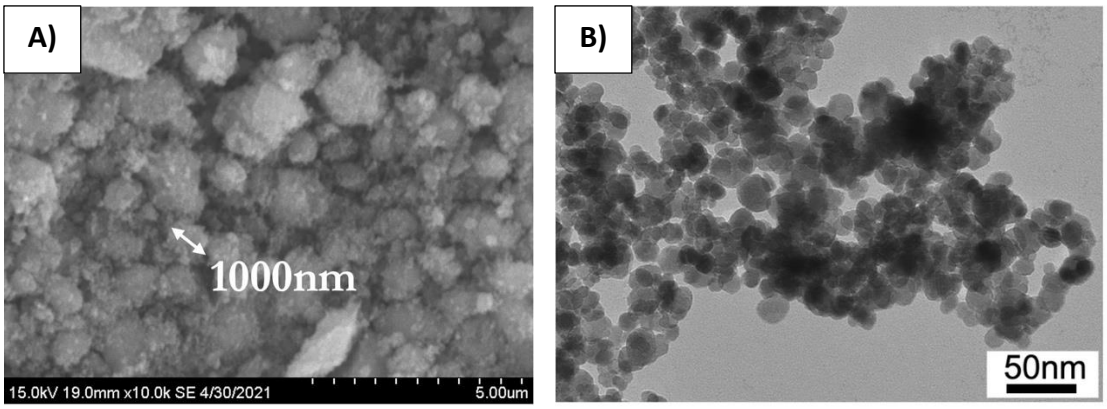

Figure 8.4 A) SEM, and B) TEM images of as-synthesized Fe_3O_4 nanoparticles.

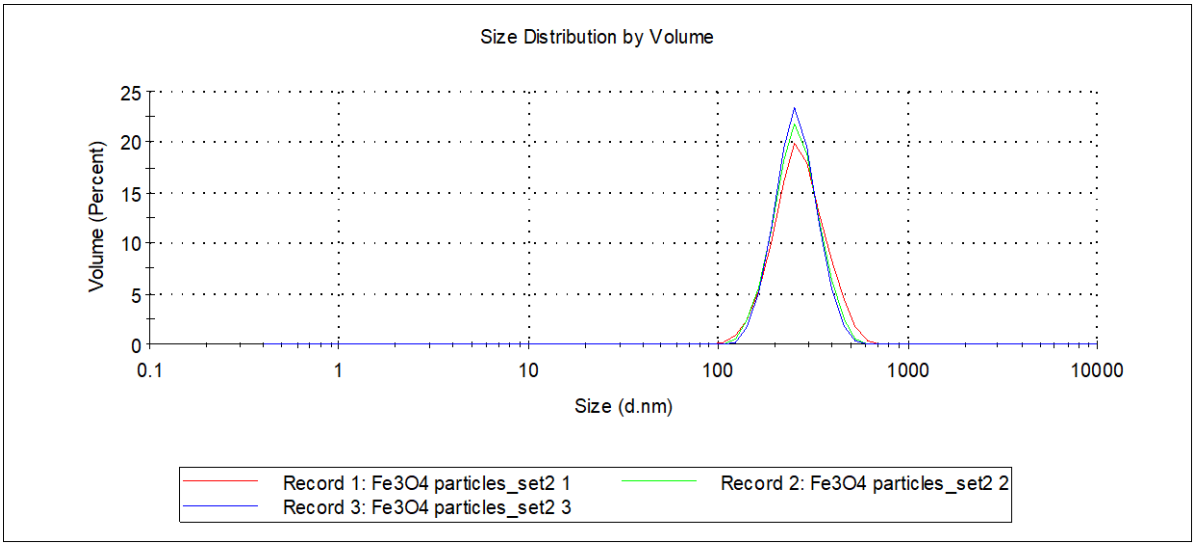

Figure 8.5 Particle size distribution of hydrophilic Fe_3O_4 nanoparticle suspensions.

References

1. Zhang Z, Sarkar D, Biswas JK, Datta R. Biodegradation of per- and polyfluoroalkyl substances (PFAS): A review. *Bioresour Technol*. 2022;344:126233. doi:10.1016/j.biortech.2021.126223

2. Gagliano E, Sgroi M, Falciglia PP, Vagliasindi FGA, Roccaro P. Removal of poly- and perfluoroalkyl substances (PFAS) from water by adsorption: Role of PFAS chain length, effect of organic matter and challenges in adsorbent regeneration. *Water Res*. 2020;171:115381. doi:10.1016/j.watres.2019.115381

3. Buck RC, Franklin J, Berger U, et al. Perfluoroalkyl and polyfluoroalkyl substances in the environment: Terminology, classification, and origins. *Integr Environ Assess Manag*. 2011;7(4):513-541. doi:10.1002/ieam.258

4. Kempisty DM, Xing Y (Writer on chemistry), Racz L. *Perfluoroalkyl Substances in the Environment : Theory, Practice, and Innovation*.; 2018.

5. Brusseau ML. Assessing the potential contributions of additional retention processes to PFAS retardation in the subsurface. *Sci Total Environ*. 2018;613-614. doi:10.1016/j.scitotenv.2017.09.065

6. Wang Y, Darling SB, Chen J. Selectivity of Per- And Polyfluoroalkyl Substance Sensors and Sorbents in Water. *ACS Appl Mater Interfaces*. 2021;13(51):60789-60814. doi:10.1021/acsami.1c16517

7. Phong Vo HN, Ngo HH, Guo W, et al. Poly-and perfluoroalkyl substances in water and wastewater: A comprehensive review from sources to remediation. *J Water Process Eng*. 2020;36:101393. doi:10.1016/j.jwpe.2020.101393

8. Coates G, Rekhroukh F, Crimmin MR. Breaking carbon-fluorine bonds with main group nucleophiles. *Synlett*. 2019;30(20). doi:10.1055/s-0039-1690738

9. Henry BJ, Carlin JP, Hammerschmidt JA, et al. A critical review of the application of polymer of low concern and regulatory criteria to fluoropolymers. *Integr Environ Assess Manag*. 2018;14(3). doi:10.1002/ieam.4035

10. Ambaye TG, Vaccari M, Prasad S, Rtimi S. Recent progress and challenges on the removal of per- and poly-fluoroalkyl substances (PFAS) from contaminated soil and water. *Environ Sci Pollut Res*. 2022;29(39):58405-58428. doi:10.1007/s11356-022-21513-2

11. States Environmental Protection Agency U. *United States Environmental Protection Agency Multi-Industry Per-and Polyfluoroalkyl Substances (PFAS) Study-2021 Preliminary Report*.; 2021.

12. Wang S, Huang J, Yang Y, et al. First report of a Chinese PFOS alternative overlooked for 30 years: Its toxicity, persistence, and presence in the environment. *Environ Sci Technol*. 2013;47(18):10163-10170. doi:10.1021/es401525n

13. Giesy JP, Kannan K. Global distribution of perfluorooctane sulfonate in wildlife. *Environ Sci Technol*. 2001;35(7). doi:10.1021/es001834k

14. Jahnke A, Huber S, Temme C, Kylin H, Berger U. Development and application of a simplified sampling method for volatile polyfluorinated alkyl substances in indoor and environmental air. *J Chromatogr A*. 2007;1164(1-2). doi:10.1016/j.chroma.2007.06.068

15. Lee H, Mabury SA. A pilot survey of legacy and current commercial fluorinated chemicals in human sera from United States donors in 2009. *Environ Sci Technol*. 2011;45(19). doi:10.1021/es200167q

16. Wang N, Szostek B, Buck RC, Folsom PW, Sulecki LM, Gannon JT. 8-2 Fluorotelomer alcohol aerobic soil biodegradation: Pathways, metabolites, and metabolite yields. *Chemosphere*. 2009;75(8). doi:10.1016/j.chemosphere.2009.01.033

17. Ebnesajjad S. *Introduction to Fluoropolymers: Materials, Technology, and Applications*.; 2013. doi:10.1016/C2012-0-06184-4

18. Luo Y, Gibson CT, Chuah C, Tang Y, Naidu R, Fang C. Raman imaging for the identification of Teflon microplastics and nanoplastics released from non-stick cookware. *Sci Total Environ*. 2022;851. doi:10.1016/j.scitotenv.2022.158293

19. Kurwadkar S, Dane J, Kanel SR, et al. Per- and polyfluoroalkyl substances in water and wastewater: A critical review of their global occurrence and distribution. *Sci Total Environ*. 2022;809:151003. doi:10.1016/j.scitotenv.2021.151003

20. Li J, Sun J, Li P. Exposure routes, bioaccumulation and toxic effects of per- and polyfluoroalkyl substances (PFASs) on plants: A critical review. *Environ Int*. 2022;158:106891. doi:10.1016/j.envint.2021.106891

21. Hu XC, Andrews DQ, Lindstrom AB, et al. Detection of Poly- and Perfluoroalkyl Substances (PFASs) in U.S. Drinking Water Linked to Industrial Sites, Military Fire Training Areas, and Wastewater Treatment Plants. *Environ Sci Technol Lett*. 2016;3(10):344-350. doi:10.1021/acs.estlett.6b00260

22. Meegoda JN, Kewalramani JA, Li B, Marsh RW. A review of the applications, environmental release, and remediation technologies of per-and polyfluoroalkyl substances. *Int J Environ Res Public Health*. 2020;17(21). doi:10.3390/ijerph17218117

23. Mauritz KA, Moore RB. State of understanding of Nafion. *Chem Rev*. 2004;104(10). doi:10.1021/cr0207123

24. Lee JH, Doo G, Kwon SH, Choi S, Kim HT, Lee SG. Dispersion-Solvent Control of Ionomer Aggregation in a Polymer Electrolyte Membrane Fuel Cell. *Sci Rep*. 2018;8(1). doi:10.1038/s41598-018-28779-y

25. Kim DJ, Jo MJ, Nam SY. A review of polymer-nanocomposite electrolyte membranes for fuel cell application. *J Ind Eng Chem*. 2015;21. doi:10.1016/j.jiec.2014.04.030

26. Zeynali ME, Mohammadi F, Rabiee A. Structural analysis and defect evaluation of ion exchange composite membranes used in electrolysis of sodium chloride in chlor-alkali process. *Iran Polym J (English Ed*. 2015;24(2). doi:10.1007/s13726-014-0302-3

27. Shi Y, Lu Z, Guo L, Yan C. Fabrication of membrane electrode assemblies by direct spray catalyst on water swollen Nafion membrane for PEM water electrolysis. *Int J Hydrogen Energy*. 2017;42(42). doi:10.1016/j.ijhydene.2017.08.205

28. Karimi MB, Mohammadi F, Hooshyari K. Recent approaches to improve Nafion performance for fuel cell applications: A review. *Int J Hydrogen Energy*. 2019;44(54). doi:10.1016/j.ijhydene.2019.09.096

29. Chen HW, Wu RJ, Chan KH, Sun YL, Su PG. The application of CNT/Nafion composite material to low humidity sensing measurement. *Sensors Actuators, B Chem*. 2005;104(1). doi:10.1016/j.snb.2004.04.105

30. Prykhodko Y, Fatyeyeva K, Hespel L, Marais S. Progress in hybrid composite Nafion®-based membranes for proton exchange fuel cell application. *Chem Eng J*. 2021;409. doi:10.1016/j.cej.2020.127329

31. Kissa E. *Fluorinated Surfactants and Repellents, 2nd Ed., Rev. and Expanded*.; 2001.

32. Stevenson P. *Foam Engineering: Fundamentals and Applications*.; 2012. doi:10.1002/9781119954620

33. Favreau P, Poncioni-Rothlisberger C, Place BJ, et al. Multianalyte profiling of per- and polyfluoroalkyl substances (PFASs) in liquid commercial products. *Chemosphere*. 2017;171. doi:10.1016/j.chemosphere.2016.11.127

34. Zafeiraki E, Costopoulou D, Vassiliadou I, Bakeas E, Leondiadis L. Determination of perfluorinated compounds (PFCs) in various foodstuff packaging materials used in the Greek market. *Chemosphere*. 2014;94. doi:10.1016/j.chemosphere.2013.09.092

35. Epa U, of Water O. *FACT SHEET PFOA & PFOS Drinking Water Health Advisories*.; 2016.

36. *Regulating Drinking Water Contaminants: EPA PFAS Actions*.; 2022. https://crsreports.congress.gov.

37. *Federal Register Notice on Lifetime Drinking Water Health Advisories for Four Perfluoroalkyl Substances*.; 2022. http://www.ferc.gov/.

38. *State Water Resources Control Board Division of Water Quality GAMA Program*.; 2019. https://www.waterboards.ca.gov/drinking_water/certlic/drinkingwater/PFOA_PFOS.html.

39. Sunderland EM, Hu XC, Dassuncao C, Tokranov AK, Wagner CC, Allen JG. A review of the pathways of human exposure to poly- and perfluoroalkyl substances (PFASs) and present understanding of health effects. *J Expo Sci Environ Epidemiol*. 2019;29(2):131-147. doi:10.1038/s41370-018-0094-1

40. Taves DR. Evidence that there are two forms of fluoride in human serum. *Nature*. 1968;217(5133). doi:10.1038/2171050b0

41. Cousins IT, Vestergren R, Wang Z, Scheringer M, McLachlan MS. The precautionary principle and chemicals management: The example of perfluoroalkyl acids in groundwater. *Environ Int*. 2016;94. doi:10.1016/j.envint.2016.04.044

42. Blake BE, Fenton SE. Early life exposure to per- and polyfluoroalkyl substances (PFAS) and latent health outcomes: A review including the placenta as a target tissue and possible driver of peri- and postnatal effects. *Toxicology*. 2020;443:152565. doi:10.1016/j.tox.2020.152565

43. Bolan N, Sarkar B, Vithanage M, et al. Distribution, behaviour, bioavailability and remediation of poly- and per-fluoroalkyl substances (PFAS) in solid biowastes and biowaste-treated soil. *Environ Int*. 2021;155. doi:10.1016/j.envint.2021.106600

44. Lv G, Wang L, Liu S, Li S. Determination of perfluorinated compounds in packaging materials and textiles using pressurized liquid extraction with gas chromatography-mass spectrometry. *Anal Sci*. 2009;25(3). doi:10.2116/analsci.25.425

45. Begley TH, White K, Honigfort P, Twaroski ML, Neches R, Walker RA. Perfluorochemicals: Potential sources of and migration from food packaging. *Food Addit Contam*. 2005;22(10). doi:10.1080/02652030500183474

46. Dolman S, Pelzing M. An optimized method for the determination of perfluorooctanoic acid, perfluorooctane sulfonate and other perfluorochemicals in different matrices using liquid chromatography/ion-trap mass spectrometry. *J Chromatogr B Anal Technol Biomed Life Sci*. 2011;879(22). doi:10.1016/j.jchromb.2011.05.032

47. Poothong S, Boontanon SK, Boontanon N. Determination of perfluorooctane sulfonate and perfluorooctanoic acid in food packaging using liquid chromatography coupled with tandem mass spectrometry. *J Hazard Mater*. 2012;205-206. doi:10.1016/j.jhazmat.2011.12.050

48. Kotthoff M, Müller J, Jürling H, Schlummer M, Fiedler D. Perfluoroalkyl and polyfluoroalkyl substances in consumer products. *Environ Sci Pollut Res*. 2015;22(19). doi:10.1007/s11356-015-4202-7

49. Liu X, Zheng X, Zhang L, et al. Joint Toxicity Mechanisms of Binary Emerging Pfas Mixture on Algae (Chlorella Pyrenoidosa) at Environmental Concentration. *SSRN Electron J*. 2022;437:129355. doi:10.2139/ssrn.4063771

50. Pan CG, Liu YS, Ying GG. Perfluoroalkyl substances (PFASs) in wastewater treatment plants and drinking water treatment plants: Removal efficiency and exposure risk. *Water Res*. 2016;106:562-570. doi:10.1016/j.watres.2016.10.045

51. Gallen C, Drage D, Eaglesham G, Grant S, Bowman M, Mueller JF. Australia-wide assessment of perfluoroalkyl substances (PFASs) in landfill leachates. *J Hazard Mater*. 2017;331. doi:10.1016/j.jhazmat.2017.02.006

52. Zhang H, Wen B, Wen W, et al. Determination of perfluoroalkyl acid isomers in biosolids, biosolids-amended soils and plants using ultra-high performance liquid chromatography tandem mass spectrometry. *J Chromatogr B Anal Technol Biomed Life Sci*. 2018;1072. doi:10.1016/j.jchromb.2017.09.036

53. Ghisi R, Vamerali T, Manzetti S. Accumulation of perfluorinated alkyl substances (PFAS) in agricultural plants: A review. *Environ Res*. 2019;169. doi:10.1016/j.envres.2018.10.023

54. Li YF, Chien WY, Liu YJ, Lee YC, Lo SL, Hu CY. Perfluorooctanoic acid (PFOA)

removal by flotation with cationic surfactants. *Chemosphere*. 2021;266:128949. doi:10.1016/j.chemosphere.2020.128949

55. Lenka SP, Kah M, Padhye LP. A review of the occurrence, transformation, and removal of poly- and perfluoroalkyl substances (PFAS) in wastewater treatment plants. *Water Res*. 2021;199:117187. doi:10.1016/j.watres.2021.117187

56. Andrews DQ, Naidenko O V. Population-Wide Exposure to Per- And Polyfluoroalkyl Substances from Drinking Water in the United States. *Environ Sci Technol Lett*. 2020;7(12):931-936. doi:10.1021/acs.estlett.0c00713

57. Daly ER, Chan BP, Talbot EA, et al. Per- and polyfluoroalkyl substance (PFAS) exposure assessment in a community exposed to contaminated drinking water, New Hampshire, 2015. *Int J Hyg Environ Health*. 2018;221(3):569-577. doi:10.1016/j.ijheh.2018.02.007

58. Fenton SE, Ducatman A, Boobis A, et al. Per- and Polyfluoroalkyl Substance Toxicity and Human Health Review: Current State of Knowledge and Strategies for Informing Future Research. *Environ Toxicol Chem*. 2021;40(3):606-630. doi:10.1002/etc.4890

59. Zhang L, Liang J, Gao A. Contact to perfluoroalkyl substances and thyroid health effects: A meta-analysis directing on pregnancy. *Chemosphere*. 2023;315. doi:10.1016/j.chemosphere.2023.137748

60. Blomberg AJ, Norén E, Haug LS, et al. Estimated Transfer of Perfluoroalkyl Substances (PFAS) from Maternal Serum to Breast Milk in Women Highly Exposed from Contaminated Drinking Water: A Study in the Ronneby Mother–Child Cohort. *Environ Health Perspect*. 2023;131(1). doi:10.1289/EHP11292

61. Liu Y, Li A, An Q, et al. Prenatal and postnatal transfer of perfluoroalkyl substances from mothers to their offspring. *Crit Rev Environ Sci Technol*. 2022;52(14):2510-2537. doi:10.1080/10643389.2021.1886556

62. Rickard BP, Rizvi I, Fenton SE. Per- and poly-fluoroalkyl substances (PFAS) and female reproductive outcomes: PFAS elimination, endocrine-mediated effects, and disease. *Toxicology*. 2022;465:153031. doi:10.1016/j.tox.2021.153031

63. Pierozan P, Kosnik M, Karlsson O. High-content analysis shows synergistic effects of low perfluorooctanoic acid (PFOS) and perfluorooctane sulfonic acid (PFOA) mixture concentrations on human breast epithelial cell carcinogenesis. *Environ Int*. January 2023:107746. doi:10.1016/j.envint.2023.107746

64. Ross I, McDonough J, Miles J, et al. A review of emerging technologies for remediation of PFASs. *Remediation*. 2018;28(2):101-126. doi:10.1002/rem.21553

65. Abbasian Chaleshtari Z, Foudazi R. A Review on Per- and Polyfluoroalkyl Substances (PFAS) Remediation: Separation Mechanisms and Molecular Interactions. *ACS ES&T Water*. 2022;2(12):2258-2272. doi:10.1021/acsestwater.2c00271

66. Tang CY, Fu QS, Criddle CS, Leckie JO. Effect of flux (transmembrane pressure) and membrane properties on fouling and rejection of reverse osmosis and nanofiltration membranes treating perfluorooctane sulfonate containing wastewater. *Environ Sci Technol*. 2007;41(6):2008-2014. doi:10.1021/es062052f

67. Steinle-Darling E, Reinhard M. Nanofiltration for trace organic contaminant removal: Structure, solution, and membrane fouling effects on the rejection of perfluorochemicals. *Environ Sci Technol*. 2008;42(14):5292-5297. doi:10.1021/es703207s

68. Ross I, Hurst J, Miles J, et al. Optimizing the PFAS puzzle: piecing together a holistic PFAS restoration strategy. In: *Proceedings of the 8th International Contaminated Site Remediation Conference*. ; 2019.

69. *Pennsylvania - PFAS Action Team Initial Report*. https://www.governor.pa.gov/wp-content/uploads/2019/12/20191205-PFAS-Action-Team-Initial-Report-Pennsylvania.pdf. Accessed March 30, 2022.

70. Abbasian Chaleshtari Z, Foudazi R. A Review on Per- and Polyfluoroalkyl Substances (PFAS) Remediation: Separation Mechanisms and Molecular Interactions. *ACS ES&T Water*. 2022;2(12):2258-2272. doi:10.1021/acsestwater.2c00271

71. Lyu Y, Brusseau ML, Chen W, Yan N, Fu X, Lin X. Adsorption of PFOA at the Air-Water Interface during Transport in Unsaturated Porous Media. *Environ Sci Technol*. 2018;52(14). doi:10.1021/acs.est.8b02348

72. Hilgenfeldt S, Koehler SA, Stone HA. Dynamics of coarsening foams: Accelerated and self-limiting drainage. *Phys Rev Lett*. 2001;86(20):4704. doi:10.1103/PhysRevLett.86.4704

73. Saint-Jalmes A. Physical chemistry in foam drainage and coarsening. *Soft Matter*. 2006;2(10):836-849. doi:10.1039/b606780h

74. Wang J, Nguyen A V., Farrokhpay S. A critical review of the growth, drainage and collapse of foams. *Adv Colloid Interface Sci*. 2016;228:55-70. doi:10.1016/j.cis.2015.11.009

75. Ravera F, Loglio G, Kovalchuk VI. Interfacial dilational rheology by oscillating bubble/drop methods. *Curr Opin Colloid Interface Sci*. 2010;15(4):217-228. doi:10.1016/j.cocis.2010.04.001

76. Wang C, Fang H, Gong Q, et al. Roles of Catanionic Surfactant Mixtures on the Stability of Foams in the Presence of Oil. *Energy and Fuels*. 2016;30(8):6355-6364. doi:10.1021/acs.energyfuels.6b01112

77. Sharma SC, Shrestha LK, Aramaki K. Foam Stability Study of Dilute Aqueous Nonionic Fluorinated Surfactant Systems. *J Nepal Chem Soc*. 2007;22:47-54. doi:10.3126/jncs.v22i0.522

78. Wang C, Zhao L, Xu B cai, et al. Effect of dynamic interfacial dilational properties on the foam stability of catanionic surfactant mixtures in the presence of oil. *Colloids Surfaces A Physicochem Eng Asp*. 2018;541:78-86. doi:10.1016/j.colsurfa.2018.01.019

79. Lexis M, Willenbacher N. Yield stress and elasticity of aqueous foams from protein and surfactant solutions - The role of continuous phase viscosity and interfacial properties. *Colloids Surfaces A Physicochem Eng Asp*. 2014;459:177-185. doi:10.1016/j.colsurfa.2014.06.030

80. Langevin D. Influence of interfacial rheology on foam and emulsion properties. *Adv Colloid Interface Sci*. 2000;88(1-2):209-222. doi:10.1016/S0001-8686(00)00045-2

81. Lee YC, Wang PY, Lo SL, Huang CP. Recovery of perfluorooctane sulfonate (PFOS) and perfluorooctanoate (PFOA) from dilute water solution by foam flotation. *Sep Purif Technol*. 2017;173:280-285. doi:10.1016/j.seppur.2016.09.012

82. Meng P, Deng S, Maimaiti A, et al. Efficient removal of perfluorooctane sulfonate from aqueous film-forming foam solution by aeration-foam collection. *Chemosphere*. 2018;203:263-270. doi:10.1016/j.chemosphere.2018.03.183

83. Zhang W, Liang Y. Removal of eight perfluoroalkyl acids from aqueous solutions by aeration and duckweed. *Sci Total Environ*. 2020;724:138357. doi:10.1016/j.scitotenv.2020.138357

84. Chen J, Adegbule A, Huang J, Brooks MC. *Surface-Active Behavior of Select Per-and Polyfluoroalkyl Substances (PFAS) and Their Mixtures (PFOA: C 8 HF 15 O 2).*; 2022.

85. Bois R, Adriao O, Delaplace G, Pezron I, Nesterenko A, Van-Hecke E. Influence of process variables on foaming ability of surfactants: Experimental study and dimensional analysis. *Chem Eng Res Des*. 2021;165:40-50. doi:10.1016/j.cherd.2020.10.021

86. Mary G, Mezdour S, Delaplace G, Lauhon R, Cuvelier G, Ducept F. Modelling of the continuous foaming operation by dimensional analysis. *Chem Eng Res Des*. 2013;91(12):2579-2586. doi:10.1016/j.cherd.2013.05.020

87. Morrison AL, Strezov V, Niven RK, et al. Impact of Salinity and Temperature on Removal of PFAS Species from Water by Aeration in the Absence of Additional Surfactants: A Novel Application of Green Chemistry Using Adsorptive Bubble Fractionation. *Ind Eng Chem Res*. 2023;62(13):5635-5645. doi:10.1021/acs.iecr.3c00150

88. Buckley T, Karanam K, Xu X, Shukla P, Firouzi M, Rudolph V. Effect of mono- and di-valent cations on PFAS removal from water using foam fractionation – A modelling and experimental study. *Sep Purif Technol*. 2022;286:120508. doi:10.1016/j.seppur.2022.120508

89. Buckley T, Karanam K, Han H, et al. Effect of different co-foaming agents on PFAS removal from the environment by foam fractionation. *Water Res*. 2023;230:119532. doi:10.1016/j.watres.2022.119532

90. Vo PHN, Buckley T, Xu X, Nguyen TMH, Rudolph V, Shukla P. Foam fractionation of per- and polyfluoroalkyl substances (PFASs) in landfill leachate using different cosurfactants. *Chemosphere*. 2023;310:136869. doi:10.1016/j.chemosphere.2022.136869

91. Martínez-Balbuena L, Arteaga-Jiménez A, Hernández-Zapata E, Márquez-Beltrán C. Applicability of the Gibbs Adsorption Isotherm to the analysis of experimental surface-tension data for ionic and nonionic surfactants. *Adv Colloid Interface Sci*. 2017;247:178-184. doi:10.1016/j.cis.2017.07.018

92. Zhou M, Foudazi R. Effect of Cosurfactant on Structure and Properties of Polymerized High Internal Phase Emulsions (PolyHIPEs). *Langmuir*. 2021;37(26):7909-7918. doi:10.1021/acs.langmuir.1c00419

93. Chang CH, Franses EI. Adsorption dynamics of surfactants at the air/water interface: a critical review of mathematical models, data, and mechanisms. *Colloids Surfaces A Physicochem Eng Asp*. 1995;100(C):1-45. doi:10.1016/0927-7757(94)03061-4

94. Rosen MJ, Kunjappu JT. *Surfactants and Interfacial Phenomena: Fourth Edition*.; 2012. doi:10.1002/9781118228920

95. Gu T, Zhu BY. The S-type isotherm equation for adsorption of nonionic surfactants at the silica gel-water interface. *Colloids and Surfaces*. 1990;44(C):81-87. doi:10.1016/0166-6622(90)80189-B

96. Choy KKH, Porter JF, McKay G. Langmuir isotherm models applied to the multicomponent sorption of acid dyes from effluent onto activated carbon. *J Chem Eng Data*. 2000;45(4):575-584. doi:10.1021/je9902894

97. Zhou M, Bandegi A, Foudazi R. Control of pore interconnectivity in emulsion-templated porous polymers. *Polymer (Guildf)*. 2023;281:126085. doi:10.1016/j.polymer.2023.126085

98. Kotsmar C, Krägel J, Kovalchuk VI, Aksenenko E V., Fainerman VB, Miller R. Dilation and shear rheology of mixed β-casein/surfactant adsorption layers. *J Phys Chem B*. 2009;113(1):103-113. doi:10.1021/jp807197s

99. Wang H, Wei X, Du Y, Wang D. Experimental investigation on the dilatational interfacial rheology of dust-suppressing foam and its effect on foam performance. *Process Saf Environ Prot*. 2019;123:351-357. doi:10.1016/j.psep.2019.01.027

100. Kotsmar C, Krägel J, Kovalchuk VI, Aksenenko E V., Fainerman VB, Miller R. Dilation and shear rheology of mixed β-casein/surfactant adsorption layers. *J Phys Chem B*. 2009;113(1):103-113. doi:10.1021/jp807197s

101. Lucassen J, Van Den Tempel M. Dynamic measurements of dilational properties of a liquid interface. *Chem Eng Sci*. 1972;27(6):1283-1291. doi:10.1016/0009-2509(72)80104-0

102. Yang J, Yu K, Tsuji T, Jha R, Zuo YY. Determining the surface dilational rheology of surfactant and protein films with a droplet waveform generator. *J Colloid Interface Sci*. 2019;537:547-553. doi:10.1016/j.jcis.2018.11.054

103. Miller R, Liggieri L. *Interfacial Rheology*. Vol 1. CRC Press; 2009.

104. Nguyen A, Schulze HJ. *Colloidal Science of Flotation*.; 2003. doi:10.1201/9781482276411

105. Drenckhan W, Saint-Jalmes A. *The Science of Foaming*. Vol 222.; 2015. doi:10.1016/j.cis.2015.04.001

106. Burns DJ, Stevenson P, Murphy PJC. PFAS removal from groundwaters using Surface-Active Foam Fractionation. *Remediation*. 2021;31(4):19-33. doi:10.1002/rem.21694

107. Tamura T, Kaneko Y, Ohyama M. Dynamic Surface Tension and Foaming Properties of Aqueous Polyoxyethylene n-Dodecyl Ether Solutions. *J Colloid Interface Sci*.

1995;173(2):493-499. doi:10.1006/jcis.1995.1351

108. Kanokkarn P, Shiina T, Santikunaporn M, Chavadej S. Equilibrium and dynamic surface tension in relation to diffusivity and foaming properties: Effects of surfactant type and structure. *Colloids Surfaces A Physicochem Eng Asp*. 2017;524:135-142. doi:10.1016/j.colsurfa.2017.04.043

109. Beneventi D, Carre B, Gandini A. Role of surfactant structure on surface and foaming properties. *Colloids Surfaces A Physicochem Eng Asp*. 2001;189(1-3):65-73. doi:10.1016/S0927-7757(01)00602-1

110. Costanza J, Arshadi M, Abriola LM, Pennell KD. Accumulation of PFOA and PFOS at the Air-Water Interface. *Environ Sci Technol Lett*. 2019;6(8):487-491. doi:10.1021/acs.estlett.9b00355

111. Behera MR, Varade SR, Ghosh P, Paul P, Negi AS. Foaming in micellar solutions: Effects of surfactant, salt, and oil concentrations. *Ind Eng Chem Res*. 2014;53(48):18497-18507. doi:10.1021/ie503591v

112. Georgieva D, Cagna A, Langevin D. Link between surface elasticity and foam stability. *Soft Matter*. 2009;5(10):2063-2071. doi:10.1039/b822568k

113. Brown N, de la Pena A, Razavi S. Interfacial rheology insights: particle texture and Pickering foam stability. *J Phys Condens Matter*. 2023;35(38):4002-4016. doi:10.1088/1361-648x/acde2c

114. Silva JAK, Martin WA, McCray JE. Air-water interfacial adsorption coefficients for PFAS when present as a multi-component mixture. *J Contam Hydrol*. 2021;236:103731. doi:10.1016/j.jconhyd.2020.103731

115. Schaefer CE, Culina V, Nguyen D, Field J. Uptake of Poly- And Perfluoroalkyl Substances at the Air-Water Interface. *Environ Sci Technol*. 2019;53(21):12442-12448. doi:10.1021/acs.est.9b04008

116. Brusseau ML. The influence of molecular structure on the adsorption of PFAS to fluid-fluid interfaces: Using QSPR to predict interfacial adsorption coefficients. *Water Res*. 2019;152:148-158. doi:10.1016/j.watres.2018.12.057

117. Yoshimura T, Ohno A, Esumi K. Equilibrium and dynamic surface tension properties of partially fluorinated quaternary ammonium salt gemini surfactants. *Langmuir*. 2006;22(10):4643-4648. doi:10.1021/la0534266

118. Shinoda K, Hatö M, Hayashi T. The physicochemical properties of aqueous solutions of fluorinated surfactants. *J Phys Chem*. 1972;76(6):909-914. doi:10.1021/j100650a021

119. Steffens SD, Cook EK, Sedlak DL, Alvarez-Cohen L. Under-reporting Potential of Perfluorooctanesulfonic Acid (PFOS) under High-Ionic Strength Conditions. *Environ Sci Technol Lett*. 2021;8(12):1032-1037. doi:10.1021/acs.estlett.1c00762

120. Bhhatarai B, Gramatica P. Prediction of aqueous solubility, vapor pressure and critical micelle concentration for aquatic partitioning of perfluorinated chemicals. *Environ Sci Technol*. 2011;45(19):8120-8128. doi:10.1021/es101181g

121. Campbell TY, Vecitis CD, Mader BT, Hoffmann MR. Perfluorinated surfactant chain-length effects on sonochemical kinetics. *J Phys Chem A*. 2009;113(36):9834-9842. doi:10.1021/jp903003w

122. Sørli JB, Låg M, Ekeren L, et al. Per- and polyfluoroalkyl substances (PFASs) modify lung surfactant function and pro-inflammatory responses in human bronchial epithelial cells. *Toxicol Vitr*. 2020;62:104656. doi:10.1016/j.tiv.2019.104656

123. Kancharla S, Jahan R, Bedrov D, Tsianou M, Alexandridis P. Role of chain length and electrolyte on the micellization of anionic fluorinated surfactants in water. *Colloids Surfaces A Physicochem Eng Asp*. 2021;628. doi:10.1016/j.colsurfa.2021.127313

124. Chen LJ, Lin SY, Huang CC. Effect of hydrophobic chain length of surfactants on enthalpy-entropy compensation of micellization. *J Phys Chem B*. 1998;102(22):4350-4356. doi:10.1021/jp9804345

125. Wanzek TA, Field JA, Kostarelos K. Repeated Aqueous Film-Forming Foams Applications: Impacts on Polyfluoroalkyl Substances Retention in Saturated Soil. *Environ Sci Technol*. 2024;58(3):1659-1668. doi:10.1021/acs.est.3c04595

126. Yu Q, Zhang R, Deng S, Huang J, Yu G. Sorption of perfluorooctane sulfonate and perfluorooctanoate on activated carbons and resin: Kinetic and isotherm study. *Water Res*. 2009;43(4):1150-1158. doi:10.1016/j.watres.2008.12.001

127. Beach SA, Newsted JL, Coady K, Giesy JP. Ecotoxicological evaluation of perfluorooctanesulfonate (PFOS). *Rev Environ Contam Toxicol*. 2006;186:133-174. doi:10.1007/0-387-32883-1_5

128. Atkin R, Craig VSJ, Wanless EJ, Biggs S. The influence of chain length and electrolyte on the adsorption kinetics of cationic surfactants at the silica-aqueous solution interface. *J Colloid Interface Sci*. 2003;266(2):236-244. doi:10.1016/S0021-9797(03)00631-3

129. Rashidi-Alavijeh M, Javadian S, Gharibi H, Moradi M, Tehrani-Bagha AR, Shahir AA. Intermolecular interactions between a dye and cationic surfactants: Effects of alkyl chain, head group, and counterion. *Colloids Surfaces A Physicochem Eng Asp*. 2011;380(1-3):119-127. doi:10.1016/j.colsurfa.2011.02.011

130. Miller R, Ferri JK, Javadi A, Krägel J, Mucic N, Wüstneck R. Rheology of interfacial layers. *Colloid Polym Sci*. 2010;288(9):937-950. doi:10.1007/s00396-010-2227-5

131. Mucic N, Javadi A, Kovalchuk NM, Aksenenko E V., Miller R. Dynamics of interfacial layers-Experimental feasibilities of adsorption kinetics and dilational rheology. *Adv Colloid Interface Sci*. 2011;168(1-2):167-178. doi:10.1016/j.cis.2011.06.001

132. Pota G, Andrés-Sanz D, Gallego M, et al. Deciphering the immobilization of lipases on hydrophobic wrinkled silica nanoparticles. *Int J Biol Macromol*. 2024;266(131022). doi:10.1016/j.ijbiomac.2024.131022

133. Fainerman VB, Aksenenko E V., Lylyk S V., et al. Adsorption layer characteristics of Tritons surfactants. 3. Dilational visco-elasticity. *Colloids Surfaces A Physicochem Eng Asp*. 2009;334(1-3):16-21. doi:10.1016/j.colsurfa.2008.10.042

134. Myers D. *Surfaces, Interfaces, and Colloids*.; 1999. doi:10.1002/0471234990

135. McCleaf P, Stefansson W, Ahrens L. Drinking water nanofiltration with concentrate foam fractionation—A novel approach for removal of per- and polyfluoroalkyl substances (PFAS). *Water Res*. 2023;232. doi:10.1016/j.watres.2023.119688

136. Smith SJ, Wiberg K, McCleaf P, Ahrens L. Pilot-Scale Continuous Foam Fractionation for the Removal of Per- A nd Polyfluoroalkyl Substances (PFAS) from Landfill Leachate. *ACS Environ Sci Technol Water*. 2022;2(5):841-851. doi:10.1021/acsestwater.2c00032

137. We ACE, Zamyadi A, Stickland AD, Clarke BO, Freguia S. A review of foam fractionation for the removal of per- and polyfluoroalkyl substances (PFAS) from aqueous matrices. *J Hazard Mater*. 2024;465:133182. doi:10.1016/j.jhazmat.2023.133182

138. Amani P, Karakashev SI, Grozev NA, et al. Effect of selected monovalent salts on surfactant stabilized foams. *Adv Colloid Interface Sci*. 2021;295:102490. doi:10.1016/j.cis.2021.102490

139. Brusseau ML, Van Glubt S. The influence of surfactant and solution composition on PFAS adsorption at fluid-fluid interfaces. *Water Res*. 2019;161. doi:10.1016/j.watres.2019.05.095

140. Vecitis CD, Park H, Cheng J, Mader BT, Hoffmann MR. Enhancement of perfluorooctanoate and perfluorooctanesulfonate activity at acoustic cavitation bubble interfaces. *J Phys Chem C*. 2008;112(43). doi:10.1021/jp804050p

141. Le S-T, Gao Y, Kibbey TCG, Glamore WC, O'Carroll DM. Predicting the impact of salt mixtures on the air-water interfacial behavior of PFAS. *Sci Total Environ*. 2021. doi:10.1016/j.scitotenv.2021.151987

142. Abraham JEF, Mumford KG, Patch DJ, Weber KP. Retention of PFOS and PFOA Mixtures by Trapped Gas Bubbles in Porous Media. *Environ Sci Technol*. 2022;56(22):15489-15498. doi:10.1021/acs.est.2c00882

143. Qazi MJ, Schlegel SJ, Backus EHG, Bonn M, Bonn D, Shahidzadeh N. Dynamic Surface Tension of Surfactants in the Presence of High Salt Concentrations. *Langmuir*. 2020;36(27):7956-7964. doi:10.1021/acs.langmuir.0c01211

144. Alonso G, Gamallo P, Mejía A, Sayós R. Assessing salt-surfactant synergistic effects on interfacial tension from molecular dynamics simulations. *J Mol Liq*. 2020;299:112223. doi:10.1016/j.molliq.2019.112223

145. Ning C, Ma H, Pedersen CM, Chang H, Wang Y, Qiao Y. Interaction between environmental contaminant PFOA and PAMAM in water: 19 F and 1 H NMR studies. *J Mol Liq*. 2019;283:45-50. doi:10.1016/j.molliq.2019.03.057

146. Steffens SD, Sedlak DL, Alvarez-Cohen L. Enhanced aggregation and interfacial adsorption of an aqueous film forming foam (AFFF) in high salinity matrices. *Environ Sci Process Impacts*. 2023;25(12):2181-2188. doi:10.1039/d3em00247k

147. Venzmer J. Determination of Surface Tension of Surfactant Solutions from a Regulatory Perspective. *SOFW J*. 2023;149(10):32-39. chrome-

extension://efaidnbmnnnibpcajpcglclefindmkaj/https://www.tegewa.de/wp-content/uploads/2023/11/Determination-of-Surface-Tension-of-Surfactant-Solutions-from-a-Regulatory-Perspective.pdf. Accessed March 25, 2024.

148. Zhang C, Geng T, Jiang Y, Zhao L, Ju H, Wang Y. Impact of NaCl concentration on equilibrium and dynamic surface adsorption of cationic surfactants in aqueous solution. *J Mol Liq*. 2017;238:423-429. doi:10.1016/j.molliq.2017.05.033

149. Kalam S, Abu-Khamsin SA, Kamal MS, Patil S. Surfactant Adsorption Isotherms: A Review. *ACS Omega*. 2021;6(48):32342-32348. doi:10.1021/acsomega.1c04661

150. Xi Yuan Hua, Rosen MJ. Dynamic surface tension of aqueous surfactant solutions. I. Basic paremeters. *J Colloid Interface Sci*. 1988;124(2):652-659. doi:10.1016/0021-9797(88)90203-2

151. Eastoe J, Dalton JS. Dynamic surface tension and adsorption mechanisms of surfactants at the air-water interface. *Adv Colloid Interface Sci*. 2000;85(2-3):103-144. doi:10.1016/S0001-8686(99)00017-2

152. Mohammadi M, Zirrahi M, Hassanzadeh H. An Analytical Model for Estimation of the Self-Diffusion Coefficient and Adsorption Kinetics of Surfactants Using Dynamic Interfacial Tension Measurements. *J Phys Chem B*. 2020;124(15):3206-3213. doi:10.1021/acs.jpcb.0c01113

153. Stasiak EM, Andrzejewski EA. DETERMINATION OF SURFACTANT EFFECTIVE DIFFUSION COEFFICIENT USING INVERSE PROBLEM FOR WARD-TORDAI EQUATION. *Math Model*. 2018;2(3):119-121.

154. Darjani S, Koplik J, Pauchard V. Extracting the equation of state of lattice gases from random sequential adsorption simulations by means of the Gibbs adsorption isotherm. *Phys Rev E*. 2017;96(5):052803. doi:10.1103/PhysRevE.96.052803

155. Aksenenko E V., Kovalchuk VI, Fainerman VB, Miller R. Surface dilational rheology of mixed adsorption layers at liquid interfaces. *Adv Colloid Interface Sci*. 2006;122(1-3):57-66. doi:10.1016/j.cis.2006.06.012

156. Nan Y, Li W, Jin Z. Ion Valency and Concentration Effect on the Structural and Thermodynamic Properties of Brine-Decane Interfaces with Anionic Surfactant (SDS). *J Phys Chem B*. 2021;125(33):9610-9620. doi:10.1021/acs.jpcb.1c04187

157. Ochoa C, Gao S, Xu C, Srivastava S, Sharma V. Foam film stratification, viscosity, and small-angle X-ray scattering of micellar SDS solutions over an extended concentration range (1< c/CMC < 75). *Soft Matter*. 2024;(8).

158. Camdzic D, Dickman RA, Aga DS. Total and class-specific analysis of per- and polyfluoroalkyl substances in environmental samples using nuclear magnetic resonance spectroscopy. *J Hazard Mater Lett*. 2021;2:100023. doi:10.1016/j.hazl.2021.100023

159. Kancharla S, Bedrov D, Tsianou M, Alexandridis P. Structure and composition of mixed micelles formed by nonionic block copolymers and ionic surfactants in water determined by small-angle neutron scattering with contrast variation. *J Colloid Interface Sci*. 2022;609:456-468. doi:10.1016/j.jcis.2021.10.176

160. Jensen GV, Lund R, Gummel J, Monkenbusch M, Narayanan T, Pedersen JS. Direct observation of the formation of surfactant micelles under nonisothermal conditions by synchrotron SAXS. *J Am Chem Soc*. 2013;135(19):7214-7222. doi:10.1021/ja312469n

161. Cui X, Mao S, Liu M, Yuan H, Du Y. Mechanism of surfactant micelle formation. *Langmuir*. 2008;24(19):10771-10775. doi:10.1021/la801705y

162. Tan X, Sawczyk M, Chang Y, et al. Revealing the Molecular-Level Interactions between Cationic Fluorinated Polymer Sorbents and the Major PFAS Pollutant PFOA. *Macromolecules*. 2022;55(3):1077-1087. doi:10.1021/acs.macromol.1c02435

163. Moody CA, Wai Chi Kwan, Martin JW, Muir DCG, Mabury SA. Determination of perfluorinated surfactants in surface water samples by two independent analytical techniques: Liquid chromatography/tandem mass spectrometry and 19F NMR. *Anal Chem*. 2001;73(10):2200-2206. doi:10.1021/ac0100648

164. Chen P, Zhuang S, Chen W, et al. Facile identification of fluorosurfactant category in aqueous film-forming foam concentrates via optimized 19F NMR. *Magn Reson Lett*. 2024. doi:10.1016/j.mrl.2023.12.005

165. Arsenault G, Chittim B, Gu J, McAlees A, McCrindle R, Robertson V. Separation and fluorine nuclear magnetic resonance spectroscopic (19F NMR) analysis of individual branched isomers present in technical perfluorooctanesulfonic acid (PFOS). *Chemosphere*. 2008;73(1 SUPPL.):S53-S59. doi:10.1016/j.chemosphere.2007.06.096

166. Cui X, Mao S, Liu M, Yuan H, Du Y. Mechanism of surfactant micelle formation. *Langmuir*. 2008;24(19):10771-10775. doi:10.1021/la801705y

167. Ochoa C, Gao S, Srivastava S, Sharma V. Foam film stratification studies probe intermicellar interactions. *Proc Natl Acad Sci U S A*. 2021;118(25):e2024805118. doi:10.1073/pnas.2024805118

168. Martinez AC, Rio E, Delon G, Saint-Jalmes A, Langevin D, Binks BP. On the origin of the remarkable stability of aqueous foams stabilised by nanoparticles: Link with microscopic surface properties. *Soft Matter*. 2008;4(7):1531-1535. doi:10.1039/b804177f

169. Stocco A, Drenckhan W, Rio E, Langevin D, Binks BP. Particle-stabilised foams: an interfacial study. *Soft Matter*. 2009;5(11):2215-2222. doi:10.1039/b901180c

170. Buckley T, Xu X, Rudolph V, Firouzi M, Shukla P. Review of foam fractionation as a water treatment technology. *Sep Sci Technol*. 2022;57(6):929-958. doi:10.1080/01496395.2021.1946698

171. Smith SJ, Wiberg K, McCleaf P, Ahrens L. so. *ACS Environ Sci Technol Water*. 2022;2(5):841-851. doi:10.1021/acsestwater.2c00032

172. Wang Y, Ji Y, Tishchenko V, Huang Q. Removing per- and polyfluoroalkyl substances (PFAS) in water by foam fractionation. *Chemosphere*. 2023;311. doi:10.1016/j.chemosphere.2022.137004

173. Burns DJ, Hinrichsen HM, Stevenson P, Murphy PJC. Commercial-scale remediation of per- and polyfluoroalkyl substances from a landfill leachate catchment using Surface-

Active Foam Fractionation (SAFF®). *Remediation*. 2022;32(3):139-150. doi:10.1002/rem.21720

174. Amani P, Firouzi M. Effect of salt and particles on the hydrodynamics of foam flows in relation to foam static characteristics. *Chem Eng Sci*. 2022;254:117611. doi:10.1016/j.ces.2022.117611

175. Feitosa K, Marze S, Saint-Jalmes A, Durian DJ. Electrical conductivity of dispersions: From dry foams to dilute suspensions. *J Phys Condens Matter*. 2005;17(41). doi:10.1088/0953-8984/17/41/001

176. Yekeen N, Manan MA, Idris AK, Samin AM. Influence of surfactant and electrolyte concentrations on surfactant Adsorption and foaming characteristics. *J Pet Sci Eng*. 2017;149:612-622. doi:10.1016/j.petrol.2016.11.018

177. Martínez-Calvo A, Sevilla A. Universal Thinning of Liquid Filaments under Dominant Surface Forces. *Phys Rev Lett*. 2020;125(11):114502. doi:10.1103/PHYSREVLETT.125.114502

178. Nguyen A V. Liquid drainage in single Plateau borders of foam. *J Colloid Interface Sci*. 2002;249(1):194-199. doi:10.1006/jcis.2001.8176

179. Stevenson P. Dimensional analysis of foam drainage. *Chem Eng Sci*. 2006;61(14):4503-4510. doi:10.1016/j.ces.2006.02.026

180. Rouyer F, Haffner B, Louvet N, Khidas Y, Pitois O. Foam clogging. *Soft Matter*. 2014;10(36):6990-6998. doi:10.1039/c4sm00496e

181. Maestro A, Rio E, Drenckhan W, Langevin D, Salonen A. Foams stabilised by mixtures of nanoparticles and oppositely charged surfactants: Relationship between bubble shrinkage and foam coarsening. *Soft Matter*. 2014;10(36):6975-6983. doi:10.1039/c4sm00047a

182. Barman S, Davidson ML, Walker LM, Anna SL, Zasadzinski JA. Inflammation product effects on dilatational mechanics can trigger the Laplace instability and acute respiratory distress syndrome. *Soft Matter*. 2020;16(29):6890-6901. doi:10.1039/d0sm00415d

183. Ndiritu AK, Kinyuru JN, Gichuhi PN, Kenji GM. Effects of NaCl and pH on the functional properties of edible crickets (Acheta domesticus) protein concentrate. *J Food Meas Charact*. 2019;13(3):1788-1796. doi:10.1007/s11694-019-00097-5

184. Lawal OS. Functionality of African locust bean (Parkia biglobossa) protein isolate: Effects of pH, ionic strength and various protein concentrations. *Food Chem*. 2004;86(3):345-355. doi:10.1016/j.foodchem.2003.09.036

185. Pugh RJ. Foaming, foam films, antifoaming and defoaming. *Adv Colloid Interface Sci*. 1996;64:67-142. doi:10.1016/0001-8686(95)00280-4

186. Manyala DL, Rajput G, Pandya N, Varade D. Enhanced foamability and foam stability of polyoxyethylene cholesteryl ether in occurrence of ionic surfactants. *Colloids Surfaces A Physicochem Eng Asp*. 2018;551:81-86. doi:10.1016/j.colsurfa.2018.04.069

187. Kamal MS. A novel approach to stabilize foam using fluorinated surfactants. *Energies*. 2019;12(6):1163. doi:10.3390/en12061163

188. Amani P, Miller R, Javadi A, Firouzi M. Pickering foams and parameters influencing their characteristics. *Adv Colloid Interface Sci*. 2022;301:102606. doi:10.1016/j.cis.2022.102606

189. Okunade OA, Yekeen N, Padmanabhan E, Al-Yaseri A, Idris AK, Khan JA. Shale core wettability alteration, foam and emulsion stabilization by surfactant: Impact of surfactant concentration, rock surface roughness and nanoparticles. *J Pet Sci Eng*. 2021;207:109139. doi:10.1016/j.petrol.2021.109139

190. Chattopadhyay P, Karthick RA. Characterization and Application of Surfactant Foams Produced from Ethanol-Sodium Lauryl Sulfate-Silica Nanoparticle Mixture for Soil Remediation. *Macromol Symp*. 2017;376(1). doi:10.1002/masy.201600182

191. Deotale SM, Dutta S, Moses JA, Anandharamakrishnan C. Stability of Instant Coffee Foam by Nanobubbles Using Spray-Freeze Drying Technique. *Food Bioprocess Technol*. 2020;13(11):1866-1877. doi:10.1007/s11947-020-02526-6

192. Hatakeyama S, Akiyama M, Yoneyama R, et al. Effects of manufacturing conditions on the foaming properties of milk and sensory characteristics of foamed milk. *LWT*. 2019;99:555-561. doi:10.1016/j.lwt.2018.09.082

193. Dachmann E, Nobis V, Kulozik U, Dombrowski J. Surface and foaming properties of potato proteins: Impact of protein concentration, pH value and ionic strength. *Food Hydrocoll*. 2020;107:105981. doi:10.1016/j.foodhyd.2020.105981

194. Guo Y, Guo Y. On the Stability of Aqueous Foams and the Effect of Surfactant. 2021.

195. Zowada R, Foudazi R. PolyFoam: foam-templated microcellular polymers. *Langmuir*. June 2020:acs.langmuir.0c00932. doi:10.1021/acs.langmuir.0c00932

196. Höhler R, Seknagi J, Kraynik A. Capillary pressure, osmotic pressure and bubble contact areas in foams. *Soft Matter*. 2021;17(29):6995-7003. doi:10.1039/d1sm00823d

197. Maestro A, Drenckhan W, Rio E, Höhler R. Liquid dispersions under gravity: Volume fraction profile and osmotic pressure. *Soft Matter*. 2013;9(8). doi:10.1039/c2sm27668b

198. Forel E, Rio E, Schneider M, et al. The surface tells it all: Relationship between volume and surface fraction of liquid dispersions. *Soft Matter*. 2016;12(38). doi:10.1039/c6sm01451h

199. De Leon A, Wei P, Bordera F, et al. Pickering Bubbles as Dual-Modality Ultrasound and Photoacoustic Contrast Agents. *ACS Appl Mater Interfaces*. 2020;12(19):22308-22317. doi:10.1021/acsami.0c02091

200. Nayar KG, Panchanathan D, McKinley GH, Lienhard JH. Surface Tension of Seawater. *J Phys Chem Ref Data*. 2014;43(4). doi:10.1063/1.4899037

Appendices

Appendix A. Supporting tables for Chapter 3

Measurement uncertainty calculations

The law of propagation of uncertainty was used based on the following equation to determine the combined standard uncertainty to assess the effect of measurement uncertainty on our reported results.

$$u_\sigma(y) = \sqrt{\sigma_y^2 + [\frac{\partial y}{\partial x_1}u(x_1)]^2 + [\frac{\partial y}{\partial x_2}u(x_2)]^2 + \cdots + [\frac{\partial y}{\partial x_n}u(x_n)]^2} \qquad \textit{Equation (A1)}$$

where $u_\sigma(y)$ is the combined standard uncertainty of the measured dependent variable y, such as surface tension, σ_y is the standard deviation of dependent variable y due to the repetitive measurements, $u(x_i)$ is the uncertainty of the equipment/apparatus used to measure the independent variable x_i. **Table A9** shows the uncertainty of the equipment/apparatus for the independent variables.

Take the example of using Wilhelmy plate tensiometer to measure the surface tension, the basic formula for calculating surface tension using the Wilhelmy plate method is shown below:

$$\gamma = \frac{F}{L} \qquad \textit{Equation (A2)}$$

where F is the force measured by the tensiometer as the plate is pulled from the liquid, and L is the wetted perimeter of the plate. $u(F) = \pm 20\ \mu g$ (see **Table A9**). The wetted perimeter is typically known with a very high degree of precision since it is determined by the dimensions of the plate. Therefore, $u(L)$ is negligible in the measurement. Hence, *Equation (A2)* becomes *Equation (A3)* shown below:

$$u_\sigma(\gamma) = \sqrt{\sigma_\gamma^2 + [\frac{\partial \gamma}{\partial F} u(F)]^2} \qquad \textit{Equation (A3)}$$

Given the formula of *Equation (A2)* for surface tension, the partial derivative is:

$$\frac{\partial \gamma}{\partial F} = \frac{1}{L} \qquad \textit{Equation (A4)}$$

Substituting these into the uncertainty formula gives:

$$u_\sigma(\gamma) = \sqrt{\sigma_\gamma^2 + [\frac{1}{L} u(F)]^2} \qquad \textit{Equation (A5)}$$

For 0.4 mM KPFOS aqueous solutions, the equilibrium surface tension is 43.540 ± 2.648 mN/m based on the measurement, and thus, $\sigma_y = 2.648$ mN/m. Our calculation indicates the combined standard uncertainty $u_\sigma(\gamma)$ of 2.648 mN/m for 0.4 mM KPFOS aqueous solutions. Therefore, the reported standard deviation, σ_y, (error bar) based on the measurement using Wilhelmy plate tensiometer is the same as the calculated combined standard uncertainty $u_\sigma(\gamma)$. In essence, using only the standard deviation of equilibrium surface tension is sufficient for reporting the uncertainty of surface tension measurements using Wilhelmy plate tensiometer.

When using the pendant drop tensiometer to perform the pendant drop oscillation to calculate the interfacial dilatational modulus, taking the example of 0.4 mM KPFOS pendant drop pulsating at 0.5 Hz, the sinusoidal functions of surface tension and surface area changes area shown below:

$$A(t) = 33.04513 + 0.53534 \sin[\pi \frac{(t-0.82142)}{1.00347}] \qquad \textit{Equation (A6)}$$

$$\gamma(t) = 52.61622 + 0.27574 \sin[\pi \frac{(t-0.78923)}{1.00032}] \qquad \textit{Equation (A7)}$$

The E and ϕ are 17.02 mN/m and 10.66 ° according to the *Equations (A6-A7)*. $u(\gamma) = \pm 0.01\ mN/m$ (see **Table A9**). The surface area instrument uncertainty cannot be found. Therefore,

we assume $u(A) = \pm 0.01\ mm^2$, and $u(\phi) = \pm 0.01°$ due to the instrument error. The *Equation (A1)* becomes:

$$u_\sigma(E') = \sqrt{\sigma_{E'}^2 + [\frac{\partial E'}{\partial A}u(A)]^2 + [\frac{\partial E'}{\partial \gamma}u(\gamma)]^2 + [\frac{\partial E'}{\partial \phi}u(\phi)]^2} \qquad \textit{Equation (A8)}$$

$$u_\sigma(E'') = \sqrt{\sigma_{E''}^2 + [\frac{\partial E''}{\partial A}u(A)]^2 + [\frac{\partial E''}{\partial \gamma}u(\gamma)]^2 + [\frac{\partial E''}{\partial \phi}u(\phi)]^2} \qquad \textit{Equation (A9)}$$

$$u(E) = \sqrt{[\frac{\partial E}{\partial A}u(A)]^2 + [\frac{\partial E}{\partial \gamma}u(\gamma)]^2 + [\frac{\partial E}{\partial \phi}u(\phi)]^2} \qquad \textit{Equation (A10)}$$

Due to *Equations (2.8-2.9)*, substituting the partial derivative into the uncertainty formula gives:

$$u_\sigma(E') = \sqrt{\sigma_{E'}^2 + [\cos(\phi)\, u(E)]^2 + [-|E|\sin(\phi)\, u(\phi)]^2} \qquad \textit{Equation (A11)}$$

$$u_\sigma(E'') = \sqrt{\sigma_{E''}^2 + [\sin(\phi)\, u(E)]^2 + [|E|\cos(\phi)\, u(\phi)]^2} \qquad \textit{Equation (A12)}$$

$$u(E) = E\sqrt{[\frac{u(\gamma)}{\Delta\gamma}]^2 + [\frac{u(A)}{\Delta\gamma}]^2} \qquad \textit{Equation (A13)}$$

Note that $u(E)$ is just the uncertainty of E due to the uncertainty of pendant drop tensiometer. $u(E) = 0.69\ mN/m$. For 0.4 mM KPFOS aqueous solutions, the E' is 15.46 ± 2.49 mN/m and the E'' is 4.64 ± 1.92 mN/m based on the measurement, and thus, $\sigma_{E'} = 2.29$ mN/m and $\sigma_{E''} = 1.92$ mN/m. The calculation shows that $u_\sigma(E') = 3.17\ mN/m$, and $u_\sigma(E'') = 2.05\ mN/m$. Therefore, using only the standard deviation of E' and E'' due to the repetitive measurements is sufficient for reporting the uncertainty of E' and E'' by using the pendant drop tensiometer.

Table A1. Gibbs isotherm fitted parameters for KPFOS in the concentration range of 0.14 to 1.1 mM.

	Slope (mN/m)	R^2
Current work	-9.736±0.929	0.95644
Silva et al.[114]	-9.273±0.650	0.99511
Costanza et al.[110]	-8.210±0.418	0.98718
Steffen et al.[119]	-12.690±0.544	0.98729
Shinoda et al.[118]	-9.674±1.191	0.97058

Table A2. Gibbs isotherm fitted parameters for KPFBS in the concentration range of 18 to 191 mM.

	Slope (mN/m)	R^2
Current work	-9.535±1.807	0.93299
Campbell et al.[121]	-12.989±0.393	0.99817
Silva et al.[114]	-9.448±0.518	0.997

Table A3. Polynomial fitted parameters for KPFOS (n=3).

	a	b	c	d	R^2
Current work	-0.03909	-1.03376	-10.26362	35.93399	0.99146
Silva et al.[114]	0.03002	-0.26509	-9.46754	28.86702	0.99882
Costanza et al.[110]	-0.08911	-1.74245	-11.66863	44.80219	0.99746
Steffen et al.[119]	0.11182	-0.86853	-13.55126	37.39369	0.99365
Shinoda et al.[118]	3.41771	5.08475	-10.35581	37.82528	0.99959

Table A4. Langmuir isotherm fitted parameters for KPFOS (based on the third-order polynomial fit).

	a ($\Gamma_m \times 10^{10}\ mol/cm^2$)	b (K_L, $L/mmol$)	R^2
Current work	1.92952±0.08526	26.58498±6.49684	0.94672
Silva et al.[114]	1.75109±0.06818	160.89567±32.63121	0.95349
Costanza et al.[110]	3.64697±0.14669	2.82944±0.37467	0.96358
Steffen et al.[119]	3.09869±0.03982	8.96834±0.61126	0.99264
Shinoda et al.[118]	failed	failed	failed

Table A5. Extended Langmuir isotherm fitted parameters for KPFOS (based on the third-order polynomial fit).

	a ($\Gamma_m \times 10^{10}\ mol/cm^2$)	b (K_L, $(L/mmol)^n$)	c $(1-n)$	R^2
Current work	3.28894±0.19123	1.57887±0.22085	0.57756±0.01709	0.99904
Silva et al.[114]	2.03734±0.08576	12.90006±4.25844	0.43523±0.05121	0.99191
Costanza et al.[110]	5.68433±0.24984	0.72891±0.06308	0.45421±0.01701	0.99849
Steffen et al.[119]	3.11488±0.06558	8.44664±1.67043	0.02231±0.07132	0.99271
Shinoda et al.[118]	2.49498±0.01554	3168.9204±723.0058	-5.6477±0.18764	0.99989

Table A6. Polynomial fitted parameters for KPFBS (n=3).

	a	b	c	d	R^2
Current work	-0.10027	-0.64343	-1.50557	69.8844	0.98189
Campbell et al.[121]	-0.36386	0.15696	-0.94196	71.01252	0.98825

Silva et al.[114]	-0.0506	-0.63946	-1.71528	71.41945	0.9984

Table A7. Langmuir isotherm fitted parameters for KPFBS (based on the third-order polynomial fit).

	a ($\Gamma_m \times 10^{10}\ mol/cm^2$)	b (K_L, $L/mmol$)	R^2
Current work	2.88381±0.10139	0.07598±0.00689	0.98756
Campbell et al.[121]	6.63302±0.13786	0.02126±0.000976492	0.99881
Silva et al.[114]	2.47269±0.14148	0.08289±0.01701	0.97153

Table A8. Extended Langmuir isotherm fitted parameters for KPFBS (based on the third-order polynomial fit).

	a ($\Gamma_m \times 10^{10}\ mol/cm^2$)	b (K_L, $(L/mmol)^n$)	c $(1-n)$	R^2
Current work	3.89226±0.20864	0.08868±0.00393	0.29193±0.02836	0.99807
Campbell et al.[121]	7.81995±0.38168	0.02294±0.000739686	0.1084±0.02451	0.99961
Silva et al.[114]	3.47449±0.28931	0.11148±0.00882	0.40087±0.04309	0.99708

Table A9. $u(x)$ of the equipment/apparatus used in this work

Equipment	$\boldsymbol{u(x)}$
Balance	±0.0001 g
Graduated cylinder	±0.1 mL
Wilhelmy plate tensiometer (Dataphysics, DCAT 25)	±0.001 mN/m (ref.[200])
Wilhelmy plate tensiometer (Dataphysics, DCAT 25)	±20 µg
Pendant drop tensiometer (Attension KSV Instruments, Biolin Scientific, Finland)	±0.01 mN/m
Pendant drop tensiometer (Attension KSV Instruments, Biolin Scientific, Finland)	±0.01 µL

Appendix B. Supporting tables for Chapter 4

Table B1. Gibbs isotherm fitted parameters for PFAS solutions with and without salts.

	Slope	R^2
KPFOS	-0.00974	0.95644
KPFOS+100 mM NaCl	-0.00504	0.99175
KPFOS+10 mM $CaCl_2$	-0.00656	0.99507
KPFOS+100 mM $CaCl_2$	-0.00753	0.99067
PFOA (Pendant drop)	-0.01383	0.96310
PFOA (Rising bubble)	-0.01268	0.98034
PFOA	-0.00959	0.98545
PFOA+100 mM NaCl	-0.00975	0.95326
PFOA+10 mM $CaCl_2$	-0.00917	0.98514
PFOA+100 mM $CaCl_2$	-0.00887	0.99758
KPFBS	-0.00954	0.93299
KPFBS+100 mM $CaCl_2$	-0.00655	0.98846

Table B2. Third-order polynomial fitted parameters for PFAS solutions with and without salts.

	a	b	c	d	R^2
KPFOS	-0.000031799	-0.00163	-0.02802	-0.09053	0.99092
KPFOS+100 mM NaCl	-0.0000151139	-0.000567757	-0.01036	-0.01015	0.99269
KPFOS+10 mM $CaCl_2$	-0.0000102767	-0.000617076	-0.0153	- 0.06004	0.9987
KPFOS+100 mM $CaCl_2$	-0.0000889176	-0.00365	-0.05215	-0.21055	0.97066
PFOA (Pendant drop)	-0.000147054	-0.00555	-0.06898	-0.20951	0.99735
PFOA (Rising bubble)	-0.0000705779	-0.00311	-0.04424	-0.13163	0.98207
PFOA	0.0000133182	-0.00061595	-0.02063	-0.0646	0.99533
PFOA+100 mM NaCl	-0.0000485295	-0.00215	-0.03271	-0.0986	0.99629
PFOA+10 mM $CaCl_2$	-0.00000701115	-0.000821074	-0.01988	-0.06497	0.99825
PFOA+100 mM $CaCl_2$	0.00000919413	-0.000226558	-0.01385	-0.05334	0.9979
KPFBS	-0.000100273	-0.00272	-0.02475	-0.00427	0.98189
KPFBS+100 mM $CaCl_2$	-0.00000168073	-0.000446215	-0.00952	0.01873	0.98754

Table B3. Extended Langmuir isotherm fitted parameters for PFAS solutions with and without salts.

	a (Γ_m)	b (K_L)	n	R^2
KPFOS	3.28894	29.21922	0.42244	0.99904
KPFOS+100 mM NaCl	4.82558	1.00000	0.07585	0.86264
KPFOS+10 mM $CaCl_2$	5.23489	6.00000	0.18705	0.98965
KPFOS+100 mM $CaCl_2$	15.33402	6.00341	0.34727	0.99873

PFOA (Pendant drop)	7.62689	48.22345	0.6507	0.99708
PFOA (Rising bubble)	5.56093	31.43616	0.549	0.99718
PFOA	3.11795	136.9772	0.6033	0.98921
PFOA+100 mM NaCl	12.00155	6.09387	0.36091	0.99959
PFOA+10 mM $CaCl_2$	6.44469	20.74556	0.37401	0.99523
PFOA+100 mM $CaCl_2$	6.32976	21.00000	0.20845	0.97758
KPFBS	3.89226	11.80471	0.70807	0.99807
KPFBS+100 mM $CaCl_2$	3.34889	18.70198	0.47280	0.99236

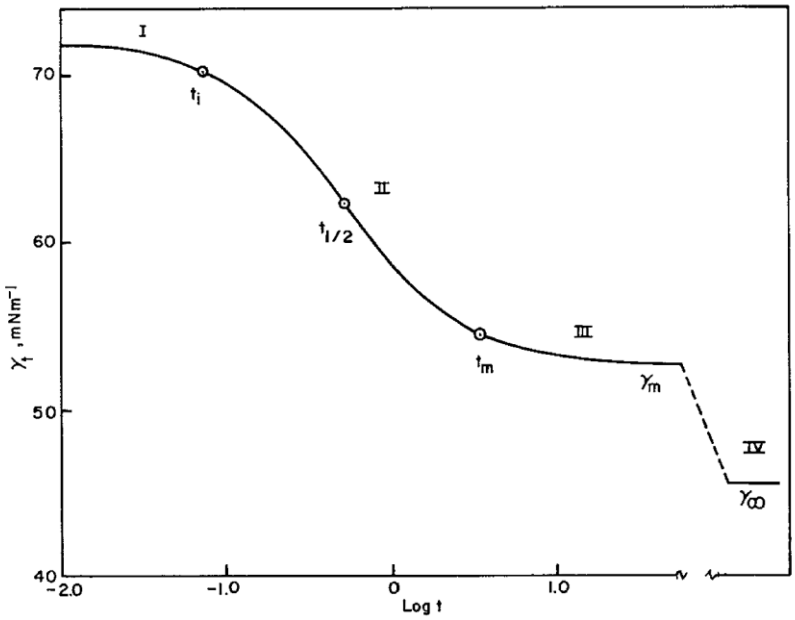

Figure B1. Typical dynamic surface tension curve showing four stages of I) induction, II) fast fall, III) meso-equilibrium, and IV) equilibrium.[150]

Table B4. Fitted parameters of *Equation (4.3)* for KPFOS with various bulk concentrations.

PFAS	Concentration (mM)	Salt	Concentration (mM)	t* [s]	n
KPFOS	1.2	-	-	0.936985	0.295203
	1			0.976069	0.298348
	0.8			3.284151	0.269974
	0.6			15.32155	0.242519
	0.4			307.6646	0.20512
	0.3			711.7598	0.199193
	0.2			2203.413	0.203915
	0.1			19801.31	0.230556
	0.05			15522.89	0.309352
	0.02			15550.16	0.352767

	0.01			35288.96	0.355652
	0.002			1951989	0.281189
	0.0009			1893031	0.139115
	0.0002			7326244	0.099944

Table B5. Fitted parameters of *Equation (4.3)* for KPFOS with various bulk concentrations in the presence of 100 mM NaCl as the background ions.

PFAS	Concentration (mM)	Salt	Concentration (mM)	t* [s]	n
KPFOS	1.2	NaCl	100	1.407726	0.667961
	1			1.663604	0.677291
	0.8			2.616811	0.656011
	0.6			3.388555	0.674606
	0.4			4.605189	0.693226
	0.3			5.462521	0.733708
	0.2			7.479746	0.754986
	0.1			10.12929	0.829493
	0.05			14.19215	0.856717
	0.02			18.20482	0.937932
	0.01			50.89052	0.973583
	0.002			60.93649	1.653996
	0.0009			575.1623	0.82458
	0.0002			562.794	0.742586

Table B6. Fitted parameters of *Equation (4.3)* for KPFOS with various bulk concentrations in the presence of 10 mM $CaCl_2$ as the background ions.

PFAS	Concentration (mM)	Salt	Concentration (mM)	t* [s]	n
KPFOS	1.2	$CaCl_2$	10	0.058154	0.599024
	1			0.060732	0.631623
	0.8			0.108082	0.624051
	0.6			0.174151	0.682401
	0.4			0.399488	0.725241
	0.3			0.744077	0.75382
	0.2			1.340712	0.844794
	0.1			3.862268	0.784629
	0.05			14.51199	0.742859
	0.02			184.8321	0.535795
	0.01			1300.935	0.425964
	0.002			98814094	0.188716
	0.0009			2.03E+14	0.095004
	0.0002			2.04E+14	0.114088

Table B7. Fitted parameters of *Equation (4.3)* for KPFOS with various bulk concentrations in the presence of 100 mM $CaCl_2$ as the background ions.

PFAS	Concentration (mM)	Salt	Concentration (mM)	t* [s]	n
KPFOS	1.2	$CaCl_2$	100	0.042337	0.765254
	1			0.066398	0.778939
	0.8			0.088044	0.790226
	0.6			0.165615	0.772025
	0.4			0.431408	0.784541
	0.3			0.831928	0.78875
	0.2			1.716451	0.846052
	0.1			5.162397	0.876909
	0.05			11.93616	1.039464
	0.02			113.6201	0.714398
	0.01			2324.632	0.486908
	0.002			1182339	0.339386
	0.0009			28938763	0.282
	0.0002			3.21E+13	0.142158

Table B8. Fitted parameters of *Equation (4.3)* for PFOA with various bulk concentrations.

PFAS	Concentration (mM)	Salt	Concentration (mM)	t* [s]	n
PFOA	12.0	-	-	0.000208	0.374562
	9.7			7.59E-05	0.29338
	7.3			0.000161	0.319094
	4.8			0.001253	0.316266
	2.4			0.022664	0.236619
	1.9			0.084217	0.250941
	1.2			0.970405	0.218217
	0.8			31.75601	0.197091
	0.4			11353.17	0.181282
	0.24			32606.63	0.192821
	0.12			1.16E+09	0.203832
	0.06			1.2E+10	0.138533
	0.024			1.1E+10	0.069483
	0.012			1.09E+10	0.042743
	0.002			1.13E+10	0.095545
	0.001			2.36E+10	0.094187
	0.0002			2.33E+10	0.049778

Table B9. Fitted parameters of *Equation (4.3)* for PFOA with various bulk concentrations in the presence of 100 mM NaCl as the background ions.

PFAS	Concentration (mM)	Salt	Concentration (mM)	t* [s]	n
PFOA	12.0	NaCl	100	0.000739	0.844073
	9.7			0.000434	0.641668
	7.3			0.00162	0.999556
	4.8			0.00133	0.573708
	2.4			0.005766	0.514987
	1.9			0.009557	0.464306
	1.2			0.023531	0.480504
	0.8			0.058918	0.481423
	0.4			0.240809	0.463291
	0.24			0.822758	0.441668
	0.12			1.342068	0.51217
	0.06			2.144273	0.581777
	0.024			8.829927	0.6663
	0.012			13.30602	0.753043
	0.002			32.57653	1.240202
	0.001			98263.12	0.17911
	0.0002			1331681	0.179315

Table B10. Fitted parameters of *Equation (4.3)* for PFOA with various bulk concentrations in the presence of 10 mM $CaCl_2$ as the background ions.

PFAS	Concentration (mM)	Salt	Concentration (mM)	t* [s]	n
PFOA	12.0	$CaCl_2$	10	0.001287	0.644817
	9.7			0.000812	0.54829
	7.3			0.000903	0.643506
	4.8			0.00145	0.881065
	2.4			0.005641	0.484002
	1.9			0.010913	0.512387
	1.2			0.034578	0.520676
	0.8			0.097325	0.544836
	0.4			0.34461	0.582458
	0.24			0.675052	0.650134
	0.12			3.433214	0.688356
	0.06			8.010113	0.585872
	0.024			16.86459	0.608654
	0.012			27.53452	0.579298
	0.002			1103.269	0.203573
	0.001			6558841	0.105982
	0.0002			11219484	0.059169

Table B11. Fitted parameters of *Equation (4.3)* for PFOA with various bulk concentrations in the presence of 100 mM $CaCl_2$ as the background ions.

PFAS	Concentration (mM)	Salt	Concentration (mM)	t* [s]	n
PFOA	12.0	$CaCl_2$	100	0.003693	0.539617
	9.7			0.002667	0.57521
	7.3			0.002314	0.522116
	4.8			0.001648	0.510832
	2.4			0.004829	0.504959
	1.9			0.009543	0.487354
	1.2			0.025154	0.54712
	0.8			0.088324	0.581748
	0.4			0.438901	0.658752
	0.24			0.679054	0.692247
	0.12			2.614235	0.727653
	0.06			42.39068	0.617623
	0.024			30.17337	0.738094
	0.012			64.50514	0.663632
	0.002			983.6452	0.415032
	0.001			997.9108	0.427407
	0.0002			2504.572	0.183129

Table B12. Fitted parameters of *Equation (4.3)* for 0.4 mM KPFOS aqueous solutions with various concentrations of NaCl as the background ions.

PFAS	Concentration (mM)	Salt	Concentration (mM)	t* [s]	n
KPFOS	0.4	NaCl	0	307.6646245	0.205120493
			0.5	37.70146658	0.222606044
			1	6.69460108	0.282595212
			5	1.484229733	0.337885631
			10	0.678251157	0.445889963
			50	3.87788525	0.623272862
			100	4.453508597	0.642921361
			200	13.11767727	0.656172306

Table B13. Fitted parameters of *Equation (4.3)* for 0.4 mM KPFOS aqueous solutions with various concentrations of $CaCl_2$ as the background ions.

PFAS	Concentration (mM)	Salt	Concentration (mM)	t* [s]	n
KPFOS	0.4	$CaCl_2$	0	307.6646245	0.205120493
			0.1	0.681613655	0.557320632

			0.5	0.452532006	0.643433695
			1	0.367505338	0.692631112
			5	0.437864718	0.696037803
			10	0.412052986	0.70767168
			50	0.399773552	0.761867957
			100	0.475131616	0.784391572

Table B14. Fitted parameters of *Equation (4.3)* for 0.4 mM PFOA aqueous solutions with various concentrations of NaCl as the background ions.

PFAS	Concentration (mM)	Salt	Concentration (mM)	t* [s]	n
PFOA	0.4	NaCl	0	11353.17128	0.181282428
			0.5	620.1246551	0.182537021
			1	46.41882951	0.235518285
			5	5.213302676	0.24461233
			10	1.213635718	0.310853989
			50	0.410993057	0.382948025
			100	0.384804362	0.430943271
			200	0.322027678	0.515041321

Table B15. Fitted parameters of *Equation (4.3)* for 0.4 mM PFOA aqueous solutions with various concentrations of $CaCl_2$ as the background ions.

PFAS	Concentration (mM)	Salt	Concentration (mM)	t* [s]	n
PFOA	0.4	$CaCl_2$	0	11353.17128	0.181282428
			0.1	0.652660471	0.453589518
			0.5	0.77614112	0.412976288
			1	1.388582144	0.409573827
			5	0.552622226	0.543718592
			10	0.481132134	0.571806486
			50	0.468817411	0.627357594
			100	0.495326027	0.67278935

Table B16. Fitted parameters of *Equation (4.3)* for 0.4 mM KPFBS aqueous solutions with various concentrations of $CaCl_2$ as the background ions.

PFAS	Concentration (mM)	Salt	Concentration (mM)	t* [s]	n
KPFBS	0.4	$CaCl_2$	0	4.14934E+21	0.01440141
			0.1	1.12171E+21	0.052388246
			0.5	9.95184E+20	0.046024103
			1	9.89137E+20	0.041103611
			5	3.55041E+19	0.047152941

			10	3.56231E+19	0.051907516
			50	4.2581E+12	0.075935982
			100	2044343017	0.084310727

Appendix C. Supporting materials for Chapter 5

Table C1. Chemical shift of peaks shown in **Figure 5.1**.

Sample	Peak 2 (-ppm)	Peak 3 (-ppm)	Peak 4 (-ppm)	Peak 5 (-ppm)	Peak 6 (-ppm)	Peak 7 (-ppm)	Peak 8 (-ppm)	Peak 1 (-ppm)
1.1 mM KPFOS	116.17	122.62	123.39	123.52	123.67	124.46	127.80	82.56
1.1 mM KPFOS+100 mM $CaCl_2$	115.87	122.48	123.44, 123.67			124.65	128.29	83.64

Table C2. Chemical shift of peaks shown in **Figure 5.4**.

Sample	Peak 2 (-ppm)	Peak 3 (-ppm)	Peak 4 (-ppm)	Peak 5 (-ppm)	Peak 6 (-ppm)	Peak 7 (-ppm)	Peak 1 (-ppm)
9.7 mM PFOA	119.26	123.58	123.81	124.53	124.99	127.82	82.58
9.7 mM PFOA+100 mM $CaCl_2$	119.28	123.59	123.83	124.55	125.00	127.84	82.59

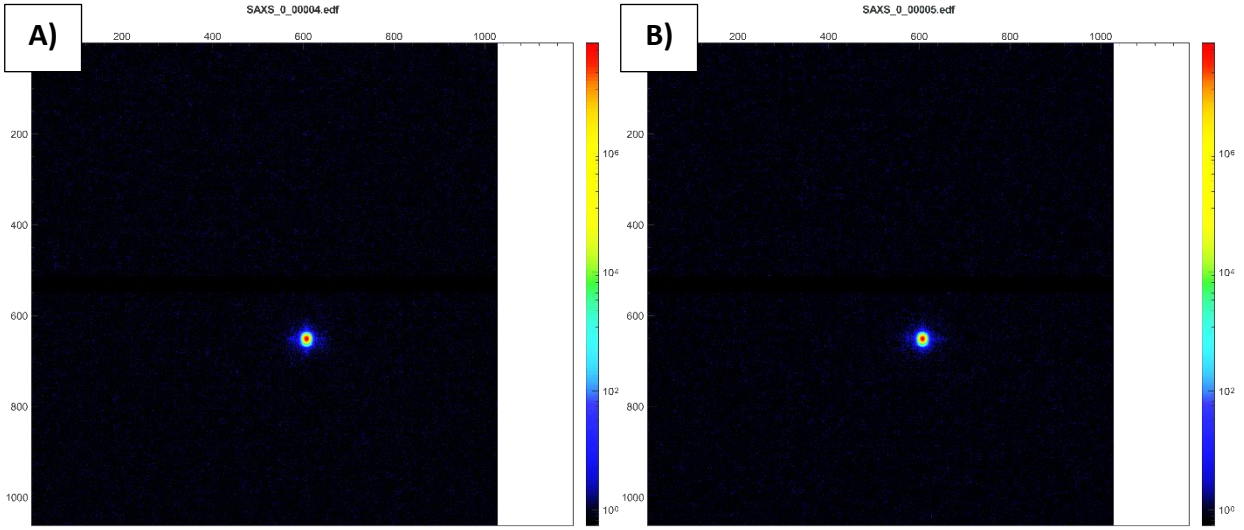

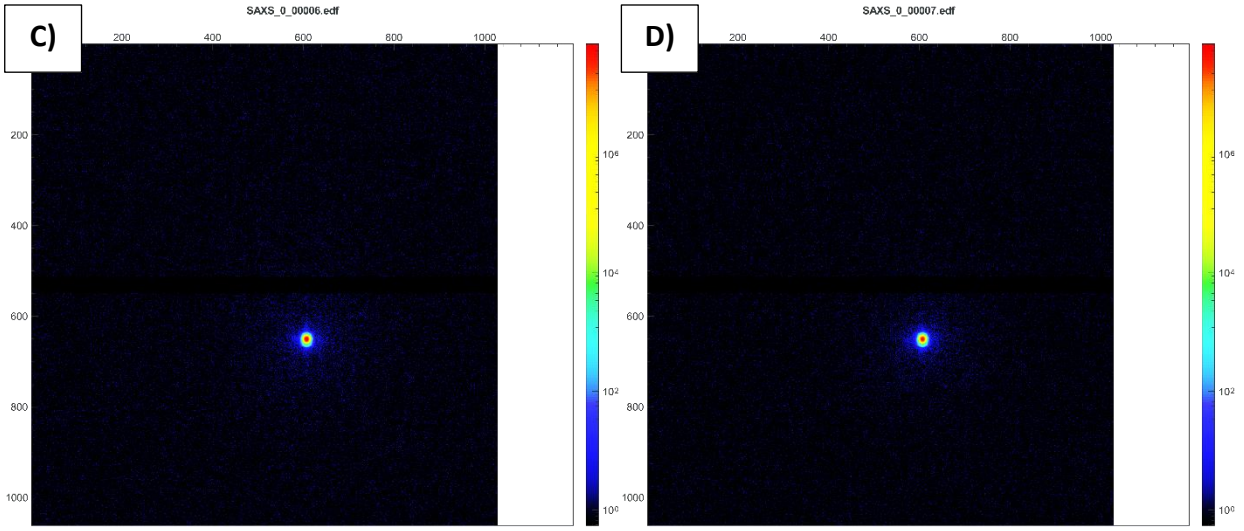

Figure C1. 2D-SAXS patterns of **A)** 600 ppm KPFOS, **B)** 600 ppm KPFOS with 10 mM $CaCl_2$, **C)** 600 ppm KPFOS with 100 mM $CaCl_2$, and **D)** 600 ppm KPFOS with 200 mM $CaCl_2$.

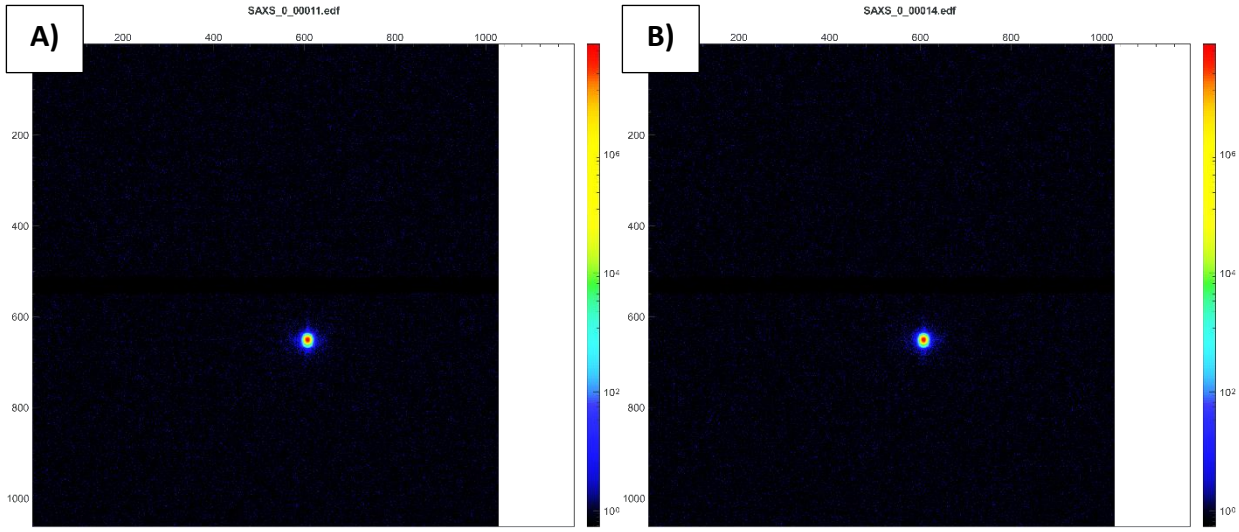

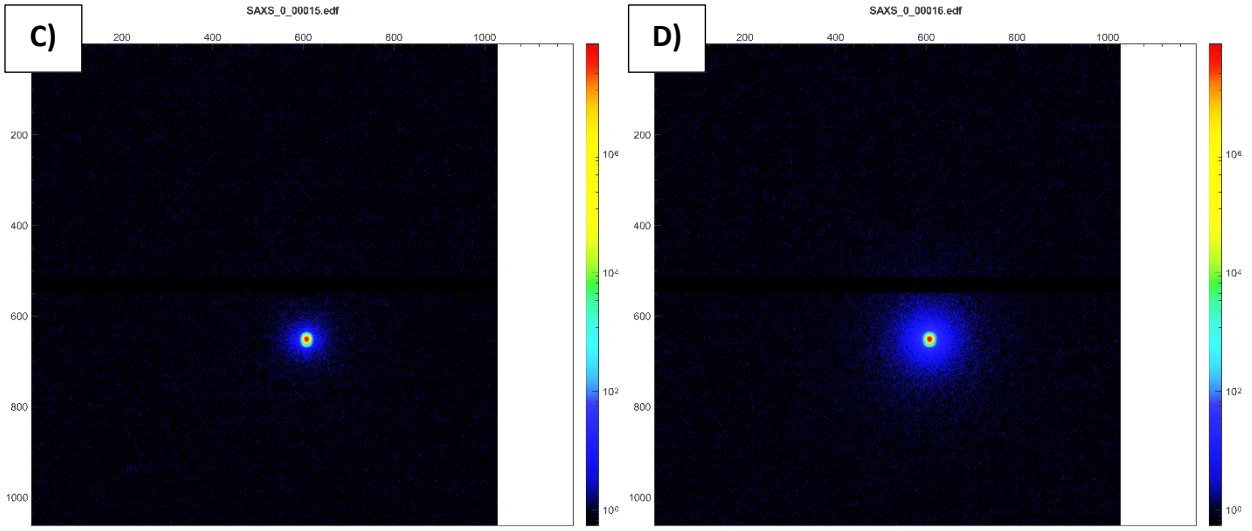

Figure C2. 2D-SAXS patterns of **A)** 4000 ppm PFOA, **B)** 4000 ppm PFOA with 10 mM NaCl, **C)** 4000 ppm PFOA with 100 mM NaCl, and **D)** 5000 ppm PFOA with 100 mM NaCl.

Appendix D. Supporting tables for Chapter 6

Table D1. Fitted equations for the relationship between the various dimensionless numbers and foaming expansion rate for KPFOS with different bulk concentrations.

Dimensionless number	Q_{air} **(L/min)**	**Equation**	R^2
Re_b	0.2	$\frac{H_f}{H_{l0}} = 0.18612Re_b^{-2.6647}$	0.88308
	0.4	$\frac{H_f}{H_{l0}} = 1.04766Re_b^{-1.9498}$	0.83175
	0.6	$\frac{H_f}{H_{l0}} = 5.35512Re_b^{-1.26729}$	0.96281
Ca	0.2	$\frac{H_f}{H_{l0}} = e^{(-9.41\times10^{10}Ca^2+5.32\times10^6Ca-72.34871)}$	0.83773
	0.4	$\frac{H_f}{H_{l0}} = e^{(-7.77\times10^{9}Ca^2+8.90\times10^5Ca-22.7653)}$	0.64006
	0.6	$\frac{H_f}{H_{l0}} = e^{(-1.17\times10^{9}Ca^2+2.29\times10^5Ca-8.69762)}$	0.90268
We_b	0.2	$\frac{H_f}{H_{l0}} = 2.52\times10^{-8}We_b^{-1.64739}$	0.74524
	0.4	$\frac{H_f}{H_{l0}} = 8.90\times10^{-10}We_b^{-2.13558}$	0.76102
	0.6	$\frac{H_f}{H_{l0}} = 6.79\times10^{-6}We_b^{-1.46065}$	0.75671
Fr_b	0.2	$\frac{H_f}{H_{l0}} = 17169.38Fr_b - 8.88804$	0.78223
	0.4	$\frac{H_f}{H_{l0}} = 2481.44Fr_b - 5.1587$	0.82486
	0.6	$\frac{H_f}{H_{l0}} = 1091.20Fr_b - 1.49395$	0.95948
Bq	0.2	$\frac{H_f}{H_{l0}} = 0.00121Bq - 2.40746$	0.70825
	0.4	$\frac{H_f}{H_{l0}} = 0.00132Bq - 4.00619$	0.87184
	0.6	$\frac{H_f}{H_{l0}} = 0.00156Bq - 1.07306$	0.93758
ζ_p	0.2	$\frac{H_f}{H_{l0}} = -1.508\zeta_p + 1.24257$	0.67863
	0.4		
	0.6		
Θ	0.2	$\frac{H_f}{H_{l0}} = e^{(0.020872\Theta^2-2.65715\Theta+7.99997)}$	0.94397

	0.4	$\frac{H_f}{H_{l0}} = e^{(0.08033\Theta^2 - 1.29406\Theta + 5.72904)}$	0.90474
	0.6	$\frac{H_f}{H_{l0}} = e^{(0.15265\Theta^2 - 2.19106\Theta + 8.98226)}$	0.95009
Ga_b	0.2	$\frac{H_f}{H_{l0}} = -0.9063 Ga_b + 2.46459$	0.72365
	0.4	$\frac{H_f}{H_{l0}} = -0.75268 Ga_b + 1.92353$	0.87702
	0.6	$\frac{H_f}{H_{l0}} = -0.42041 Ga_b + 1.64421$	0.92808

Table D2. Fitted equations for the relationship between the various dimensionless numbers and foaming expansion rate for 0.4 mM PFOA with different NaCl concentrations.

Dimensionless number	Q_{air} **(L/min)**	**Equation**	R^2
Re_b	0.2	$\frac{H_f}{H_{l0}} = 4.01841 Re_b - 6.494$	0.96513
	0.4	$\frac{H_f}{H_{l0}} = 10.00765 Re_b - 9.24582$	0.7546
	0.6	$\frac{H_f}{H_{l0}} = 8.83394 Re_b - 1.86567$	0.96281
Ca	0.2	$\frac{H_f}{H_{l0}} = e^{(-5.57\times10^{10} Ca^2 + 2.91\times10^{6} Ca - 37.12093)}$	0.77979
	0.4	$\frac{H_f}{H_{l0}} = e^{(-1.09\times10^{10} Ca^2 + 1.11\times10^{6} Ca - 26.25044)}$	0.85435
	0.6	$\frac{H_f}{H_{l0}} = e^{(-1.72\times10^{9} Ca^2 + 2.71\times10^{5} Ca - 8.63821)}$	0.77038
We_b	0.2	$\frac{H_f}{H_{l0}} = -1.71 \times 10^5 We_b + 3.58111$	0.93229
	0.4	$\frac{H_f}{H_{l0}} = -1.47 \times 10^5 We_b + 9.12474$	0.73749
	0.6	$\frac{H_f}{H_{l0}} = -1.56 \times 10^4 We_b + 8.37155$	0.60821
Fr_b	0.2	$\frac{H_f}{H_{l0}} = 66.9518 Fr_b^{0.0493} - 45.51554$	0.86342
	0.4		
	0.6		
ζ_p	0.2	$\frac{H_f}{H_{l0}} = 0.58829 \zeta_p - 0.28905$	0.85787
	0.4		
	0.6		
Θ	0.2	$\frac{H_f}{H_{l0}} = 2.38586\Theta - 5.0019$	0.53985

	0.4	$\frac{H_f}{H_{l0}} = 3.517570 - 1.93135$	0.39088
	0.6	$\frac{H_f}{H_{l0}} = 4.574810 - 2.53595$	0.88125
Ga_b	0.2	$\frac{H_f}{H_{l0}} = -0.17095Ga_b + 0.69391$	0.97834
	0.4	$\frac{H_f}{H_{l0}} = -0.27556Ga_b + 1.21368$	0.72808
	0.6	$\frac{H_f}{H_{l0}} = -0.05878Ga_b + 0.97785$	0.6643

Table D3. Fitted equations for the relationship between the various dimensionless numbers and foaming expansion rate for 0.4 mM KPFBS with two $CaCl_2$ concentrations.

Dimensionless number	Q_{air} **(L/min)**	**Equation**	R^2
Re_b	0.6	$\frac{H_f}{H_{l0}} = (1.31495 - 0.12052Re_b)^{\frac{1}{0.09908}}$	0.70942
	0.8		
	1.0		
Ca	0.2	$\frac{H_f}{H_{l0}} = e^{(-5.05\times10^{10}Ca^2+2.14\times10^6Ca-22.18)}$	0.48255
	0.4	$\frac{H_f}{H_{l0}} = e^{(-7.97\times10^{10}Ca^2+6.64\times10^6Ca-136.84641)}$	0.54927
	0.6	$\frac{H_f}{H_{l0}} = e^{(-1.25\times10^{10}Ca^2+1.58\times10^6Ca-47.98364)}$	0.78938
	0.8	$\frac{H_f}{H_{l0}} = e^{(-8.71\times10^{9}Ca^2+1.48\times10^6Ca-61.02557)}$	0.63319
	1.0	$\frac{H_f}{H_{l0}} = e^{(-3.30\times10^{9}Ca^2+6.90\times10^5Ca-33.80138)}$	0.93183
We_b	0.6	$\frac{H_f}{H_{l0}} = 0.00261We_b^{-0.75396}$	0.49497
	0.8	$\frac{H_f}{H_{l0}} = 3.28\times10^{-6}We_b^{-1.51664}$	0.82483
	1.0	$\frac{H_f}{H_{l0}} = 4.19\times10^{-4}We_b^{-1.07105}$	0.86344
Fr_b	0.6	$\frac{H_f}{H_{l0}} = 666.54643Fr_b - 0.16715$	0.58216
	0.8	$\frac{H_f}{H_{l0}} = 497.94522Fr_b - 2.4526$	0.76269
	1.0	$\frac{H_f}{H_{l0}} = 352.70274Fr_b - 2.3281$	0.92017
	0.2		

ζ_p	0.4	$\frac{H_f}{H_{l0}} = 0.6598\zeta_p - 0.6121$	0.62076
	0.6		
	0.8		
	1.0		
Ga_b	0.6	$\frac{H_f}{H_{l0}} = -0.66788Ga_b - 1.99023$	0.88273
	0.8		
	1.0		

Table D4. Foaming parameters and experimental values for KPFOS aqueous solutions used for dimensional analysis of foaming expansion rate with $D_c = 0.05\ m$, $D_f = 0.00007\ m$, $\rho = 990\ kg/m^3$, $\eta = 0.001\ kg/s \cdot m$.

KPFOS concentration (ppm)	Q_{air} (m^3/s)	t_e (s)	**Equilibrium?**	γ $(N/m = kg/s^2)$	E $(N/m = kg/s^2)$	η_s $(N \cdot s/m = kg/s)$	Re_b	Ca	We_b	Fr_b	Bq	Θ	ζ_p	$\frac{R}{H_{l0}}$	$\frac{H_f}{H_{l0}}$
100	3E-06	104.9	Yes	0.0523738	0.013956	0.0018475	0.215	3E-05	5E-06	0.001	11334	4.127	98.01	0.011	10.92
100	3E-06	93.55	Yes	0.0523738	0.013956	0.0018475	0.275	3E-05	7E-06	9E-04	8882	4.127	87.43	0.014	4.379
200	3E-06	95.68	Yes	0.0435405	0.0161413	0.0014776	0.232	3E-05	7E-06	0.001	8396	2.816	89.42	0.012	9.726
200	3E-06	87.96	Yes	0.0435405	0.0161413	0.0014776	0.218	3E-05	7E-06	0.001	8955	2.816	82.2	0.011	11.32
300	3E-06	21.33	Yes	0.0420005	0.0127471	0.0014075	0.305	3E-05	1E-05	8E-04	6093	3.513	19.93	0.015	3.41
300	3E-06	22.73	Yes	0.0420005	0.0127471	0.0014075	0.367	3E-05	1E-05	7E-04	5063	3.513	21.24	0.018	4.902
400	3E-06	13.49	Yes	0.0394964	0.0097478	0.0010724	0.352	3E-05	1E-05	7E-04	4017	4.318	12.61	0.017	2.526
500	3E-06	16.97	Yes	0.0381165	0.0068885	0.0011099	0.425	3E-05	1E-05	6E-04	3447	6.416	15.86	0.021	1.1
10	7E-06	17.78	Yes	0.0623411	0.0078525	0.0010023	0.594	4E-05	3E-05	0.003	4455	8.666	33.23	0.015	2.585
10	7E-06	19.29	Yes	0.0623411	0.0078525	0.0010023	1.038	4E-05	4E-05	0.002	2550	8.666	36.06	0.026	0.648
300	7E-06	39.17	Yes	0.0420005	0.0127471	0.0014075	0.282	6E-05	2E-05	0.007	13154	3.513	73.21	0.007	12.01
300	7E-06	42.46	Yes	0.0420005	0.0127471	0.0014075	0.425	6E-05	3E-05	0.005	8742	3.513	79.36	0.011	8.731
400	7E-06	40.6	Yes	0.0394964	0.0097478	0.0010724	0.285	7E-05	2E-05	0.007	9930	4.318	75.89	0.007	12.41
500	7E-06	22.9	Yes	0.0381165	0.0068885	0.0011099	0.499	7E-05	3E-05	0.004	5873	6.416	42.8	0.012	2.513
500	7E-06	45.47	Yes	0.0381165	0.0068885	0.0011099	0.52	7E-05	4E-05	0.004	5634	6.416	84.99	0.013	2.821
500	7E-06	48.35	Yes	0.0381165	0.0068885	0.0011099	0.412	7E-05	3E-05	0.005	7115	6.416	90.37	0.01	4.13
600	7E-06	17.58	Yes	0.032702	0.0063839	0.001128	0.48	8E-05	4E-05	0.004	6198	6.159	32.86	0.012	3.358
600	7E-06	24.07	Yes	0.032702	0.0063839	0.001128	0.523	8E-05	4E-05	0.004	5697	6.159	44.99	0.013	2.395
600	7E-06	25.57	Yes	0.032702	0.0063839	0.001128	0.335	8E-05	3E-05	0.006	8882	6.159	47.79	0.008	7.73
10	1E-05	16.87	Yes	0.0623411	0.0078525	0.0010023	1.156	6E-05	7E-05	0.006	3433	8.666	47.3	0.019	4.385
10	1E-05	18.88	Yes	0.0623411	0.0078525	0.0010023	2.095	6E-05	1E-04	0.003	1895	8.666	52.93	0.035	2.526
10	1E-05	18.7	Yes	0.0623411	0.0078525	0.0010023	1.612	6E-05	1E-04	0.004	2463	8.666	52.43	0.027	3.135
400	1E-05	34.71	Yes	0.0394964	0.0097478	0.0010724	0.475	1E-04	5E-05	0.014	8937	4.318	97.32	0.008	13.61
500	1E-05	48.05	Yes	0.0381165	0.0068885	0.0011099	0.741	1E-04	8E-05	0.009	5935	6.416	134.7	0.012	9.098

500	1E-05	41.8	Yes	0.0381165	0.0068885	0.0011099	0.606	1E-04	6E-05	0.011	7254	6.416	117.2	0.01	9.988
600	1E-05	17.67	Yes	0.032702	0.0063839	0.001128	0.824	1E-04	1E-04	0.008	5423	6.159	49.54	0.014	6.211
600	1E-05	14.47	Yes	0.032702	0.0063839	0.001128	0.939	1E-04	1E-04	0.007	4760	6.159	40.57	0.016	6.682
600	1E-05	18.65	Yes	0.032702	0.0063839	0.001128	0.939	1E-04	1E-04	0.007	4760	6.159	52.29	0.016	4.614

Table D5. Foaming parameters and experimental values for 0.4 mM PFOA aqueous solutions containing varied concentrations of NaCl used for dimensional analysis of foaming expansion rate with $D_c = 0.05\ m$, $D_f = 0.00007\ m$, $\rho = 990\ kg/m^3$, $\eta = 0.001\ kg/s \cdot m$.

NaCl concentration (mM)	Q_{air} (m^3/s)	t_e (s)	**Equilibrium?**	γ $(N/m = kg/s^2)$	E $(N/m = kg/s^2)$	η_s $(N \cdot s/m = kg/s)$	Re_b	Ca	We_b	Fr_b	Bq	Θ	ζ_p	$\frac{R}{H_{l0}}$	$\frac{H_f}{H_{l0}}$
10	3E-06	11.85	Yes	0.054358	0.003888	0.000627	0.18744	2.45E-05	4.6E-06	0.001277	4416.146	13.98273	11.07447	0.009294	2.814343
50	3E-06	20.38	Yes	0.051833	0.004609	0.00075	0.21648	2.57E-05	5.57E-06	0.001105	4571.279	11.24561	19.04622	0.010734	2.578724
100	3E-06	20.51	Yes	0.049115	0.003541	0.000638	0.23496	2.71E-05	6.38E-06	0.001018	3582.166	13.8722	19.16771	0.01165	2.513274
0	7E-06	14.32	Yes	0.052562	0.009497	0.00086	0.5808	5.07E-05	2.95E-05	0.003296	3906.82	5.534512	26.76564	0.014399	3.756821
0	7E-06	18.1	Yes	0.052562	0.009497	0.00086	0.528	5.07E-05	2.68E-05	0.003626	4297.502	5.534512	33.83087	0.01309	4.25424
0.5	7E-06	13.09	Yes	0.057208	0.008201	0.000947	0.6468	4.66E-05	3.01E-05	0.00296	3864.334	6.976007	24.46664	0.016035	4.07098
0.5	7E-06	20.67	Yes	0.057208	0.008201	0.000947	0.48048	4.66E-05	2.24E-05	0.003984	5201.988	6.976007	38.63448	0.011912	4.457135
0.5	7E-06	19.06	Yes	0.057208	0.008201	0.000947	0.60456	4.66E-05	2.82E-05	0.003167	4134.331	6.976007	35.62522	0.014988	4.457135
1	7E-06	50.29	Yes	0.056617	0.007263	0.001171	0.48576	4.71E-05	2.29E-05	0.003941	6364.537	7.79571	93.9975	0.012043	6.080291
1	7E-06	54.76	Yes	0.056617	0.007263	0.001171	0.52272	4.71E-05	2.46E-05	0.003662	5914.519	7.79571	102.3524	0.012959	6.636614
5	7E-06	38.71	Yes	0.056704	0.005839	0.000771	0.3432	4.7E-05	1.61E-05	0.005578	5929.746	9.711208	72.35321	0.008508	5.622142
5	7E-06	45.56	Yes	0.056704	0.005839	0.000771	0.36168	4.7E-05	1.7E-05	0.005293	5626.766	9.711208	85.15661	0.008967	5.078908
10	7E-06	25.76	Yes	0.054358	0.003888	0.000627	0.35112	4.91E-05	1.72E-05	0.005452	4714.983	13.98273	48.14825	0.008705	6.780604
10	7E-06	36.6	Yes	0.054358	0.003888	0.000627	0.43824	4.91E-05	2.15E-05	0.004368	3777.667	13.98273	68.40939	0.010865	6.643159

10	7E-06	53.45	Yes	0.054358	0.003888	0.000627	0.41712	4.91E-05	2.05E-05	0.004589	3968.942	13.98273	99.90388	0.010341	6.636614
50	7E-06	45.74	Yes	0.051833	0.004609	0.00075	0.34056	5.14E-05	1.75E-05	0.005621	5811.549	11.24561	85.49305	0.008443	6.734789
100	7E-06	25.6	Yes	0.049115	0.003541	0.000638	0.51744	5.43E-05	2.81E-05	0.0037	3253.192	13.8722	47.84919	0.012828	5.059273
100	7E-06	37.55	Yes	0.049115	0.003541	0.000638	0.50952	5.43E-05	2.77E-05	0.003757	3303.76	13.8722	70.18505	0.012632	5.137813
200	7E-06	17.07	Yes	0.046207	0.00411	0.000744	0.55704	5.77E-05	3.21E-05	0.003437	3526.18	11.24333	31.90569	0.01381	4.45059
200	7E-06	40.52	Yes	0.046207	0.00411	0.000744	0.63096	5.77E-05	3.64E-05	0.003034	3113.071	11.24333	75.7363	0.015643	4.16261
200	7E-06	15.54	Yes	0.046207	0.00411	0.000744	0.6732	5.77E-05	3.89E-05	0.002844	2917.741	11.24333	29.04596	0.01669	4.005531
0	1E-05	29.89	Yes	0.052562	0.009497	0.00086	1.15632	7.61E-05	8.8E-05	0.005587	2943.494	5.534512	83.80151	0.019111	7.016224
0.5	1E-05	23.7	Yes	0.057208	0.008201	0.000947	1.01376	6.99E-05	7.09E-05	0.006373	3698.288	6.976007	66.44683	0.016755	6.675884
0.5	1E-05	28.72	Yes	0.057208	0.008201	0.000947	0.94644	6.99E-05	6.62E-05	0.006827	3961.347	6.976007	80.52122	0.015643	6.531895
1	1E-05	36.35	Yes	0.056617	0.007263	0.001171	0.83952	7.06E-05	5.93E-05	0.007696	5523.938	7.79571	101.9132	0.013875	7.579092
1	1E-05	30.72	Yes	0.056617	0.007263	0.001171	0.9108	7.06E-05	6.43E-05	0.007094	5091.63	7.79571	86.12855	0.015053	7.009679
5	1E-05	16.28	Yes	0.056704	0.005839	0.000771	0.54648	7.05E-05	3.85E-05	0.011823	5585.993	9.711208	45.64364	0.009032	7.297658
5	1E-05	22.47	Yes	0.056704	0.005839	0.000771	0.82368	7.05E-05	5.81E-05	0.007844	3706.091	9.711208	62.99832	0.013614	7.225663
5	1E-05	24.65	Yes	0.056704	0.005839	0.000771	0.58608	7.05E-05	4.13E-05	0.011024	5208.561	9.711208	69.11031	0.009687	6.780604
10	1E-05	33.55	Yes	0.054358	0.003888	0.000627	0.693	7.36E-05	5.1E-05	0.009323	3583.387	13.98273	94.06291	0.011454	7.736172
10	1E-05	33.16	Yes	0.054358	0.003888	0.000627	0.59796	7.36E-05	4.4E-05	0.010805	4152.932	13.98273	92.96949	0.009883	7.101308
50	1E-05	41.59	Yes	0.051833	0.004609	0.00075	0.80784	7.72E-05	6.23E-05	0.007998	3674.95	11.24561	116.6044	0.013352	7.611817
100	1E-05	36.97	Yes	0.049115	0.003541	0.000638	0.68508	8.14E-05	5.58E-05	0.009431	3685.697	13.8722	103.6514	0.011323	7.644542
200	1E-05	33.53	Yes	0.046207	0.00411	0.000744	0.83952	8.66E-05	7.27E-05	0.007696	3509.547	11.24333	94.00684	0.013875	7.232208

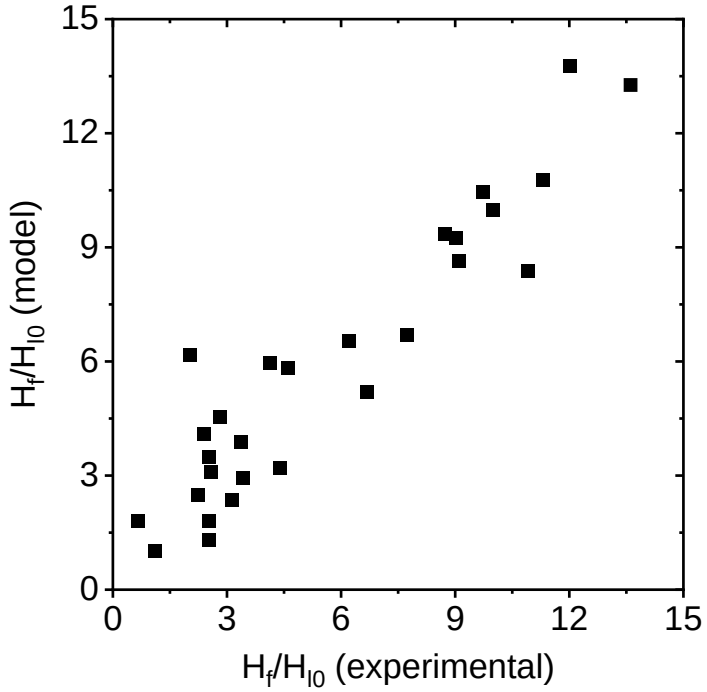

Figure D1. Predicted expansion rate of foaming for KPFOS aqueous solutions based on *Equation (6.10)*, compared to the experimental expansion rate of foaming for KPFOS aqueous solutions.

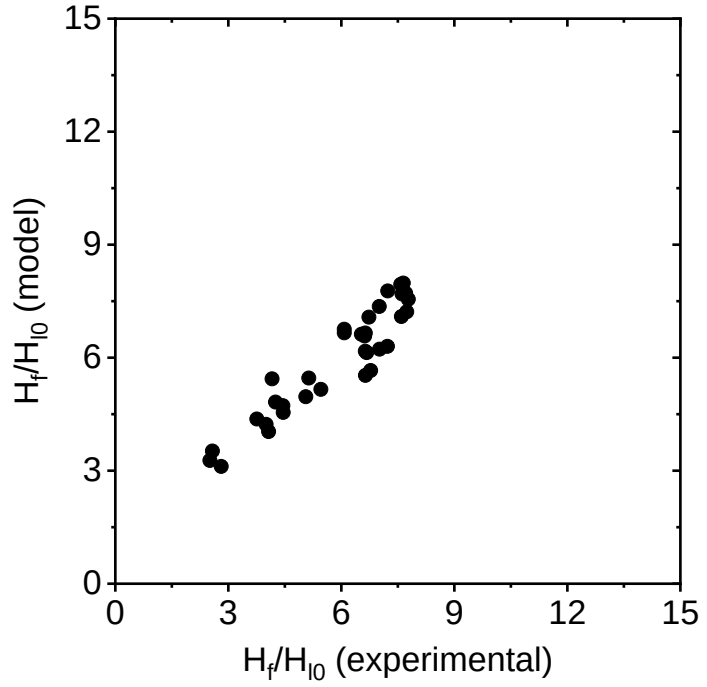

Figure D2. Predicted expansion rate of foaming for PFOA aqueous solutions based on *Equation (6.12)*, compared to the experimental expansion rate of foaming for PFOA aqueous solutions.

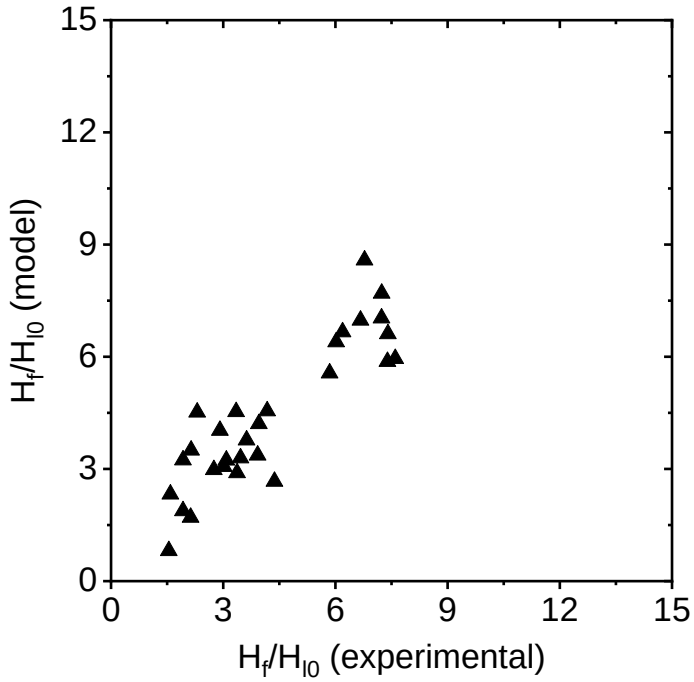

Figure D3. Predicted expansion rate of foaming for KPFBS aqueous solutions based on *Equation (6.14)*, compared to the experimental expansion rate of foaming for KPFBS aqueous solutions.

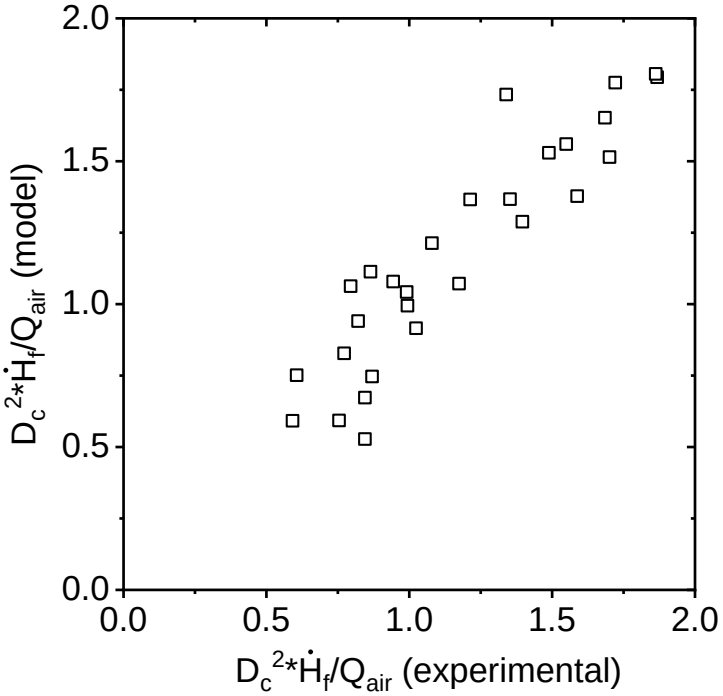

Figure D4. Predicted kinetics of foaming for KPFOS aqueous foams based on *Equation (6.18)*, compared to the experimental kinetics of foaming for KPFOS aqueous foams.

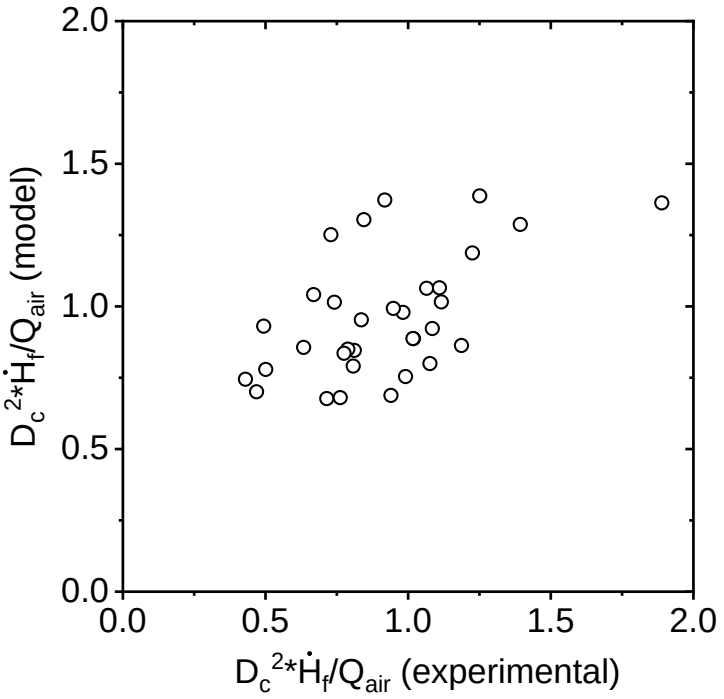

Figure D5. Predicted kinetics of foaming for PFOA aqueous foams based on *Equation (6.20)*, compared to the experimental kinetics of foaming for PFOA aqueous foams.

Appendix E. Supporting tables for Chapter 7

Table E1. Power-law fitted parameters for the average bubble radius of 0.4 mM PFAS aqueous foams prepared by air-sparging the PFAS solutions with different times.

PFAS	Q_{air} (L/min)	D_f (μm)	$R_{ave}(t)$	R^2
KPFOS	0.2	40-100	$R_{ave} = 124.46004(1+t)^{0.05239}$	0.67296
KPFOS	0.2	16-40	$R_{ave} = 11.60611(1+t)^{0.46146}$	0.96087
KPFOS	0.4	40-100	$R_{ave} = 37.08698(1+t)^{0.28132}$	0.85778
PFOA	0.4	40-100	$R_{ave} = 108.74753(1+t)^{0.03827}$	0.78822
KPFOS	0.6	40-100	$R_{ave} = 44.02877(1+t)^{0.24318}$	0.76776
PFOA	0.6	40-100	$R_{ave} = 100.77242(1+t)^{0.07987}$	0.71735
KPFBS	0.6	40-100	$R_{ave} = 106.58734(1+t)^{0.32672}$	0.95061
KPFBS	0.8	40-100	$R_{ave} = 84.3757(1+t)^{0.35}$	0.64376
KPFBS	1.0	40-100	$R_{ave} = 81.319(1+t)^{0.30895}$	0.5202

Table E2. Exponential fitted parameters for 0.4 mM PFAS aqueous foams with an air-sparging time of 30 s.

PFAS	$C_{(Electrolytes)}$	D_f (μm)	Q_{air} (L/min)	A	B	C	R^2	τ_f (s)
KPFOS	-	40-100	0.2	14.87395	51.71243	-0.004	0.99163	250.00
	-	40-100	0.4	39.71867	86.79649	-0.00763	0.89098	131.06
	-	40-100	0.5	58.90647	92.58365	-0.00407	0.92664	245.70
	-	40-100	0.6	22.72034	142.66056	-0.00865	0.9729	115.61
	-	16-40	0.2	19.9006	62.90061	-0.0076	0.91745	131.58
	-	16-40	0.4	19.06466	109.63355	-0.01306	0.97392	76.57
	-	16-40	0.5	14.86755	121.54171	-0.01163	0.96905	85.98
	-	16-40	0.6	13.84958	184.64829	-0.01844	0.98894	54.23
	0.5 mM NaCl	40-100	0.2	0	84.63337	-0.00228	0.9905	438.60
	1 mM NaCl	40-100	0.2	0	93.91653	-0.00195	0.96817	512.82
	5 mM NaCl	40-100	0.2	0	102.93815	-0.0105	0.92587	95.24
	10 mM NaCl	40-100	0.2	0	97.18437	-0.01575	0.97312	63.49
	50 mM NaCl	40-100	0.2	-	-	-	-	-
	100 mM NaCl	40-100	0.2	-	-	-	-	-
	200 mM NaCl	40-100	0.2	-	-	-	-	-
	0.1 mM $CaCl_2$	40-100	0.2	0	81.34983	-0.00178	0.96887	561.80
	0.5 mM $CaCl_2$	40-100	0.2	0	72.38159	-0.0016	0.97104	625.00
	1 mM $CaCl_2$	40-100	0.2	0	72.00426	-0.00144	0.85321	694.44
	5 mM $CaCl_2$	40-100	0.2	0	75.86233	-0.00209	0.91456	478.47

	10 mM $CaCl_2$	40-100	0.2	0	95.76795	-0.00205	0.92983	487.80
	50 mM $CaCl_2$	40-100	0.2	54.5569	18.86008	-0.00255	0.89991	392.16
	100 mM $CaCl_2$	40-100	0.2	48.25012	48.81527	-0.000930211	0.95445	1075.02
PFOA	-	40-100	0.4	0	61.03051	-0.16671	0.93631	6.00
	-	40-100	0.6	0	94.50536	-0.10818	0.96573	9.24
	0.5 mM NaCl	40-100	0.4	0	67.91103	-0.07957	0.97719	12.57
	1 mM NaCl	40-100	0.4	0	101.83718	-0.06369	0.94334	15.70
	5 mM NaCl	40-100	0.4	0	89.46906	-0.07117	0.94306	14.05
	10 mM NaCl	40-100	0.4	0	107.08906	-0.07	0.95475	14.29
	50 mM NaCl	40-100	0.4	0	106.32204	-0.0795	0.96748	12.58
	100 mM NaCl	40-100	0.4	0	88.19734	-0.10507	0.95996	9.52
	200 mM NaCl	40-100	0.4	2.47891	73.10407	-0.13618	0.96003	7.34
	0.1 mM $CaCl_2$	40-100	0.4	1.78206	73.61091	-0.10974	0.97945	9.11
	0.5 mM $CaCl_2$	40-100	0.4	0	110.70162	-0.07806	0.96042	12.81
	1 mM $CaCl_2$	40-100	0.4	0	109.26776	-0.06673	0.96634	14.99
	5 mM $CaCl_2$	40-100	0.4	12.59775	51.77223	-0.3393	0.97831	2.95
	10 mM $CaCl_2$	40-100	0.4	13.2652	24.58281	-0.3849	0.94644	2.60
	50 mM $CaCl_2$	40-100	0.4	6.41991	25.65214	-0.3291	0.95379	3.04
	100 mM $CaCl_2$	40-100	0.4	1.46029	45.18034	-0.27436	0.96836	3.64
KPFBS	-	40-100	0.4	10.31035	16.76729	-0.34377	0.90878	2.91
	-	40-100	0.6	0	66.72564	-0.22637	0.9342	4.42
	100 mM $CaCl_2$	40-100	0.6	0.01649	15.38455	-1.6853	0.97557	0.59
	-	40-100	0.8	0	101.27021	-0.21963	0.96631	4.55
	100 mM $CaCl_2$	40-100	0.8	16.82981	30.70009	-0.74101	0.91307	1.35
	-	40-100	1.0	0	138.04385	-0.19615	0.90155	5.10
	100 mM $CaCl_2$	40-100	1.0	5.21316	52.52819	-0.29426	0.95692	3.40

Table E3. Exponential fitted parameters for the average bubble radius of 0.4 mM KPFOS aqueous foams containing various $CaCl_2$ concentrations. The air-sparging time to prepare the foams was 30 s.

$CaCl_2$ concentration (mM)	$\boldsymbol{R_{ave}(t)}$	$\boldsymbol{R^2}$	**Bubble growth rate ($\boldsymbol{R_{ave}(t)'}$)**
0	$R_{ave} = 166.07998 - 40.79252e^{-0.02554t}$	0.7022	$\dot{R}_{ave} = -40.79252 - 0.02554e^{-0.02554t}$
0.1	$R_{ave} = 1105.24412 - 973.66196e^{-0.000298278t}$	0.97139	$\dot{R}_{ave} = -973.66196 - 0.000298278e^{-0.000298278t}$
0.5	$R_{ave} = 309.2326 - 148.64775e^{-0.00262t}$	0.90119	$\dot{R}_{ave} = -148.64775 - 0.00262e^{-0.00262t}$
1	$R_{ave} = -18.60006 + 193.80184e^{0.00114t}$	0.94684	$\dot{R}_{ave} = 193.80184 * 0.00114e^{0.00114t}$
5	$R_{ave} = 161.94127 + 25.71288e^{0.00629t}$	0.92655	$\dot{R}_{ave} = 25.71288 * 0.00629e^{0.00629t}$
10	$R_{ave} = -37041.50585 + 37201.78821e^{0.0000129159t}$	0.94118	$\dot{R}_{ave} = 37201.78821 * 0.0000129159e^{0.0000129159t}$
50	$R_{ave} = 770.49423 - 634.37779e^{-0.00101t}$	0.98012	$\dot{R}_{ave} = -634.37779 - 0.00101e^{-0.00101t}$
100	$R_{ave} = 1022.90552 - 882.44637e^{-0.000597296t}$	0.985	$\dot{R}_{ave} = -882.44637 - 0.000597296e^{-0.000597296t}$

VITA

Muchu Zhou, originally from Urumqi, Xinjiang in China, dedicated her freshman through junior years to her undergraduate studies at the East China University of Science and Technology (ECUST) in Shanghai, China, from September 2012 to June 2015. During her undergraduate years, Muchu took advantage of an exchange program to study at New Mexico State University (NMSU) starting in August 2015. The following summer, she achieved a significant milestone by earning dual bachelor's degrees in chemical engineering from both ECUST and NMSU.

In the spring of 2016, Muchu began her graduate studies under the guidance of Dr. Reza Foudazi and successfully completed her master's degree by the summer of 2018. Opting to further her education, she continued her research with Dr. Foudazi, eventually transitioning to the University of Oklahoma (OU) in the summer of 2021 to pursue her Ph.D. In Spring 2024, Muchu completed her Ph.D. in the School of Sustainable Chemical, Biological, and Materials Engineering at OU.

Following her Ph.D. graduation, Muchu relocated to Knoxville, TN, where she embarked on a new chapter in her academic career as a Postdoctoral Research Associate. She joined the Soft Matter Group at the Oak Ridge National Laboratory (ORNL), pursuing further research in her field.

SELECTED PUBLICATIONS

1. **Zhou, M.**, Abbasian, Z., Shiau, B., Grady, B., Foudazi, R. Air-water Interfacial Properties of Perfluorosulfonic Acids Salts with Different Chain Lengths. *Colloids and Surfaces A: Physicochemical and Engineering Aspects* (2024): 134129.
2. Durgut, E., **Zhou, M.**, Dikici, BA., Foudazi, R., Claeyssens, F. Modifying Pickering Polymerized High Internal Phase Emulsion Morphology by Adjusting Particle Hydrophilicity. *Colloids and Surfaces A: Physicochemical and Engineering Aspects* (2023):132629.

3. **Zhou, M.**, Bandegi, A., Foudazi, R. Control of Pore Interconnectivity in Emulsion Templated Porous Polymers. *Polymer* (2023): 126085.
4. Abbasian, Z., **Zhou, M.**, Foudazi, R. Nanoemulsion Polymerization and Templating: Potentials and Perspectives. *Journal of Applied Physics* 131.15 (2022): 150902.
5. **Zhou, M.**, Foudazi, R. Effect of Co-surfactant on the Properties of Polymerized High Internal Phase Emulsions (PolyHIPEs). *Langmuir* 2021 37(26), 7907-7918.
6. Sanatkaran, N., **Zhou, M.**, Foudazi, R. Interdroplet and Structural Interactions in Depletion-induced Attractive Macro- and Nano-emulsions. *Journal of Rheology* 65.3 (2021): 453-461.
7. Malakian, A.[*], **Zhou, M.**[*], Zowada, RT., Foudazi, R. Synthesis and in situ functionalization of microfiltration membranes via high internal phase emulsion templating. *Polymer International* 68.7 (2019): 1378-1386.

[*]**Equal contribution**

SELECTED PRESENTATIONS

- 2024 American Physical Society (APS) March Meeting
  - Oral presentation: *Effect of Physicochemical Properties of Per- and Polyfluoroalkyl Substances (PFAS) on Their Foaming Behavior*
- 2023 American Institute of Chemical Engineers (AIChE) Annual Meeting
  - Oral presentation: *Effect of Salt on Per- and Polyfluoroalkyl Substances (PFAS) Air-Water Interfacial Properties*
- 2023 Future of Rheology Seminar Series by Society of Rheology (SoR) (**Competitive**)
- 2023 APS March Meeting
  - Oral presentation: *Per- and Polyfluoroalkyl Substances (PFAS) Foams: Effect of Interfacial Properties* (**Promotion to the press**)

- Invited research presentation for the role of Cleaner Engineer at Chemetall (BASF) (Shanghai)
- 2022 SoR 93rd Annual Meeting
  - Oral presentation: *Dilatational Rheological Properties of Per- and Polyfluoroalkyl Substances (PFAS)-Adsorbed Air-water Interfaces*
  - Poster presentation: *Flow of Per- and Polyfluoroalkyl Substances (PFAS) Foams*
- 2021 AIChE Annual Meeting
  - Oral presentations: *Rheology of High Internal Phase Emulsions with Different Interdroplet Interactions* & *Effect of Interdroplet Interactions on Pore Interconnectivity of High Internal Phase Emulsions*
- 2020 18th International Congress on Rheology (ICR)
  - Oral presentation: *Rheological Behavior of High Internal Phase Emulsions with Adhesive and Repulsive Droplets*
- 2019 SoR 91st Annual Meeting
  - Oral presentation: *Effect of Interfacial Properties on the Formation of Polymerized High Internal Phase Emulsions*
  - Poster presentation: *Rheology of Concentrated Emulsions with Adhesive and Non-adhesive Droplets*
  - Gallery of Rheology Competition: *The Saliva Pacifier*
- 2018 National Graduate Research Polymer Conference
  - Poster presentation: *Controlling the Pore Size of Polymerized High Internal Phase Emulsions*